

THE UNIVERSITY OF TULSA
THE GRADUATE SCHOOL

MODELING DOWNHOLE NATURAL SEPARATION

by

Richard Márquez

A dissertation submitted in partial fulfillment of
the requirements for the degree of Doctor of Philosophy
in the Discipline of Petroleum Engineering

The Graduate School

The University of Tulsa

2004

THE UNIVERSITY OF TULSA

THE GRADUATE SCHOOL

MODELING DOWNHOLE NATURAL SEPARATION

by

Richard Márquez

A DISSERTATION

APPROVED FOR THE DISCIPLINE OF

PETROLEUM ENGINEERING

By Dissertation Committee

_____, Chairman

ABSTRACT

Richard Marquez (Doctor of Philosophy in Petroleum Engineering)

Modeling Downhole Natural Separation

Directed by Dr. Mauricio Prado

(176 words)

This work presents three approaches for determining down hole natural separation efficiency.

The first approach is based on a one-cell simplified model that uses macroscopic versions of the drift flux two-phase flow model equations. Closure of the model is obtained through gas-liquid slip correlations for both the vertical and radial directions. The vertical closure equation is a well-known relationship used for vertical flow in pipes. The radial slip correlation is obtained based on available experimental data.

This second approach is based on a mechanistic model for the liquid flow field. A certain geometry for the liquid streamlines is assumed and the liquid velocities and pressure field is determined. Extension to two-phase flow conditions is obtained by tracking the trajectories of individual gas bubbles into this flow domain. Closure equations for bubble characteristic sizes were obtained based on available experimental data.

The third approach is based on a new technique for solving the two-dimensional governing equations of the two-phase drift flux model. Closure equations for the interface characteristic length are obtained based on the available experimental data.

ACKNOWLEDGEMENTS

I want to thank to God for His guidance in finishing this work. Also, I wish to dedicate this thesis to my wife, Leydy, for her infinite patience and motivation, my daughter, Mariana, and my sons, Leonardo and Juan. I will always be thankful to them.

I will be extremely grateful to my advisor, Dr. Mauricio Prado, director of Tulsa University Artificial Lift Projects (TUALP), for his supervision, guidance and special encouragement throughout this study.

The author also wishes to thank Dr. Siamack Shirazi, Dr. Leslie Thompson, and Dr. Cem Sarica, members of the Thesis Committee, for their important comments and suggestions.

Acknowledgments are also extended to Mr. Homer Wheeler and Ms. Kelley Friedberg, members of TUALP. I also would like to thank Bin Liu, Carlos Torres, Datong Sun, Rui Pessoa, and other TUALP students for their help. Appreciation is also extended to Ms. Carol Antle and Ms. Paula Brooks. Sincere thanks to Hernan Rincon for his positive encouragement and constant help.

This thesis is also dedicated to my parents Lorenzo and Maria Márquez and in-laws Jose and Hilaidis Medina. I am also thankful to Sara Sanchez for her constant encouragement.

I am very grateful to the Universidad del Zulia (LUZ) and the Centro Internacional de Educación y Desarrollo (CIED) for their financial support and opportunity to accomplish this achievement.

TABLE OF CONTENTS

ABSTRACT	iii
ACKNOWLEDGEMENTS	v
TABLE OF CONTENTS	vii
LIST OF TABLES	xii
LIST OF FIGURES	xiii
CHAPTER I	1
INTRODUCTION	1
CHAPTER II	7
LITERATURE REVIEW AND BACKGROUND	7
Lea and Bearden	7
Alhanati	9
McCoy	10
Serrano	12
Harun	13
Liu	13
CHAPTER III	15
EXPERIMENTAL DATA	15
Prediction of Flow Pattern Boundaries	15
Classification of the Available Experimental Data	24

CHAPTER IV	28
SIMPLIFIED MODEL	28
General Formulation	30
Alhanati's Simplified Model.....	38
Serrano's Simplified Model.....	39
New Simplified Model.....	41
Slip Velocity Analysis	42
Slip Velocity in the Vertical Direction	42
Slip Velocity in the radial Direction	43
Slip Velocity Ratio.....	43
New Correlation.....	44
CHAPTER V	50
MECHANISTIC MODEL	50
Simplified Model	50
Liquid-Phase Velocity	51
Gas-Phase Velocity	55
Vertical Direction.....	56
Radial Direction.....	58
Trajectory of a Single Gas Bubble.....	60

Prediction of Natural Separation Efficiency	62
Interface Characteristic Length.....	63
CHAPTER VI.....	66
NEW TWO-DIMENSIONAL TWO-PHASE FLOW MODEL.....	66
Two-Phase Flow Model.....	66
Two Phase Flow Mass and Momentum Balance Equations	66
Vorticity Stream Function Approach.....	67
Pressure Equation.....	68
Slip Velocity	70
Model Governing Equations	71
Procedure to Solve the System of Equations	73
Spatial Domain.....	77
Boundary Conditions	78
Annulus Inlet Boundary.....	80
Annulus Outlet Boundary	81
Casing Wall and Upper/Lower Pump Wall Boundaries	82
Pump Intake Boundary	83
Natural Separation Efficiency Predictions.....	84
Interface Characteristic Length.....	85

CHAPTER VII.....	91
RESULTS AND DISCUSSIONS.....	91
New Correlation.....	91
Mechanistic Model.....	95
Two-Phase Flow Model.....	99
Accuracy of the Model.....	99
Two Phase Flow Field Results.....	100
Sensitivity Analysis	106
CHAPTER VIII	128
CONCLUSIONS AND RECOMMENDATIONS	128
Conclusions.....	128
Recommendations.....	128
NOMENCLATURE	130
REFERENCES	136
APPENDIX A.....	142
Bubbles Terminal Rise Velocity	142
APPENDIX B	147
Kinematics Constitutive Equation	147
APPENDIX C	149

Slip Velocity Analysis	149
APPENDIX D	158
Drag Coefficient Models.....	158
APPENDIX E	161
Two-Phase Flow Model Discretization Scheme.....	161
APPENDIX F.....	185
Gas Void Fraction in the Inlet Boundary	185
APPENDIX G.....	187
Error Calculations	187

LIST OF TABLES

TABLE 3.1 – EXPERIMENTAL CONDITIONS - DISTRIBUTED PER AUTHOR	25
TABLE 3.2 – AVAILABLE EXPERIMENTAL DATA DATABASE	27
TABLE 6.1 – FITTED INTERFACE CHARACTERISTIC LENGTH - TWO-PHASE MODEL APPROACH.....	86

LIST OF FIGURES

FIGURE 1.1 – DETERIORATION OF WATER HEAD CURVES WITH GAS (I-42 RADIAL PUMP) - LEA AND BEARDEN (1982)	3
FIGURE 1.2 – TYPICAL PRODUCTION SYSTEM.....	4
FIGURE 2.1 – SCHEMATIC OF AMOCO TEST FACILITY - LEA AND BEARDEN (1980).....	8
FIGURE 2.2 – NATURAL SEPARATION EFFICIENCY - FROM LEA AND BEARDEN (1980).....	8
FIGURE 2.3 – EXPERIMENTAL FACILITY OF ALHANATI’S WORK (1993)	9
FIGURE 2.4 – ALHANATI’S SIMPLIFIED MODEL (1993)	11
FIGURE 2.5 – DECENTRALIZED DOWNHOLE GAS SEPARATOR - FROM MCCOY ET AL. (1995).....	11
FIGURE 2.6 – CASING SECTION - SERRANO (1999)	12
FIGURE 2.7 – GRID INTO THE CELL DOMAIN - BIN LIU (2001).....	14
FIGURE 3.1 – FLOW PATTERN MAP FOR AIR-WATER.....	19
FIGURE 3.2 – FRICTION GEOMETRY FACTOR - CAETANO ET AL. (1992).....	21
FIGURE 3.3 – DEGREE OF ECCENTRICITY - CAETANO ET AL. (1992)	22
FIGURE 3.4 – MAXIMUM ALLOWABLE PACKING.....	23
FIGURE 3.5 – EXPERIMENTAL DATA DISTRIBUTION PER AUTHOR	24
FIGURE 3.6 – EXPERIMENTAL DATA DISTRIBUTION PER AUTHOR - NATURAL SEPARATION ONLY	25
FIGURE 3.7 – CLASSIFICATION OF THE EXPERIMENTAL DATA - FLOW PATTERN REGIME ...	26
FIGURE 4.1 – RADIAL DRAG EFFECT	29
FIGURE 4.2 – FLOW DOMAIN IN THE BOTTOMHOLE	30
FIGURE 4.3 – VOLUMETRIC BALANCE AROUND A SINGLE CONTROL VOLUME.....	31
FIGURE 4.4 – SLIP VELOCITY ANALYSIS IN THE RADIAL DIRECTION	33

FIGURE 4.5 – SINGLE CONTROL VOLUMES	36
FIGURE 4.6 – M PARAMETER - NEW SIMPLIFIED MODEL	44
FIGURE 4.7 – M PARAMETER - NEW CORRELATION	46
FIGURE 4.8 – BOUNDARIES OF THE NEW CORRELATION	47
FIGURE 4.9 – MODIFIED NEW CORRELATION.....	48
FIGURE 5.1 – LIQUID STREAMLINES.....	51
FIGURE 5.2 – FLOW THROUGHOUT TWO LIQUID STREAMLINES.....	52
FIGURE 5.3 – ACCELERATION OF THE LIQUID PHASE IN FRONT THE PUMP INTAKE	53
FIGURE 5.4 – LIQUID PHASE VELOCITY PROFILE IN THE RADIAL DIRECTION	55
FIGURE 5.5 – FREE-BODY DIAGRAM - VERTICAL DIRECTION	56
FIGURE 5.6 – FREE-BODY DIAGRAM - RADIAL DIRECTION.....	58
FIGURE 5.7 – TRAJECTORY OF THE BUBBLES INTO THE FLOW DOMAIN	62
FIGURE 5.8 – CROSS-SECTION OF THE WELL BORE	63
FIGURE 5.9 – INTERFACIAL AREA CONCENTRATION a_i	64
FIGURE 5.10 – INTERFACIAL AREA CONCENTRATION a_i - CORRELATION.....	65
FIGURE 6.1 – SOLUTION PROCEDURE FLOWCHART.....	77
FIGURE 6.2 – FLOW DOMAIN	77
FIGURE 6.3 – CORE AND BOUNDARY CONDITIONS	78
FIGURE 6.4 – INFLOW CONDITIONS.....	79
FIGURE 6.5 – SPECIAL POINTS INSIDE THE FLOW DOMAIN.....	83
FIGURE 6.6 – STREAM FUNCTION FOR GAS PHASE	84
FIGURE 6.7 – CROSS-SECTION OF THE WELL BORE	85

FIGURE 6.8 – ESTIMATED INTERFACE CHARACTERISTIC LENGTH - SLUG/CHURN FLOW REGIME.....	87
FIGURE 6.9 – INTERFACE CHARACTERISTIC LENGTH PREDICTION - BUBBLE FLOW REGIME.....	89
FIGURE 6.10 – CORRELATION FOR PREDICTION OF INTERFACE CHARACTERISTIC LENGTH - BUBBLE FLOW REGIME	90
FIGURE 7.1 – PREDICTED AND MEASURED SEPARATION EFFICIENCY - NEW CORRELATION	92
FIGURE 7.2 – GEOMETRY EFFECT - NEW CORRELATION.....	93
FIGURE 7.3 – PREDICTED EFFICIENCY VS. MEASURED EFFICIENCY - MECHANISTIC MODEL	96
FIGURE 7.4 – GEOMETRY EFFECT - MECHANISTIC MODEL	97
FIGURE 7.5 – GAS EFFECT - MECHANISTIC MODEL	99
FIGURE 7.6 – LIQUID STREAM FUNCTION FIELD - TWO-PHASE FLOW MODEL.....	101
FIGURE 7.7 – GAS STREAM FUNCTION FIELD - TWO-PHASE FLOW MODEL	102
FIGURE 7.8 – GAS VOID FRACTION FIELD - TWO-PHASE FLOW MODEL	102
FIGURE 7.9 – LIQUID VELOCITY FIELD IN THE RADIAL DIRECTION - TWO-PHASE FLOW MODEL	103
FIGURE 7.10 – GAS VELOCITY FIELD IN THE RADIAL DIRECTION - TWO-PHASE FLOW MODEL	104
FIGURE 7.11 – GAS VELOCITY FIELD IN THE VERTICAL DIRECTION - TWO-PHASE FLOW MODEL	105
FIGURE 7.12 – PRESSURE GRADIENT FIELD IN THE RADIAL DIRECTION - TWO- PHASE FLOW MODEL	105
FIGURE 7.13 – 1000 BPD AND 50 PSI - BUBBLE FLOW REGIME.....	107

FIGURE 7.14 – 1500 BPD AND 50 PSI - BUBBLE FLOW REGIME.....	108
FIGURE 7.15 – 2000 BPD AND 50 PSI - BUBBLE FLOW REGIME.....	108
FIGURE 7.16 – 1000 BPD AND 100 PSI - BUBBLE FLOW REGIME	109
FIGURE 7.17 – 1500 BPD AND 100 PSI - BUBBLE FLOW REGIME	109
FIGURE 7.18 – 2000 BPD AND 100 PSI - BUBBLE FLOW REGIME	110
FIGURE 7.19 – 1000 BPD AND 150 PSI - BUBBLE FLOW REGIME	110
FIGURE 7.20 – 1500 BPD AND 150 PSI - BUBBLE FLOW REGIME	111
FIGURE 7.21 – 2000 BPD AND 150 PSI - BUBBLE FLOW REGIME	111
FIGURE 7.22 – 600 BPD AND 100 PSI - SLUG/CHURN FLOW REGIME	113
FIGURE 7.23 – 900 BPD AND 100 PSI - SLUG/CHURN FLOW REGIME	113
FIGURE 7.24 – 600 BPD AND 200 PSI - SLUG/CHURN FLOW REGIME	114
FIGURE 7.25 – 900 BPD AND 200 PSI - SLUG/CHURN FLOW REGIME	114
FIGURE 7.26 – 1200 BPD AND 160 PSI - SLUG/CHURN FLOW REGIME	115
FIGURE 7.27 – 1800 BPD AND 160 PSI - SLUG/CHURN FLOW REGIME	116
FIGURE 7.28 – 2200 BPD AND 200 PSI - SLUG/CHURN FLOW REGIME	116
FIGURE 7.29 – GLR EFFECT - BUBBLE FLOW REGIME.....	117
FIGURE 7.30 – GLR EFFECT - SLUG/CHURN FLOW REGIME	118
FIGURE 7.31 – CASING SIZE EFFECT - BUBBLE FLOW REGIME	119
FIGURE 7.32 – CASING SIZE EFFECT - 30 SCF/B - SLUG/CHURN FLOW REGIME	120
FIGURE 7.33 – CASING SIZE EFFECT - 60 SCF/B - SLUG/CHURN FLOW REGIME	121
FIGURE 7.34 – VISCOSITY EFFECT - BUBBLE FLOW REGIME	122
FIGURE 7.35 – VISCOSITY EFFECT - SLUG/CHURN FLOW REGIME	123
FIGURE 7.36 – PREDICTED VS. MEASURED EFFICIENCY - TWO-PHASE MODEL	123

FIGURE 7.37 – NO-SLIP GAS VOID FRACTION EFFECT - TWO-PHASE FLOW MODEL	126
FIGURE 7.38 – NO-SLIP GAS VOID FRACTION AT THE PUMP INTAKE.....	127
FIGURE A.1 – DISTORTED BUBBLE SHAPE.....	142
FIGURE A.2 – FORCE BALANCE ANALYSIS – SINGLE BUBBLE/PARTICLE	143
FIGURE A.3 – VARIATION OF THE DRAG COEFFICIENT WITH THE EOTVOS NUMBER	146
FIGURE D.1 – DRAG COEFFICIENT CORRELATIONS.....	160
FIGURE E.1 – GRID OF THE ANNULUS DOMAIN.....	161
FIGURE E.2 – PRIMARY GRID.....	162
FIGURE E.3 – SECONDARY GRID.....	162
FIGURE E.4 – FLOW DOMAIN.....	163

CHAPTER I

INTRODUCTION

Problems associated with multiphase phenomena are very common in the oil industry. Production engineers must design production systems to transport the fluids from the reservoir to a final separation and treatment system. Most of the time, the fluid flowing inside flowlines and tubing strings consist of a multiphase mixture. The presence of a liquid phase and a gaseous phase in those systems occurs due to the phase change induced by pressure and temperature variations along the system. This may occur, for instance, when the bottomhole flowing pressure is smaller than the bubble point. In this case, the simultaneous production of a liquid phase and a gaseous phase from the reservoir into the casing occurs. Even if the fluids being produced from the reservoir are in the single-phase state, pressure and temperature variations along the tubing string and production flowlines will promote the appearance of a gaseous phase inside the tubulars. The presence of liquid and gas inside the casing or production tubing string can also be the result of gas coning or the communication of an oil zone and a gas zone due to bad cementing conditions.

Artificial lift techniques are commonly used to increase the production from oil or gas wells. For instance, positive displacement pumps such as sucker rod pumps and progressing cavity pumps or roto-dynamic pumps such as electrical submersible pumps can be used to provide the extra momentum to produce a desired flowrate to the surface.

When using pumping artificial lift systems, production engineers face the challenge of designing the system to work in a multiphase environment.

For positive displacement pumps, the presence of free gas reduces the volumetric efficiency, E_v , which is defined as the ratio between the actual volume of liquid pumped, V_l , and the total volumetric capacity of the pump, V_p . According to Campbell (1989), in sucker rod installations, free gas occupies a portion of the volume destined for the handling of liquids and as a consequence, the volumetric efficiency is reduced. The presence of free gas inside sucker rod pumps can also delay the opening of the traveling valve. In this case, during the downstroke, the plunger needs to compress the multiphase mixture to increase the pressure inside the barrel and force the traveling valve to open. In some situations, this may cause the plunger to hit the liquid surface at a high speed causing a phenomenon known as fluid pound that is very detrimental to the mechanical integrity of the system. In extreme cases, the pressure inside the barrel may not be sufficient to open the traveling valve and the pump becomes gas locked.

In progressing cavity pumps, considerable amounts of free gas also reduce the capacity of the fluid to lubricate the elastomer-stator component and to dissipate the heat produced due to friction, limiting the life of the equipment.

In electrical submersible pump systems, the presence of free gas causes a deterioration of the head capacity curve of the pump. Centrifugal pumps work by accelerating the liquid phase inside the impeller, increasing the kinetic energy of the fluid that is later transformed into pressure at the diffuser. Those pumps usually work at a high rotational speed (3500 rpm at 60Hz), and the result is a significant radial acceleration that in some cases can be as high as 1000 times that of gravity. The pumps usually have a

small diameter and the pressure gradient inside the impeller channel is very high. A gas phase is then forced to flow inside the impeller from a lower pressure region (eye of the impeller) to a higher pressure region (impeller discharge). In order for this to occur, there must be sufficient drag between the liquid and the gas phase. The result is the gas flowing with a smaller radial velocity than the liquid, increasing the gas fraction concentration inside the channel. Depending on the amount of free gas through the pump and the fluid properties, the performance degradation could vary from a slight deterioration to a complete blockage known as gas locking. An example of the performance deterioration due to gas in electrical submersible pumps is shown in Fig. 1.1.

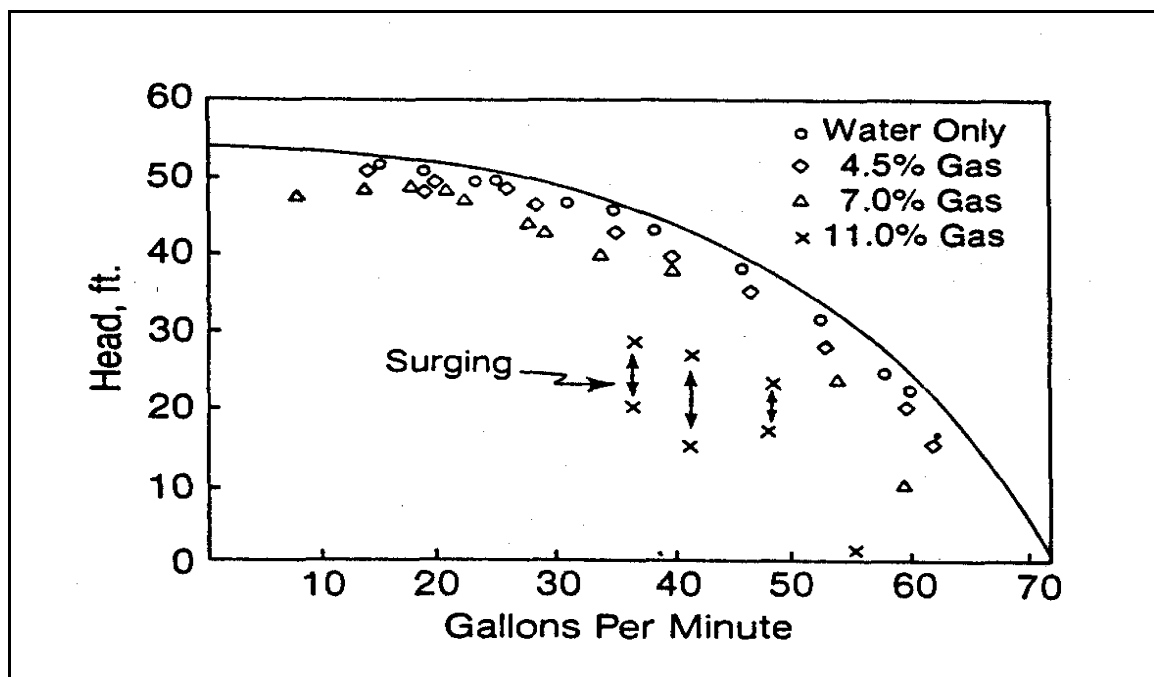


Figure 1.1 – Deterioration of Water Head Curves with Gas (I-42 Radial Pump) - Lea and Bearden (1982)

The results displayed in Fig. 1.1 indicate the relationship between the head developed by the pump and the liquid flow rate at a certain rotational speed for different amounts of free gas flowing through the pump.

A sketch of the multiphase conditions in front of the pump intake is shown in Fig. 1.2. Under some conditions, part of the gas is dragged by the liquid phase toward the pump intake and part of the gas is allowed to flow vertically through the tubing-casing annulus.

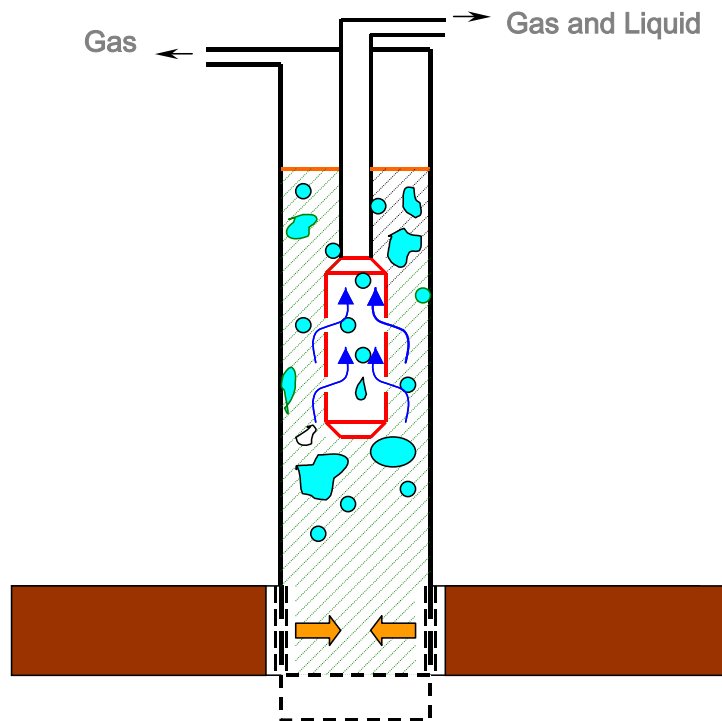


Figure 1.2 – Typical Production System.

In an open completion system, such as the one shown in Fig. 1.2, the gas that escapes the pump intake can be vented to the surface, thus reducing the amount of gas that needs to be digested by the pump.

The ratio between the gas flow rate vented, q_g^v , to the total free gas flow rate coming from the annulus, q_g^i , is defined as natural separation efficiency, E , and its correct prediction represents a very important parameter in the design and optimization of any pumping artificial lift system. In some situations, this natural separation efficiency can be sufficient to prevent the operational problems mentioned previously, but in some extreme cases, special devices such as rotary and static separators must be used to minimize the problem. The correct prediction of natural separation efficiency is still an important parameter to properly select and size downhole separators.

Since 1993, Tulsa University Artificial Lift Projects (TUALP) has been conducting important research in the area of natural separation. Experimental facilities have been constructed and experimental data on natural separation has been collected under a wide range of conditions. Also, simplified models have been developed such as those of Alhanati (1993), Serrano (1999) and Harun (2000) as well as a more detailed model proposed by Liu (2001).

Previous analysis of those models showed that the accuracy in the prediction of natural separation efficiency depends not only on the treatment of the governing equations, but also on the assumptions considered in the solution of the problem. Although previous models captured part of the physics involved in the process, their extension for all operational conditions has been limited.

Therefore, the main objective of this research is to reduce the uncertainty in predicting bottomhole natural separation efficiency through the development of a more robust model and its calibration with the existing experimental data.

This dissertation has been organized into eight chapters. Chapter II presents a literature review of both experimental and theoretical works on the topic. Chapter III describes not only the methodology used to determine the flow pattern regimes in annular flow, but also the procedure used to consolidate the available experimental data in a database. Chapter IV presents a simplified one-cell model where the mass and momentum balance equations are used to predict natural separation efficiency. This model is a generalization of the approach presented by Alhanati (1993) to the problem, but also includes the effects of the radial acceleration. Based on the available experimental data, a correlation is presented to close this model. Chapter V presents a mechanistic model that explains the radial acceleration effects. Chapter VI describes the new proposed two-phase flow model. The governing equations for gas and liquid stream functions, pressure and gas void fractions in cylindrical coordinates are described in detail and applied to the flow domain. Results of the simplified models and the two-phase model are presented in Chapter VII. Finally, conclusions and recommendations are provided in Chapter VIII.

CHAPTER II

LITERATURE REVIEW AND BACKGROUND

In recent years, downhole gas liquid separation has seized particular interest in the oil industry. The available literature concentrates mainly on the analysis of rotary and static separators. However, a few studies have been conducted on natural separation as well. In this Chapter, a brief literature review of both experimental and theoretical works presented by Lea and Bearden, Alhanati, McCoy et al., Serrano, Harun and Liu, is presented.

Lea and Bearden

Lea and Bearden (1980) conducted experimental tests to define the effects of free gas on the performance of electrical submersible pumps. Test facilities, method of data collection and results were presented separately for two independent test programs, conducted by Amoco Production Research and Centrilift.

Results regarding natural separation were mainly obtained from the Amoco Production Research facility. A schematic of the test loop is shown in Fig. 2.1.

Tests were conducted with 500 series equipment (5.13 in. pump outside diameter) inside a 7 in. casing and with air and water as the experimental fluids at low pressures (25 to 30 psig).

The percentage of free gas dragged by the pump was measured and plotted against the liquid flow rates, as shown in Fig. 2.2.

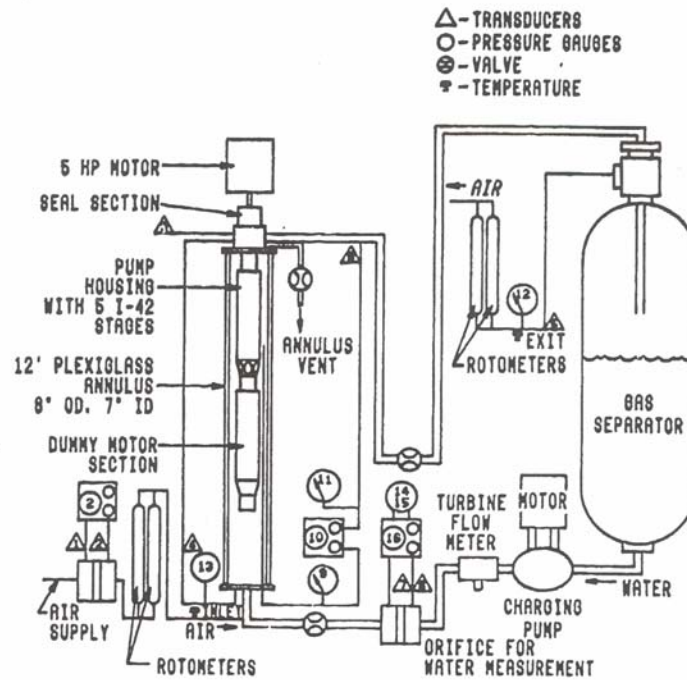


Figure 2.1 – Schematic of Amoco Test Facility - Lea and Bearden (1980).

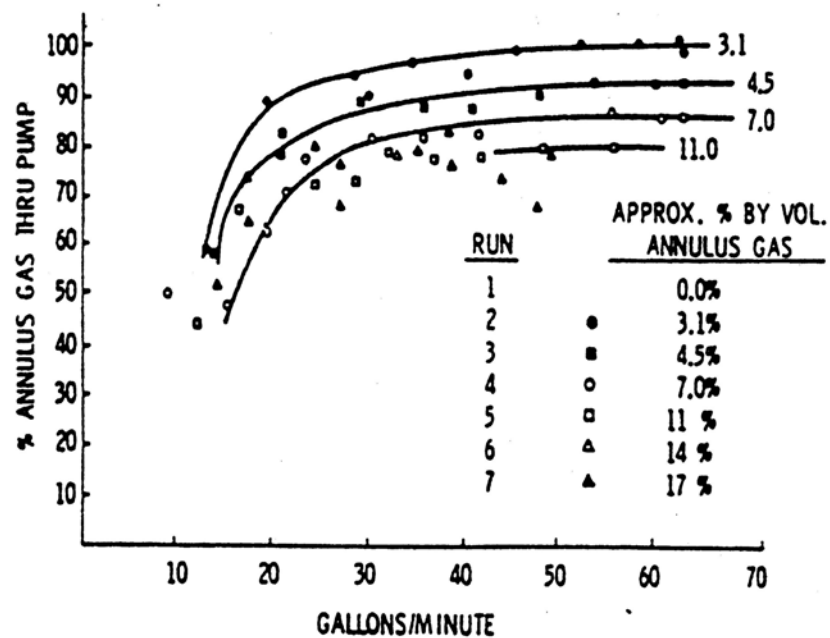


Figure 2.2 – Natural Separation Efficiency - From Lea and Bearden (1980).

According to Lea and Bearden, the greater the amount of gas that is present, the greater the percentage of gas that escaped up the annulus. In addition, they noted that the separation efficiency decreases with increasing liquid flow rates. Lea and Bearden emphasized the need to determine downhole volume of gas that can be expected at the pump intake.

Alhanati

In 1993, Alhanati designed and built an experimental facility, as shown in Fig. 2.3, in order to gather data on separation efficiency. The vertical casing section, shown in Fig. 2.3, was especially designed and constructed to enable acquisition of the data. Air and water, used as experimental fluids, were mixed in the lower part of that section.

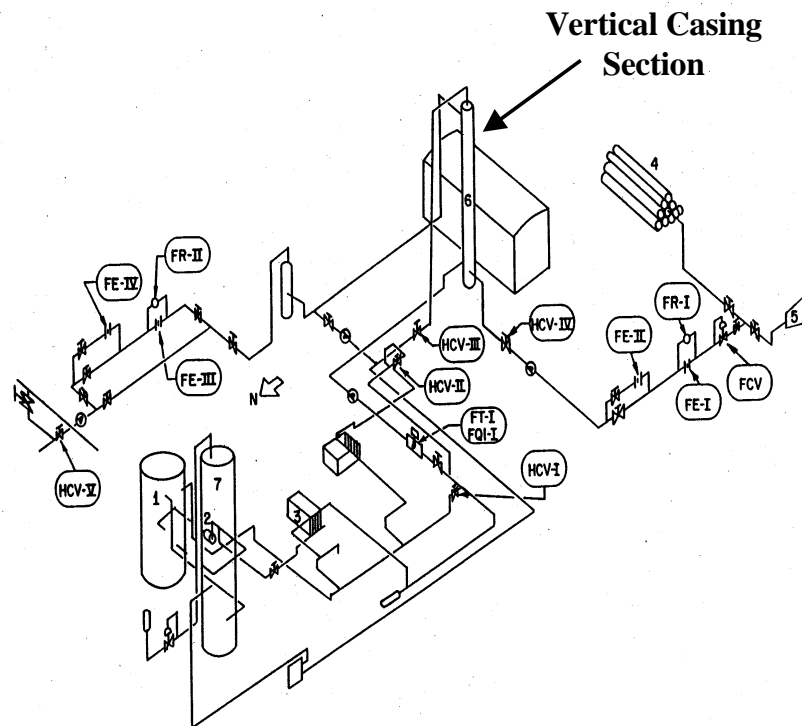


Figure 2.3 – Experimental Facility of Alhanati's Work (1993).

Experimental results obtained by Alhanati showed that natural separation efficiency decreases with increasing liquid flow rate and pressure, and decreasing gas liquid ratio (GLR).

Ahlanati proposed, for the first time, a theoretical model for predicting gas separation efficiency considering a rotary gas separator. In addition, and based on the drift-flux model approach proposed by Ishii (1975), Alhanati developed the first simplified model for predicting the natural separation efficiency in vertical flow, assuming no slip between the liquid and gas velocities in the radial direction. The simplified model is given by the following relationship:

$$E = \frac{V_{slz}^i}{V_{slz}^i + V_{\infty z}}, \quad (2.1)$$

where V_{slz}^i is the superficial liquid velocity, which is directly related to the volumetric liquid flow rate per unit area. $V_{\infty z}$ represents the vertical terminal velocity of gas bubbles in an infinite medium. Available expressions for $V_{\infty z}$ are dependent on the flow regime and the physical properties of the fluids. Therefore, for a certain set of fluid properties, the efficiency predicted by Eq. 2.1 is exclusively dependent on the superficial liquid velocity. Eq. 2.1 can also be represented graphically, as shown in Fig. 2.4.

McCoy

Visual studies, obtained by Caetano (1992), of air-water and air-kerosene two-phase vertical flow in transparent pipes showed that, in the presence of an eccentric tubing casing arrangement, gas would flow preferentially through the larger side of the eccentric annulus.

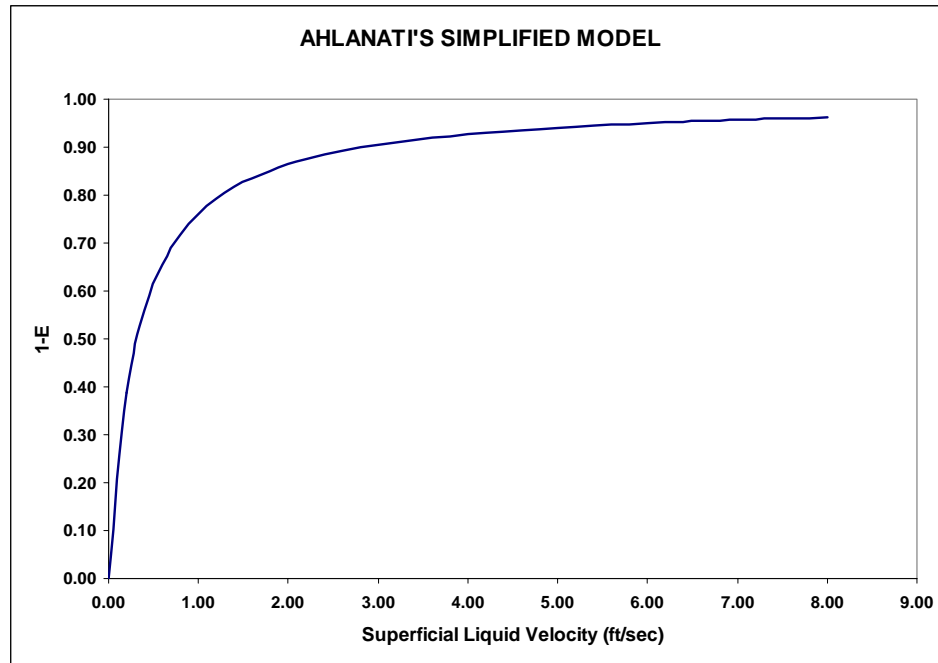


Figure 2.4 – Alhanati's Simplified Model (1993).

Based on Caetano's results, McCoy et al. (1995) developed a decentralized downhole gas separator to minimize the gas effect, as shown in Fig. 2.5.

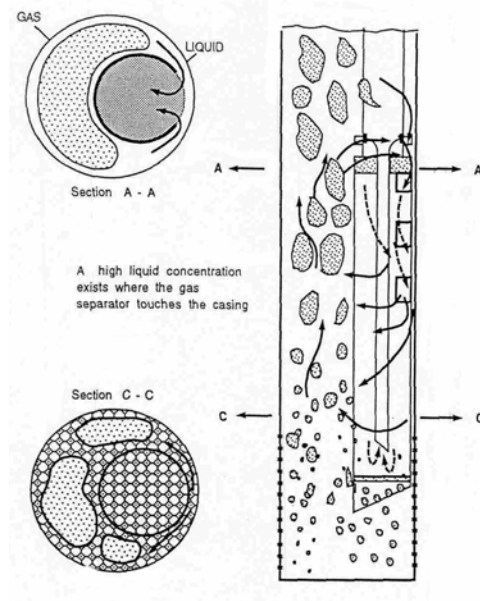


Figure 2.5 – Decentralized Downhole Gas Separator - From McCoy et al. (1995).

The decentralization of the gas separator in the casing would insure that a minimum amount of gas enters the separators.

Serrano

In 1999, Serrano also conducted an experimental study to validate and extend Alhanati's model, using the experimental facility shown in Fig. 2.3. The casing section was modified to allow inclination changes. The new inclined test section consisted of a 50 ft high tower that supported a 30 ft long casing which is shown in Fig. 2.6.

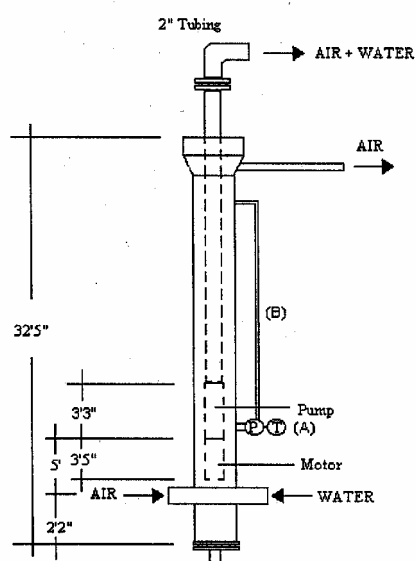


Figure 2.6 – Casing Section - Serrano (1999).

The 5 in. inner diameter casing section contained a DN1750 ESP. The casing also contained a 10 HP electric submersible motor (3.75 in. outer diameter) connected to the pump and with a flat cable to supply power to the motor.

Experiments were carried out at different pressures (50, 100 and 150 psig), three liquid flow rates (1000, 1500 and 2000 BPD), and a wide range of gas flow rates from

2000 to 20000 SCFD. Air and water were used as experimental fluids. Three different inclination angles, measured from horizontal, were considered: 90 (vertical), 60 and 30 degrees.

Serrano developed empirical correlations for prediction of the local gas void fraction for the region in front of the pump intake, assuming no slip velocity in the radial direction.

Harun

Harun (2000) proposed a mechanistic model to predict natural separation efficiency in vertically pumped wells. The model is based on the combined phase momentum equation and a general slip closure relationship, applied to a single control volume situated in front of the pump intake port. Available experimental data were used to generate a correlation for drag coefficient and to close the system of equations. Natural separation efficiency was obtained by solving the resulting system of equations.

Liu

In 2001, Liu presented a model based on a bubble tracking technique. Initially, the liquid flow field into the annulus was determined by using the vorticity-stream function approach in a two-dimensional Cartesian coordinates system. This solution gave the velocities and pressure fields inside the flow domain around the pump intake, as shown in Fig. 2.7.

Using a force balance analysis, the movement of a single gas bubbles was traced in the domain. By tracking the position of each bubble, the natural separation efficiency was estimated as a geometric function of the trajectory of the bubbles into the domain.

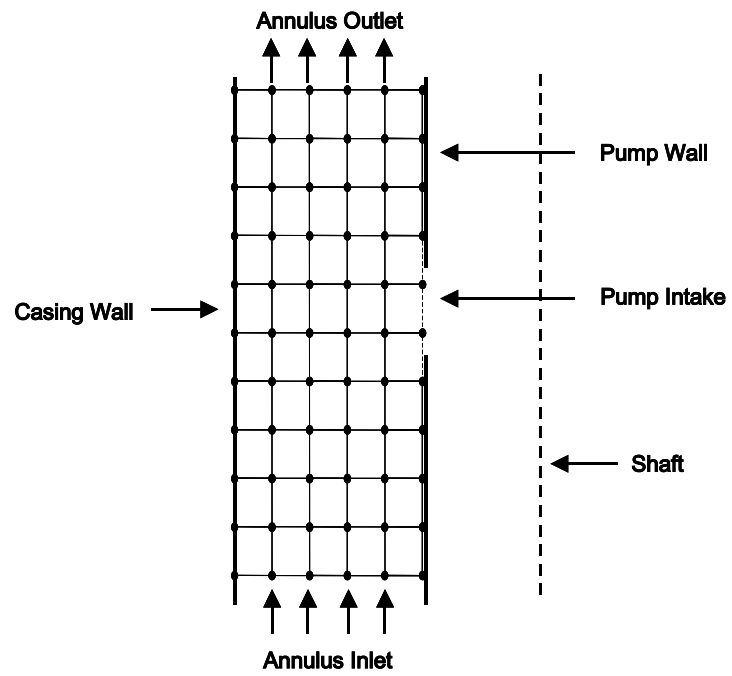


Figure 2.7 – Grid into the Cell Domain - Bin Liu (2001).

CHAPTER III

EXPERIMENTAL DATA

Since 1993, four experimental works were carried out in TUALP by Alhanati (1993), Sambangi (1994), Lackner (1997) and Serrano (1999). Important experimental data regarding natural separation efficiency was collected under different conditions of pressure, temperature, inclination angle, casing size and gas and liquid flow rates.

The data sets collected by previous authors are used in this research to validate or to obtain a closure relationship for the models. One of the important parameters considered in this work is the flow pattern at the pump intake. Therefore, this chapter presents the theory and methodology used to determine those regimes.

Prediction of Flow Pattern Boundaries

Caetano et al. (1992) conducted a combined experimental and theoretical study of upward, gas-liquid two-phase flow in vertical concentric and fully eccentric annuli. The experimental part of the study involved flowing air with either water or kerosene up a vertical annulus. The theoretical part included the development of flow pattern prediction models. Caetano defined five flow pattern transitions, given as follows:

1. Bubble Flow Region Existence

Different characteristic velocities of the small gas bubbles and the Taylor bubble determine the existence of the bubble flow regime.

In 1960, Harmathy proposed the following equation for the terminal velocity of the bubbles in the vertical direction, $V_{\infty z}$:

$$V_{\infty z} = 1.53 \left[\frac{\sigma (\rho_l - \rho_g) |g|}{\rho_l^2} \right]^{1/4}, \quad (3.1)$$

where σ , ρ_l , ρ_g and g represent the surface tension, liquid and gas densities and the gravitational acceleration term in the vertical direction, respectively. Details on how Eq. 3.1 was obtained are shown in Appendix A. On the other hand, Nicklin et al. (1962) proposed the following equation for the Taylor bubble rise velocity, V_{Tb}

$$V_{Tb} = 0.35 \sqrt{g D_{ep}}. \quad (3.2)$$

Eq. 3.2 depends on the pipe diameter and it is valid for inertia-dominated conditions. D_{ep} represents the equi-periphery diameter and can be estimated by the following relationship proposed by Sadatomi et al. (1982).

$$D_{ep} = D_c + D_t, \quad (3.3)$$

where D_c and D_t represent the inside casing diameter and outside tubing diameter, respectively. The stability criterion states that bubble flow can be exits if:

$$V_{Tb} \geq V_{\infty z}. \quad (3.4)$$

2. Bubble to Slug Flow Transition

Slip velocity V_s represents the difference between the actual gas and liquid velocity, V_g and V_l respectively, and is given by:

$$V_s = V_g - V_l = \frac{V_{sg}}{\alpha_g} - \frac{V_{sl}}{(1 - \alpha_g)}, \quad (3.5)$$

where V_{sg} , V_{sl} and α_g represent the superficial gas and liquid velocities and gas void fraction, respectively. On the other hand, a solution for slip velocity for bubbly flow can be obtained by using the drift-flux model approach proposed by Ishii (1975). Assuming the effect due to the presence of other bubbles and the diffusivity of the phases in the fluid medium is negligible, the slip velocity can be written as:

$$V_s = V_\infty (1 - \alpha_g)^{n-1}, \quad (3.6)$$

where V_∞ represents the terminal vertical velocity of the gas bubbles. At the bubble to slug transition boundary, Caetano measured average gas void fraction values of 0.20 and 0.15 for flow throughout the concentric and fully eccentric annulus, respectively. In this boundary, Caetano also proposed to use the same methodology established by Taitel et al. model (1980) for predicting this transition in pipes.

The combination of Eqs. 3.1 and 3.6 yields:

$$V_s (1 - \alpha_g) = 1.53 \left[\frac{\sigma (\rho_l - \rho_g) |g|}{\rho_l^2} \right]^{1/4}. \quad (3.7)$$

Note also that the combination of Eqs. 3.5 and 3.7 gives a relationship between the superficial gas and liquid velocities, gas void fraction and properties of the fluid. This relationship is given by:

$$V_{sg} = \frac{\alpha_g}{(1 - \alpha_g)} V_{sl} + 1.53 \alpha_g \left[\frac{\sigma (\rho_l - \rho_g) |g|}{\rho_l^2} \right]^{1/4}. \quad (3.8)$$

Eq. 3.8 is used to predict the transition between bubbly to slug flow. For flow throughout a concentric and fully eccentric annulus, where gas void fraction values of 0.20 and 0.15 were measured, respectively, the following equations results valid:

$$V_{sg} = \frac{V_{sl}}{4} + 0.306 \left[\frac{\sigma (\rho_l - \rho_g) |g|}{\rho_l^2} \right]^{1/4}, \quad (3.9)$$

$$V_{sg} = \frac{V_{sl}}{5.67} + 0.230 \left[\frac{\sigma (\rho_l - \rho_g) |g|}{\rho_l^2} \right]^{1/4}. \quad (3.10)$$

A flow pattern map can be represented by a graph of superficial liquid velocity as a function of superficial gas velocity for each flow regime boundary. For a concentric annulus, the bubble to slug flow transition for air-water, Eq. 3.9, is given by the boundary “A” in Fig. 3.1.

3. Bubble or Slug to Dispersed Bubble Flow Transition

At high superficial liquid velocities, Taitel et al. (1980) suggested that turbulent forces causes the gas phase in either slug or bubble flow patterns to break into small bubbles and become dispersed in the continuous liquid phase.

Hinze (1955) proposed the following relationship for the maximum stable diameter d_{\max} of those bubbles under a dispersed condition.

$$d_{\max} = k \left[\frac{\sigma}{\rho_l} \right]^{3/5} \left[\frac{2 V_M^3}{D_h} f \right]^{-2/5}, \quad (3.11)$$

where V_M and D_h represent the mixture velocity and hydraulic-diameter, respectively.

The constant k is estimated by using the following correlation proposed by Calderbank (1958):

$$k = \left[0.725 + 4.15 \left(\frac{V_{sg}}{V_M} \right)^{1/2} \right]. \quad (3.12)$$

Substituting Eq. 3.12 into Eq. 3.11, the following relationship for d_{\max} results valid:

$$d_{\max} = \left[0.725 + 4.15 \left(\frac{V_{sg}}{V_M} \right)^{1/2} \right] \left[\frac{\sigma}{\rho_l} \right]^{3/5} \left[\frac{2V_M^3}{D_h} f \right]^{-2/5}. \quad (3.13)$$

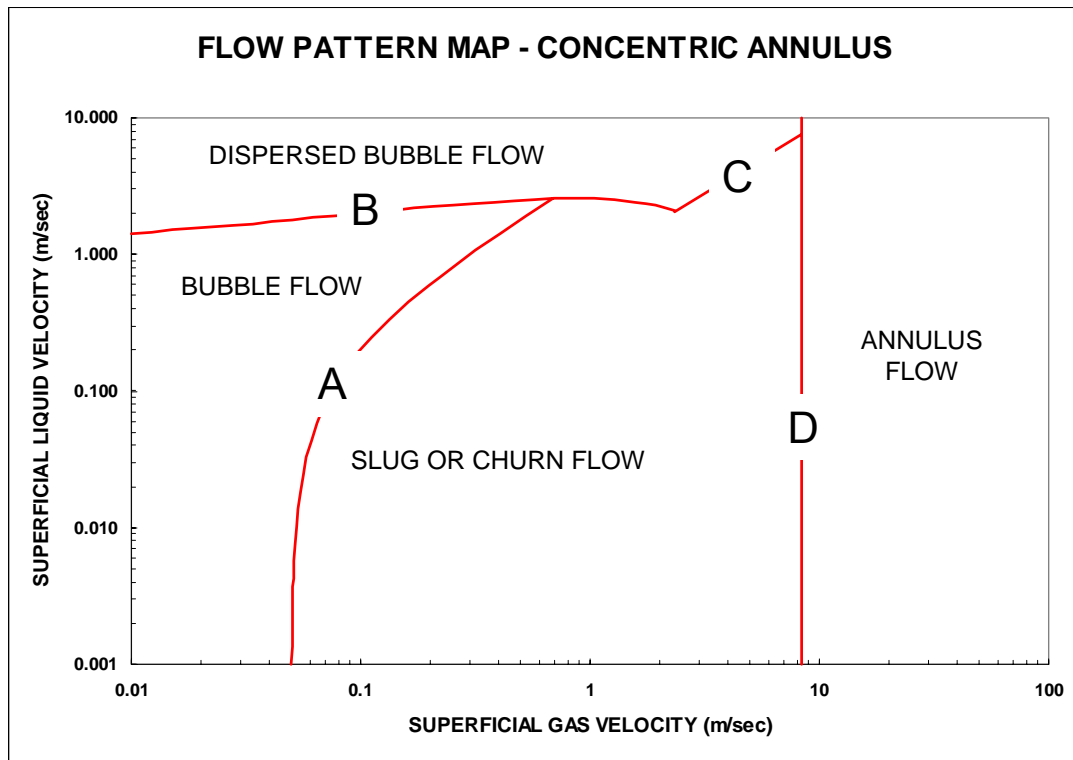


Figure 3.1 – Flow Pattern Map for Air-Water.

On the other hand, the turbulent breakup process can prevent agglomeration only if the bubble size produced is small enough to cause the bubbles to remain spherical. The critical bubble size d_{crit} at which this happens is given by Brodkey (1967) as:

$$d_{crit} = \left[\frac{0.4 \sigma}{(\rho_l - \rho_g) |g|} \right]^{1/2}. \quad (3.14)$$

Barnea et al. (1985), based on the data of Migagi (1925), suggested that d_{crit} could be the double of the original value obtained by Brodkey expression. Finally, the criterion states that the bubble to dispersed bubble flow transition can exist if:

$$d_{crit} \geq d_{max}. \quad (3.15)$$

Therefore, the combination of Eqs. 3.13 - 3.15, with along the Barnea's recommendation, yields the following equation for this transition:

$$2 \left[\frac{0.4 \sigma}{(\rho_l - \rho_g) |g|} \right]^{1/2} \left(\frac{\rho_l}{\sigma} \right)^{3/5} \left(\frac{2}{D_h} \right)^{2/5} f^{2/5} V_M^{6/5} = 0.725 + 4.15 \left(\frac{V_{sg}}{V_M} \right)^{1/2}, \quad (3.16)$$

where the hydraulic diameter D_h is defined as:

$$D_h = D_c - D_t. \quad (3.17)$$

Note that from Eq. 3.16, the only unknown variable is the Fanning friction factor, f . For laminar flow, f can be estimated, by assuming a homogeneous mixture, as:

For concentric annulus;

$$f = \frac{F_{ca}}{\text{Re}} = \frac{16}{\text{Re}} \frac{(1-k)^2}{\left[\frac{1-k^4}{1-k^2} - \frac{1-k^2}{\ln(1/k)} \right]}. \quad (3.18)$$

For eccentric annulus;

$$f = \frac{F_{ea}}{\text{Re}} = \frac{1}{\text{Re}} \frac{4(1-k^2)(1-k)^2}{\phi (\sinh \eta_o)^4}, \quad (3.19)$$

where the Reynolds number is given by:

$$\text{Re} = \frac{\rho V_m D_h}{\mu}, \quad (3.20)$$

and the annulus pipe diameter ratio k is defined as the ratio between the outside tubing diameter to the inside casing diameter. The friction geometric parameter for an eccentric annulus F_{ea} can be determined either graphically by Fig. 3.2 or analytically by the following equations:

$$\phi = (\cot \eta_i - \cot \eta_o)^2 \left[\frac{1}{\eta_i - \eta_o} - 2 \sum_{n=1}^{\infty} \frac{2n}{(e^{2n\eta_i} - e^{2n\eta_o})} \right] + \frac{1}{4} \left[\frac{1}{(\sinh \eta_i)^4} - \frac{1}{(\sinh \eta_o)^4} \right], \quad (3.21)$$

$$\cosh \eta_i = \frac{k(1+e^2) + (1-e^2)}{2ke}, \quad (3.22)$$

$$\cosh \eta_o = \frac{k(1-e^2) + (1+e^2)}{2ke}. \quad (3.23)$$

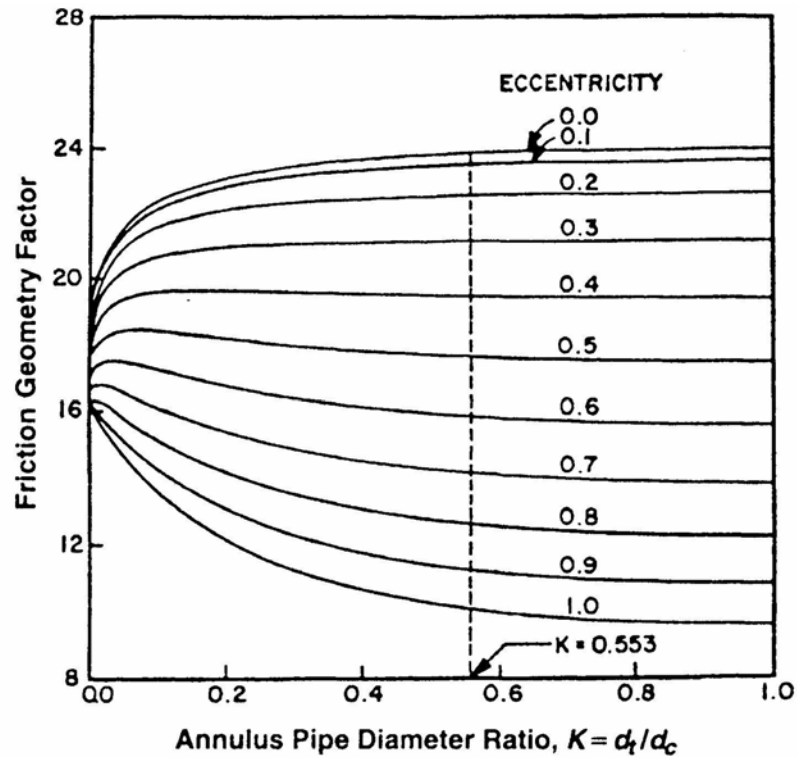


Figure 3.2 – Friction Geometry Factor - Caetano et al. (1992).

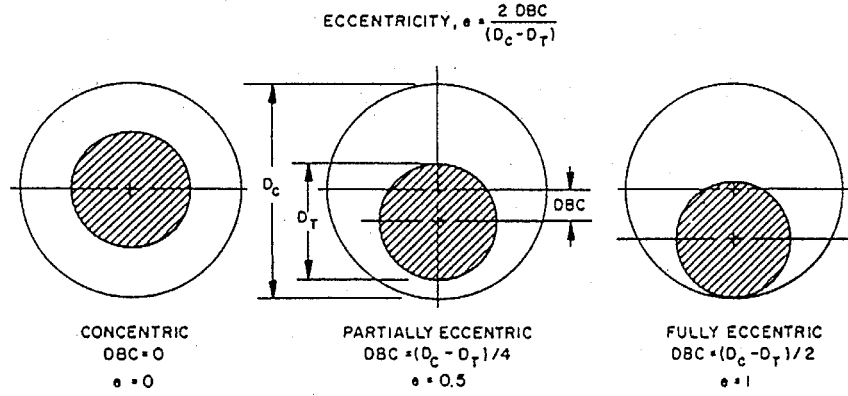


Figure 3.3 – Degree of Eccentricity - Caetano et al. (1992).

For turbulent flow, Caetano et al. recommended that f be determined by Gunn and Darling's (1963) procedures due to its simplicity and good performance.

For concentric annulus;

$$\frac{1}{\left\{ f \left(\frac{F_p}{F_{ca}} \right)^{0.45 \exp(-(Re-3000)/10^6)} \right\}^{1/2}} = 4 \log \left[\text{Re} \left\{ f \left(\frac{F_p}{F_{ca}} \right)^{0.45 \exp(-(Re-3000)/10^6)} \right\}^{1/2} \right] - 0.4 \quad (3.24)$$

For eccentric annulus;

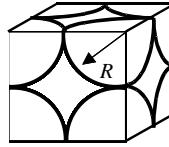
$$\frac{1}{\left\{ f \left(\frac{F_p}{F_{ea}} \right)^{0.45 \exp(-(Re-3000)/10^6)} \right\}^{1/2}} = 4 \log \left[\text{Re} \left\{ f \left(\frac{F_p}{F_{ea}} \right)^{0.45 \exp(-(Re-3000)/10^6)} \right\}^{1/2} \right] - 0.4 \quad (3.25)$$

A constant value of 16 is considered for F_p in Eqs. 3.24 and 3.25. Assuming concentric annulus, this bubble or slug to dispersed bubble flow transition is given by the boundary “B” in Fig. 3.1.

4. Dispersed Bubble to Slug Flow Transition

This transition is based on the maximum possible gas void fraction allowable in one cubic lattice packing. According to Fig. 3.4, this value is approximately equal to 0.52. Higher values of void fraction may cause transition to slug flow. This criterion along with Eq. 3.8 allows obtaining the following expression for this transition.

$$V_{sg} = 1.083 V_{sl} + 0.796 \left[\frac{\sigma (\rho_l - \rho_g) |g|}{\rho_l^2} \right]^{1/4} \quad (3.26)$$



$$\alpha_g = \frac{\frac{4}{3} \pi R^3}{8 R^3} = 0.52$$

Figure 3.4 – Maximum Allowable Packing.

For concentric annulus, the dispersed bubble to slug flow transition is given by boundary “C” in Fig. 3.1.

5. Transition to Annular Flow

The transition criterion for annular flow is based on the minimum gas velocity necessary to transport the largest liquid droplet entrained in the gas core. This required

minimum gas velocity could be determined from a balance between gravity and drag forces. Neglecting the effect of the film thickness, the transition is given by:

$$V_{sg} = 3.1 \left[\frac{\sigma (\rho_l - \rho_g) |g|}{\rho_g^2} \right]^{1/4}. \quad (3.27)$$

For concentric annulus, the transition to annular flow is given by the boundary “D” in Fig. 3.1.

Classification of the Available Experimental Data

A total of 270 data points were gathered from four different studies: Alhanati (1993), Sambangi (1994), Lackner (1997) and Serrano (1999). Fig. 3.5 shows the experimental data distribution per study.

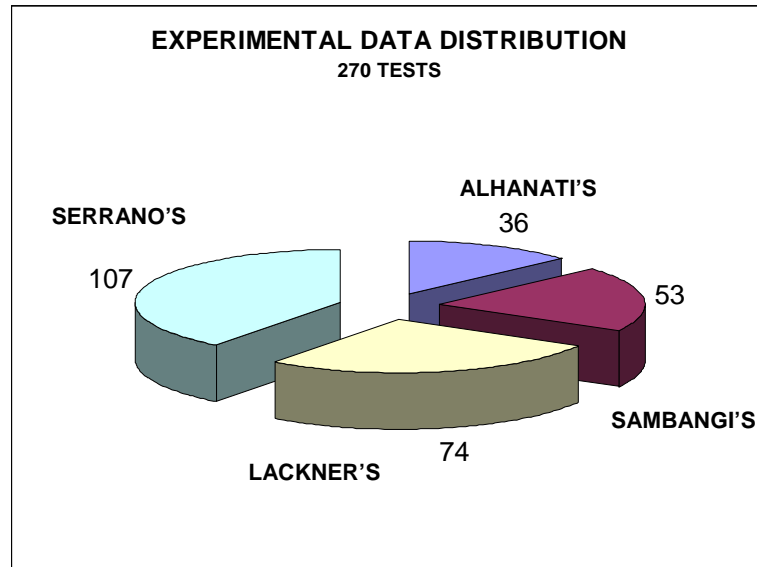


Figure 3.5 – Experimental Data Distribution per Author.

Additionally, Table 3.1 shows the main characteristics of each work, such as type of fluid, operational conditions and inclination angle of the pump.

Table 3.1 – Experimental Conditions - Distributed per Author.

VARIABLE	ALHANATI	SAMBANGI	LACKNER	SERRANO
FLUID	AIR-WATER	AIR-WATER	AIR-MINERAL OILS	AIR-WATER
LIQUID FLOW RATE (BPD)	300, 600, 900	FROM 600 TO 3000	FROM 600 TO 2700	1000, 1500, 2000
GLR (SCF/B)	50, 100, 200	50, 100, 200, 300	50, 100, 200, 300	-
PRESSURE (Psig)	100, 200	100, 200, 300	100, 200, 300	50, 100, 150
SPEED (Hz)	0, 18, 60	0, 60	0, 30, 60	-
INCLINATION ANGLE	90° (VERTICAL)	90° (VERTICAL)	90° (VERTICAL)	90° (VERTICAL), 60°, 30°

In this work, only 63 tests are available for vertical natural separation efficiency and its distribution per author is shown in Fig. 3.6.

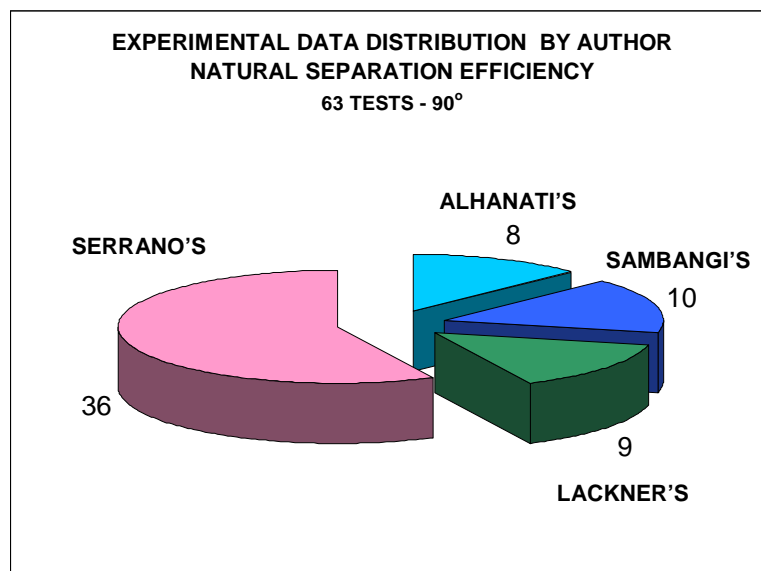


Figure 3.6 – Experimental Data Distribution per Author - Natural Separation Only.

Moreover, additional and useful information such as fluid physical properties and two-phase flow variables, among them density, viscosity, surface tension and mass flow

rate, gas void fraction, superficial velocities, mass flux, etc, respectively, were determined at operational conditions and included in this database as well. The prediction of the flow pattern is based on the Taitel et al. model modified by Caetano, which was described previously. Fig. 3.7 shows the distribution of the data by author according to the flow pattern regime.

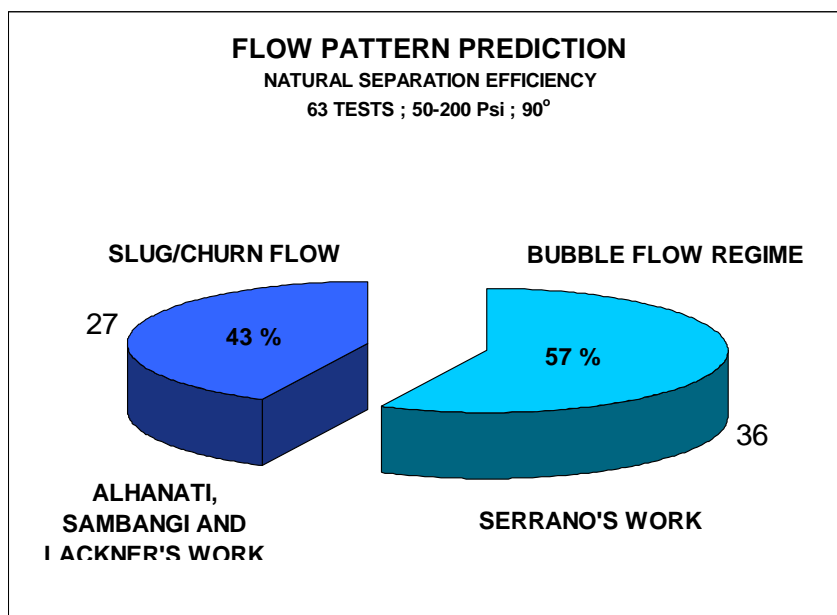


Figure 3.7 – Classification of the Experimental Data - Flow Pattern Regime.

According to Fig. 3.7, 43% of the experimental data for natural separation in vertical flow exists in the slug/churn regime. This experimental data correspond to Alhanati, Sambangi and Lackner. The remaining data belonging to Serrano were observed under the bubble flow regime. Unfortunately, 9 points corresponding to Lackner's work were rejected since the surface tension for the mineral oil used as experimental fluid in this work could be obtained only at room temperatures of 76 °F. Finally, the database is shown in Table 3.2.

Table 3.2 – Available Experimental Data Database.

φ _c	φ _m	T	P	Fluid Properties									Feed				E	V _{sg}	V _{sl}	FLOW PATTERN
				σ	Liquid			Gas				Liquid		Gas						
					v _l	ρ _l	μ _l	ρ _g	μ _g	Z	B _g	Q _l	Q _g	Q _g	Q _g					
in	in	°F	Psig	lb/ft	St	lbm/ft ³	lb sec/ft ²	lbm/ft ³	lb sec/ft ²		ft ³ /scf	bpd	ft ³ /sec	scf/day	ft ³ /sec		ft/sec	ft/sec		
6.366	4	101	121	0.00477	2.069E-04	62.0	1.380E-05	0.655	3.972E-07	0.997	0.117	641	0.0417	51000	0.0688	0.625	0.5146	0.3114	SLUGCHURN FLOW	
6.366	4	101	122	0.00477	2.069E-04	62.0	1.380E-05	0.660	3.972E-07	0.997	0.116	960	0.0624	82300	0.1103	0.507	0.8243	0.4684	SLUGCHURN FLOW	
6.366	4	98	115	0.00479	2.145E-04	62.0	1.432E-05	0.630	3.953E-07	0.997	0.121	634	0.0412	119400	0.1677	0.637	1.2539	0.3080	SLUGCHURN FLOW	
6.366	4	93	109	0.00482	2.282E-04	62.1	1.525E-05	0.606	3.921E-07	0.997	0.126	912	0.0593	176300	0.2574	0.584	1.9242	0.4431	SLUGCHURN FLOW	
6.366	4	94	219	0.00482	2.253E-04	62.1	1.505E-05	1.145	3.928E-07	0.994	0.067	614	0.0399	59900	0.0462	0.477	0.3457	0.2983	SLUGCHURN FLOW	
6.366	4	103	233	0.00476	2.021E-04	62.0	1.348E-05	1.195	3.984E-07	0.994	0.064	871	0.0566	90500	0.0670	0.434	0.5007	0.4232	SLUGCHURN FLOW	
6.366	4	102	220	0.00476	2.045E-04	62.0	1.364E-05	1.134	3.978E-07	0.994	0.067	631	0.0410	117400	0.0916	0.552	0.6845	0.3066	SLUGCHURN FLOW	
6.366	4	98	200	0.00479	2.145E-04	62.0	1.432E-05	1.044	3.953E-07	0.995	0.073	915	0.0595	178400	0.1494	0.467	1.1168	0.4445	SLUGCHURN FLOW	
6.366	4	102	125	0.00476	2.045E-04	62.0	1.364E-05	0.673	3.978E-07	0.997	0.113	915	0.0595	278930	0.3662	0.580	2.7374	0.4445	SLUGCHURN FLOW	
6.366	4	110	164	0.00471	1.868E-04	61.9	1.244E-05	0.850	4.028E-07	0.996	0.090	1200	0.0780	295330	0.3072	0.510	2.2967	0.5830	SLUGCHURN FLOW	
6.366	4	107	160	0.00473	1.931E-04	61.9	1.286E-05	0.835	4.009E-07	0.996	0.091	1203	0.0782	243850	0.2581	0.470	1.9297	0.5845	SLUGCHURN FLOW	
6.366	4	113	194	0.00469	1.809E-04	61.8	1.204E-05	0.988	4.047E-07	0.995	0.077	1490	0.0968	308360	0.2759	0.400	2.0626	0.7239	SLUGCHURN FLOW	
6.366	4	112	168	0.00470	1.829E-04	61.8	1.217E-05	0.866	4.041E-07	0.996	0.088	1810	0.1176	188860	0.1928	0.440	1.4414	0.8793	SLUGCHURN FLOW	
6.366	4	108	210	0.00473	1.909E-04	61.9	1.272E-05	1.074	4.016E-07	0.995	0.071	2105	0.1368	214170	0.1764	0.350	1.3185	1.0227	SLUGCHURN FLOW	
6.366	4	112	214	0.00470	1.829E-04	61.8	1.217E-05	1.086	4.041E-07	0.994	0.070	1508	0.0980	316000	0.2575	0.420	1.9246	0.7326	SLUGCHURN FLOW	
6.366	4	111	202	0.00471	1.849E-04	61.9	1.230E-05	1.030	4.034E-07	0.995	0.074	1790	0.1163	326670	0.2805	0.430	2.0967	0.8696	SLUGCHURN FLOW	
6.366	4	110	221	0.00471	1.868E-04	61.9	1.244E-05	1.123	4.028E-07	0.994	0.068	2115	0.1375	216425	0.1705	0.400	1.2743	1.0275	SLUGCHURN FLOW	
6.366	4	98	223	0.00479	2.145E-04	62.0	1.432E-05	1.157	3.953E-07	0.994	0.066	2417	0.1571	242040	0.1950	0.340	1.3833	1.1742	SLUGCHURN FLOW	
5	4	67	60	0.00499	3.245E-04	62.3	2.177E-05	0.383	3.758E-07	0.998	0.199	960	0.0624	5000	0.0115	0.387	0.2350	1.2710	BUBBLE FLOW	
5	4	78	57	0.00492	2.783E-04	62.2	1.864E-05	0.360	3.827E-07	0.998	0.212	1011	0.0657	3856	0.0095	0.373	0.1928	1.3385	BUBBLE FLOW	
5	4	66	58	0.00499	3.292E-04	62.3	2.208E-05	0.374	3.752E-07	0.998	0.204	1011	0.0657	1766	0.0042	0.447	0.0851	1.3385	BUBBLE FLOW	
5	4	77	54	0.00492	2.821E-04	62.2	1.890E-05	0.346	3.821E-07	0.999	0.221	1028	0.0668	2395	0.0061	0.391	0.1247	1.3610	BUBBLE FLOW	
5	4	76	54	0.00493	2.860E-04	62.2	1.916E-05	0.347	3.815E-07	0.999	0.220	1474	0.0958	4329	0.0110	0.200	0.2250	1.9515	BUBBLE FLOW	
5	4	76	54	0.00493	2.860E-04	62.2	1.916E-05	0.347	3.815E-07	0.999	0.220	1491	0.0969	2687	0.0069	0.215	0.1397	1.9740	BUBBLE FLOW	
5	4	76	54	0.00493	2.860E-04	62.2	1.916E-05	0.347	3.815E-07	0.999	0.220	1491	0.0969	5406	0.0138	0.186	0.2810	1.9740	BUBBLE FLOW	
5	4	60	60	0.00503	3.587E-04	62.4	2.407E-05	0.389	3.714E-07	0.998	0.197	1508	0.0980	6736	0.0153	0.182	0.3124	1.9965	BUBBLE FLOW	
5	4	74	52	0.00494	2.941E-04	62.3	1.971E-05	0.338	3.802E-07	0.999	0.226	1971	0.1281	6706	0.0176	0.108	0.3577	2.6095	BUBBLE FLOW	
5	4	74	52	0.00494	2.941E-04	62.3	1.971E-05	0.338	3.802E-07	0.999	0.226	1971	0.1281	7720	0.0202	0.094	0.4118	2.6095	BUBBLE FLOW	
5	4	74	50	0.00494	2.941E-04	62.3	1.971E-05	0.328	3.802E-07	0.999	0.233	2005	0.1303	4649	0.0126	0.109	0.2657	2.6545	BUBBLE FLOW	
5	4	73	50	0.00495	2.982E-04	62.3	1.999E-05	0.328	3.796E-07	0.999	0.233	2023	0.1315	3120	0.0094	0.116	0.1713	2.6783	BUBBLE FLOW	
5	4	67	98	0.00499	3.245E-04	62.3	2.177E-05	0.579	3.758E-07	0.997	0.132	943	0.0613	6785	0.0104	0.360	0.2111	1.2485	BUBBLE FLOW	
5	4	75	105	0.00494	2.900E-04	62.2	1.943E-05	0.606	3.809E-07	0.997	0.126	977	0.0635	4966	0.0072	0.377	0.1477	1.2935	BUBBLE FLOW	
5	4	74	105	0.00494	2.941E-04	62.3	1.971E-05	0.607	3.802E-07	0.997	0.126	1011	0.0657	3378	0.0049	0.384	0.1003	1.3385	BUBBLE FLOW	
5	4	74	103	0.00494	2.941E-04	62.3	1.971E-05	0.597	3.802E-07	0.997	0.128	1491	0.0969	12203	0.0181	0.165	0.3684	1.9740	BUBBLE FLOW	
5	4	56	104	0.00506	3.800E-04	62.4	2.551E-05	0.623	3.689E-07	0.997	0.123	1508	0.0980	3547	0.0050	0.206	0.1026	1.9965	BUBBLE FLOW	
5	4	73	102	0.00495	2.982E-04	62.3	1.999E-05	0.593	3.796E-07	0.997	0.129	1508	0.0980	7037	0.0105	0.184	0.2139	1.9965	BUBBLE FLOW	
5	4	74	102	0.00494	2.941E-04	62.3	1.971E-05	0.592	3.802E-07	0.997	0.129	1525	0.0991	9391	0.0140	0.169	0.2859	2.0190	BUBBLE FLOW	
5	4	58	99	0.00505	3.692E-04	62.4	2.478E-05	0.594	3.702E-07	0.997	0.129	1954	0.1270	8256	0.0123	0.123	0.2503	2.5870	BUBBLE FLOW	
5	4	57	90	0.00505	3.745E-04	62.4	2.514E-05	0.548	3.696E-07	0.998	0.139	1971	0.1281	4630	0.0075	0.173	0.1522	2.6095	BUBBLE FLOW	
5	4	59	99	0.00504	3.639E-04	62.4	2.443E-05	0.593	3.708E-07	0.997	0.129	1971	0.1281	12426	0.0185	0.105	0.3775	2.6095	BUBBLE FLOW	
5	4	59	98	0.00504	3.639E-04	62.4	2.443E-05	0.588	3.708E-07	0.997	0.130	1988	0.1292	10265	0.0154	0.113	0.3146	2.6320	BUBBLE FLOW	
5	4	68	148	0.00498	3.200E-04	62.3	2.146E-05	0.835	3.765E-07	0.996	0.091	943	0.0613	3264	0.0035	0.418	0.0704	1.2485	BUBBLE FLOW	
5	4	77	160	0.00492	2.821E-04	62.2	1.890E-05	0.882	3.821E-07	0.996	0.087	960	0.0624	5820	0.0058	0.371	0.1189	1.2710	BUBBLE FLOW	
5	4	77	160	0.00492	2.821E-04	62.2	1.890E-05	0.882	3.821E-07	0.996	0.087	977	0.0635	7340	0.0074	0.373	0.1499	1.2935	BUBBLE FLOW	
5	4	68	147	0.00498	3.200E-04	62.3	2.146E-05	0.830	3.765E-07	0.996	0.092	1011	0.0657	9722	0.0104	0.333	0.2110	1.3385	BUBBLE FLOW	
5	4	77	155	0.00492	2.821E-04	62.2	1.890E-05	0.857	3.821E-07	0.996	0.089	1474	0.0958	10088	0.0104	0.178	0.2121	1.9515	BUBBLE FLOW	
5	4	60	150	0.00503	3.587E-04	62.4	2.407E-05	0.859	3.714E-07	0.996	0.089	1508	0.0980	6639	0.0088	0.185	0.1393	1.9965	BUBBLE FLOW	
5	4	77	155	0.00492	2.821E-04	62.2	1.890E-05	0.857	3.821E-07	0.996	0.089	1525	0.0991	12910	0.0133	0.167	0.2715	2.0190	BUBBLE FLOW	
5	4	77	154	0.00492	2.821E-04	62.2	1.890E-05	0.852	3.821E-07	0.996	0.090	1525	0.0991	17049	0.0177	0.152	0.3807	2.0190	BUBBLE FLOW	
5	4	59	154	0.00504	3.639E-04	62.4	2.443E-05	0.881	3.708E-07	0.996	0.087	1954	0.1270	18178	0.0182	0.107	0.3716	2.5870	BUBBLE FLOW	
5	4	75	150	0.00494	2.900E-04	62.2	1.943E-05	0.835	3.809E-07	0.996	0.092	2005	0.1303	7688	0.0091	0.131	0.1660	2.6545	BUBBLE FLOW	
5	4	76	150	0.00493	2.860E-04	62.2	1.916E-05	0.833	3.815E-07	0.996	0.092	2005	0.1303	14811	0.0157	0.107	0.3204	2.6545	BUBBLE FLOW	
5	4	76	150	0.00493	2.860E-04	62.2	1.916E-05	0.833	3.815E-07	0.996	0.092									

CHAPTER IV

SIMPLIFIED MODEL

In this Chapter, a new simplified model is proposed, which includes the effect of the slip velocity in the radial direction, a variable never considered in previous simplified models proposed by Alhanati (1993) and Serrano (1999). Based on a similar procedure used by Ishii and Zuber (1979) and shown in Appendix C, it was demonstrated that the ratio of the slip velocity in the radial and vertical directions is directly proportional to the ratio of the liquid radial acceleration to the gravitational acceleration, i.e.

$$\frac{V_{sr}}{V_{sz}} \propto \left(\frac{V_{lr}}{|g|} \frac{dV_{lr}}{dr} \right), \quad (4.1)$$

where, V_{sr} and V_{sz} represent the slip velocity in the radial and vertical direction, respectively. V_{lr} and g represent the liquid velocity in the radial direction and the gravitational acceleration term, respectively. The liquid radial velocity at the pump intake, V_{lr} can be estimated by:

$$V_{lr} = -\frac{q_l^i}{2 \pi r_p h_p}, \quad (4.2)$$

where, q_l^i , r_p and h_p represent the liquid flow rate, the outside pump radius and the pump intake port height, respectively. The liquid radial velocity gradient can be approximated by:

$$\frac{dV_{lr}}{dr} = -\frac{V_{lr}}{(r_c - r_p)}, \quad (4.3)$$

where r_c represent the inside casing radius. Substituting Eqs. 4.2 and 4.3 into Eq. 4.1, the following relationship results valid:

$$\frac{V_{sr}}{V_{sz}} \propto -\frac{1}{(r_c - r_p) g} \left(\frac{q_l^i}{2 \pi r_p h_p} \right)^2. \quad (4.4)$$

Based on three different casing inside diameter of 5 in., 6 in. and 8 in., a pump outside diameter of 4 in., a pump intake height of 2 in., and assuming several liquid flow rates values, the slip velocity ratio given by Eq. 4.4 can be estimated and represented graphically, as shown in Fig. 4.1.

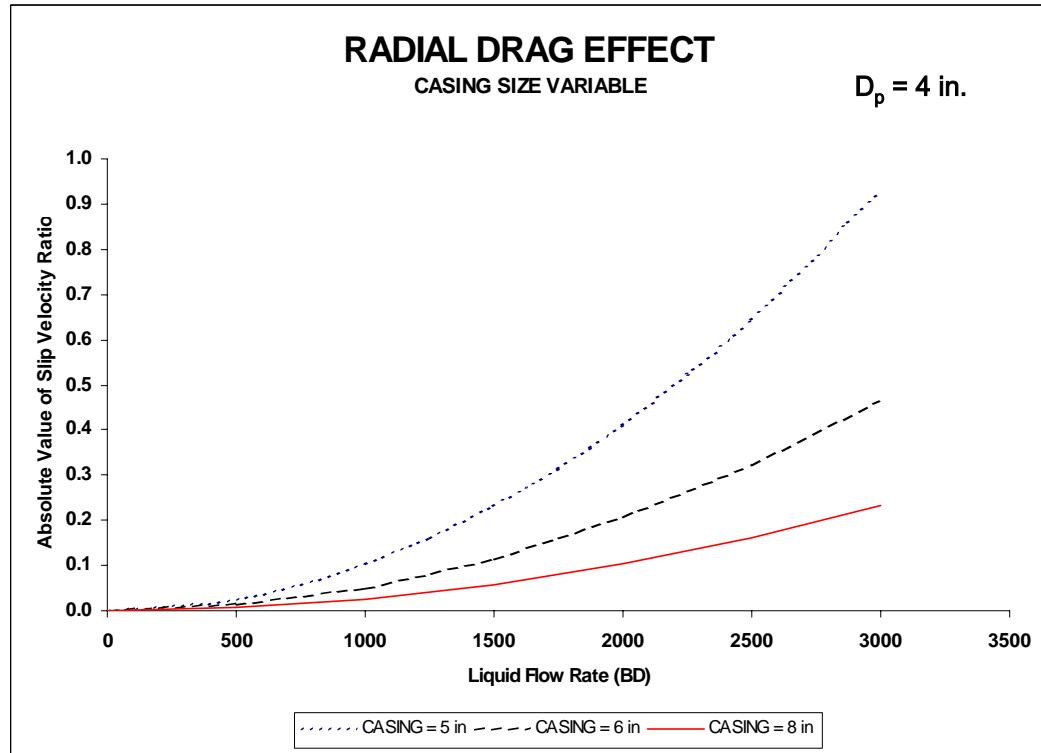


Figure 4.1 – Radial Drag Effect.

According to Fig. 4.1, the higher the liquid flow rate, the higher the slip velocity effect in the radial direction. Besides, the radial slip velocity effect is increased for smaller casing sizes, assuming a constant pump size.

General Formulation

A control volume is defined in front of the pump intake as shown in Fig. 4.2. The gas coming from the annulus is divided into two streams as shown in Fig. 4.3. One stream flows into the pump intake together with the liquid production, and the other flows vertically to the surface to be vented. The gas void fraction coming from the annulus and the gas void fraction going into the pump are represented by α_a and α_p , respectively.

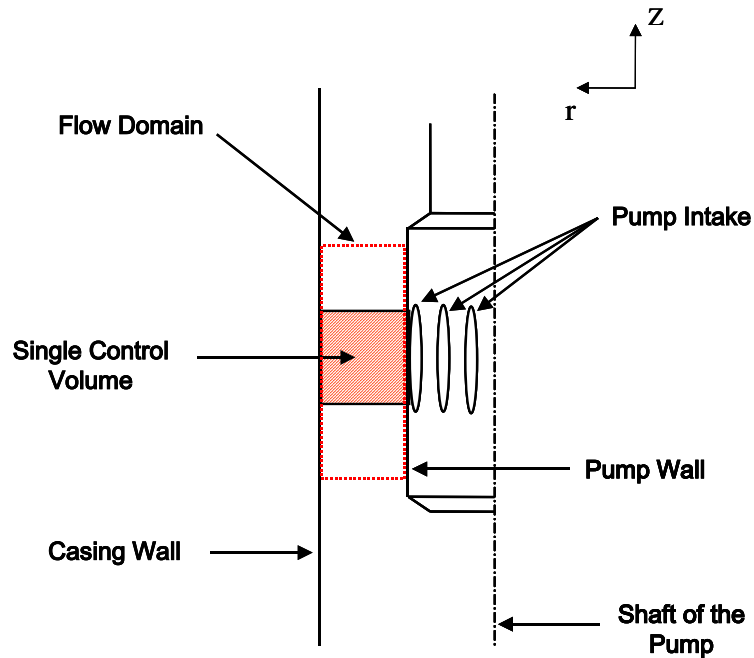


Figure 4.2 – Flow Domain in the Bottomhole.

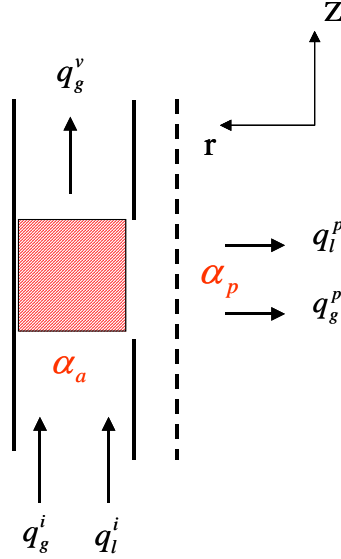


Figure 4.3 – Volumetric Balance Around a Single Control Volume.

The continuity equation for incompressible flow yields the following volumetric equations for the liquid and gas phases as:

$$q_l^i = q_l^p, \quad (4.5)$$

$$q_g^i = q_g^p + q_g^v, \quad (4.6)$$

where q_l^i and q_l^p represent the liquid flow rate coming from the annulus and liquid flow rate going inside the pump, respectively and q_g^i , q_g^p and q_g^v are the gas flow rate coming from the annulus, gas flow rate going into the pump and the gas flow rate vented, respectively. Note that Eq. 4.6 can also be rewritten as:

$$\frac{q_g^v}{q_g^i} = 1 - \frac{q_g^p}{q_g^i}. \quad (4.7)$$

Natural separation efficiency E is defined as the ratio between the gas flow rate vented to the total gas flow rate, i.e.

$$E = \frac{q_g^v}{q_g^i}. \quad (4.8)$$

Then, the combination of Eqs. 4.7 and 4.8 defines the natural separation efficiency by:

$$E = 1 - \frac{q_g^p}{q_g^i}. \quad (4.9)$$

The gas flow rates can also be expressed as a function of superficial gas velocities:

$$q_g^p = -V_{sgr}^p A_p, \quad (4.10)$$

$$q_g^i = V_{sgz}^i A_a, \quad (4.11)$$

where V_{sgr}^p and V_{sgz}^i represent the radial superficial gas velocity going into the pump and the vertical superficial gas velocity coming from the annulus, respectively. A_p and A_a are the area of the pump intake ports and the area of the casing-pump annulus, respectively.

Substituting Eqs. 4.10 and 4.11 into Eq. 4.9, the natural separation efficiency can be rewritten as a function of superficial gas and liquid velocities as:

$$E = 1 + \frac{V_{sgr}^p}{V_{sgz}^i} \left(\frac{A_p}{A_a} \right). \quad (4.12)$$

The superficial gas velocity coming from the annulus V_{sgz}^i is easily calculated since it is related to the production conditions. In order to calculate the efficiency it is necessary to determine the radial superficial gas velocity going into the pump, V_{sgr}^p . For

the flow in the radial direction as shown in Fig. 4.4, the slip velocity is given by the following relationship:

$$V_{sr} = \frac{V_{sgr}^p}{\alpha_p} - \frac{V_{slr}^p}{1 - \alpha_p}. \quad (4.13)$$

Therefore, the superficial gas velocity going into the pump V_{sgr}^p can be obtained, from Eq. 4.13, as:

$$V_{sgr}^p = \alpha_p V_{sr} + \frac{\alpha_p}{1 - \alpha_p} V_{slr}^p. \quad (4.14)$$

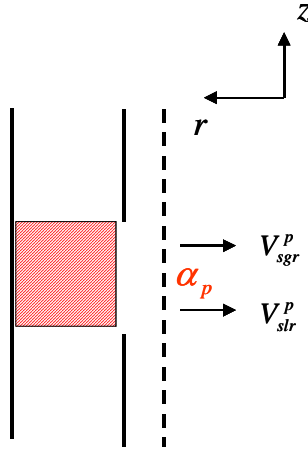


Figure 4.4 – Slip Velocity Analysis in the Radial Direction.

From Eq. 4.5 the following relationship for the V_{slr}^p must also be valid:

$$V_{slr}^p = -V_{slz}^i \left(\frac{A_a}{A_p} \right). \quad (4.15)$$

Thus, combining Eqs. 4.14 and 4.15 the following equation for V_{sgr}^p is obtained:

$$V_{sgr}^p = \alpha_p V_{sr} - \frac{\alpha_p}{1 - \alpha_p} \frac{A_a}{A_p} V_{slz}^i. \quad (4.16)$$

Combining Eqs. 4.12 and 4.16, the following equation is obtained for natural separation efficiency:

$$E = 1 - \frac{1}{V_{sgz}^i} \left(\frac{A_p}{A_a} \right) \left[-\alpha_p V_{sr} + \frac{\alpha_p}{1 - \alpha_p} \frac{A_a}{A_p} V_{slz}^i \right]. \quad (4.17)$$

Additional relationships for the slip velocity in the radial direction, V_{sr} , and for the gas void fraction in front of the pump, α_p , are also required for the solution of Eq. 4.17. Those relationships can be obtained from the drift-flux model proposed by Ishii (1975). In the drift-flux model, the drift velocity V_{dj} for the dispersed phase is given by:

$$V_{dj} = V_\infty (1 - \alpha_d)^n - \frac{D_d^\alpha}{\alpha_d} \nabla \alpha_d, \quad (4.18)$$

where V_∞ represents the terminal velocity of a single bubble, n is a coefficient for the effects of the presence of other bubbles and D_d^α is the diffusivity of the phase in the fluid medium. Since very few studies have been carried out on the parameter, D_d^α , a value of zero for diffusivity of the phases is assumed in this work. Therefore, Eq. 4.18 can be written for the drift velocity for the gas phase, V_{gj} , as:

$$V_{gj} = V_\infty (1 - \alpha_g)^n. \quad (4.19)$$

Based on the kinematics constitutive equation, shown in Appendix B, the following relationship is also valid:

$$-\frac{\alpha_g \rho_g}{\rho_m} V_s = -\frac{\alpha_g \rho_g}{(1 - \alpha_g) \rho_m} V_{gj}. \quad (4.20)$$

From Eq. 4.20, the following equation for the gas drift velocity results:

$$V_{gj} = V_s (1 - \alpha_g). \quad (4.21)$$

Combining Eqs. 4.19 and 4.21 the following equation for the slip velocity is obtained.

$$V_s = V_\infty (1 - \alpha_g)^{n-1}. \quad (4.22)$$

For the radial direction and the vertical direction, Eq. 4.22 can be written, respectively, as:

$$V_{sr} = V_{\infty r} (1 - \alpha_p)^{n-1}, \quad (4.23)$$

$$V_{sz} = V_{\infty z} (1 - \alpha_a)^{n-1}. \quad (4.24)$$

Substituting Eq. 4.23 into Eq. 4.17 yields:

$$E = 1 - \frac{1}{V_{sgz}^i} \left(\frac{A_p}{A_a} \right) \left[-\alpha_p V_{\infty r} (1 - \alpha_p)^{n-1} + \frac{\alpha_p}{1 - \alpha_p} \frac{A_a}{A_p} V_{slz}^i \right]. \quad (4.25)$$

An additional relationship for α_p is still required in order to solve Eq. 4.25 for the efficiency. For flow in the vertical direction, the slip velocity is given by the following relationship:

$$V_{sz} = \frac{V_{sgz}}{\alpha} - \frac{V_{slz}}{1 - \alpha}. \quad (4.26)$$

On the other hand, the slip velocity in the vertical direction is given, from Eq. 4.24, by:

$$V_{sz} = V_{\infty z} (1 - \alpha)^{n-1}. \quad (4.27)$$

Combining Eqs. 4.26 and 4.27, one additional equation for the slip velocity in the vertical direction is found. This equation is given by:

$$V_{\infty z} (1 - \alpha)^{n-1} = \frac{V_{sgz}}{\alpha} - \frac{V_{slz}}{1 - \alpha}. \quad (4.28)$$

Eq. 4.28 will depend on the position of the control volume in the bottomhole, as shown in Fig. 4.5.

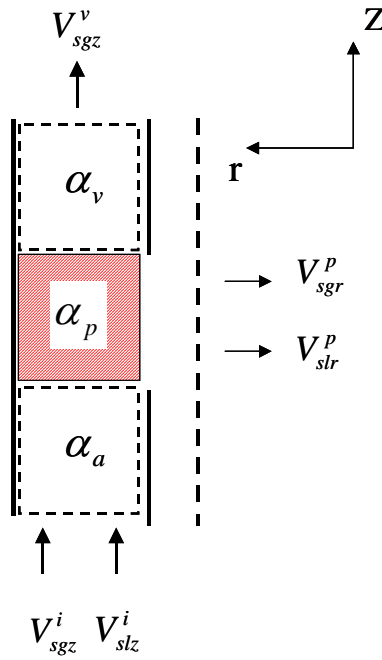


Figure 4.5 – Single Control Volumes.

Below the pump intake, it is assumed that the liquid and gas are flowing in the vertical direction only and that the gas void fraction is α_a . As a consequence, Eq. 4.28 can be rewritten as:

$$V_{\infty z} (1 - \alpha_a)^{n-1} = \frac{V_{sgz}^i}{\alpha_a} - \frac{V_{slz}^i}{1 - \alpha_a}. \quad (4.29)$$

In front of the pump intake, it is assumed that the liquid's vertical movement is slowed down and that the liquid is mainly moving in the radial direction towards the pump intake. It is also assumed that in this region, the gas is still moving vertically and that the gas void fraction is represented by α_p . Therefore, Eq. 4.28 can be rewritten, in front of the pump intake, as:

$$V_{\infty z} (1 - \alpha_p)^{n-1} = \frac{V_{sgz}^i}{\alpha_p}. \quad (4.30)$$

Finally, above the pump intake, it is assumed that the vented gas is moving vertically through a stagnant liquid column and that the gas void fraction in this region is represented by α_v . Therefore, Eq. 4.28 in this region reduces to:

$$V_{\infty z} (1 - \alpha_v)^{n-1} = \frac{V_{sgz}^i E}{\alpha_v}. \quad (4.31)$$

Finally, the governing equations in this general formulation for predicting natural separation efficiency are given by the following system of equations:

$$\left\{ \begin{array}{l} E = 1 - \frac{1}{V_{sgz}^i} \left(\frac{A_p}{A_a} \right) \left[-\alpha_p V_{\infty r} (1 - \alpha_p)^{n-1} + \frac{\alpha_p}{1 - \alpha_p} \frac{A_a}{A_p} V_{slz}^i \right] \\ V_{\infty z} (1 - \alpha_a)^{n-1} = \frac{V_{sgz}^i}{\alpha_a} - \frac{V_{slz}^i}{1 - \alpha_a} \\ V_{\infty z} (1 - \alpha_p)^{n-1} = \frac{V_{sgz}^i}{\alpha_p} \\ V_{\infty z} (1 - \alpha_v)^{n-1} = \frac{V_{sgz}^i E}{\alpha_v} \end{array} \right\}. \quad (4.32)$$

Alhanati's Simplified Model

Alhanati considered that the gas void fraction in front of the pump intake is constant and equal to the gas void fraction below the pump intake. He also assumed that the slip velocity in the radial direction $V_{\infty r}$ was zero. As a result, Eqs. 4.25 and 4.29 can be rewritten as:

$$E = 1 - \left(\frac{\alpha_a}{1 - \alpha_a} \right) \frac{V_{slz}^i}{V_{sgz}^i}, \quad (4.33)$$

$$\alpha_a \left[(1 - \alpha_a)^n + \left(\frac{V_{sgz}^i + V_{slz}^i}{V_{\infty z}} \right) \right] = \frac{V_{sgz}^i}{V_{\infty z}}. \quad (4.34)$$

Note that the solution of Eq. 4.34 will require one additional equation for the terminal velocity of the bubbles in the vertical direction, $V_{\infty z}$. Since the flow pattern regime predominantly observed in the experimental data gathered by Alhanati is slug/churn flow, Alhanati recommended using the terminal velocity equation proposed by Ishii (1979), which is given by:

$$V_{\infty z} = \sqrt{2} \left[\frac{\sigma (\rho_l - \rho_g) |g|}{\rho_l^2} \right]^{1/4}. \quad (4.35)$$

On the other hand and under a slug/churn flows regime, Ishii and Zuber (1979) admitted that a value of zero for the exponent n , considered in Eq. 4.34 and which takes into account the effect due to the presence of others bubbles, could be assumed. Consequently, Eq. 4.34 can be rewritten and used to define a relationship for the gas void fraction. This equation is given by:

$$\alpha_a = \frac{V_{sgz}^i}{(V_{sgz}^i + V_{slz}^i + V_{\infty z})}. \quad (4.36)$$

According to Alhanati's model, the governing equations reduces to the following set of equations:

$$\left\{ \begin{array}{l} E = 1 - \left(\frac{\alpha_a}{1 - \alpha_a} \right) \frac{V_{slz}^i}{V_{sgz}^i} \\ \alpha_a = \frac{V_{sgz}^i}{(V_{sgz}^i + V_{slz}^i + V_{\infty z})} \end{array} \right\}. \quad (4.37)$$

Solving the set of equations given by 4.37 the following equation for predicting natural separation efficiency E is obtained:

$$E = \frac{V_{\infty z}}{V_{slz}^i + V_{\infty z}}. \quad (4.38)$$

Serrano's Simplified Model

Serrano (1999) conducted an experimental work to validate and extend Alhanati's model to inclined flow. Three different inclination angles from horizontal were chosen (90, 60, and 30 degrees). In addition, the flow pattern regime was included in the predictions regarding to natural separation.

Serrano also considered no slip velocity in the radial direction. Therefore, this assumption allows defining, from Eq. 4.17, the following relationship for predicting natural separation efficiency.

$$E = 1 - \frac{\alpha_p}{1 - \alpha_p} \frac{V_{slz}^i}{V_{sgz}^i}. \quad (4.39)$$

Besides, Serrano assumed that the gas void fraction going into the pump α_p is different than the gas void fraction coming from the annulus α_a . Serrano never used Eq. 4.30 to estimate α_p , but based on the available experimental data, proposed a correlation to predict α_p , as a function of α_a and the inclination angle θ .

The main difference between the Alhanati and Serrano models is found in the gas void fraction treatment. The following comparison can then be made between the two approaches. In the radial direction, the assumption of no slip velocity allows rewriting Eq. 4.13, according to Alhanati and Serrano's assumptions regarding the gas void fraction, as:

$$(1 - \alpha_p) (1 - E^{Serrano}) V_{sgr}^i - \alpha_p V_{slr}^i = 0, \quad (4.40)$$

$$(1 - \alpha_a) (1 - E^{Alhanatii}) V_{sgr}^i - \alpha_a V_{slr}^i = 0. \quad (4.41)$$

The following relationship between both models efficiencies can be obtained:

$$E^{Serrano} = \left(\frac{\alpha_p}{1 - \alpha_p} \right) \left(\frac{1 - \alpha_a}{\alpha_a} \right) E^{Alhanatii} + \left[1 - \left(\frac{\alpha_p}{1 - \alpha_p} \right) \left(\frac{1 - \alpha_a}{\alpha_a} \right) \right]. \quad (4.42)$$

Defining

$$\beta = \left(\frac{\alpha_p}{1 - \alpha_p} \right) \left(\frac{1 - \alpha_a}{\alpha_a} \right), \quad (4.43)$$

Eq. 4.42 can be rewritten as a function of this β parameter by:

$$E^{Serrano} = \beta E^{Alhanatii} + (1 - \beta). \quad (4.44)$$

New Simplified Model

Three assumptions are considered valid in the new simplified model for natural separation efficiency:

1. In this model, it is assumed that the liquid vertical movement is slowed down and that in front of the pump intake the liquid is mainly moving in the radial direction. Therefore, the gas void fraction is represented by α_p and can be estimated by using Eq. 4.30, i.e.,

$$\alpha_p (1 - \alpha_p)^{n-1} = \frac{V_{sgz}^i}{V_{\infty z}}. \quad (4.45)$$

2. The second assumption considers the existence of slip velocity in the vertical and radial direction. This assumption represents a new and important contribution in the analysis and development of the new simplified model, since previous simplified models never considered the slip velocity effect in the radial direction.
3. Under slug/churn flow regime, authors have neglected the effect due to other bubbles. Since most of the available experimental data is mainly under this flow regime, a value of n equal to zero will be considered in this simplified model.

Based on assumptions described above, the system of equations to be solved is given, from Eqs. 4.25 and 4.30, by:

$$E = 1 - \frac{1}{V_{sgz}^i} \left(\frac{\alpha_p}{1 - \alpha_p} \right) \left(\frac{A_p}{A_a} \right) \left[-V_{\infty r} + V_{slz}^i \left(\frac{A_a}{A_p} \right) \right], \quad (4.46)$$

$$\frac{\alpha_p}{(1 - \alpha_p)} = \frac{V_{sgz}^i}{V_{\infty z}}. \quad (4.47)$$

Combining Eqs. 4.46 and 4.47, natural separation efficiency assumes the form:

$$E = 1 - \left[-\frac{V_{\infty r}}{V_{\infty z}} \left(\frac{A_p}{A_a} \right) + \frac{V_{slz}^i}{V_{\infty z}} \right]. \quad (4.48)$$

According to Eq. 4.48, natural separation depends on superficial liquid velocity V_{slz}^i , the geometric configuration of the bottomhole A_p / A_a , and the terminal velocity ratio $V_{\infty r} / V_{\infty z}$.

Terminal velocity in the vertical direction $V_{\infty z}$ can be estimated from models such as Harmathy (1960), Wallis (1974), Ishii and Zuber (1979), among others. However, the terminal velocity in the radial direction $V_{\infty r}$ cannot be easily determined. The next section will present an analysis of the slip velocity in the vertical and radial directions.

Slip Velocity Analysis

Slip Velocity in the Vertical Direction

Based on a similar procedure used by Ishii and Zuber (1979), it was demonstrated in Appendix C that the slip velocity in the vertical direction V_{sz} could be determined using the following equation:

$$V_{sz} \left| \vec{V}_s \right| = \frac{8}{3} \frac{r_d (1 - \alpha_g) (\rho_l - \rho_g) |g|}{C_d \rho_l}, \quad (4.49)$$

where, according to Eq. 4.49, slip velocity V_{sz} is a function of the average drag radius r_d , gas void fraction α_g , fluid densities, and drag coefficient C_d .

Slip Velocity in the Radial Direction

In Appendix C, it was also demonstrated that the slip velocity in the radial direction V_{sr} could be given by:

$$V_{sr} |\vec{V}_s| = \frac{8 r_d (1 - \alpha_g)}{3 C_d} \left(V_{lr} \frac{dV_{lr}}{dr} \right). \quad (4.50)$$

According to Eq. 4.50, V_{sr} is directly proportional to the liquid phase radial acceleration in front of the pump intake. Also, note that under one-dimensional flow, the resultant slip velocity $|\vec{V}_s|$ is equal to V_{sr} .

Slip Velocity Ratio

Note that if Eq. 4.50 is divided by Eq. 4.49, one relationship for the slip velocity ratio can be found. This relationship is given by:

$$\frac{V_{sr}}{V_{sz}} = \frac{\rho_l}{(\rho_l - \rho_g) |g|} \left(V_{lr} \frac{dV_{lr}}{dr} \right). \quad (4.51)$$

On the other hand, from the drift-flux model approach, the following set of equations is obtained:

$$\left\{ \begin{array}{l} V_{sr} = V_{\infty r} (1 - \alpha_g)^{n-1} \\ V_{sz} = V_{\infty z} (1 - \alpha_g)^{n-1} \end{array} \right\}, \quad (4.52)$$

Solving the system given by 4.52, the following ratio would result valid:

$$\frac{V_{sr}}{V_{sz}} = \frac{V_{\infty r}}{V_{\infty z}}. \quad (4.53)$$

According to Eq. 4.53, Eq. 4.51 can be rewritten as a function of the terminal velocities, i.e.,

$$\frac{V_{\infty r}}{V_{\infty z}} = \frac{\rho_l}{(\rho_l - \rho_g)|g|} \left(V_{lr} \frac{dV_{lr}}{dr} \right). \quad (4.54)$$

Finally, natural separation efficiency can be predicted by solving the following set of equations:

$$\left\{ \begin{array}{l} E = 1 - \left[-\frac{V_{\infty r}}{V_{\infty z}} \left(\frac{A_p}{A_a} \right) + \frac{V_{slz}^i}{V_{\infty z}} \right] \\ \frac{V_{\infty r}}{V_{\infty z}} = \frac{\rho_l}{(\rho_l - \rho_g)|g|} \left(V_{lr} \frac{dV_{lr}}{dr} \right) \end{array} \right\}, \quad (4.55)$$

In order to use this system to solve for the natural separation efficiency, it is necessary to determine the liquid radial acceleration. This will be presented in Chapter V. In the next section, an alternative way for determining the effects of the liquid radial acceleration will be presented.

New Correlation

As shown in Fig. 4.6, the available experimental data indicates that it is possible to lump the geometric effects and the slip velocity ratio in an “ M ” Parameter.

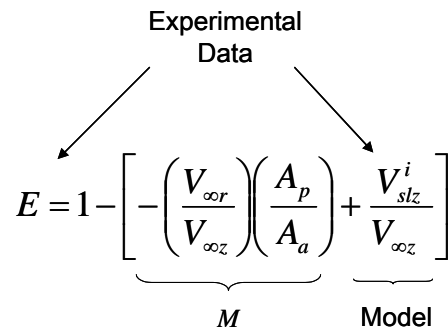


Figure 4.6 – M Parameter - New Simplified Model.

According to Fig. 4.6, the variables such as the natural separation efficiency E and superficial liquid velocity V_{slz}^i are known from the available experimental data. The terminal velocity in the vertical direction $V_{\infty z}$ can be determined from any available model previously mentioned.

In this work, Ishii and Zuber's (1979) model has been selected to predict the slip velocity in the vertical direction $V_{\infty z}$. Ishii et al. proposed the following model to estimate the terminal velocity of the bubbles in the vertical direction $V_{\infty z}$, under slug/churn flow regime, as:

$$V_{\infty z} = \sqrt{2} \left[\frac{\sigma (\rho_l - \rho_g) |g|}{\rho_l^2} \right]^{1/4}. \quad (4.56)$$

The simplified model for predicting natural separation, given by Eq. 4.48 and shown in Fig. 4.6, can be rewritten as:

$$M = 1 - \left[E + \frac{V_{slz}^i}{V_{\infty z}} \right], \quad (4.57)$$

where the “ M Parameter” is defined as:

$$M = -\frac{V_{\infty r}}{V_{\infty z}} \frac{A_p}{A_a}. \quad (4.58)$$

Note that Eq. 4.58 is a function of the terminal velocity ratio $V_{\infty r} / V_{\infty z}$, area of the port or pump intake A_p and the area of the annulus A_a . Using available experimental data from Serrano only, a graph of the parameter M as a function of $V_{slz}^i / V_{\infty z}$ was obtained. This graph is shown in Fig. 4.7.

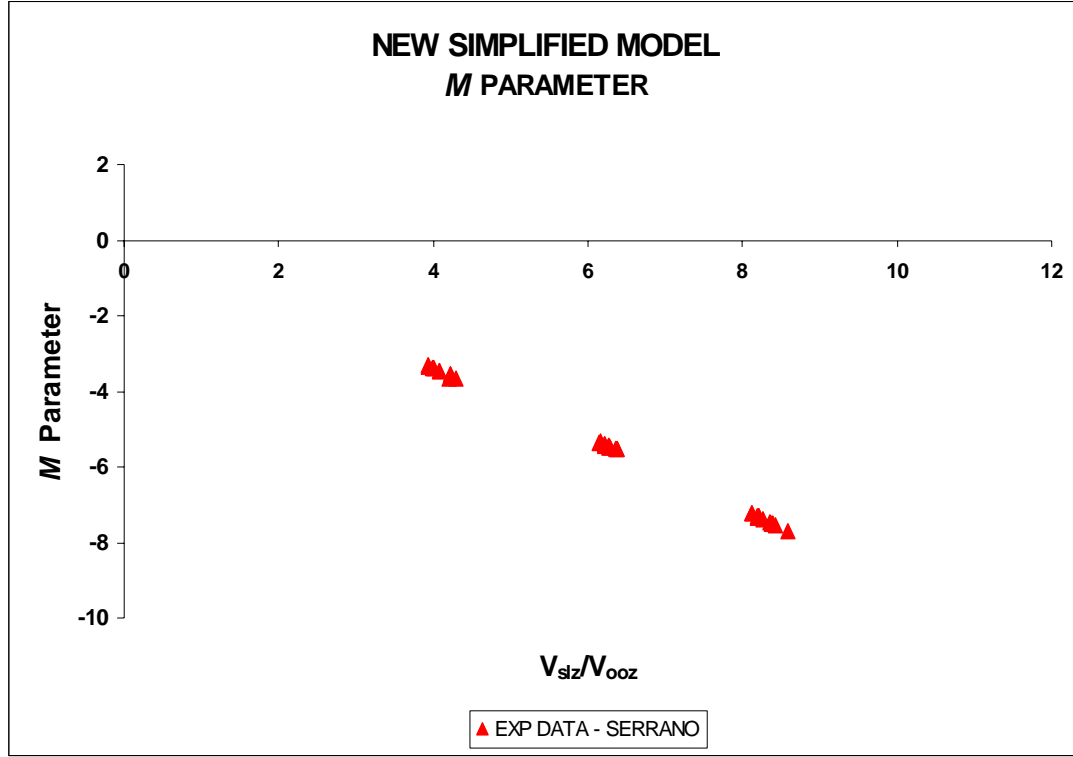


Figure 4.7 – M Parameter - New Correlation.

Since no radial slip exists when gas is flowing through a vertical stagnant liquid column, the value of M should be zero when the liquid superficial velocity is zero. Based on the data shown in Fig 4.7, a nonlinear regression model yields the following correlation for the parameter M .

$$M = - \left[\frac{a b + c \left(\frac{V_{slz}^i}{V_{ooz}} \right)^d}{b + \left(\frac{V_{slz}^i}{V_{ooz}} \right)^d} \right], \quad (4.59)$$

where the coefficients a , b , c and d are given by:

$$\begin{aligned} a &= -0.0093 & b &= 57.758 \\ c &= 34.40 & d &= 1.308 \end{aligned}.$$

Eq. 4.59 must be consistent with the values of efficiency, which varies between 0 and 1. For a natural separation efficiency value equal to 0, a limiting value for M , called M_1 , is given by:

$$M_1 = -\frac{V_{slz}^i}{V_{\infty z}} . \quad (4.60)$$

The upper limiting value is determined assuming the efficiency equal to 1. Therefore, this limiting value, called M_2 , is given by:

$$M_2 = 1 - \frac{V_{slz}^i}{V_{\infty z}} . \quad (4.61)$$

The new correlation and those two boundaries are shown in Fig. 4.8.

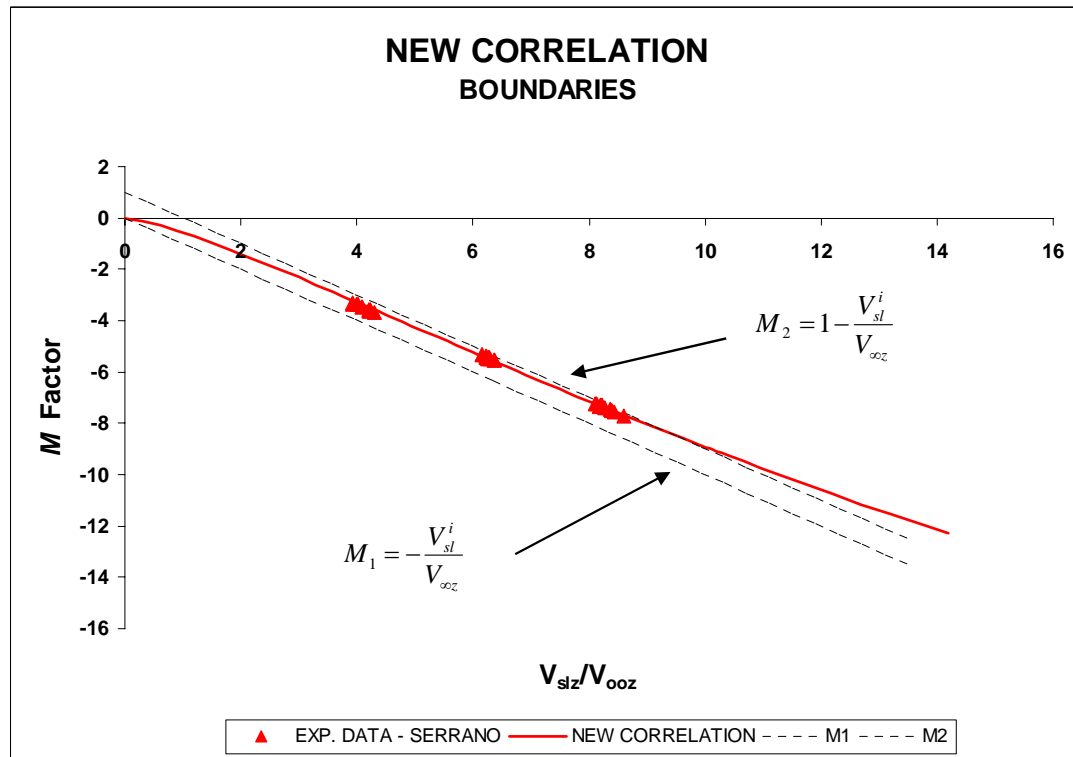


Figure 4.8 – Boundaries of the New Correlation.

In order to define the values of natural separation efficiency to the proper interval, a modification of the correlation for M is proposed as:

$$M = 1 - \left[\left(1 + \frac{a b + c \left(\frac{V_{slz}^i}{V_{ooz}} \right)^d}{b + \left(\frac{V_{slz}^i}{V_{ooz}} \right)^d} \right)^{272} + \left(\frac{V_{slz}^i}{V_{ooz}} \right)^{272} \right]^{1/272} \quad (4.62)$$

Eq. 4.62 shows a better agreement with the boundaries than the previous one given by Eq. 4.59, as shown in Fig. 4.9.

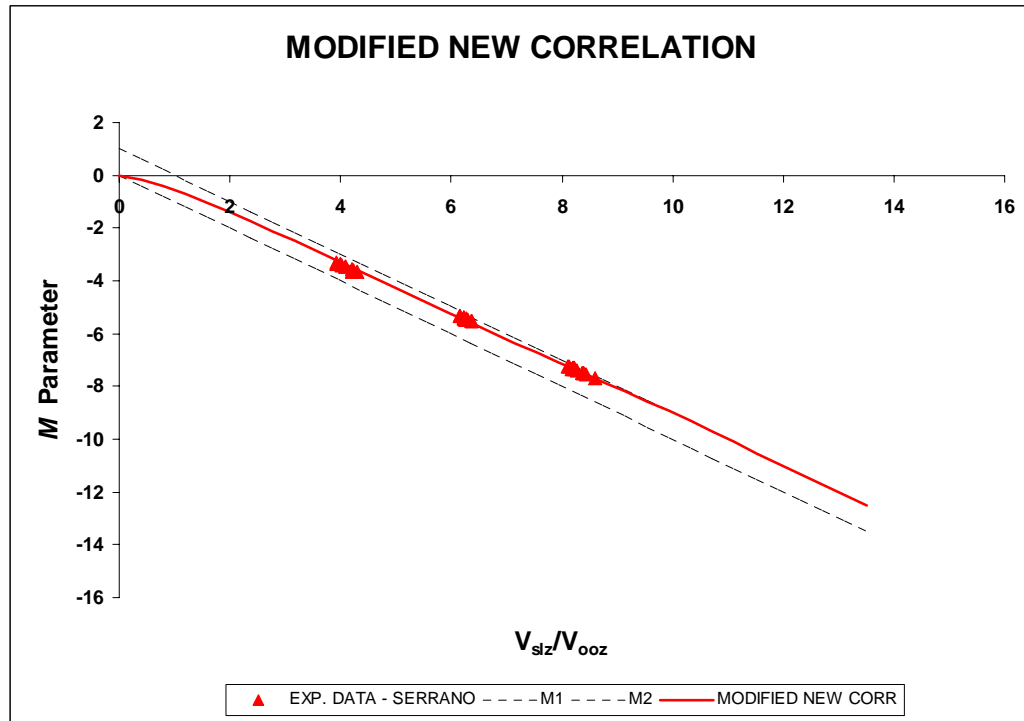


Figure 4.9 – Modified New Correlation.

Finally, natural separation efficiency can be calculated by:

$$E = 1 - \left\{ 1 - \left[\left(1 + \frac{a b + c \left(\frac{V_{slz}^i}{V_{ooz}} \right)^d}{b + \left(\frac{V_{slz}^i}{V_{ooz}} \right)^d} \right)^{272} + \left(\frac{V_{slz}^i}{V_{ooz}} \right)^{272} \right]^{1/272} + \left[\frac{V_{slz}^i}{V_{ooz}} \right] \right\}, \quad (4.63)$$

or simply,

$$E = \left\{ \left[1 + \frac{a b + c \left(\frac{V^i}{V_{\sigma\sigma}} \right)^d}{b + \left(\frac{V^i}{V_{\sigma\sigma}} \right)^d} \right]^{272} + \left[\frac{V^i}{V_{\sigma\sigma}} \right]^{272} \right\}^{1/272} - \left(\frac{V^i}{V_{\sigma\sigma}} \right). \quad (4.64)$$

CHAPTER V

MECHANISTIC MODEL

In Chapter IV, a new simplified model is proposed which considers the effect of the slip velocity in the radial direction and the geometric characteristics of the bottomhole. A new correlation was obtained to solve the new simplified model based on TUALP experimental data.

In this Chapter, a mechanistic model is proposed to explain the effect of the radial slip under bubbly flow conditions. The shape for liquid phase streamlines in the region in front of the pump intake is assumed and the liquid velocity field can then be calculated. This liquid velocity field is later used to obtain the liquid radial acceleration and its effects on the gas phase are described by a force balance on the gas bubbles. By following the trajectories of individual bubbles in the annulus, separation efficiency can be calculated by a simple geometric relationship.

Simplified Model

The simplified model for predicting natural separation efficiency defined in Chapter IV consists of the following set of equations:

$$E = 1 - \left[-\frac{V_{\infty r}}{V_{\infty z}} \left(\frac{A_p}{A_a} \right) + \frac{V_{slz}^i}{V_{\infty z}} \right], \quad (5.1)$$

$$\frac{V_{sr}}{V_{sz}} = \frac{\rho_l}{(\rho_l - \rho_g) |g|} \left(V_{lr} \frac{dV_{lr}}{dr} \right). \quad (5.2)$$

The next sections will present the mechanistic model proposed to determine the liquid phase velocity field.

Liquid-Phase Velocity

It is assumed that the liquid phase follows the streamlines shown in Fig. 5.1 in front of the pump intake.

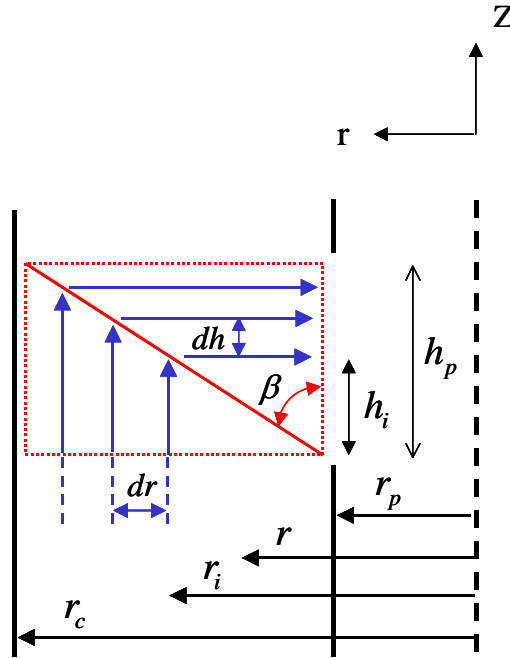


Figure 5.1 – Liquid Streamlines.

The line connecting the points where the liquid streamline changes from the vertical to the radial direction defines an angle, β , with the vertical axis. The following relationship can then be written:

$$\frac{dr}{dh} = \tan \beta = \frac{(r_c - r_p)}{h_p} = \frac{(r_c - r_i)}{(h_p - h_i)}, \quad (5.3)$$

where r_c and r_p represent the inside casing and outside pump radius, respectively and h_p is the pump intake port height.

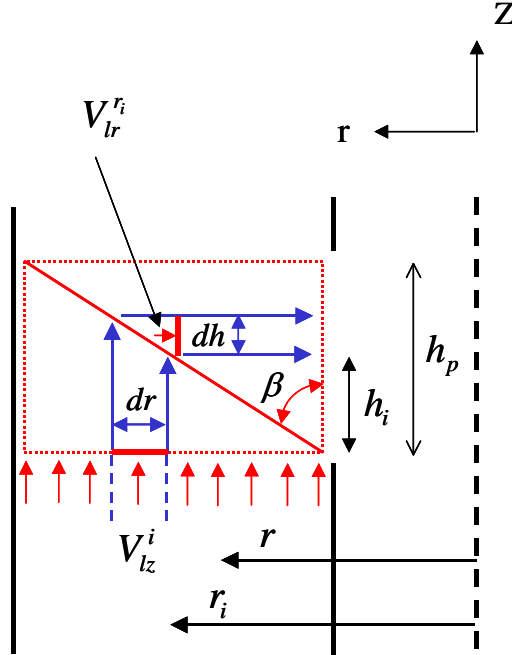


Figure 5.2 – Flow Throughout Two Liquid Streamlines.

Assuming that the liquid velocity V_{lz}^i distribution is constant and known at the inlet boundary of the control volume, the continuity equation for incompressible flow can be expressed by:

$$V_{lz}^i (2 \pi r_i dr) = -V_{lr}^{r_i} (2 \pi r_i dh), \quad (5.4)$$

where V_{lz}^i and $V_{lr}^{r_i}$ represent the liquid velocity in the vertical direction, in the inlet boundary of the control volume, and the liquid velocity in the radial direction for an arbitrary radius value r_i , respectively, in the beginning of the radial portion of the streamline. From Eq. 5.4, the following equation for $V_{lr}^{r_i}$ results:

$$V_{lr}^{r_i} = - \left(\frac{dr}{dh} \right) V_{lz}^i. \quad (5.5)$$

Combining Eqs. 5.3 and 5.5, $V_{lr}^{r_i}$ can also be defined as:

$$V_{lr}^{r_i} = - \tan \beta V_{lz}^i. \quad (5.6)$$

As shown in Fig. 5.3, the liquid phase velocity is accelerated as the liquid flows toward the pump intake.

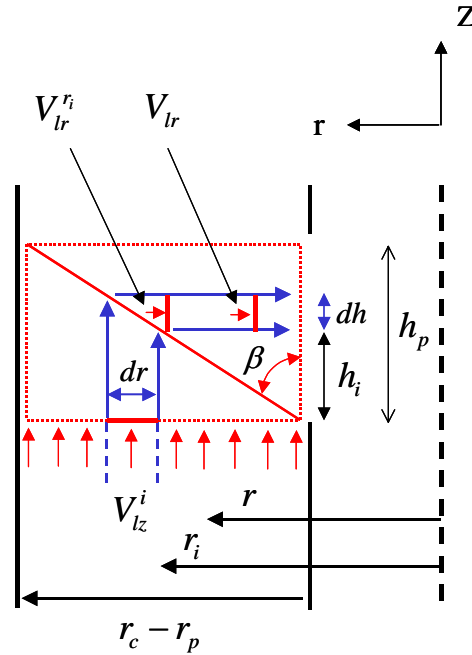


Figure 5.3 – Acceleration of the Liquid Phase in Front the Pump Intake.

The continuity equation can then be applied along this part of the streamline:

$$V_{lr}^{r_i} (2 \pi r_i dh) = V_{lr} (2 \pi r dh). \quad (5.7)$$

Therefore, the variation of the liquid velocity in the radial direction V_{lr} can be estimated, from Eq. 5.7, as:

$$V_{lr} = \left(\frac{r_i}{r} \right) V_{lr}^{r_i}. \quad (5.8)$$

Note that Eq. 5.8 is valid for $r_i \geq r \geq r_p$. On the other hand, the combination of Eqs. 5.6 and 5.8 yields:

$$V_{lr} = - \left(\frac{r_i}{r} \right) \tan \beta V_{lz}^i. \quad (5.9)$$

Since the model proposed in this chapter is based on the geometric characteristics of the bottomhole, r_i can be estimated as a function of h_i . From Eq. 5.3, the relationship is defined as:

$$r_i = r_p + \frac{h_i}{h_p} (r_c - r_p). \quad (5.10)$$

Finally, Eqs. 5.9 and 5.10 can be used to obtain the liquid radial velocity V_{lr} as:

$$V_{lr} = - \left(\frac{r_p}{r} + \frac{h_i}{h_p} \frac{(r_c - r_p)}{r} \right) \tan \beta V_{lz}^i, \quad (5.11)$$

In the mechanistic model proposed in this work, V_{lz}^i will be given by:

$$V_{lz}^i = \frac{q_l^i}{\pi (r_c^2 - r_p^2)}, \quad (5.12)$$

where, q_l^i represents the liquid flow rate coming from the annulus.

As an example, consider 500 BPD of liquid flowing between a casing of 6 in. I.D. and a pump of 2 in. O.D., and a pump intake size of 3 in.. Assuming three arbitrary

values of $r_i = 2.75$ in., 2.50 in., 2.25 in., the performance of Eq. 5.11 is illustrated in Fig.

5.4.

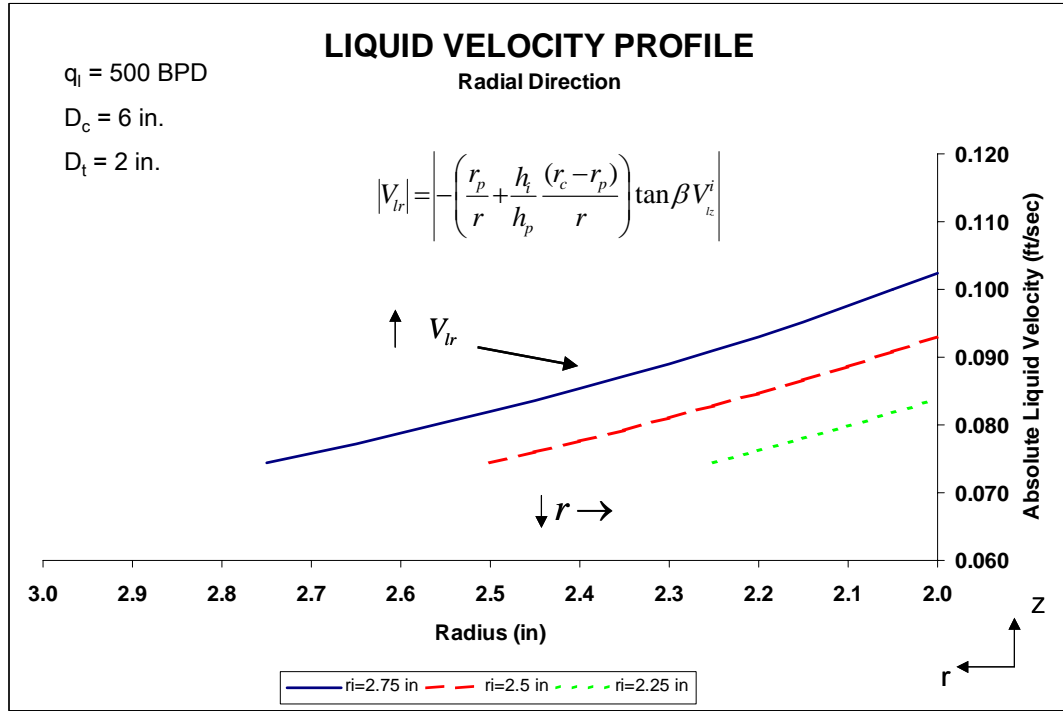


Figure 5.4 – Liquid Phase Velocity Profile in the radial Direction.

Gas-Phase Velocity

The extension from single-phase to two-phase flow is carried out through a force balance on a single gas bubble. It is assumed that the movement of the bubbles will not disturb the properties of the single-phase liquid flow field.

In addition, it is assumed that the bubble movement is in steady state condition and no merging or splitting of bubbles inside the domain occurs. The following sections will present a force balance analysis on a single gas bubble in the vertical and radial direction.

Vertical Direction

In the vertical direction, there are three forces acting on a gas bubble. A drag force, \vec{F}_d , which occurs in the direction of the slip due to pressure and shear forces on the surface of the bubble/droplet; a fluid force called the buoyancy force, \vec{F}_b ; and a force due to gravity called the gravity force, \vec{F}_g . Fig. 5.5 shows the distribution of those three forces, \vec{F}_d , \vec{F}_b and \vec{F}_g , in the vertical direction.

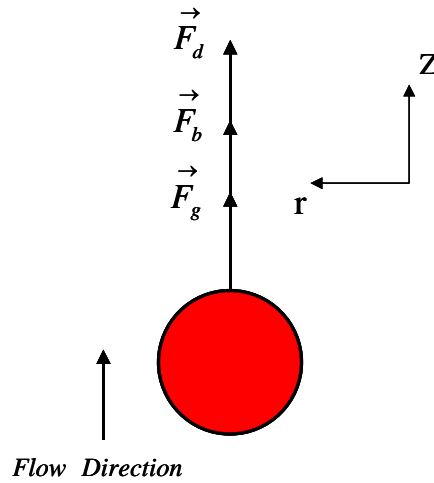


Figure 5.5 – Free-Body Diagram - Vertical Direction.

For steady state conditions, the force balance is given by the following set of equations:

$$\vec{F}_d + \vec{F}_b + \vec{F}_g = 0, \quad (5.13)$$

$$F_d = -\frac{1}{2} C_{d\infty} \rho_l A_d V_{sz} |\vec{V}_s|, \quad (5.14)$$

$$F_b = B_d \rho_l |g|, \quad (5.15)$$

$$F_g = -B_d \rho_g |g|, \quad (5.16)$$

where, C_d , ρ_l and ρ_g represent the drag coefficient, and the liquid and gas densities, respectively. ρ_m represents the mixture density. P is pressure and V_s represents the slip velocity.

A_d and B_d are the projected area of a typical bubble/particle and the volume of a typical bubble/particle, respectively. Assuming spherical gas bubbles, those variables are given by:

$$A_d = \pi r_d^2, \quad (5.17)$$

$$B_d = \frac{4}{3} \pi r_d^3, \quad (5.18)$$

where, r_d represents the average drag radius of a typical bubble/particle. The combination of Eqs. 5.13 - 5.18 yields a relationship for the slip velocity in the vertical direction V_{sz} , which is defined as:

$$V_{sz} = \frac{8 r_d (\rho_l - \rho_g) |g|}{3 C_{d\infty} \rho_l |\vec{V}_s|}, \quad (5.19)$$

where,

$$C_{d\infty} = \frac{C_d}{(1 - \alpha_g)}. \quad (5.20)$$

The slip velocity in the vertical direction is given by:

$$V_{sz} = V_{gz} - V_{lz}. \quad (5.21)$$

Assuming that in front of the pump intake, the liquid is mainly moving in the radial direction, the actual gas velocity V_{gz} is given by:

$$V_{gz} = V_{sz} . \quad (5.22)$$

Therefore, the combination of Eqs. 5.19 and 5.22 define V_{gz} as:

$$V_{gz} = \frac{2}{9} \frac{r_d (\rho_l - \rho_g) |g|}{C_{d\infty} \rho_l |\vec{V}_s|} . \quad (5.23)$$

Radial Direction

A force balance analysis around a single bubble in the radial direction is composed of a system of two forces, which are given by \vec{F}_d and \vec{F}_p . Those two forces are represented in Fig. 5.6.

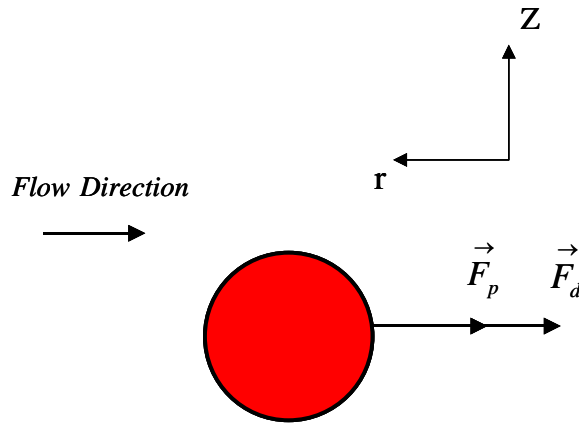


Figure 5.6 – Free-Body Diagram - Radial Direction.

Assuming no acceleration and one-dimensional flow in the radial direction only, the sum of those two forces acting on the bubble is given by:

$$\vec{F}_d + \vec{F}_p = 0 , \quad (5.24)$$

where

$$F_d = -\frac{1}{2} C_d \rho_l A_d V_{sr} |\vec{V}_s|, \quad (5.25)$$

$$F_b = -B_d \vec{\nabla} P = -B_d \frac{dP}{dr}. \quad (5.26)$$

Combining Eqs. 5.17, 5.18 and 5.20, with along Eqs. 5.24 - 5.26, the slip velocity in the radial direction V_{sr} can be defined as:

$$V_{sr} = -\frac{8}{3} \frac{r_d}{C_{d\infty} (1-\alpha_g) \rho_l |\vec{V}_s|} \frac{dp}{dr}. \quad (5.27)$$

As shown in Appendix C, the pressure gradient in the radial direction dp/dr is defined as:

$$\frac{dp}{dr} = -(1-\alpha_g) \rho_l V_{lr} \frac{dV_{lr}}{dr}. \quad (5.28)$$

Substituting Eq. 5.28 inside Eq. 5.27, the slip velocity in the radial direction V_{sr} may be defined as a function of the liquid velocity, V_{lr} . This equation is given by:

$$V_{sr} = \frac{8}{3} \frac{r_d}{C_{d\infty} |\vec{V}_s|} V_{lr} \frac{dV_{lr}}{dr}. \quad (5.29)$$

The solution of Eq. 5.29 will depend on the liquid phase velocity equation V_{lr} and its derivative with respect to r , which is given by:

$$\frac{dV_{lr}}{dr} = \left(\frac{r_p}{r^2} + \frac{h_i}{h_p} \frac{(r_c - r_p)}{r^2} \right) \tan \beta V_{lr}^i, \quad (5.30)$$

thus, the combination of Eqs. 5.11, 5.29 and 5.30 can define the following equation for V_{sr} as:

$$V_{sr} = -\frac{8}{3} \frac{r_d}{C_{d\infty} |\vec{V}_s|} \frac{1}{r^3} \left[\left(r_p + \frac{h_i}{h_p} (r_c - r_p) \right) \tan \beta V_{lz}^i \right]^2. \quad (5.31)$$

Based on the slip velocity definition, the actual gas phase velocity in the radial direction, V_{gr} , is given by:

$$V_{gr} = V_{sr} + V_{lr}. \quad (5.32)$$

Therefore, the combination of Eqs. 5.11, 5.31 and 5.32 yields the following equation for V_{gr} :

$$V_{gr} = -\left(r_p + \frac{h_i}{h_p} (r_c - r_p) \right) \tan \beta V_{lz}^i \left[\frac{8}{3} \frac{r_d}{C_{d\infty} |\vec{V}_s|} \frac{1}{r^3} \left(r_p + \frac{h_i}{h_p} (r_c - r_p) \right) \tan \beta V_{lz}^i + \frac{1}{r} \right]. \quad (5.33)$$

Trajectory of a Single Gas Bubble

The trajectory or displacement in the vertical and radial directions of a gas bubble can be obtained by:

$$dz = V_{gz} dt. \quad (5.34)$$

$$dr = V_{gr} dt. \quad (5.35)$$

Dividing Eq. 5.35 by Eq. 5.34, a geometric relationship for the bubble trajectory is obtained as:

$$\frac{dr}{dz} = \frac{V_{gr}}{V_{gz}}. \quad (5.36)$$

Since the actual gas velocity in the radial and vertical direction are known and given by Eqs. 5.33 and 5.23 respectively, Eq. 5.36 is an ordinary differential equation for the gas bubble trajectories that can be written as:

$$\frac{dr}{dz} = -\frac{9}{2} \frac{C_{d\infty} |\vec{V}_s|}{r_d} \frac{\rho_l}{(\rho_l - \rho_g) |g|} \left(r_p + \frac{h_l}{h_p} (r_c - r_p) \right) \tan \beta V_{lz}^i \left[\frac{8}{3} \frac{r_d}{C_{d\infty} |\vec{V}_s|} \frac{1}{r^3} \left(r_p + \frac{h_l}{h_p} (r_c - r_p) \right) \tan \beta V_{lz}^i + \frac{1}{r} \right]. \quad (5.37)$$

Eq. 5.37 will require two additional equations for $C_{d\infty}$ and r_d , for its numerical solution. There is an extensive amount of correlations available in the literature for the drag coefficient. In this work, some of them have been summarized and analyzed in Appendix D. In this simplified model, the simplest solution for solving the differential equation given by Eq. 5.37 is assuming Stokes flow. Therefore, the equation for $C_{d\infty}$ is given by:

$$C_{d\infty} = \frac{24}{\text{Re}_\infty}, \quad (5.38)$$

where the Reynolds number Re_∞ is defined as:

$$\text{Re}_\infty = \frac{2 r_d |\vec{V}_s| \rho_l}{\mu_l}, \quad (5.39)$$

and where ρ_l and μ_l represent the density and viscosity of the liquid phase, respectively. $|\vec{V}_s|$ and r_d are the resultant slip velocity and the average drag radius of a typical bubble, respectively. The combination of Eqs. 5.37 - 5.39 yields:

$$\frac{dr}{dz} = -54 \frac{\mu_l}{r_d^2} \frac{1}{(\rho_l - \rho_g) g} \left(r_p + \frac{h_i}{h_p} (r_c - r_p) \right) \tan \beta V_{lz}^i \left[\frac{2 r_d^2 \rho_l}{9 \mu_l} \frac{1}{r^3} \left(r_p + \frac{h_i}{h_p} (r_c - r_p) \right) \tan \beta V_{lz}^i + \frac{1}{r} \right]. \quad (5.40)$$

The numerical solution of Eq. 5.40 is used to estimate the trajectory of any gas bubble of drag radius r_d inside the flow domain. Predictions regarding natural separation efficiency are based on those trajectories, according to the methodology proposed in the following section.

Prediction of Natural Separation efficiency

Initially, it is assumed that gas bubbles are evenly distributed at the annulus inlet boundary. Tracking the trajectory of each gas bubble, there will be a point at the annulus inlet boundary where a gas bubble starts and finally hits the upper side of the pump intake, as shown in Fig. 5.7.

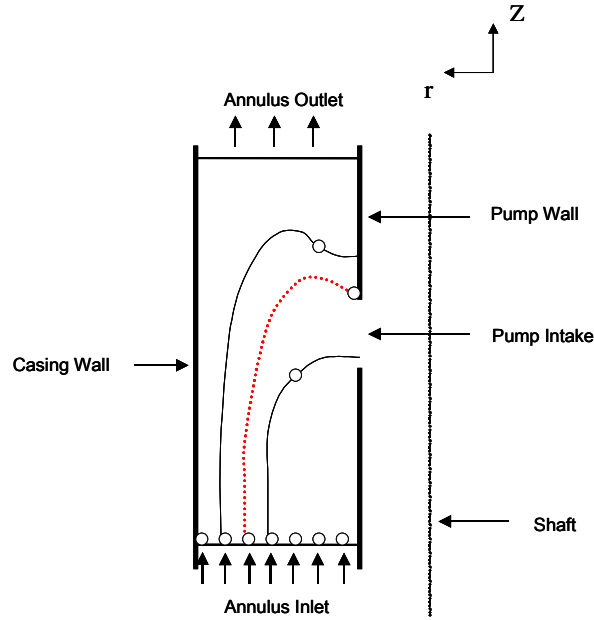


Figure 5.7 – Trajectory of the Bubbles into the Flow Domain.

The starting positions of the gas bubbles that hit the upper side of the pump intake define an imaginary circle called the “separation circle”, as shown in Fig. 5.8.

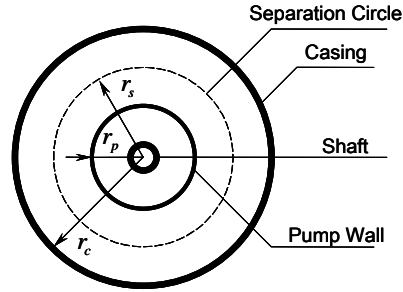


Figure 5.8 – Cross-Section of the Well Bore.

All the gas bubbles beyond this imaginary circle will be considered vented through the annulus. Otherwise, the bubble is considered dragged by the pump. Natural separation efficiency is then determined by the fraction of the cross sectional area beyond the separation circle to the total cross sectional area of the annulus. This equation is given by:

$$E = \frac{r_c^2 - r_s^2}{r_c^2 - r_p^2}. \quad (5.41)$$

Interface Characteristic Length

In order to obtain the bubble trajectories using Eq. 5.40 the bubble size needs to be known. In this model it is proposed to substitute the bubble size, r_d , by an interface characteristic length, ℓ_i . The bubble trajectory equation then becomes:

$$\frac{dr}{dz} = -54 \frac{\mu_l}{\ell_i^2} \frac{1}{(\rho_l - \rho_g) g} \left(r_p + \frac{h_i}{h_p} (r_c - r_p) \right) \tan \beta V_{l_z}^i \left[\frac{2}{9} \frac{\ell_i^2 \rho_l}{\mu_l} \frac{1}{r^3} \left(r_p + \frac{h_i}{h_p} (r_c - r_p) \right) \tan \beta V_{l_z}^i + \frac{1}{r} \right]. \quad (5.42)$$

TUALP experimental data was used as an input to the model and a trial and error procedure was followed to obtain values of the interface characteristic length that match the experimental results. The interface characteristic length values were used to calculate the interfacial area concentration a_i , for bubbly flow, as:

$$a_i = 3 \frac{\alpha_g}{\ell_i}. \quad (5.43)$$

Fig. 5.9 shows a plot of the interfacial area concentration, a_i , as a function of the superficial gas velocity, V_{sgz}^i , based on available experimental data to 100 Psig operational conditions only.

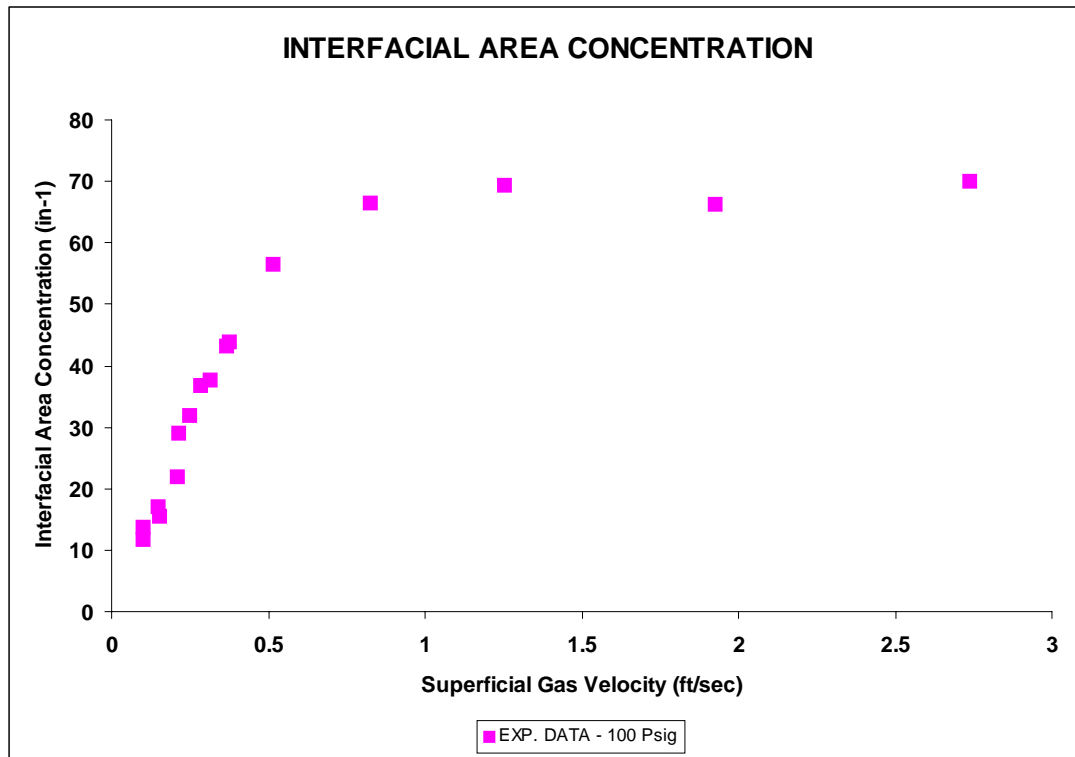


Figure 5.9 – Interfacial Area Concentration a_i .

In this work the following correlation is proposed for a_i :

$$a_i = 71.617 (1 - e^{-2.368 V_{sgz}^i}). \quad (5.44)$$

The proposed correlation for estimating the interfacial area concentration a_i , Eq. 5.44, is also shown in Fig. 5.10.

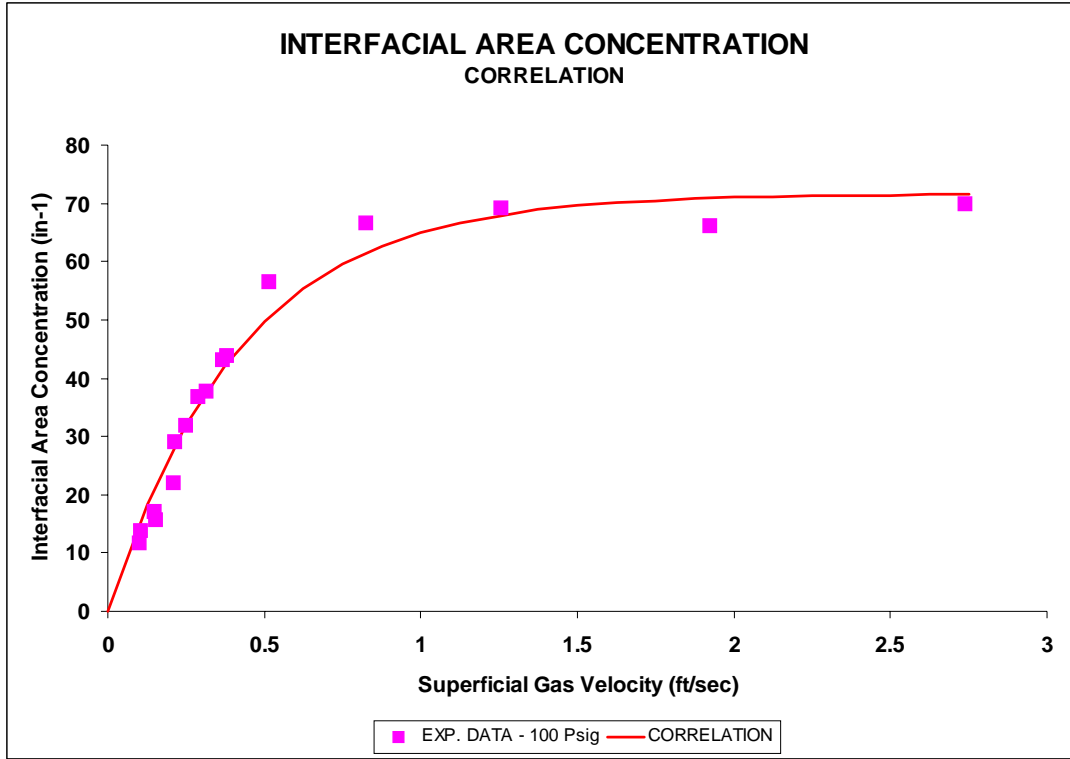


Figure 5.10 – Interfacial Area Concentration a_i - Correlation.

Combining Eqs. 5.43 and 5.44, the interface characteristic length, ℓ_i , can be defined as:

$$\ell_i = \frac{3}{71.617 (1 - e^{-2.368 V_{sgz}^i})} \frac{V_{sgz}^i}{(V_{sgz}^i + V_{\infty z})}. \quad (5.45)$$

Finally, the trajectory of the bubbles into the flow domain can be obtained by numerically solving Eq. 5.42 along with Eq. 5.45.

CHAPTER VI

NEW TWO-DIMENSIONAL TWO-PHASE FLOW MODEL

The simplified models proposed in Chapters IV and V showed the importance of the slip velocity and the acceleration of the liquid phase in the radial direction. A better approach to the problem can be obtained if a better description of the actual flow field in the region in front of the pump intake can be determined. Liu (2001) presented an improved model where mass and momentum balance equations are solved initially for the liquid phase flow only by using the Vorticity-Stream Function (VSF) approach in cartesian coordinate system. The extension to two-phase flow conditions is carried out through a force balance around a single bubble that enables tracking the trajectories of the gas bubble in the flow domain.

In this Chapter, a new methodology to simultaneously solve the mass and momentum balance equations for a gas-liquid mixture through the vorticity-stream function approach in a cylindrical coordinate system is proposed. This model obtains the solution for the liquid and gas velocities fields as well as the two-phase flow pressure and gas fraction fields.

Two-Phase Flow Model

Two Phase Flow Mass and Momentum Balance Equations

Assuming steady state, constant density, inviscid, axisymmetric and two-dimensional flow, and the mass and momentum balance equations in cylindrical coordinates for any phase k may be written as:

Mass Balance Equation:

$$\frac{\partial}{\partial r}(r \alpha_k V_{kr}) + \frac{\partial}{\partial z}(r \alpha_k V_{kz}) = 0. \quad (6.1)$$

Momentum Balance Equation:

r-Direction

$$\alpha_k \rho_k \left(V_{kr} \frac{\partial V_{kr}}{\partial r} + V_{kz} \frac{\partial V_{kr}}{\partial z} \right) + \alpha_k \frac{\partial P}{\partial r} - \alpha_k \rho_k g_r + \delta_k \vec{M}_{kr} = 0, \quad (6.2)$$

z-Direction

$$\alpha_k \rho_k \left(V_{kr} \frac{\partial V_{kz}}{\partial r} + V_{kz} \frac{\partial V_{kz}}{\partial z} \right) + \alpha_k \frac{\partial P}{\partial z} - \alpha_k \rho_k g_z + \delta_k \vec{M}_{kz} = 0, \quad (6.3)$$

where V_{kr} and V_{kz} represent the actual velocity of a phase k in the radial and vertical direction, respectively. P , \vec{M}_k and ρ_k are pressure, interfacial momentum transfer term and density, respectively. g_r and g_z represent the gravitational acceleration terms in the radial and vertical direction, respectively. The phase volumetric fraction is α_k . δ_k is a variable introduced to account for the interface momentum jump condition and is 1 for the gas phase and -1 for the liquid phase.

Vorticity Stream Function Approach

In cylindrical coordinates, the definition of the stream function for phase k is given by:

$$V_{kr} = \frac{1}{r \alpha_k} \frac{\partial \varphi_k}{\partial z}, \quad (6.4)$$

$$V_{kz} = -\frac{1}{r \alpha_k} \frac{\partial \varphi_k}{\partial r}. \quad (6.5)$$

Combining Eqs. 6.1, 6.4 and 6.5, it can be easily verified that the stream function satisfies the mass balance equation for any phase k , i.e.

$$\frac{\partial}{\partial r}(r \alpha_k V_{kr}) + \frac{\partial}{\partial z}(r \alpha_k V_{kz}) = \frac{\partial}{\partial r} \left(\frac{\partial \varphi_k}{\partial z} \right) + \frac{\partial}{\partial z} \left(-\frac{\partial \varphi_k}{\partial r} \right) = 0. \quad (6.6)$$

On the other hand, the vorticity Ω_k for any k phase, in cylindrical coordinates, is defined as:

$$\Omega_k = \left(\frac{\partial V_{kr}}{\partial z} - \frac{\partial V_{kz}}{\partial r} \right). \quad (6.7)$$

Combining Eqs. 6.4, 6.5 and 6.7, the vorticity can also be expressed as:

$$\Omega_k = -\frac{1}{r^2 \alpha_k} \frac{\partial \varphi_k}{\partial r} - \frac{1}{r \alpha_k^2} \left(\frac{\partial \alpha_k}{\partial r} \frac{\partial \varphi_k}{\partial r} + \frac{\partial \alpha_k}{\partial z} \frac{\partial \varphi_k}{\partial z} \right) + \frac{1}{r \alpha_k} \left(\frac{\partial^2 \varphi_k}{\partial r^2} + \frac{\partial^2 \varphi_k}{\partial z^2} \right). \quad (6.8)$$

Eq. 6.8 can be written for the gas and liquid phases, respectively, as:

$$\Omega_g = -\frac{1}{r^2 \alpha_g} \frac{\partial \varphi_g}{\partial r} - \frac{1}{r \alpha_g^2} \left(\frac{\partial \alpha_g}{\partial r} \frac{\partial \varphi_g}{\partial r} + \frac{\partial \alpha_g}{\partial z} \frac{\partial \varphi_g}{\partial z} \right) + \frac{1}{r \alpha_g} \left(\frac{\partial^2 \varphi_g}{\partial r^2} + \frac{\partial^2 \varphi_g}{\partial z^2} \right), \quad (6.9)$$

$$\Omega_l = -\frac{1}{r^2 (1-\alpha_g)} \frac{\partial \varphi_l}{\partial r} + \frac{1}{r (1-\alpha_g)^2} \left(\frac{\partial \alpha_g}{\partial r} \frac{\partial \varphi_l}{\partial r} + \frac{\partial \alpha_g}{\partial z} \frac{\partial \varphi_l}{\partial z} \right) + \frac{1}{r (1-\alpha_g)} \left(\frac{\partial^2 \varphi_l}{\partial r^2} + \frac{\partial^2 \varphi_l}{\partial z^2} \right). \quad (6.10)$$

Pressure Equation

In the radial direction, the momentum balance equation, given by Eq. 6.2, can be written separately for the gas and liquid phases. The combination of those yields one additional equation for the mixture. This equation is given by:

$$\frac{\partial P}{\partial r} = -\rho_g \left(\alpha_g V_{gr} \frac{\partial V_{gr}}{\partial r} + \alpha_g V_{gz} \frac{\partial V_{gr}}{\partial z} \right) - \rho_l \left(\alpha_l V_{lr} \frac{\partial V_{lr}}{\partial r} + \alpha_l V_{lz} \frac{\partial V_{lr}}{\partial z} \right). \quad (6.11)$$

In the vertical direction, a similar procedure yields a pressure gradient equation for a mixture. Assuming that $g_z = -|g|$, this equation would be defined as:

$$\frac{\partial P}{\partial z} = -\rho_g \left(\alpha_g V_{gr} \frac{\partial V_{gz}}{\partial r} + \alpha_g V_{gz} \frac{\partial V_{gr}}{\partial z} \right) - \rho_l \left(\alpha_l V_{lr} \frac{\partial V_{lz}}{\partial r} + \alpha_l V_{lz} \frac{\partial V_{lr}}{\partial z} \right) - ((1 - \alpha_g) \rho_l + \alpha_g \rho_g) |g|. \quad (6.12)$$

Eqs. 6.11 and 6.12, can also be rewritten without the external body force term as:

$$\frac{\partial P^*}{\partial r} = -\rho_g \left(\alpha_g V_{gr} \frac{\partial V_{gr}}{\partial r} + \alpha_g V_{gz} \frac{\partial V_{gr}}{\partial z} \right) - \rho_l \left(\alpha_l V_{lr} \frac{\partial V_{lr}}{\partial r} + \alpha_l V_{lz} \frac{\partial V_{lr}}{\partial z} \right), \quad (6.13)$$

$$\frac{\partial P^*}{\partial z} = -\rho_g \left(\alpha_g V_{gr} \frac{\partial V_{gz}}{\partial r} + \alpha_g V_{gz} \frac{\partial V_{gz}}{\partial z} \right) - \rho_l \left(\alpha_l V_{lr} \frac{\partial V_{lz}}{\partial r} + \alpha_l V_{lz} \frac{\partial V_{lz}}{\partial z} \right), \quad (6.14)$$

where

$$\frac{\partial P^*}{\partial r} = \frac{\partial P}{\partial r}, \quad (6.15)$$

$$\frac{\partial P^*}{\partial z} = \frac{\partial P}{\partial z} + ((1 - \alpha_g) \rho_l + \alpha_g \rho_g) |g|. \quad (6.16)$$

Eqs. 6.13 and 6.14 can also be rewritten by substituting some terms with the stream function definitions as:

$$\frac{\partial P^*}{\partial r} = -\frac{\rho_g}{r} \left(\frac{\partial \varphi_g}{\partial z} \frac{\partial V_{gr}}{\partial r} - \frac{\partial \varphi_g}{\partial r} \frac{\partial V_{gz}}{\partial z} \right) - \frac{\rho_l}{r} \left(\frac{\partial \varphi_l}{\partial z} \frac{\partial V_{lr}}{\partial r} - \frac{\partial \varphi_l}{\partial r} \frac{\partial V_{lz}}{\partial z} \right), \quad (6.17)$$

$$\frac{\partial P^*}{\partial z} = -\frac{\rho_g}{r} \left(\frac{\partial \varphi_g}{\partial z} \frac{\partial V_{gz}}{\partial r} - \frac{\partial \varphi_g}{\partial r} \frac{\partial V_{gz}}{\partial z} \right) - \frac{\rho_l}{r} \left(\frac{\partial \varphi_l}{\partial z} \frac{\partial V_{lz}}{\partial r} - \frac{\partial \varphi_l}{\partial r} \frac{\partial V_{lz}}{\partial z} \right). \quad (6.18)$$

Taking the derivative of Eq. 6.17 in respect to r and adding to the derivative of Eq. 6.18 in respect to z , an equation for the pressure is determined:

$$\begin{aligned} \frac{\partial^2 P^*}{\partial r^2} + \frac{\partial^2 P^*}{\partial z^2} = & -\frac{\rho_g}{r} \left[-\frac{1}{r} \left(\frac{\partial \varphi_g}{\partial z} \frac{\partial V_{gr}}{\partial r} - \frac{\partial \varphi_g}{\partial r} \frac{\partial V_{gz}}{\partial z} \right) + \frac{\partial^2 \varphi_g}{\partial r \partial z} \left(\frac{\partial V_{gr}}{\partial r} - \frac{\partial V_{gz}}{\partial z} \right) + \frac{\partial \varphi_g}{\partial z} \left(\frac{\partial^2 V_{gr}}{\partial r^2} + \frac{\partial^2 V_{gz}}{\partial r \partial z} \right) - \left(\frac{\partial^2 \varphi_g}{\partial r^2} \frac{\partial V_{gr}}{\partial z} - \frac{\partial^2 \varphi_g}{\partial z^2} \frac{\partial V_{gz}}{\partial r} \right) - \frac{\partial \varphi_g}{\partial r} \left(\frac{\partial^2 V_{gr}}{\partial r \partial z} + \frac{\partial^2 V_{gz}}{\partial z^2} \right) \right] \\ & -\frac{\rho_l}{r} \left[-\frac{1}{r} \left(\frac{\partial \varphi_l}{\partial z} \frac{\partial V_{lr}}{\partial r} - \frac{\partial \varphi_l}{\partial r} \frac{\partial V_{lz}}{\partial z} \right) + \frac{\partial^2 \varphi_l}{\partial r \partial z} \left(\frac{\partial V_{lr}}{\partial r} - \frac{\partial V_{lz}}{\partial z} \right) + \frac{\partial \varphi_l}{\partial z} \left(\frac{\partial^2 V_{lr}}{\partial r^2} + \frac{\partial^2 V_{lz}}{\partial r \partial z} \right) - \left(\frac{\partial^2 \varphi_l}{\partial r^2} \frac{\partial V_{lr}}{\partial z} - \frac{\partial^2 \varphi_l}{\partial z^2} \frac{\partial V_{lz}}{\partial r} \right) - \frac{\partial \varphi_l}{\partial r} \left(\frac{\partial^2 V_{lr}}{\partial r \partial z} + \frac{\partial^2 V_{lz}}{\partial z^2} \right) \right] \end{aligned} \quad (6.19)$$

Slip Velocity

According to Prado (1995), the slip velocity between the gas and liquid phases is given by the following equation:

$$V_s = -8 \frac{r_d}{r_{sm}} \frac{\alpha_g (1 - \alpha_g) (\rho_l - \rho_g) \nabla P}{a_i C_{d\infty} \rho_l \rho_m |\vec{V}_s|} - \frac{D_d^\alpha}{\alpha_g (1 - \alpha_g)} \nabla \alpha_g. \quad (6.20)$$

Assuming spherical particles and neglecting D_d^α , the slip velocity can also be expressed in the radial and vertical direction, respectively, as:

$$V_{sr} = -8 \frac{\alpha_g (1 - \alpha_g) (\rho_l - \rho_g) \partial P}{a_i C_{d\infty} \rho_l \rho_m |\vec{V}_s|} \frac{\partial P}{\partial r}, \quad (6.21)$$

$$V_{sz} = -8 \frac{\alpha_g (1 - \alpha_g) (\rho_l - \rho_g) \partial P}{a_i C_{d\infty} \rho_l \rho_m |\vec{V}_s|} \frac{\partial P}{\partial z}. \quad (6.22)$$

Note that Eqs. 6.21 and 6.22 can also be rewritten as:

$$V_{sr} = -8 \frac{\alpha_g (1 - \alpha_g) (\rho_l - \rho_g) \partial P^*}{a_i C_{d\infty} \rho_l \rho_m |\vec{V}_s|} \frac{\partial P^*}{\partial r}, \quad (6.23)$$

$$V_{sz} = -8 \frac{\alpha_g (1 - \alpha_g) (\rho_l - \rho_g)}{a_i C_{d\infty} \rho_l \rho_m |\vec{V}_s|} \left(\frac{\partial P^*}{\partial z} - ((1 - \alpha_g) \rho_l + \alpha_g \rho_g) |g| \right). \quad (6.24)$$

The combination of the slip velocity definition and Eqs. 6.23 and 6.24 yields the following set of equations for the gas radial and vertical velocities:

$$V_{gr} = -8 \frac{\alpha_g (1 - \alpha_g) (\rho_l - \rho_g) \partial P^*}{a_i C_{d\infty} \rho_l \rho_m |\vec{V}_s|} \frac{\partial P^*}{\partial r} + V_{lr}, \quad (6.25)$$

$$V_{gz} = -8 \frac{\alpha_g (1 - \alpha_g) (\rho_l - \rho_g)}{a_i C_{d\infty} \rho_l \rho_m |\vec{V}_s|} \left(\frac{\partial P^*}{\partial z} - ((1 - \alpha_g) \rho_l + \alpha_g \rho_g) |g| \right) + V_{lz}. \quad (6.26)$$

Model Governing Equations

For the liquid stream function, irrotational flow will be assumed. In this case, Eq. 6.10 is given by:

$$-\frac{1}{r^2(1-\alpha_g)} \frac{\partial \varphi_l}{\partial r} + \frac{1}{r(1-\alpha_g)^2} \left(\frac{\partial \alpha_g}{\partial r} \frac{\partial \varphi_l}{\partial r} + \frac{\partial \alpha_g}{\partial z} \frac{\partial \varphi_l}{\partial z} \right) + \frac{1}{r(1-\alpha_g)} \left(\frac{\partial^2 \varphi_l}{\partial r^2} + \frac{\partial^2 \varphi_l}{\partial z^2} \right) = 0. \quad (6.27)$$

For the gas phase, the Vorticity is given by:

$$\Omega_g = \left(\frac{\partial V_{gr}}{\partial z} - \frac{\partial V_{gz}}{\partial r} \right), \quad (6.28)$$

where the gas velocities can be obtained from the slip velocity relationship given by Eqs. 6.21 and 6.22, by:

$$V_{gr} = -8 \frac{\alpha_g (1-\alpha_g) (\rho_l - \rho_g)}{a_i C_{d\infty} \rho_l \rho_m |\vec{V}_s|} \frac{\partial P}{\partial r} + V_{lr}, \quad (6.29)$$

$$V_{gz} = -8 \frac{\alpha_g (1-\alpha_g) (\rho_l - \rho_g)}{a_i C_{d\infty} \rho_l \rho_m |\vec{V}_s|} \frac{\partial P}{\partial z} + V_{lz}. \quad (6.30)$$

In this work, the interfacial area concentration a_i is defined as:

$$a_i = 3 \frac{\alpha_g (1-\alpha_g)}{r_d}. \quad (6.31)$$

Conversely, assume that the drag coefficient $C_{d\infty}$ is determined from the Ihme's correlation. Therefore, $C_{d\infty}$ is given by:

$$C_{d\infty} = \frac{24}{\text{Re}_\infty} \left[1 + 5.48 \text{Re}_\infty^{-0.573} \left(\frac{\text{Re}_\infty}{24} \right) + 0.36 \left(\frac{\text{Re}_\infty}{24} \right) \right] = \frac{24}{\text{Re}_\infty} [f(\text{Re}_\infty)], \quad (6.32)$$

where

$$\text{Re}_\infty = \frac{2 r_d \rho_m |\vec{V}_s|}{\mu_l}. \quad (6.33)$$

Therefore, Eqs. 6.31 - 6.33 can be used to rewrite Eqs. 6.29 and 6.30 as:

$$V_{gr} = -\frac{2}{9} \frac{r_d^2 (\rho_l - \rho_g)}{\mu_l \rho_l f(\text{Re}_\infty)} \frac{\partial P}{\partial r} + V_{lr}, \quad (6.34)$$

$$V_{gz} = -\frac{2}{9} \frac{r_d^2 (\rho_l - \rho_g)}{\mu_l \rho_l f(\text{Re}_\infty)} \frac{\partial P}{\partial z} + V_{lz}. \quad (6.35)$$

Substituting Eqs. 6.34 and 6.35 into Eq. 6.28, the following equation for gas phase vorticity is obtained:

$$\Omega_g = -\frac{\partial}{\partial z} \left(\frac{2}{9} \frac{r_d^2 (\rho_l - \rho_g)}{\mu_l \rho_l f(\text{Re}_\infty)} \frac{\partial P}{\partial r} \right) + \frac{\partial}{\partial r} \left(\frac{2}{9} \frac{r_d^2 (\rho_l - \rho_g)}{\mu_l \rho_l f(\text{Re}_\infty)} \frac{\partial P}{\partial z} \right) - \left(\frac{\partial V_{lr}}{\partial z} - \frac{\partial V_{lz}}{\partial r} \right). \quad (6.36)$$

Note that the third term of the right side of the equation is equal to zero from the irrotational flow assumption for the liquid phase. If it is assumed that $f(\text{Re}_\infty)$ is constant, Eq. 6.36 can be rewritten as:

$$\Omega_g = \frac{2}{9} \frac{r_d^2 (\rho_l - \rho_g)}{\mu_l \rho_l f(\text{Re}_\infty)} \left(\frac{\partial^2 P}{\partial r \partial z} - \frac{\partial^2 P}{\partial r \partial z} \right). \quad (6.37)$$

According to Eq. 6.37, the gas phase vorticity is zero as well. As a result, the gas stream function is given by:

$$-\frac{1}{r^2} \frac{\partial \varphi_g}{\partial r} - \frac{1}{r} \frac{\partial}{\partial r} \left(\frac{\partial \alpha_g}{\partial r} \frac{\partial \varphi_g}{\partial r} + \frac{\partial \alpha_g}{\partial z} \frac{\partial \varphi_g}{\partial z} \right) + \frac{1}{r} \frac{\partial}{\partial z} \left(\frac{\partial^2 \varphi_g}{\partial r^2} + \frac{\partial^2 \varphi_g}{\partial z^2} \right) = 0. \quad (6.38)$$

The equation for the gas void fraction is obtained from the mass balance equation for the gas phase. Assuming steady state conditions, this equation for α_g is given by:

$$\frac{\partial}{\partial r} (\alpha_g V_{gr}) + \frac{\partial}{\partial z} (\alpha_g V_{gz}) + \frac{1}{r} (\alpha_g V_{gr}) = 0, \quad (6.39)$$

where the equations for the gas velocity fields, V_{gr} and V_{gz} , are given from Eqs. 6.25 and 6.26, respectively, by:

$$V_{gr} = -8 \frac{\alpha_g (1 - \alpha_g) (\rho_l - \rho_g)}{a_i C_{d\infty} \rho_l \rho_m |\vec{V}_s|} \frac{\partial P^*}{\partial r} + V_{lr},$$

$$V_{gz} = -8 \frac{\alpha_g (1 - \alpha_g) (\rho_l - \rho_g)}{a_i C_{d\infty} \rho_l \rho_m |\vec{V}_s|} \left(\frac{\partial P^*}{\partial z} - ((1 - \alpha_g) \rho_l + \alpha_g \rho_g) |g| \right) + V_{lz}.$$

Finally, the pressure field is obtained, from Eq. 6.19, as:

$$\begin{aligned} \frac{\partial^2 P^*}{\partial r^2} + \frac{\partial^2 P^*}{\partial z^2} = & -\frac{\rho_g}{r} \left[-\frac{1}{r} \left(\frac{\partial \varphi_g}{\partial z} \frac{\partial V_{gr}}{\partial r} - \frac{\partial \varphi_g}{\partial r} \frac{\partial V_{gr}}{\partial z} \right) + \frac{\partial^2 \varphi_g}{\partial r \partial z} \left(\frac{\partial V_{gr}}{\partial r} - \frac{\partial V_{gz}}{\partial z} \right) + \frac{\partial \varphi_g}{\partial z} \left(\frac{\partial^2 V_{gr}}{\partial r^2} + \frac{\partial^2 V_{gz}}{\partial r \partial z} \right) - \left(\frac{\partial^2 \varphi_g}{\partial r^2} \frac{\partial V_{gr}}{\partial z} - \frac{\partial^2 \varphi_g}{\partial z^2} \frac{\partial V_{gz}}{\partial r} \right) - \frac{\partial \varphi_g}{\partial r} \left(\frac{\partial^2 V_{gr}}{\partial r \partial z} + \frac{\partial^2 V_{gz}}{\partial z^2} \right) \right] \\ & -\frac{\rho_l}{r} \left[-\frac{1}{r} \left(\frac{\partial \varphi_l}{\partial z} \frac{\partial V_{lr}}{\partial r} - \frac{\partial \varphi_l}{\partial r} \frac{\partial V_{lr}}{\partial z} \right) + \frac{\partial^2 \varphi_l}{\partial r \partial z} \left(\frac{\partial V_{lr}}{\partial r} - \frac{\partial V_{lz}}{\partial z} \right) + \frac{\partial \varphi_l}{\partial z} \left(\frac{\partial^2 V_{lr}}{\partial r^2} + \frac{\partial^2 V_{lz}}{\partial r \partial z} \right) - \left(\frac{\partial^2 \varphi_l}{\partial r^2} \frac{\partial V_{lr}}{\partial z} - \frac{\partial^2 \varphi_l}{\partial z^2} \frac{\partial V_{lz}}{\partial r} \right) - \frac{\partial \varphi_l}{\partial r} \left(\frac{\partial^2 V_{lr}}{\partial r \partial z} + \frac{\partial^2 V_{lz}}{\partial z^2} \right) \right] \end{aligned}$$

Procedure to Solve the System of Equations

Due to the non-linearities in the system of equations, an iterative procedure must be considered as follows:

a-. Select initial estimates for gas and liquid stream function, pressure and gas void fraction, i.e., $\hat{\varphi}_g$, $\hat{\varphi}_l$, \hat{P}^* , $\hat{\alpha}_g$, respectively.

b-. Set the following initial estimated values for the gas and liquid velocities:

$$\hat{V}_{gr} = \frac{1}{r \hat{\alpha}_g} \frac{\partial \hat{\varphi}_g}{\partial z},$$

$$\hat{V}_{gz} = -\frac{1}{r \hat{\alpha}_g} \frac{\partial \hat{\varphi}_g}{\partial r},$$

$$\hat{V}_{lr} = \frac{1}{r (1 - \hat{\alpha}_g)} \frac{\partial \hat{\varphi}_l}{\partial z},$$

$$\hat{V}_{lz} = -\frac{1}{r (1 - \hat{\alpha}_g)} \frac{\partial \hat{\varphi}_l}{\partial r},$$

c-. Solve the following system of equations:

$$\frac{\partial^2 \varphi_g}{\partial r^2} + \frac{\partial^2 \varphi_g}{\partial z^2} = \frac{1}{r} \frac{\partial \hat{\varphi}_g}{\partial r} + \frac{1}{\hat{\alpha}_g} \left(\frac{\partial \hat{\alpha}_g}{\partial r} \frac{\partial \hat{\varphi}_g}{\partial r} + \frac{\partial \hat{\alpha}_g}{\partial z} \frac{\partial \hat{\varphi}_g}{\partial z} \right),$$

$$\frac{\partial^2 \varphi_l}{\partial r^2} + \frac{\partial^2 \varphi_l}{\partial z^2} = \frac{1}{r} \frac{\partial \hat{\varphi}_l}{\partial r} - \frac{1}{(1-\hat{\alpha}_g)} \left(\frac{\partial \hat{\alpha}_g}{\partial r} \frac{\partial \hat{\varphi}_l}{\partial r} + \frac{\partial \hat{\alpha}_g}{\partial z} \frac{\partial \hat{\varphi}_l}{\partial z} \right),$$

$$\begin{aligned} \frac{\partial^2 P^*}{\partial r^2} + \frac{\partial^2 P^*}{\partial z^2} = & -\frac{\rho_g}{r} \left[-\frac{1}{r} \left(\frac{\partial \hat{\varphi}_g}{\partial z} \frac{\partial \hat{V}_{gr}}{\partial r} - \frac{\partial \hat{\varphi}_g}{\partial r} \frac{\partial \hat{V}_{gr}}{\partial z} \right) + \frac{\partial^2 \hat{\varphi}_g}{\partial r \partial z} \left(\frac{\partial \hat{V}_{gr}}{\partial r} - \frac{\partial \hat{V}_{gz}}{\partial z} \right) + \frac{\partial \hat{\varphi}_g}{\partial z} \left(\frac{\partial^2 \hat{V}_{gr}}{\partial r^2} + \frac{\partial^2 \hat{V}_{gz}}{\partial r \partial z} \right) - \left(\frac{\partial^2 \hat{\varphi}_g}{\partial r^2} \frac{\partial \hat{V}_{gr}}{\partial z} - \frac{\partial^2 \hat{\varphi}_g}{\partial z^2} \frac{\partial \hat{V}_{gz}}{\partial r} \right) - \frac{\partial \hat{\varphi}_g}{\partial r} \left(\frac{\partial^2 \hat{V}_{gr}}{\partial r \partial z} + \frac{\partial^2 \hat{V}_{gz}}{\partial z^2} \right) \right] \\ & -\frac{\rho_l}{r} \left[-\frac{1}{r} \left(\frac{\partial \hat{\varphi}_l}{\partial z} \frac{\partial \hat{V}_{lr}}{\partial r} - \frac{\partial \hat{\varphi}_l}{\partial r} \frac{\partial \hat{V}_{lr}}{\partial z} \right) + \frac{\partial^2 \hat{\varphi}_l}{\partial r \partial z} \left(\frac{\partial \hat{V}_{lr}}{\partial r} - \frac{\partial \hat{V}_{lz}}{\partial z} \right) + \frac{\partial \hat{\varphi}_l}{\partial z} \left(\frac{\partial^2 \hat{V}_{lr}}{\partial r^2} + \frac{\partial^2 \hat{V}_{lz}}{\partial r \partial z} \right) - \left(\frac{\partial^2 \hat{\varphi}_l}{\partial r^2} \frac{\partial \hat{V}_{lr}}{\partial z} - \frac{\partial^2 \hat{\varphi}_l}{\partial z^2} \frac{\partial \hat{V}_{lz}}{\partial r} \right) - \frac{\partial \hat{\varphi}_l}{\partial r} \left(\frac{\partial^2 \hat{V}_{lr}}{\partial r \partial z} + \frac{\partial^2 \hat{V}_{lz}}{\partial z^2} \right) \right] \\ & \frac{\partial}{\partial r} (\alpha_g \hat{V}_{gr}) + \frac{\partial}{\partial z} (\alpha_g \hat{V}_{gz}) = -\frac{1}{r} (\hat{\alpha}_g \hat{V}_{gr}). \end{aligned}$$

d-. Solution of the system yields new values for φ_g , φ_l , P^* , α_g .

e-. Calculate the changes in φ_g , φ_l , P^* , α_g . For convergence, the following criteria should be satisfied:

$$\left| \varphi_{g,i,j} - \hat{\varphi}_{g,i,j} \right| \leq \varepsilon,$$

$$\left| \varphi_{l,i,j} - \hat{\varphi}_{l,i,j} \right| \leq \varepsilon,$$

$$\left| P_{i,j}^* - \hat{P}_{i,j}^* \right| \leq \varepsilon,$$

$$\left| \alpha_{g,i,j} - \hat{\alpha}_{g,i,j} \right| \leq \varepsilon.$$

f-. If the convergence criterion is not satisfied, then replace the newly calculated values of gas and liquid stream functions, pressure and gas void fraction for the estimated values, as follows:

$$\hat{\varphi}_g = \varphi_g ,$$

$$\hat{\varphi}_l = \varphi_l ,$$

$$\hat{P}^* = P^* ,$$

$$\hat{\alpha}_g = \alpha_g .$$

Estimate the following variables:

1-. Liquid velocities: Using the gas and liquid stream function field results

$$\hat{V}_{lr} = \frac{1}{r (1 - \hat{\alpha}_g)} \frac{\partial \hat{\varphi}_l}{\partial z} ,$$

$$\hat{V}_{lz} = - \frac{1}{r (1 - \hat{\alpha}_g)} \frac{\partial \hat{\varphi}_l}{\partial r} .$$

2-. The interfacial area concentration, a_i , calculated from Eq. 6.31.

$$\hat{a}_i = 3 \frac{\hat{\alpha}_g (1 - \hat{\alpha}_g)}{r_d} .$$

3-. The mixture density:

$$\hat{\rho}_m = (1 - \hat{\alpha}_g) \rho_l + \hat{\alpha}_g \rho_g .$$

4-. Calculate the gas velocity fields, v_{gr} and v_{gz} : Using the following iterative procedure:

4.1-. Select one initial estimate for a resultant slip velocity $|\hat{V}_s|$.

4.2-. Estimate the drag coefficient using Ihme's correlation. From Appendix D, this correlation is given by:

$$\hat{C}_{d\infty} = \frac{24}{\hat{Re}_\infty} + 5.48 \hat{Re}_\infty^{-0.573} + 0.36 , \quad (6.40)$$

where

$$\hat{Re}_\infty = \frac{2 r_d \hat{\rho}_m |\hat{V}_s|}{\mu_l}.$$

4.3-. Estimate the gas velocities by:

$$V_{gr} = -8 \frac{\hat{\alpha}_g (1 - \hat{\alpha}_g) (\rho_l - \rho_g) \frac{\partial \hat{P}^*}{\partial r}}{\hat{a}_i \hat{C}_{d\infty} \hat{\rho}_l \hat{\rho}_m |\hat{V}_s|} + \hat{V}_{lr},$$

$$V_{gz} = -8 \frac{\hat{\alpha}_g (1 - \hat{\alpha}_g) (\rho_l - \rho_g)}{\hat{a}_i \hat{C}_{d\infty} \hat{\rho}_l \hat{\rho}_m |\hat{V}_s|} \left(\frac{\partial \hat{P}^*}{\partial z} - ((1 - \hat{\alpha}_g) \rho_l + \hat{\alpha}_g \rho_g) |g| \right) + \hat{V}_{lz}.$$

4.4-. Estimate new calculated values for $|V_s|$ at each node by:

$$|V_s| = \sqrt{(V_{gr} - \hat{V}_{lr})^2 + (V_{gz} - \hat{V}_{lz})^2}.$$

4.5-. Verify criteria for convergence:

$$\left| |V_s| - |\hat{V}_s| \right| \leq \varepsilon.$$

4.6-. If the convergence criterion is not satisfied:

$$|\hat{V}_s| = |V_s|.$$

4.7-. Repeat steps 4.2 to 4.5 until the convergence criterion is satisfied.

4.8-. When convergence is satisfied, update the estimates for the gas radial and vertical velocities.

$$\hat{V}_{gr} = V_{gr},$$

$$\hat{V}_{gz} = V_{gz}.$$

g-. Repeat steps c to f until the convergence criterion is satisfied.

This solution procedure proposed is summarized in Fig. 6.1.

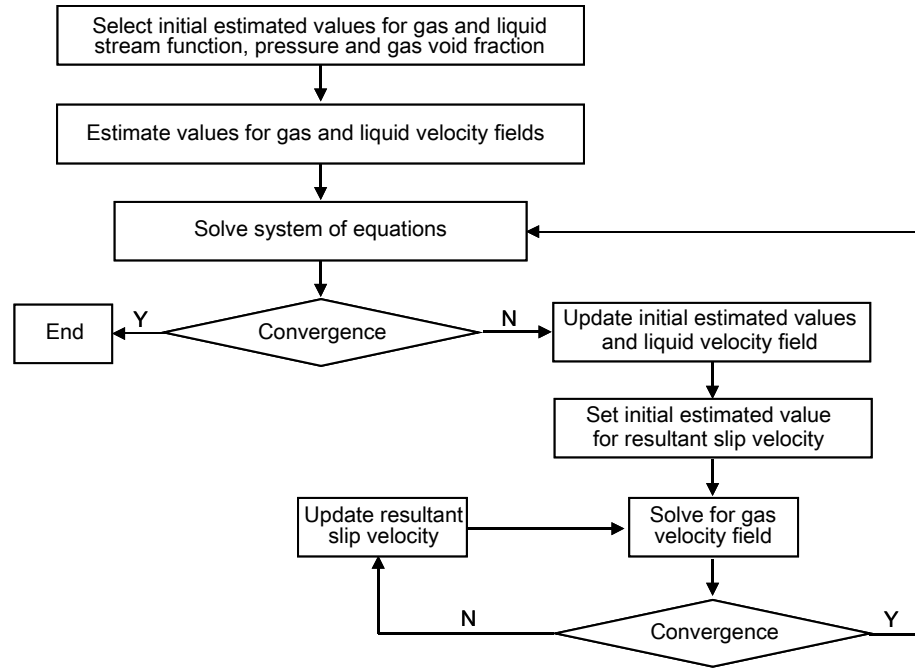


Figure 6.1 – Solution Procedure Flowchart.

Spatial Domain

As shown in Fig. 6.2, the spatial domain is located in the annulus space between the casing, and the pump intake and pump wall. In that region, governing equations for gas and liquid stream functions, pressure and gas void fraction equations will be discretized. Details of the discretization can be found in Appendix E.

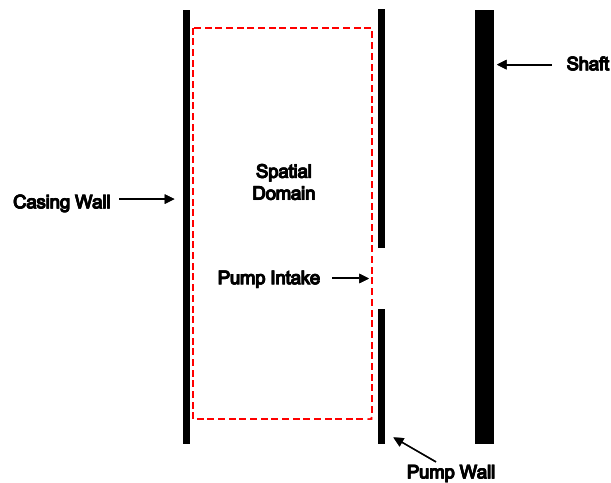


Figure 6.2 – Flow Domain.

Boundary Conditions

Boundary conditions must be defined for the gas and liquid stream functions as well as for the pressure and gas void fraction equations in six domain boundaries as shown in Fig. 6.3.

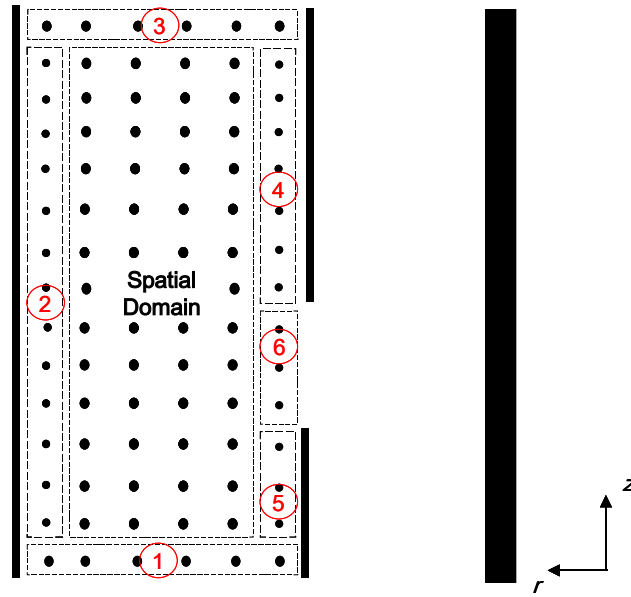


Figure 6.3 – Core and Boundary Conditions.

Before specifying the appropriate boundary conditions, it is necessary to specify the inflow conditions for the problem. It is assumed that the pump is installed in the well above the perforations.

At the entrance of the domain, as shown in Fig. 6.4, the gas and liquid flow rates, q_g^i and q_l^i respectively, are known. It is also assumed that the area average pressure at this location, $\langle P_{Inlet} \rangle$, is also known. It is assumed that the liquid and gas are flowing only in the vertical direction only, through an annulus cross-section area A_a , as shown in Fig. 6.4.

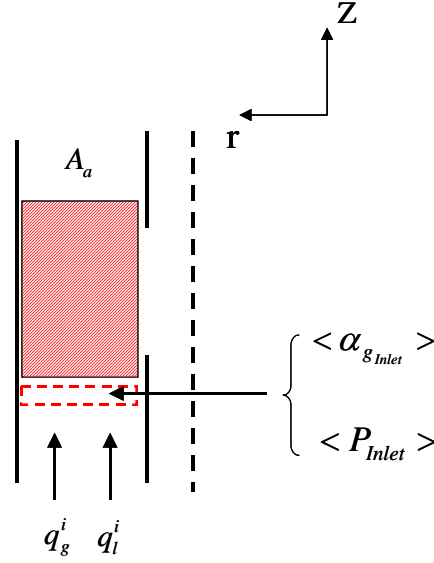


Figure 6.4 – Inflow Conditions.

The area averaged superficial gas and liquid velocities, $\langle V_{sgz}^i \rangle$ and $\langle V_{slz}^i \rangle$ respectively, can then be calculated as:

$$\langle V_{sgz}^i \rangle = \frac{q_g^i}{A_a}, \quad (6.41)$$

$$\langle V_{slz}^i \rangle = \frac{q_l^i}{A_a}. \quad (6.42)$$

As shown in Appendix F, the combination of mass and momentum balance equations, along with the slip velocity equation proposed by Prado (1995), and the area averaged superficial gas and liquid velocities, V_{sgz}^i and V_{slz}^i respectively, yields a relationship for the gas void fraction. This equation can be also applied to the area average variables yielding:

$$\frac{1}{96} a_i C_{d\infty} \rho_l \left(\frac{\langle V_{sgz}^i \rangle}{\langle \alpha_{g\ Inlet} \rangle} - \frac{\langle V_{slz}^i \rangle}{1 - \langle \alpha_{g\ Inlet} \rangle} \right)^2 - \langle \alpha_{g\ Inlet} \rangle (1 - \langle \alpha_{g\ Inlet} \rangle) (\rho_l - \rho_g) |g| = 0, \quad (6.43)$$

where a_i and $C_{d\infty}$ are given by Eqs. 6.31 and 6.32, respectively. The solution of Eq. 6.43 is obtained by using a trial and error iterative procedure to yield the area average gas void fraction $\langle \alpha_{g\text{Inlet}} \rangle$ at the inlet.

The next sections will describe the appropriate boundary conditions for gas and liquid stream functions, pressure and gas void fraction, at each one of the six boundaries shown in Fig. 6.3 and given by: annulus inlet boundary, annulus outlet boundary, casing and upper/lower wall boundaries, and pump intake boundary.

Annulus Inlet Boundary

The annulus inlet boundary is noted as section 1 in Fig. 6.3. The boundary conditions for the governing equations are presented as follows:

a. Gas and liquid stream function

The gas and liquid velocities in the vertical direction, V_{gz}^i and V_{lz}^i respectively and the gas void fraction, are considered constant and equal to the area average values at this boundary. In the radial direction, no r -component for the gas and liquid velocities is assumed. Starting with a zero value at the pump wall, the boundary conditions for the gas and liquid stream functions, φ_g and φ_l respectively, are given by:

$$\langle V_{gz}^i \rangle = -\frac{1}{r \langle \alpha_{g\text{Inlet}} \rangle} \frac{\partial \varphi_g}{\partial r}, \quad (6.44)$$

$$\langle V_{lz}^i \rangle = -\frac{1}{r (1 - \langle \alpha_{g\text{Inlet}} \rangle)} \frac{\partial \varphi_l}{\partial r}. \quad (6.45)$$

b. Pressure

The pressure is assumed constant and equal to the area average value, i.e.

$$P^* = \langle P_{\text{Inlet}} \rangle. \quad (6.46)$$

c. Gas void fraction

As stated previously, the gas void fraction in this boundary is assumed constant and equal to the area averaged value calculated as the solution to Eq. 6.43. The values for the local gas void fraction at this boundary are calculated as:

$$\alpha_g = \langle \alpha_{g_{inlet}} \rangle. \quad (6.47)$$

Annulus Outlet Boundary

The annulus outlet boundary is noted as section 3 in Fig. 6.3. The boundary conditions for the governing equations are given by:

a. Gas and liquid stream function

Based on the average actual gas velocity and gas void fraction between two nodes, the gas stream function is estimated using the following definition:

$$V_{gz} = -\frac{1}{r \alpha_g} \frac{\partial \phi_g}{\partial r}. \quad (6.48)$$

For the liquid stream function, fully developed flow conditions are assumed. Therefore, the following relationship results valid:

$$\frac{\partial \phi_l}{\partial z} = 0. \quad (6.49)$$

b. Pressure

The boundary condition for pressure is the pressure gradient equation in the vertical direction, which is given, from Eq. 6.18, by:

$$\frac{\partial P^*}{\partial z} = -\frac{\rho_g}{r} \left(\frac{\partial \hat{\phi}_g}{\partial z} \frac{\partial \hat{V}_{gz}}{\partial r} - \frac{\partial \hat{\phi}_g}{\partial r} \frac{\partial \hat{V}_{gz}}{\partial z} \right) - \frac{\rho_l}{r} \left(\frac{\partial \hat{\phi}_l}{\partial z} \frac{\partial \hat{V}_{lz}}{\partial r} - \frac{\partial \hat{\phi}_l}{\partial r} \frac{\partial \hat{V}_{lz}}{\partial z} \right).$$

c. Gas void fraction

At this boundary, fully developed flow is considered. Therefore, the gas void fraction can be estimated as:

$$\frac{\partial \alpha_g}{\partial z} = 0. \quad (6.50)$$

Casing Wall and Upper/Lower Pump Wall Boundaries

The casing wall and the upper/lower pump wall boundaries are given by sections 2, 4 and 5 in Fig. 6.3, where the following boundary conditions for the governing equations are defined as:

a. Gas and liquid stream function

The average gas and liquid velocities in the radial direction are assumed equal to zero, i.e., the wall is considered as impermeable. Therefore, the stream functions for the gas and liquid phases in this region are given, respectively, by:

$$\frac{\partial \varphi_g}{\partial z} = 0, \quad (6.51)$$

$$\frac{\partial \varphi_l}{\partial z} = 0. \quad (6.52)$$

As shown in Fig. 6.5, there is a special point at the upper corner of the pump intake where the liquid stream function is defined as:

$$\varphi_l = \varphi_{l_c}, \quad (6.53)$$

and where φ_{l_c} represents the closer liquid stream function value to the casing wall.

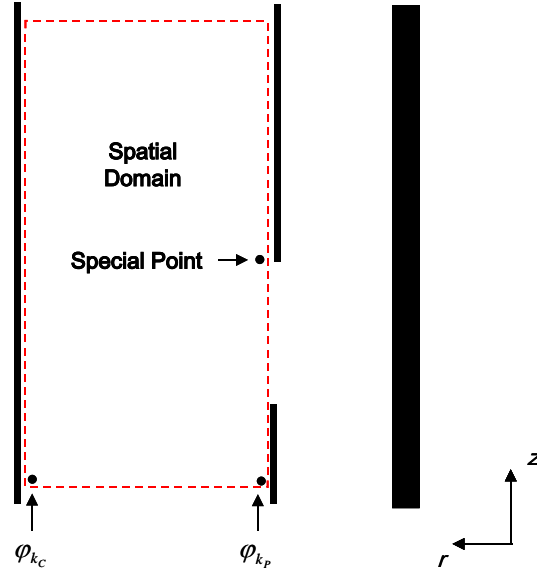


Figure 6.5 – Special Points inside the Flow Domain.

b. Pressure

The pressure is obtained from the pressure gradient equation in the radial direction, which is given by Eq. 6.17, i.e.

$$\frac{\partial P^*}{\partial r} = -\frac{\rho_g}{r} \left(\frac{\partial \hat{\varphi}_g}{\partial z} \frac{\partial \hat{V}_{gr}}{\partial r} - \frac{\partial \hat{\varphi}_g}{\partial r} \frac{\partial \hat{V}_{gr}}{\partial z} \right) - \frac{\rho_l}{r} \left(\frac{\partial \hat{\varphi}_l}{\partial z} \frac{\partial \hat{V}_{lr}}{\partial r} - \frac{\partial \hat{\varphi}_l}{\partial r} \frac{\partial \hat{V}_{lr}}{\partial z} \right)$$

c. Gas void fraction

The gas void fraction field is obtained from Eq. 6.39, i.e.

$$\frac{\partial}{\partial r} (\alpha_g V_{gr}) + \frac{\partial}{\partial z} (\alpha_g V_{gz}) = -\frac{1}{r} (\hat{\alpha}_g \hat{V}_{gr}) \cdot$$

Pump Intake Boundary

The pump intake boundary is represented by section 6 in Fig. 6.3. There, the following boundary conditions for the governing equation are given by:

a. Gas and liquid stream function

In this boundary, gas and liquid stream functions are assumed evenly increased, from the lower to the upper side of the pump intake.

b. Pressure

Similar to the casing and upper/lower pump wall boundaries, the pressure is obtained from the pressure gradient equation in the radial direction, given by Eq. 6.17.

c. Gas void fraction

The gas void fraction field is also obtained from Eq. 6.39 by:

$$\frac{\partial}{\partial r}(\alpha_g V_{gr}) + \frac{\partial}{\partial z}(\alpha_g V_{gz}) = -\frac{1}{r}(\hat{\alpha}_g \hat{V}_{gr}) \cdot$$

Natural Separation Efficiency Predictions

The solution for the gas phase stream function, ϕ_g , enables the determination of the gas streamline field, as shown in Fig. 6.6.

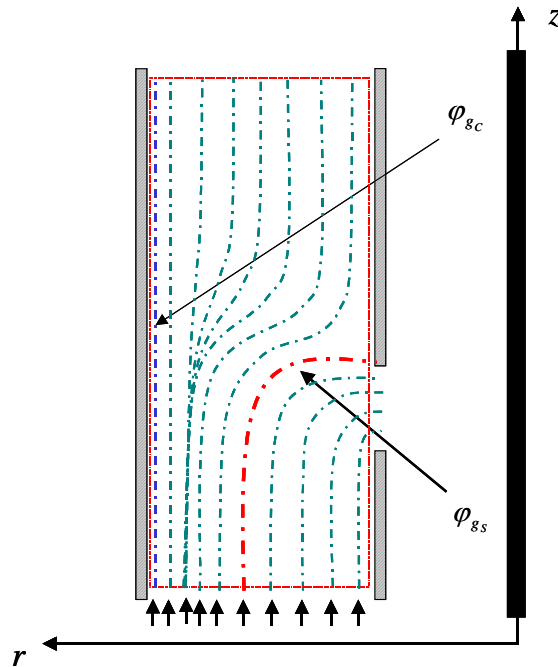


Figure 6.6 – Stream Function for Gas Phase.

The streamline that hits the upper pump wall boundary, immediately above the pump intake, will establish an imaginary separation circle in the cross section of the well bore, as shown in Fig. 6.7.

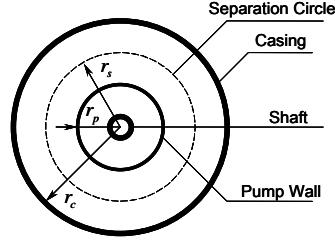


Figure 6.7 – Cross-Section of the Well Bore.

This streamline is called here the critical streamline and is given by φ_{gs} in Fig. 6.6. The gas that enters the flow domain at a radial position greater than the critical streamline radius is considered naturally separated. Therefore, natural separation efficiency may be predicted as the ratio between the difference of the total gas streamline φ_{gc} and gas streamline that hits the upper pump wall boundary φ_{gs} to the total gas streamline, i.e.

$$E = \frac{\varphi_{gc} - \varphi_{gs}}{\varphi_{gc}}. \quad (6.54)$$

Interface Characteristic Length

An auxiliary relationship for the drag radius of a gas bubble, r_d , is required to close the system of equations. In this model, it is proposed to substitute the bubble radius, r_d , by the interface characteristic length, ℓ_i . In this case, available experimental data was used to estimate several fitting values for the interface characteristic length, throughout a tune up work. Setting the input parameter in a computational program, a trial and error method was considered until an adequate interface characteristic length was found, reproducing natural separation efficiency equal to the experimental results. Results are shown in Table 6.1.

Table 6.1 – Fitted Interface Characteristic Length - Two-Phase Model Approach.

Source	Mechanical Conditions		Actual Test Condition							E	V _{SG}	V _{SL}	FLOW PATTERN	(Interface Characteristic Length) _{Pred}
	ϕ _c	ϕ _m	T	P	Feed									
					Liquid		Gas							
					Q _L	Q _L	Q _G	Q _G						
in	in	°F	Psig	bpd	ft ³ /sec	scf/day	ft ³ /sec	ft/sec	ft/sec	in				
Alhanati's Work	6.366	4	101	121	641	0.0417	51000	0.0688	0.625	0.5146	0.3114	SLUGICHRN FLOW	0.0591	
Alhanati's Work	6.366	4	101	122	960	0.0624	82300	0.1103	0.507	0.8243	0.4664	SLUGICHRN FLOW	0.0653	
Alhanati's Work	6.366	4	98	115	634	0.0412	119400	0.1677	0.637	1.2539	0.3080	SLUGICHRN FLOW	0.1244	
Alhanati's Work	6.366	4	93	109	912	0.0593	176300	0.2574	0.584	1.9242	0.4431	SLUGICHRN FLOW	0.3175	
Alhanati's Work	6.366	4	94	219	614	0.0399	59900	0.0462	0.477	0.3457	0.2983	SLUGICHRN FLOW	0.0266	
Alhanati's Work	6.366	4	103	233	871	0.0566	90500	0.0670	0.434	0.5007	0.4232	SLUGICHRN FLOW	0.0350	
Alhanati's Work	6.366	4	102	220	631	0.0410	117400	0.0916	0.552	0.6845	0.3066	SLUGICHRN FLOW	0.0533	
Alhanati's Work	6.366	4	98	200	915	0.0595	176400	0.1494	0.467	1.1168	0.4445	SLUGICHRN FLOW	0.0708	
Serrano's Work	5	4	67	60	960	0.0624	5000	0.0115	0.387	0.2350	1.2710	BUBBLE FLOW	0.0591	
Serrano's Work	5	4	78	57	1011	0.0657	3856	0.0095	0.373	0.1928	1.3385	BUBBLE FLOW	0.0569	
Serrano's Work	5	4	66	58	1011	0.0657	1786	0.0042	0.447	0.0851	1.3385	BUBBLE FLOW	0.0837	
Serrano's Work	5	4	77	54	1028	0.0668	2395	0.0061	0.391	0.1247	1.3610	BUBBLE FLOW	0.0619	
Serrano's Work	5	4	76	54	1474	0.0958	4329	0.0110	0.200	0.2250	1.9515	BUBBLE FLOW	0.0297	
Serrano's Work	5	4	76	54	1491	0.0969	2687	0.0069	0.215	0.1397	1.9740	BUBBLE FLOW	0.0316	
Serrano's Work	5	4	76	54	1491	0.0969	5406	0.0138	0.186	0.2810	1.9740	BUBBLE FLOW	0.0277	
Serrano's Work	5	4	60	60	1508	0.0980	6736	0.0153	0.182	0.3124	1.9965	BUBBLE FLOW	0.0287	
Serrano's Work	5	4	74	52	1971	0.1281	6706	0.0176	0.108	0.3577	2.6095	BUBBLE FLOW	0.0189	
Serrano's Work	5	4	74	52	1971	0.1281	7720	0.0202	0.094	0.4118	2.6095	BUBBLE FLOW	0.0166	
Serrano's Work	5	4	74	50	2005	0.1303	4649	0.0126	0.109	0.2557	2.6545	BUBBLE FLOW	0.0181	
Serrano's Work	5	4	73	50	2023	0.1315	3120	0.0084	0.116	0.1713	2.6783	BUBBLE FLOW	0.0197	
Serrano's Work	5	4	67	98	943	0.0613	6785	0.0104	0.360	0.2111	1.2485	BUBBLE FLOW	0.0481	
Serrano's Work	5	4	75	105	977	0.0635	4966	0.0072	0.377	0.1477	1.2935	BUBBLE FLOW	0.0531	
Serrano's Work	5	4	74	105	1011	0.0657	3378	0.0049	0.384	0.1003	1.3385	BUBBLE FLOW	0.0566	
Serrano's Work	5	4	74	103	1491	0.0969	12203	0.0181	0.165	0.3694	1.9740	BUBBLE FLOW	0.0248	
Serrano's Work	5	4	56	104	1508	0.0980	3547	0.0050	0.206	0.1026	1.9965	BUBBLE FLOW	0.0295	
Serrano's Work	5	4	73	102	1508	0.0980	7037	0.0105	0.184	0.2139	1.9965	BUBBLE FLOW	0.0266	
Serrano's Work	5	4	74	102	1525	0.0991	9391	0.0140	0.169	0.2859	2.0190	BUBBLE FLOW	0.0275	
Serrano's Work	5	4	58	99	1954	0.1270	8256	0.0123	0.123	0.2503	2.5870	BUBBLE FLOW	0.0211	
Serrano's Work	5	4	57	90	1971	0.1281	4630	0.0075	0.173	0.1522	2.6095	BUBBLE FLOW	0.0322	
Serrano's Work	5	4	59	99	1971	0.1281	12426	0.0185	0.105	0.3775	2.6095	BUBBLE FLOW	0.0181	
Serrano's Work	5	4	59	98	1988	0.1292	10265	0.0154	0.113	0.3146	2.6320	BUBBLE FLOW	0.0150	
Serrano's Work	5	4	68	148	943	0.0613	3264	0.0035	0.418	0.0704	1.2485	BUBBLE FLOW	0.0622	
Serrano's Work	5	4	77	160	960	0.0624	5820	0.0058	0.371	0.1189	1.2710	BUBBLE FLOW	0.0450	
Serrano's Work	5	4	77	160	977	0.0635	7340	0.0074	0.373	0.1499	1.2935	BUBBLE FLOW	0.0537	
Serrano's Work	5	4	68	147	1011	0.0657	9722	0.0104	0.333	0.2110	1.3385	BUBBLE FLOW	0.0455	
Serrano's Work	5	4	77	155	1474	0.0958	10088	0.0104	0.178	0.2121	1.9515	BUBBLE FLOW	0.0275	
Serrano's Work	5	4	60	150	1508	0.0980	6639	0.0068	0.185	0.1393	1.9965	BUBBLE FLOW	0.0261	
Serrano's Work	5	4	77	155	1525	0.0991	12910	0.0133	0.167	0.2715	2.0190	BUBBLE FLOW	0.0247	
Serrano's Work	5	4	77	154	1525	0.0991	17049	0.0177	0.152	0.3607	2.0190	BUBBLE FLOW	0.0227	
Serrano's Work	5	4	59	154	1954	0.1270	18178	0.0182	0.107	0.3716	2.5870	BUBBLE FLOW	0.0194	
Serrano's Work	5	4	75	150	2005	0.1303	7688	0.0081	0.131	0.1660	2.6545	BUBBLE FLOW	0.0212	
Serrano's Work	5	4	76	150	2005	0.1303	14811	0.0157	0.107	0.3204	2.6545	BUBBLE FLOW	0.0194	
Serrano's Work	5	4	76	150	2005	0.1303	16871	0.0179	0.107	0.3649	2.6545	BUBBLE FLOW	0.0191	
Serrano's Work	5	4	75	149	2057	0.1337	11215	0.0120	0.116	0.2436	2.7233	BUBBLE FLOW	0.0203	

As shown in Table 6.1, the interface characteristic length was determined for each experimental condition of pressure, temperature, gas and liquid flow rates, geometric characteristic of the bottomhole and flow pattern regime.

The model proposed allowed the estimation of the interface characteristic length by using Alhanati and Serrano's data, only. Certain disagreements with Sambangi's data were found. Dominant parameters, such as superficial gas and liquid velocities, gas void

fraction, pressure, among others, were analyzed along with the fitting interface characteristic length. Two relationships for estimating the interface characteristic length are proposed in this work, which depends strongly on the flow pattern regime present into the flow domain.

Under slug/churn flow regime, a relationship between the tuned interface characteristic length and the superficial gas velocity was found. It can be observed in Fig. 6.8.

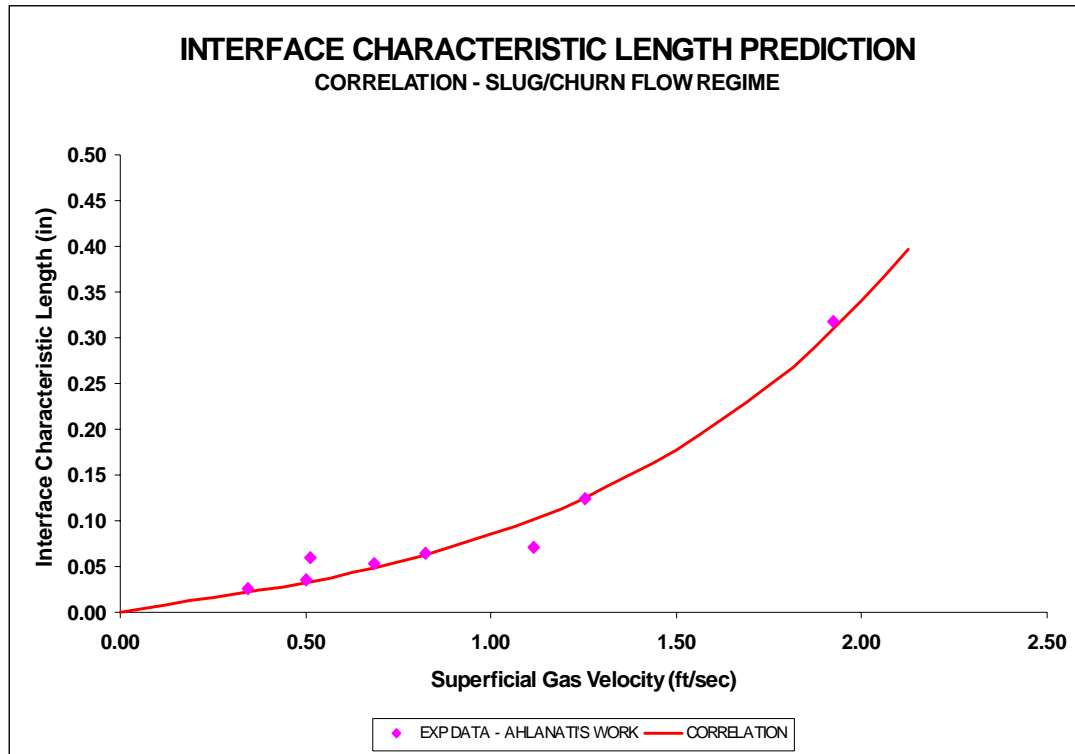


Figure 6.8 – Estimated Interface Characteristic Length - Slug/Churn Flow Regime.

According to results obtained from Fig. 6.8, the interface characteristic length increases proportionally with the superficial gas velocity. It is important to mention that under a slug/churn flow condition, the predominant parameter is represented by the gas phase and therefore, the larger the gas flow rate, the larger the interface characteristic length, promoting coalescence and increasing the separation process. A correlation for predicting the interface characteristic length of gas bubbles, as a function of V_{sgz}^i , is proposed in this work. This correlation is given by:

$$\ell_i = 0.036 (2.364^{V_{sgz}^i}) (V_{sgz}^i)^{0.762} \quad (6.55)$$

It is assumed that for higher superficial gas velocity than 2 ft/sec, the interface characteristic length values tend to follow the curve given in Fig. 6.8.

Under a bubble flow condition, the tuned interface characteristic length was compared with some models available in the literature. Hinze (1955) proposed the following expression for calculating the maximum stable diameter of a dispersed-phase through a continuous liquid-phase.

$$d_{\max} = 1.14 \left[\frac{\sigma}{\rho_l} \right]^{3/5} \left[\frac{2 V_M^3}{D_h} f \right]^{-2/5}, \quad (6.56)$$

where V_M and D_h represent the mixture velocity and hydraulic-diameter, respectively. σ , ρ_l and f represent the surface tension, the liquid density and the Fanning friction factor, respectively. Note that Eq. 6.56 can also be rewritten as:

$$r_{\max} = 0.57 \left[\frac{\sigma}{\rho_l} \right]^{3/5} \left[\frac{2 V_M^3}{D_h} f \right]^{-2/5}, \quad (6.57)$$

Brodkey (1967) also proposed other expression for estimating the critical bubble diameter. Gas bubble sizes smaller than the critical bubble diameter mean that bubbles are spherical, behaving as solid spheres, with low rates of coalescence. The critical bubble diameter is estimated as:

$$d_{crit} = \left[\frac{0.4 \sigma}{(\rho_l - \rho_g) |g|} \right]^{1/2}, \quad (6.58)$$

or simply,

$$r_{crit} = \frac{1}{2} \left[\frac{0.4 \sigma}{(\rho_l - \rho_g) |g|} \right]^{1/2}. \quad (6.59)$$

Comparisons between the tuned interface characteristic length and the models, given by Eqs. 6.57 and 6.59, as a function of the superficial liquid velocity, are shown in Fig. 6.9.

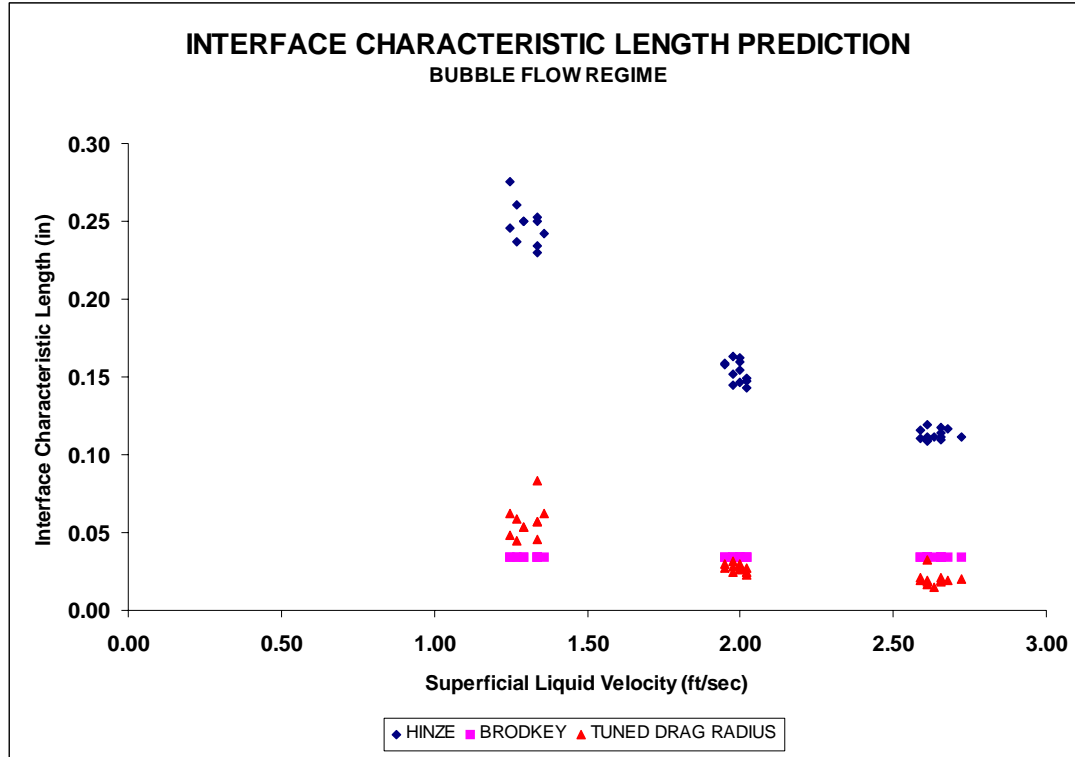


Figure 6.9 – Interface Characteristic Length Prediction - Bubble Flow Regime.

It is important mention that the drag radius values predicted by the Brodkey's model are independent of the superficial liquid velocity. However, the values showed in Figure 6.9 were estimated to the same operational conditions of the experimental data.

Results for the tuned interface characteristic length in the bubble flow regime is shown in Fig. 6.10. Different than the conditions observed under slug/churn flow regime, the interface characteristic length depends on the superficial liquid velocity only.

In this case, the smaller the bubble size, the larger the superficial liquid velocity. Similar behavior was obtained by Liu's work, even though the bubble-tracking model never catches it directly.

Based on Fig. 6.10, a correlation for predicting the interface characteristic length in bubble flow regime is given by:

$$\ell_i = -0.1653 (-0.0492 - \exp(-1.0476 V_{slz}^i)). \quad (6.60)$$

Since no experimental data is available for low superficial liquid velocities than 1.25 ft/sec, it is assumed that the correlation for predicting the interface characteristic

length follow the curve given by Fig. 6.10. Under a bubble flow regime, the interface characteristic length can be predicted either Eq. 6.59 or Eq. 6.60

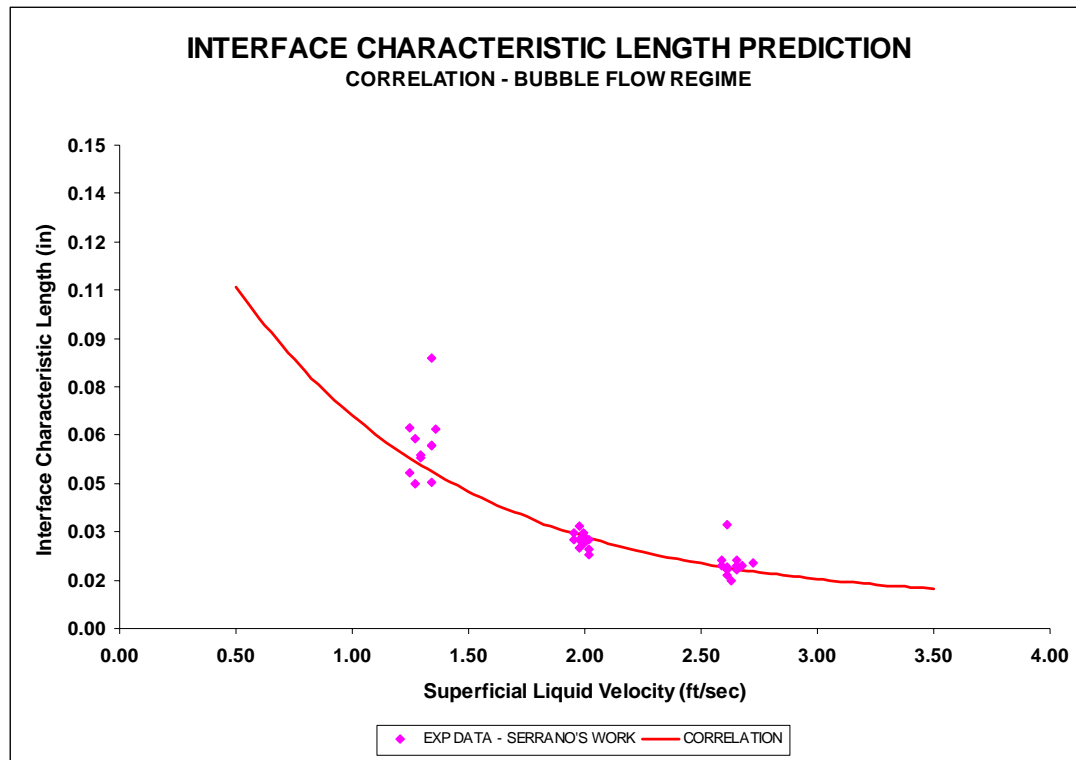


Figure 6.10 – Correlation for Prediction of Interface Characteristic Length - Bubble Flow Regime.

CHAPTER VII

RESULTS AND DISCUSSIONS

In this section, results and discussion are presented for the simplified models and the new two-phase model, described in Chapters IV, V and VI.

New Correlation

In Chapter IV, a correlation for estimating the effects of the liquid radial acceleration based on experimental data was introduced. Using this correlation, natural separation efficiency E can be calculated by:

$$E = 1 - \left\{ 1 - \left[\left(1 + \frac{a b + c \left(\frac{V_{slz}^i}{V_{\infty z}} \right)^d}{b + \left(\frac{V_{slz}^i}{V_{\infty z}} \right)^d} \right)^{272} + \left(\frac{V_{slz}^i}{V_{\infty z}} \right)^{272} \right]^{1/272} + \left[\frac{V_{slz}^i}{V_{\infty z}} \right] \right\}, \quad (7.1)$$

where V_{slz}^i and $V_{\infty z}$ represent the superficial liquid velocity and the terminal velocity of gas bubbles in the vertical direction, respectively. a , b , c and d are constant coefficients, given in Chapter IV. A comparison of the results obtained with Eq. 7.1 against the measured efficiency is shown in Fig. 7.1.

The new correlation reflects good agreement with the experimental data obtained from Alhanati (1993), Sambangi (1994) and Serrano (1999)'s work. Based on the error calculation equations explained in Appendix G, an average percentage error of 20.4 % is obtained when natural separation is predicted by using Eq. 7.1. As a reference, Alhanati's model predictions show an average percentage error of 25.64% for the same data set.

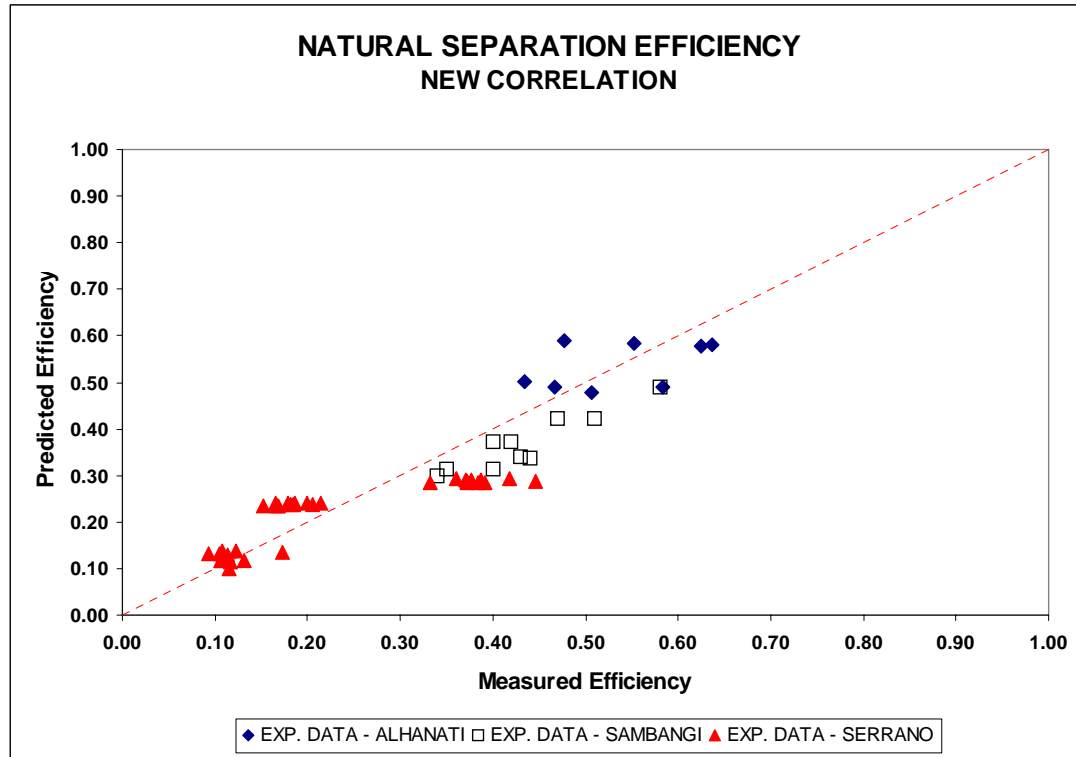


Figure 7.1 – Predicted and Measured Separation Efficiency - New Correlation.

Alhanati (1993) reported that important variables such as liquid flow rate, pressure and gas-liquid ratio, showed a strong influence on the separation process. Therefore, the effect of those variables in the prediction of natural separation by using the correlation will be analyzed and discussed as follows:

1. Geometric Effects

Ghauri (1979) reported that the larger the annulus area, the better the natural separation efficiency. As a result, the casing size is an important factor in the natural separation process. Fig. 7.2 shows the results obtained with the correlation for the case of a 4 in. outside pump diameter and 5 in., 7 in. and 10 in. casings.

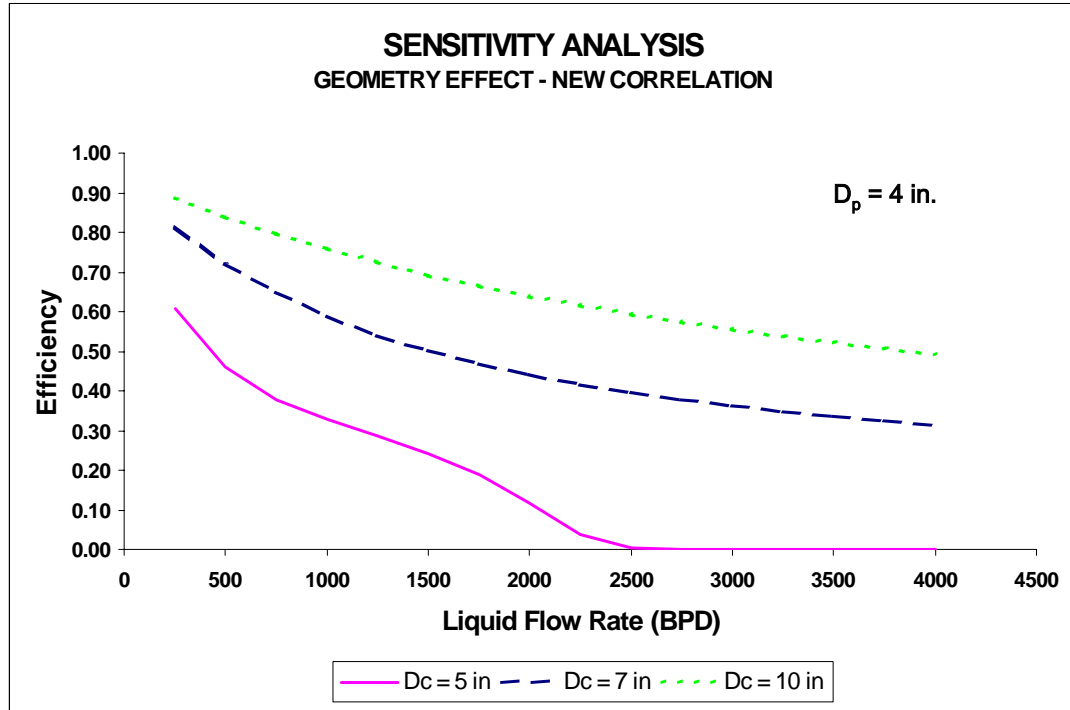


Figure 7.2 – Geometry Effect - New Correlation.

Two important conclusions can be obtained from Fig. 7.2. First, the separation efficiency decreases with increasing liquid flow rates, as reported by Alhanati. Second, natural separation efficiency increases with the casing size, as reported by Ghauri.

2. Gas Liquid Ratio Effects

Alhanati (1993) observed in his experimental results that the annulus efficiency decreases with decreasing GLR. Unfortunately, the new correlation is not dependent on the GLR.

3. Pressure Effects

Alhanati (1993) also reported the natural separation efficiency decreases with increasing pressure. The only effect of pressure on the correlation is through the fluid

physical property used to calculate the gas bubbles' terminal velocity, $V_{\infty z}$. In this work, this equation is given by:

$$V_{\infty z} = \sqrt{2} \left[\frac{\sigma (\rho_l - \rho_g) |g|}{\rho_l^2} \right]^{1/4}, \quad (7.2)$$

where σ represents the surface tension. However, a sensitivity analysis considering changes in pressure never exhibited any significant effect on the prediction results.

4. Viscosity Effects.

As demonstrated in Eqs. 7.1 and 7.2, the correlation predictions are not dependent on the fluid viscosity. However, the fluid viscosity could be incorporate in the model, if a new expression for estimating $V_{\infty z}$ is considered. As shown in Appendix C, $V_{\infty z}$ can also be defined as:

$$V_{\infty z}^2 = \frac{8}{3} \frac{r_d (\rho_l - \rho_g) |g|}{C_{d\infty} \rho_l}, \quad (7.3)$$

where under Stoke's flow conditions, the drag coefficient would be given by:

$$C_{d\infty} = \frac{24}{\text{Re}_{\infty}}, \quad (7.4)$$

and where the particle Reynolds number, Re_{∞} , is obtained as:

$$\text{Re}_{\infty} = \frac{2 r_d |\vec{V}_s| \rho_l}{\mu_l}. \quad (7.5)$$

Therefore, the combination of Eqs. 7.3 - 7.5 yields an alternate relationship for the terminal velocity in the vertical direction, $V_{\infty z}$, which is a function of the liquid viscosity.

This relationship is given by:

$$V_{\infty z} = \frac{2}{9} \frac{r_d^2 (\rho_l - \rho_g) |g|}{\mu_l}. \quad (7.6)$$

Although Eq. 7.6 considers the viscosity effect, it introduces a new additional unknown, namely the drag radius r_d .

Mechanistic Model

Due to the limitations of the correlation in explaining the influence of some parameters, such as the GLR and liquid viscosity, a mechanistic model was also developed. As shown in Chapter V, the mechanistic model predicts natural separation efficiency by tracking the trajectories of gas bubbles inside the flow domain. Those trajectories can be determined by solving the following differential equation:

$$\frac{dr}{dz} = -54 \frac{\mu_l}{\ell_i^2} \frac{1}{(\rho_l - \rho_g) |g|} \left(r_p + \frac{h_i}{h_p} (r_c - r_p) \right) \tan \beta V_{iz}^i \quad (7.7)$$

$$\left[\frac{2}{9} \frac{\ell_i^2 \rho_l}{\mu_l} \frac{1}{r^3} \left(r_p + \frac{h_i}{h_p} (r_c - r_p) \right) \tan \beta V_{iz}^i + \frac{1}{r} \right].$$

The solution of Eq. 7.7 requires the determination of the interface characteristic length, ℓ_i . The model was refined using TUALP experimental data to obtain a correlation for predicting this variable. This correlation is given by:

$$\ell_i = \frac{3}{71.617 (1 - e^{-2.368 V_{sgz}^i}) (V_{sgz}^i + V_{\infty z})}, \quad (7.8)$$

where V_{sgz}^i represents the superficial gas velocity in the vertical direction. Values obtained from Eq. 7.8 should not be considered as the actual size of gas bubbles but merely as a fitting interface characteristic length for the two-phase interface momentum transfer.

The mechanistic model's efficiency predictions are compared against the measured values, as shown in Fig. 7.3. Based on statistical parameters illustrated in Appendix G, the average percentage error is 13.36 %.

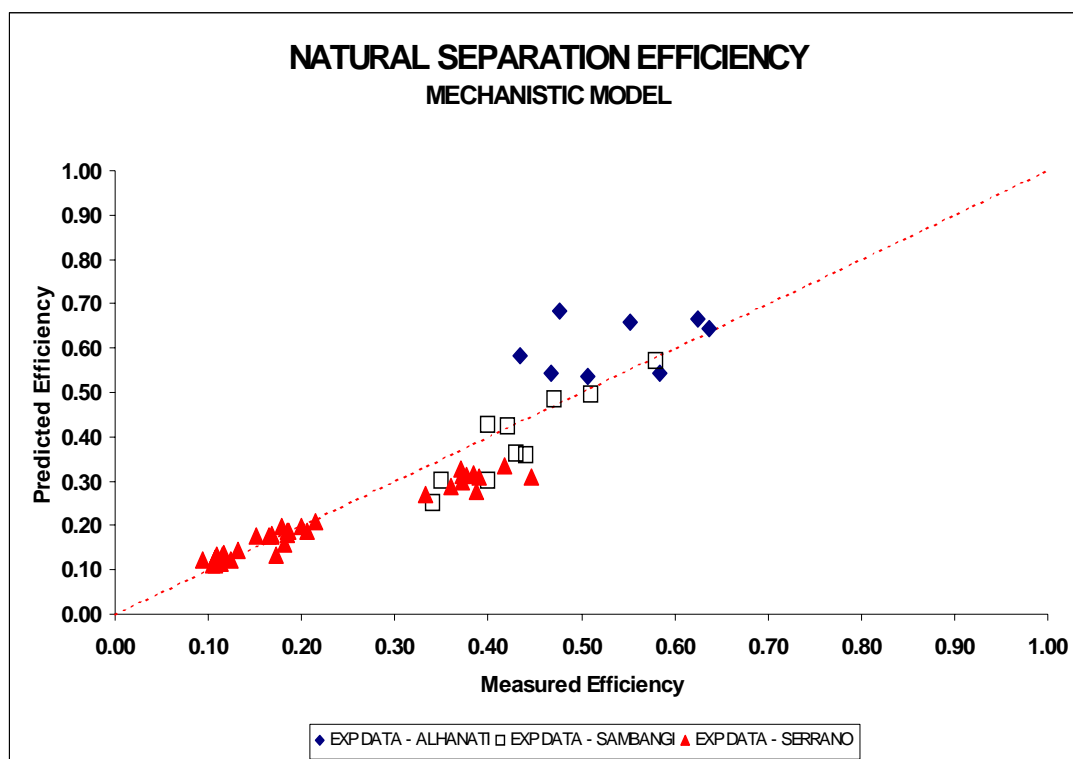


Figure 7.3 – Predicted Efficiency vs. Measured Efficiency - Mechanistic Model.

The effect of important variables, such as geometric conditions, pressure, gas-liquid ratio and gas and liquid flow rates, has been considered in the following sensitivity analysis.

1. Geometry Effect

Assuming a 4 in. outside pump diameter inside 5 in., 6.366 in. and 10 in. casings, the mechanistic model was used to predict natural separation efficiency. Results are shown in Fig. 7.4.

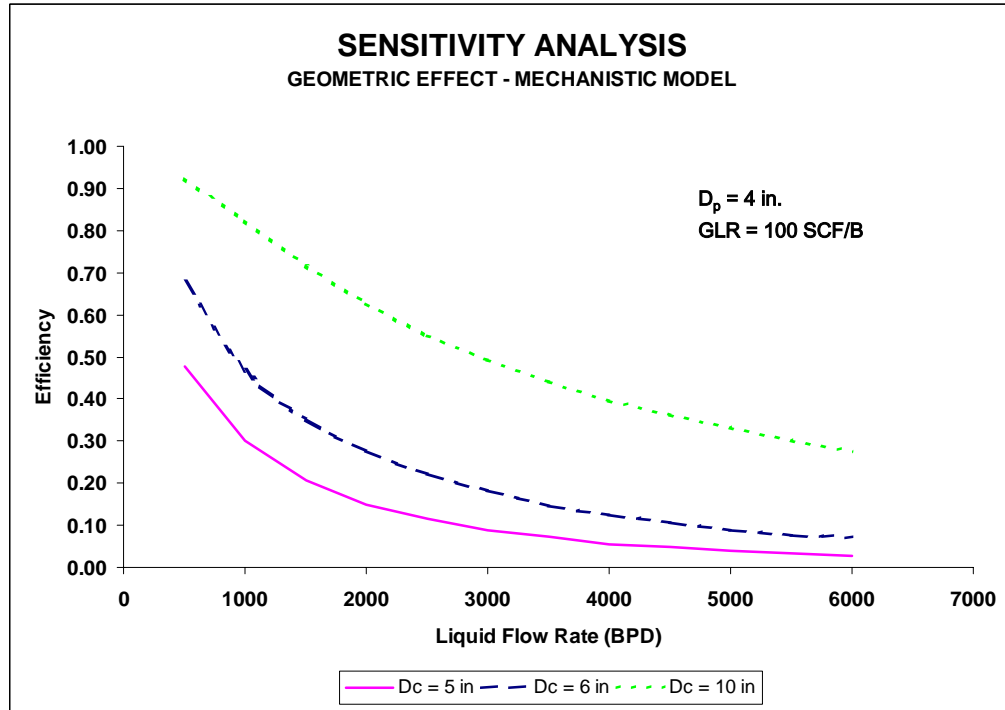


Figure 7.4 – Geometry Effect - Mechanistic Model.

As reported by Ghauri (1979), the larger the casing size, the larger the natural separation efficiency. In addition, it can be observed in this graph that natural separation for each casing size, decreases with increasing liquid flow rate.

A sensitivity analysis of the port size was also considered. Assuming three different h_p sizes of 1 in., 3 in. and 6 in., results demonstrated that this variable has little effect in the prediction of natural separation.

2. Pressure Effect

Although Alhanati (1993) reported that annulus efficiency decreases with increasing pressure, results obtained with this mechanistic model indicated that pressure has little effect in the prediction of natural separation.

In this mechanistic model, the gas density is the only term affected by pressure. Therefore, for low-pressure values only small changes in the gas density could be obtained. On the other hand, the pressure effect could be important in the prediction of the interface characteristic length. However, the correlation proposed to predict this variable, given by Eq. 7.8, is not a direct function of the pressure system observed in the experimental data.

3. Gas Effect

According to Lea and Bearden (1980), the greater the amount of gas present, the greater the percentage of gas that escaped up the annulus. Alhanati (1993) also observed in his experimental results that the annulus efficiency increases as the gas-liquid ratio is increased.

One of the advantages of the mechanistic model proposed in this work is the prediction of proper values of the interface characteristic length, which is a function not only of the terminal velocity of the bubbles, V_{∞} , but also of the superficial gas velocity, V_{sgz}^i .

Assuming two different constant values of V_{sgz}^i (1 and 8 ft/sec), natural separation efficiency was predicted by the mechanistic model. According to Fig. 7.5, the separation efficiency increases with V_{sgz}^i .

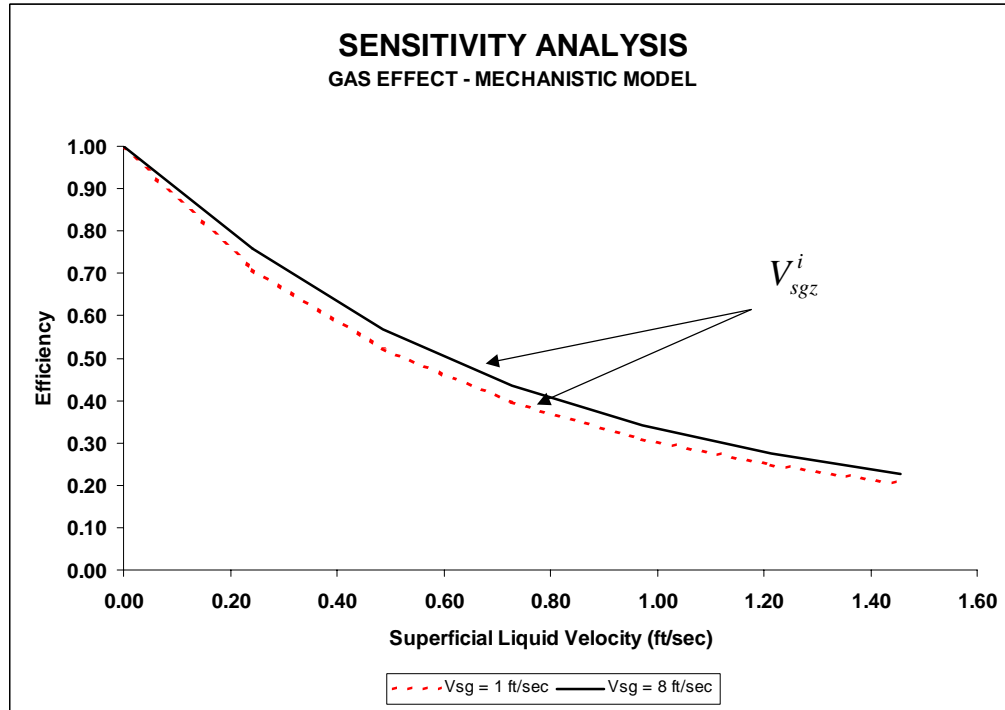


Figure 7.5 – Gas Effect - Mechanistic Model.

Two-Phase Flow Model

Accuracy of the Model

In order to check the implementation of the model, several runs were conducted for cases where analytically correct results are known. Not many analytical solutions are available for two-phase flow problems. This testing phase was limited to the vertical flow of liquid and gas through the annulus. The model can simulate this, assuming that no liquid flows into the pump.

For example, assuming a casing and pump diameter of 6.4 in. and 4 in., respectively, 150 psi, 75° F, pump intake of 3 in., bubble flow regime (GLR of 5 SCF/B or 0.4578 CF/Bbl), liquid flow rate of 1500 BPD and air and water as experimental

fluids, the actual fully-developed gas void fraction value can be obtained from Eq. 6.43, given in Chapter VI. That calculated value for this case is equal to 0.0310.

In order to test the two-phase model, an incorrect value was set at the annulus inlet boundary and equal to 90% of the actual fully developed gas void fraction. For this case, the annulus inlet gas fraction was set to 0.0279.

Since initial estimated values for gas void fraction must be selected at each node inside the flow domain, it was considered a value equal to 50% of the no-slip gas void fraction λ_g^i . For the no-slip condition, λ_g^i is simply equal to the ratio of the gas volumetric flow rate to the total volumetric flow rate, i.e.:

$$\lambda_g^i = \frac{q_g^i}{q_g^i + q_l^i}. \quad (7.9)$$

For the conditions given in this example, λ_g^i is equal to 0.07539, and the initial guess for the gas void fraction was set to 0.0377. The new two-phase flow model was able to correctly calculate the actual equilibrium gas void fraction of 0.0310 at the upper boundary.

Two Phase Flow Field Results

In the case of natural separation, all of the liquid is forced to go into the pump. In this section, the results from the model will be presented for the same conditions given in the previous example. The liquid stream function field is shown in Fig. 7.6.

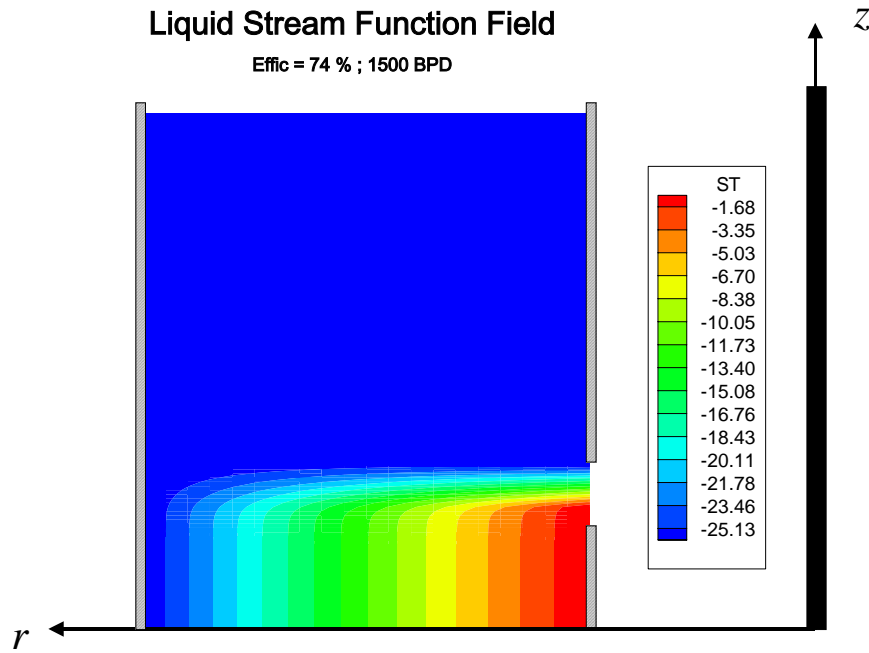


Figure 7.6 – Liquid Stream Function Field - Two-Phase Flow Model.

Fig. 7.7 demonstrates the gas stream function field obtained under the conditions given in the previous example. Based on the methodology proposed in Chapter VI, natural separation efficiency may be predicted as the ratio between the difference of the total gas streamline, φ_{gc} , and the gas streamline that strikes the upper pump wall boundary, φ_{gs} , to the total gas streamline. Natural separation efficiency can then be calculated as:

$$E = \frac{\varphi_{gc} - \varphi_{gs}}{\varphi_{gc}}. \quad (7.10)$$

According to Fig. 7.7, φ_{gc} and φ_{gs} are equal to -2.05 and -0.53 , respectively.

Therefore, a value of 74 % is estimated for natural separation efficiency.

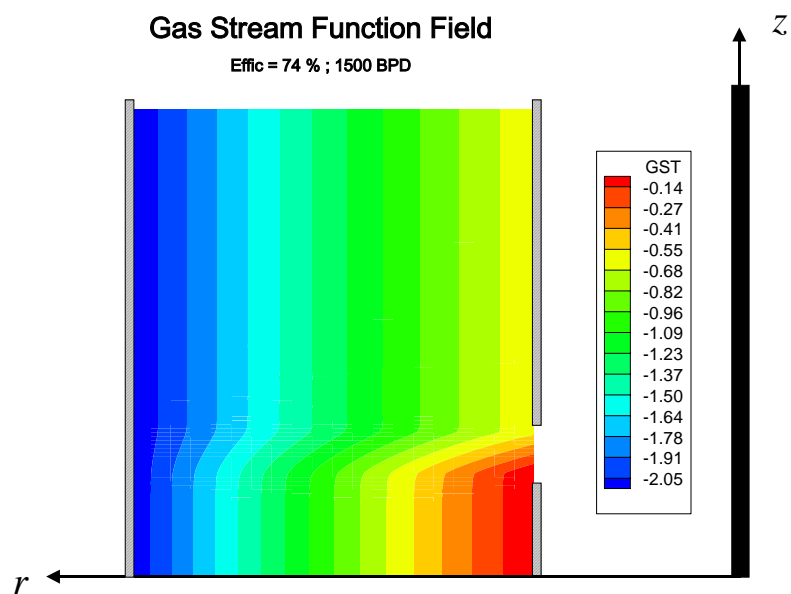


Figure 7.7 – Gas Stream Function Field - Two-Phase Flow Model.

The gas void fraction field was also determined for the given example. Results are shown in Fig. 7.8.

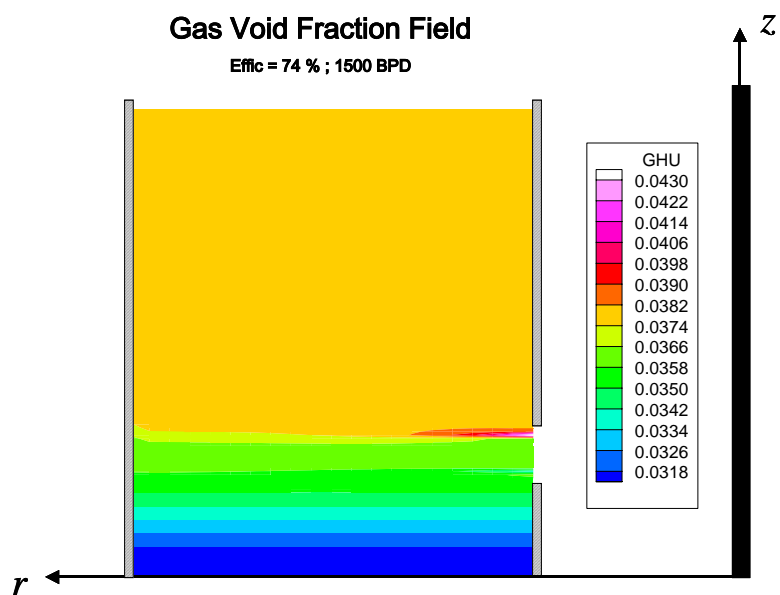


Figure 7.8 – Gas Void Fraction Field - Two-Phase Flow Model.

According to Fig. 7.8, three different values of the gas void fraction are observed inside the flow domain for this particular example. In the annulus inlet boundary, the gas void fraction is approximately equal to 0.0310. In front of the pump intake, an average value of 0.0365 is estimated. Above the pump intake, the gas void fraction estimated inside the field is equal to 0.0377.

Additionally, the liquid velocity field can be obtained from the stream function solutions by using the following definitions:

$$V_{lr} = \frac{1}{r(1-\alpha_g)} \frac{\partial \phi_l}{\partial z}, \quad (7.11)$$

$$V_{lz} = -\frac{1}{r(1-\alpha_g)} \frac{\partial \phi_l}{\partial r}. \quad (7.12)$$

Fig. 7.9 shows the liquid velocity field in the radial direction.

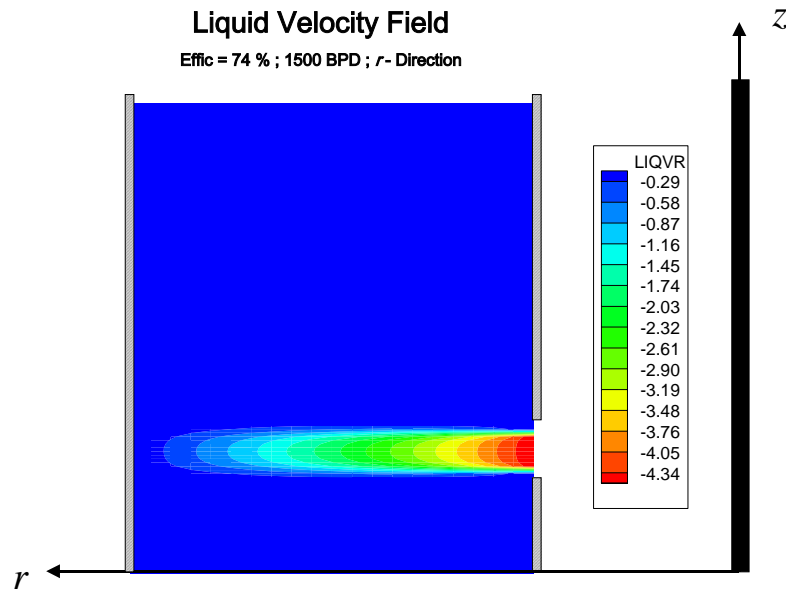


Figure 7.9 – Liquid Velocity Field in the Radial Direction - Two-Phase Flow Model.

Note in Fig. 7.9 that the largest velocity is observed just in front of the pump intake. Changes in that velocity in the radial direction have been considered, and according to previous results, is the main factor responsible for the transport of free gas into the pump. The gas velocity field in the radial direction is also illustrated in Fig. 7.10.

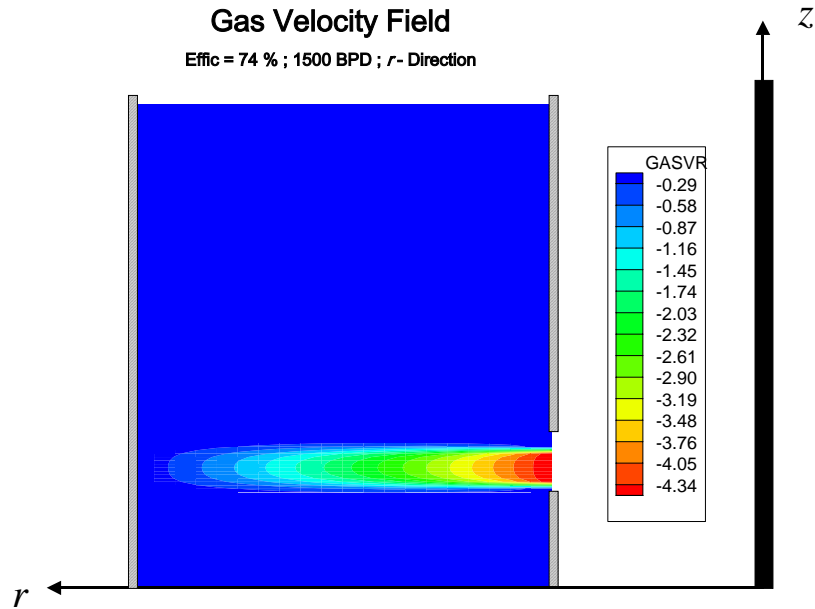


Figure 7.10 – Gas Velocity Field in the Radial Direction - Two-Phase Flow Model.

As shown in Fig. 7.11, three regions can be identified in the gas velocity field in the vertical direction. Below the pump intake, the gas velocity is approximately constant and equal to 22.6 in/sec. However, the gas phase reduces the velocity in front of the pump intake. This effect occurs because part of the gas is being dragged by the liquid phase inside the pump. Above the pump intake, the gas velocity is constant. Since the liquid phase is considered stagnant in this region, the gas velocity could be considered equal to the terminal velocity of the gas bubbles. In this region, the gas velocity obtained for this example is approximately equal to 13.7 in/sec.

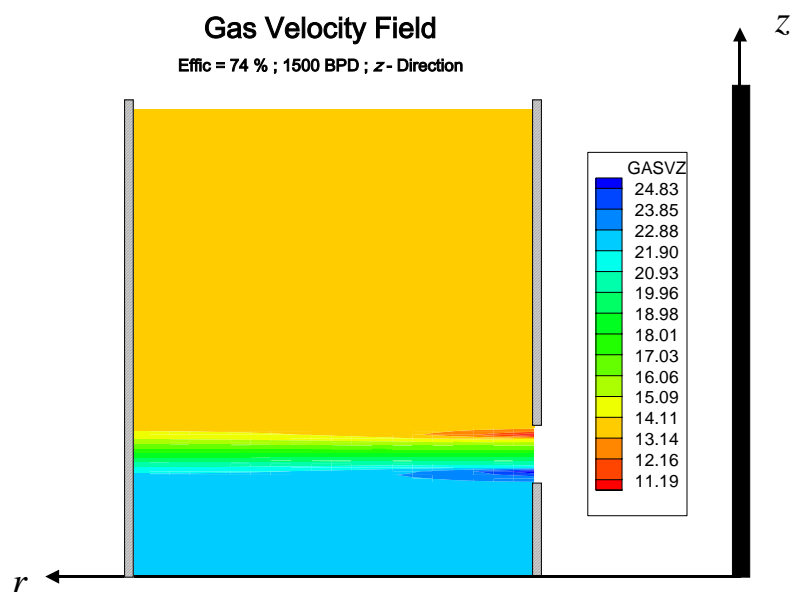


Figure 7.11 – Gas Velocity Field in the Vertical Direction - Two-Phase Flow Model.

The pressure gradient field in the radial direction is also presented in Fig. 7.12. Results indicate a larger pressure gradient in front of the pump intake.

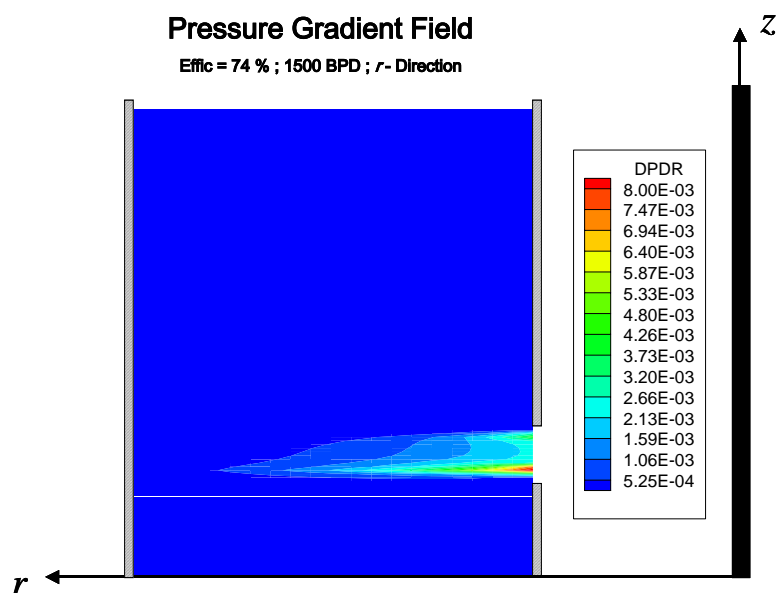


Figure 7.12 – Pressure Gradient Field in the Radial Direction - Two-Phase Flow Model.

Sensitivity Analysis

The following analysis is based on the results obtained from the proposed two-phase model, using available experimental data. It is important to mention that the auxiliary relationships for the drag radius, proposed in Chapter VI, were used to close the system of equations.

1. Pressure and Liquid Flow Rate Effects

The available experimental data has been divided into four groups, according to the pressure of the system, i.e. 50, 100, 150 and 200 psi. For each pressure group, the predicted values of natural separation efficiency, using the two-phase model, have been plotted as a function of gas flow rates, assuming a constant liquid flow rate. Finally, results obtained are also separated according to the flow pattern regime, keeping the classification previously presented.

At the same time, the measured efficiency and the predicted efficiency using the mechanistic model, the correlation and Alhanati's model are also plotted on the same graph for comparison.

Under bubble flow regime conditions, the two-phase and simplified models were used to predict natural separation efficiency. Results are presented and compared on a graph against available experimental data.

Three different liquid flow rates and pressures of 1000, 1500 and 2000 BPD and 50, 100 and 150 psi, respectively, are considered in this analysis. Figs. 7.13 - 7.21 illustrate those results. According to these figures, the two-phase model better predicts

the separation efficiency than simplified models given by the correlation, mechanistic model and Alhanati's model.

In addition, it is observed that the larger the liquid flow rates, the lower the natural separation efficiency. Moreover, pressure does not appear to have a significant effect on the separation process under a bubble flow regime. This conclusion is based on results obtained from these graphs.

For example, assuming a constant liquid flow rate of 1000 BPD, when making comparisons between Figs. 7.13, 7.16 and 7.19, where the pressure of the system is equal to 50, 100 and 150 psi, respectively, reflects a very similar value of efficiency, which is approximately 40%. Similar results are observed for other liquid flow rates of 1500 and 2000 BPD.

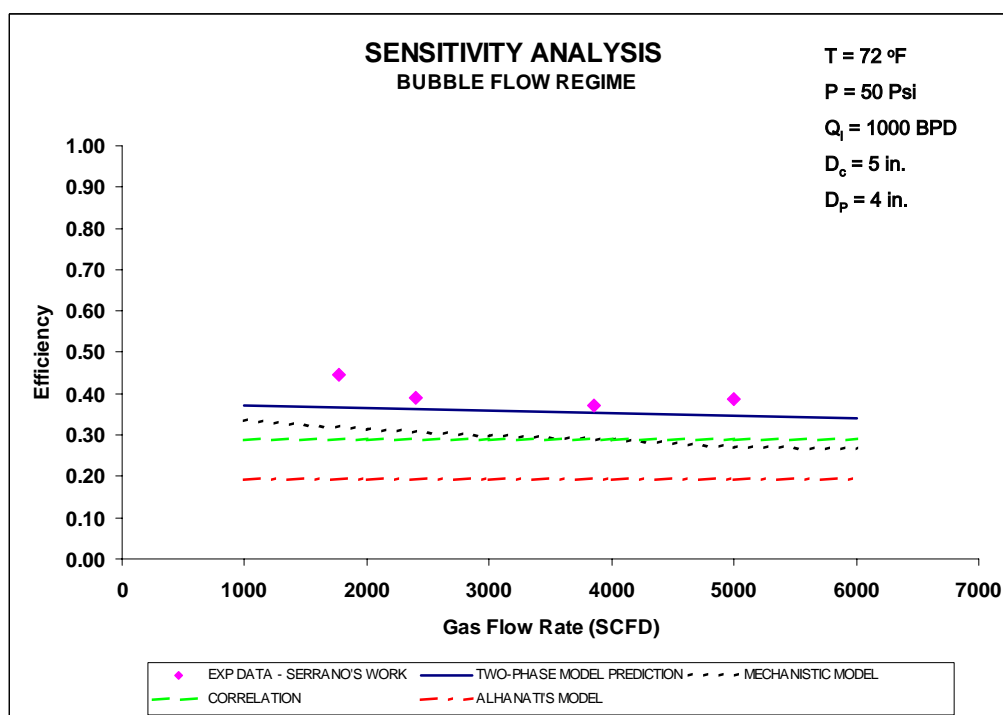


Figure 7.13 – 1000 BPD and 50 Psi - Bubble Flow Regime.

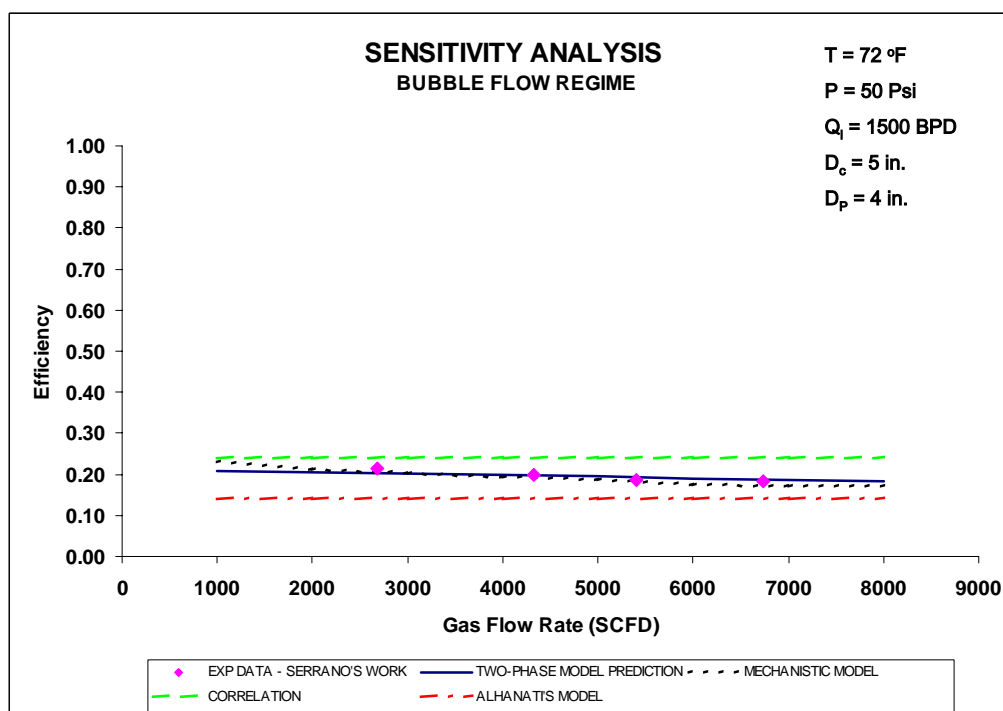


Figure 7.14 – 1500 BPD and 50 Psi - Bubble Flow Regime.

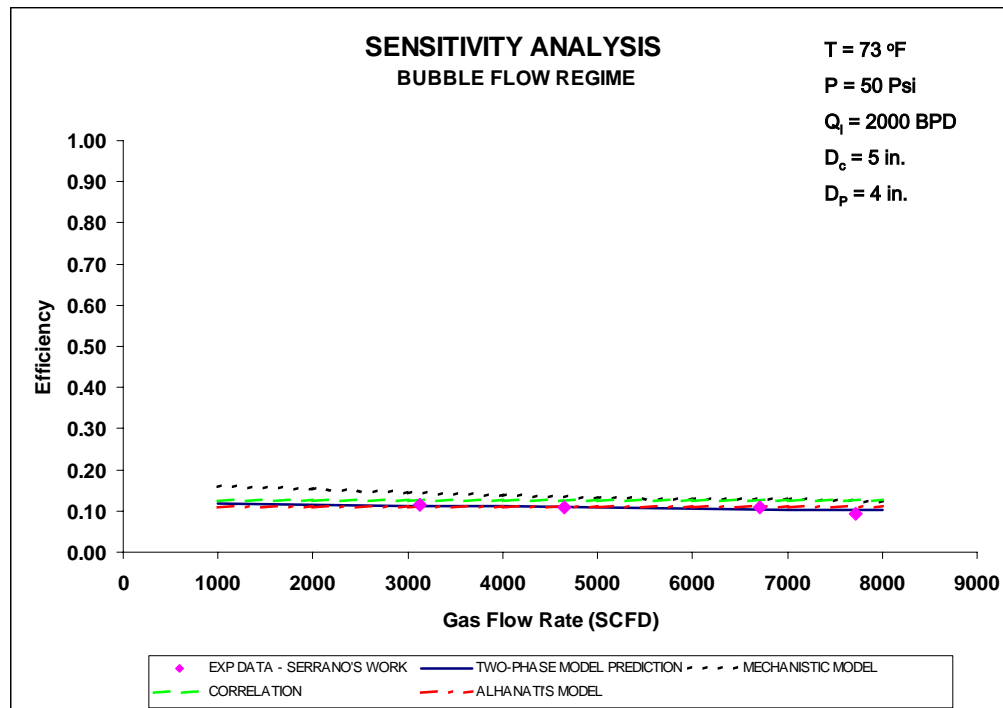


Figure 7.15 – 2000 BPD and 50 Psi - Bubble Flow Regime.

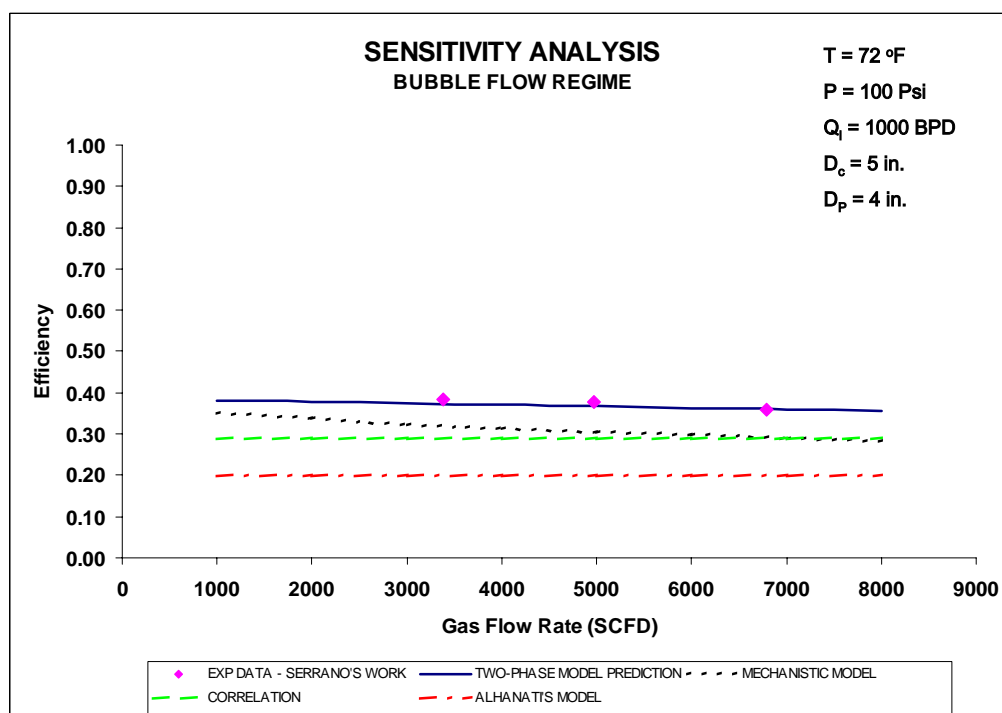


Figure 7.16 – 1000 BPD and 100 Psi - Bubble Flow Regime.

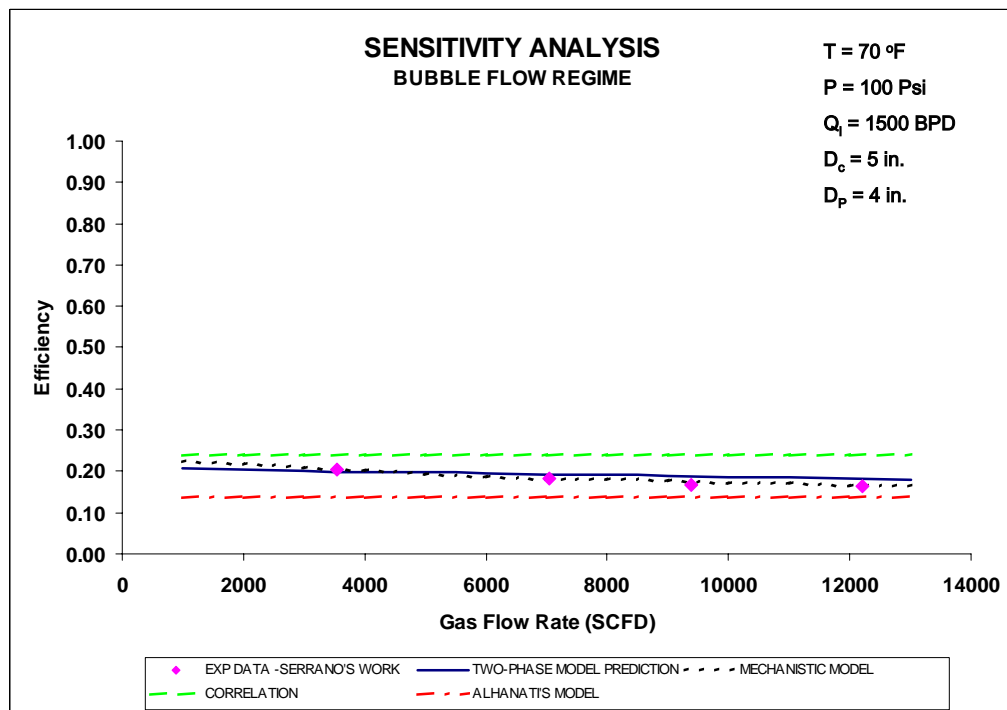


Figure 7.17 – 1500 BPD and 100 Psi - Bubble Flow Regime.

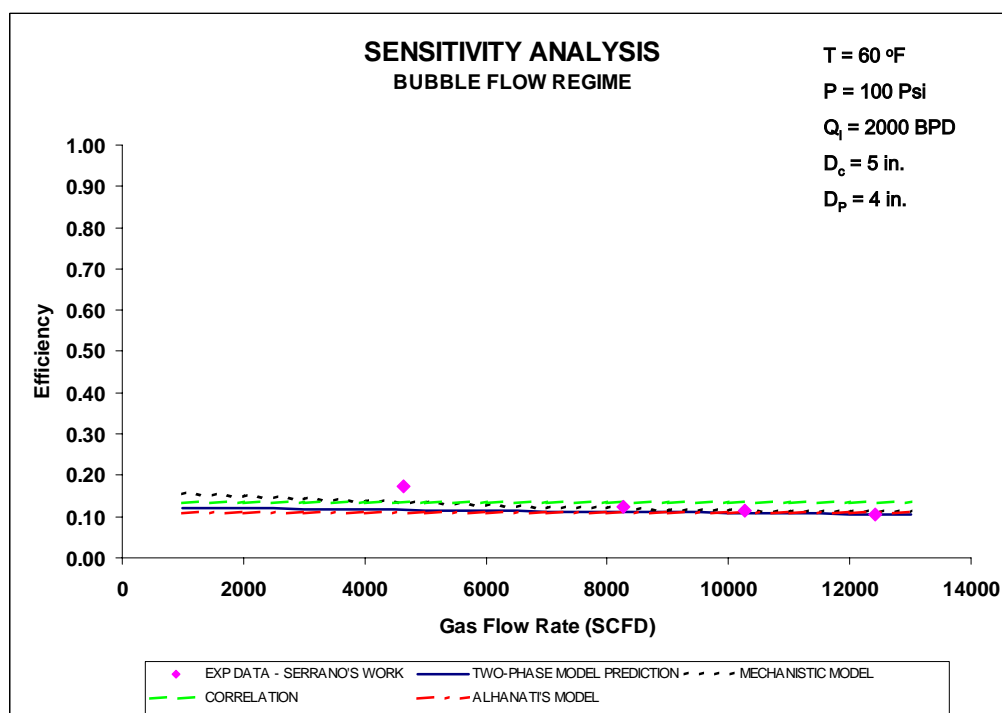


Figure 7.18 – 2000 BPD and 100 Psi - Bubble Flow Regime.

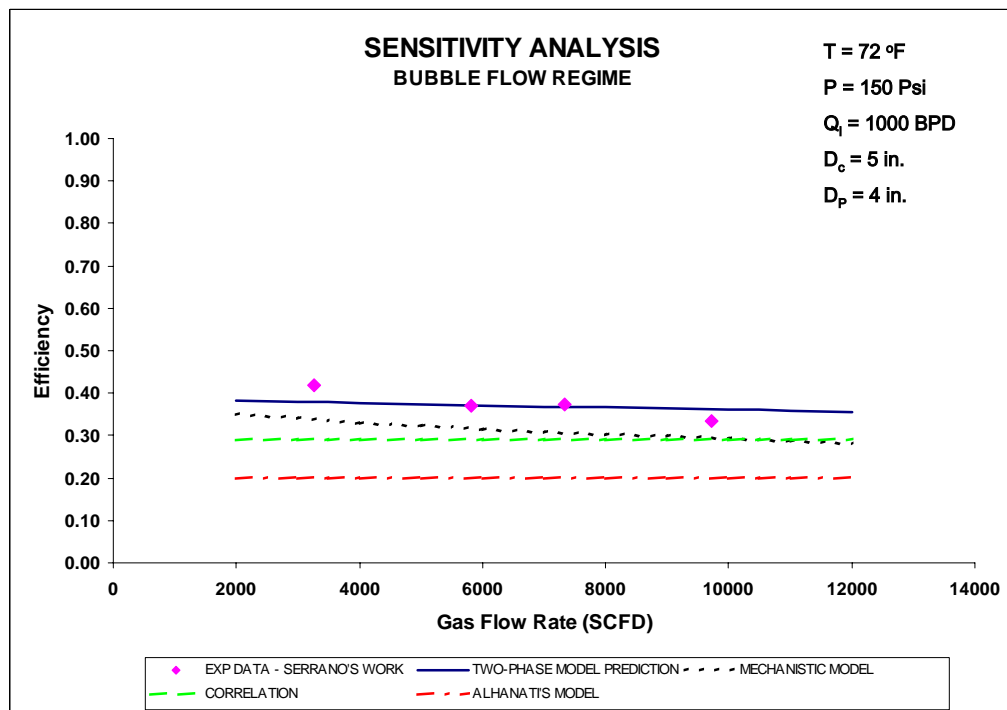


Figure 7.19 – 1000 BPD and 150 Psi - Bubble Flow Regime.

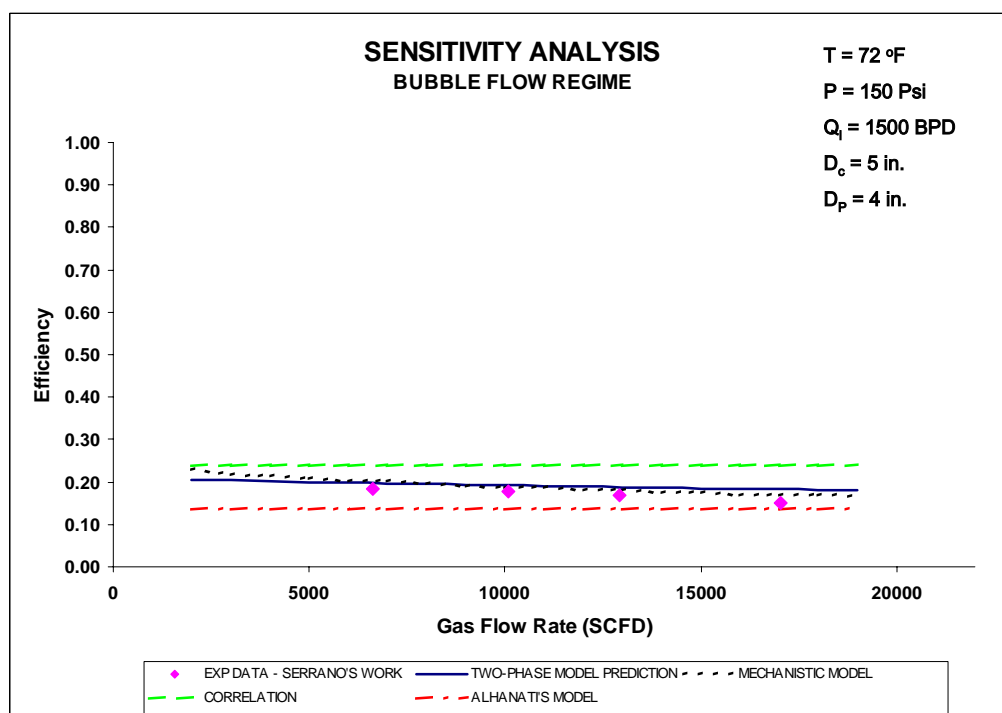


Figure 7.20 – 1500 BPD and 150 Psi - Bubble Flow Regime.

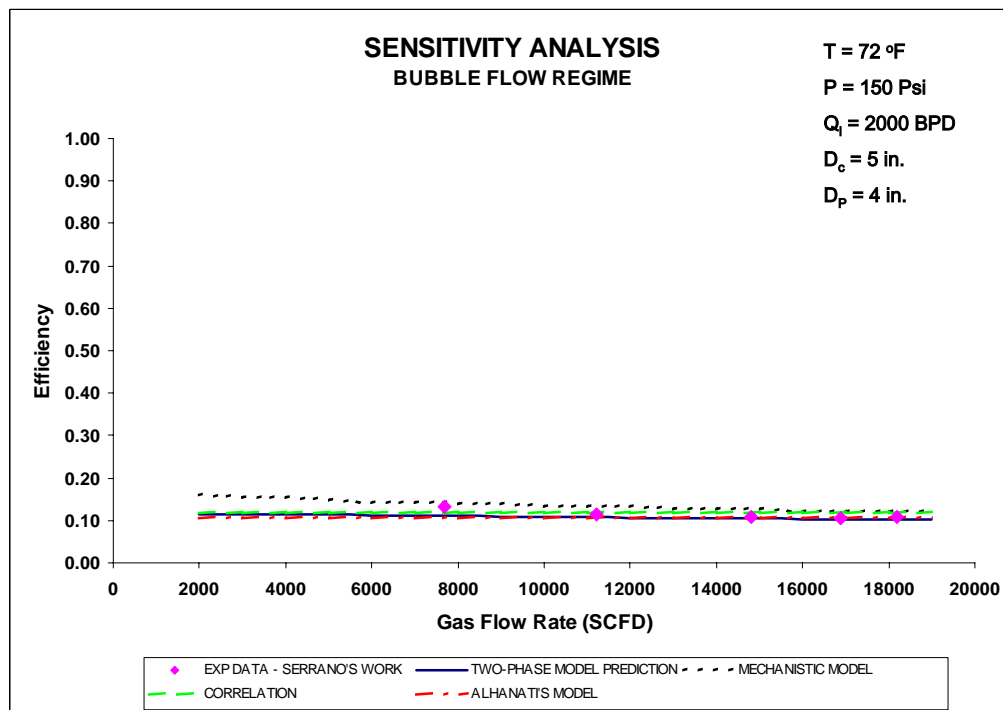


Figure 7.21 – 2000 BPD and 150 Psi - Bubble Flow Regime.

Under a slug/churn flow regime, two-phase and simplified models were used to predict natural separation efficiency. Two constant liquid flow rates of 600 and 900 BPD are available for the analysis. Additionally, two values of pressure of 100 and 200 psi are also available for each liquid flow rate previously mentioned.

Results, along with available experimental data, are shown in Figs. 7.22 - 7.28. According to these Figures, the two-phase model satisfactorily predicts the natural separation efficiency when it is compared with the experimental data. However, the prediction obtained from simplified models sometimes appears closer to the actual values of efficiency than the two-phase flow model.

This behavior is particularly critical for high gas flow rates, where the prediction of the two-phase model shows a larger disagreement with the experimental data. See Figs. 7.23, 7.26 and 7.28 as examples. One of the possible causes could be related to the correlation used to predict the drag radius.

On the other hand, discontinuities observed in the two-phase model curves are due to change of flow pattern, from bubble to slug/churn flow regime. It happens mainly in low gas flow rates, where the liquid is the dominant phase.

Based on the conditions of pressure, temperature, gas and liquid flow rates, and the characteristics of the bottomhole, among others, the computational program developed in this work predicts the flow pattern and selects the appropriate equation to predict the drag radius.

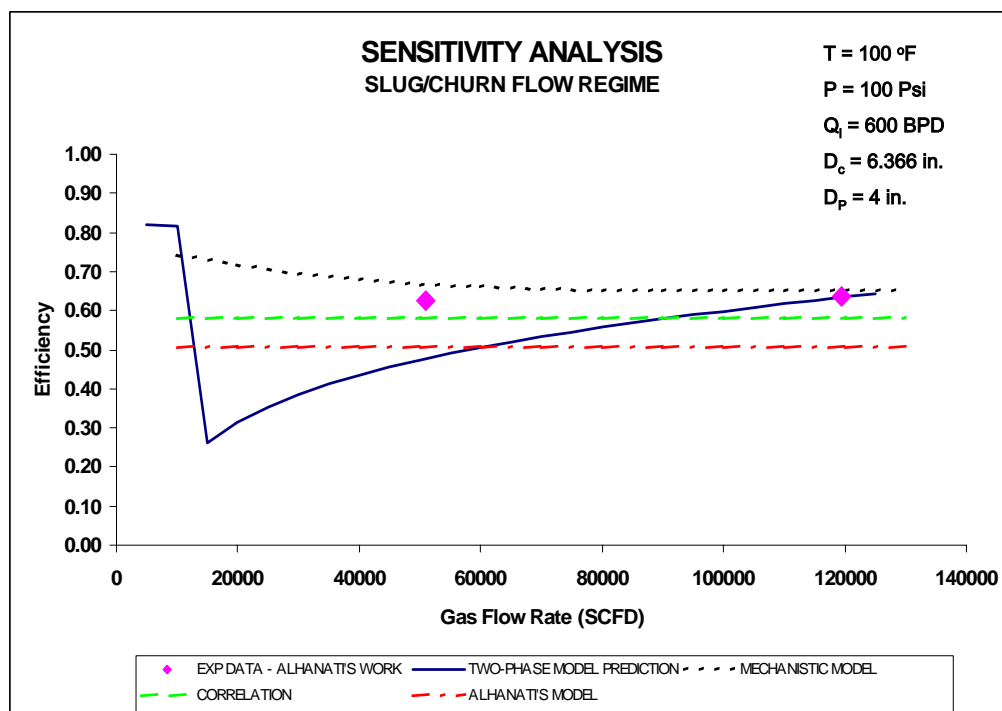


Figure 7.22 – 600 BPD and 100 Psi - Slug/Churn Flow Regime.

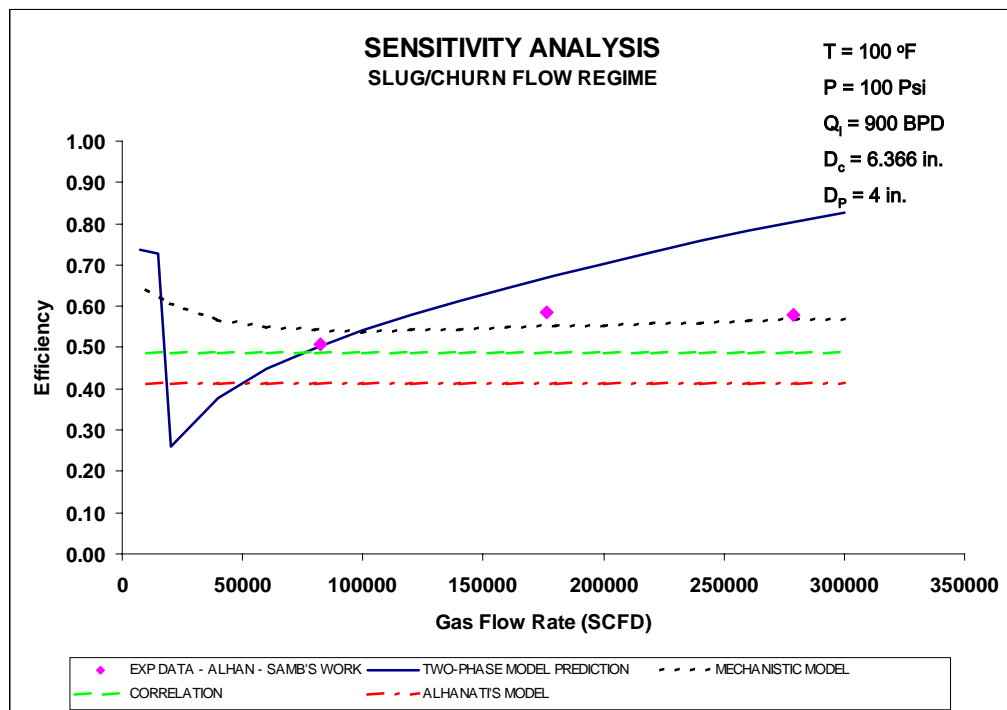


Figure 7.23 – 900 BPD and 100 Psi - Slug/Churn Flow Regime.

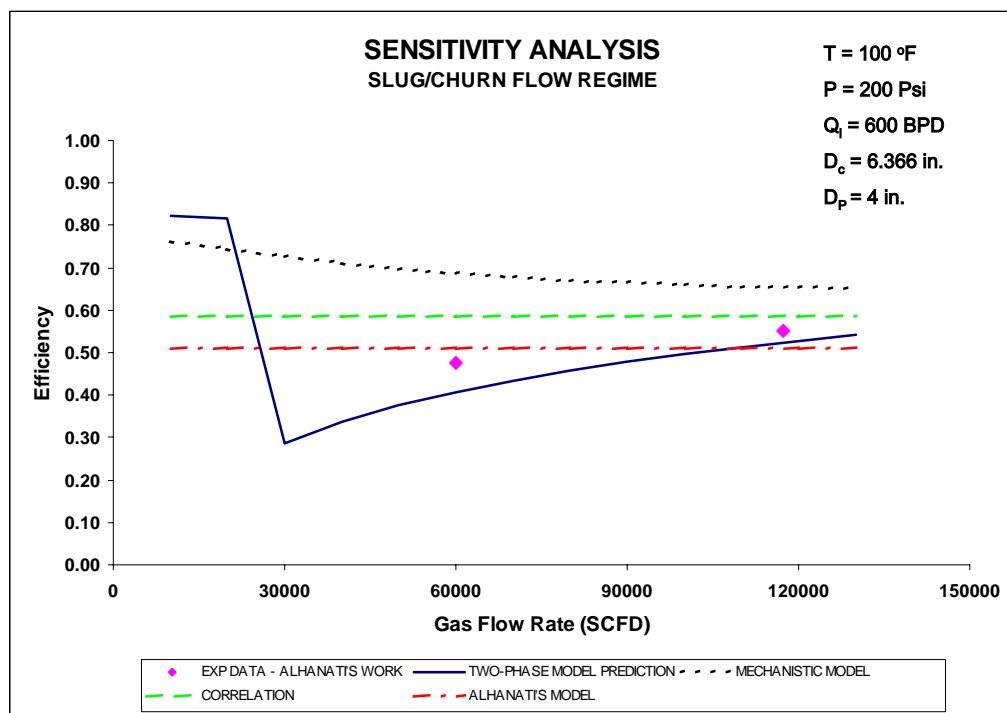


Figure 7.24 – 600 BPD and 200 Psi - Slug/Churn Flow Regime.

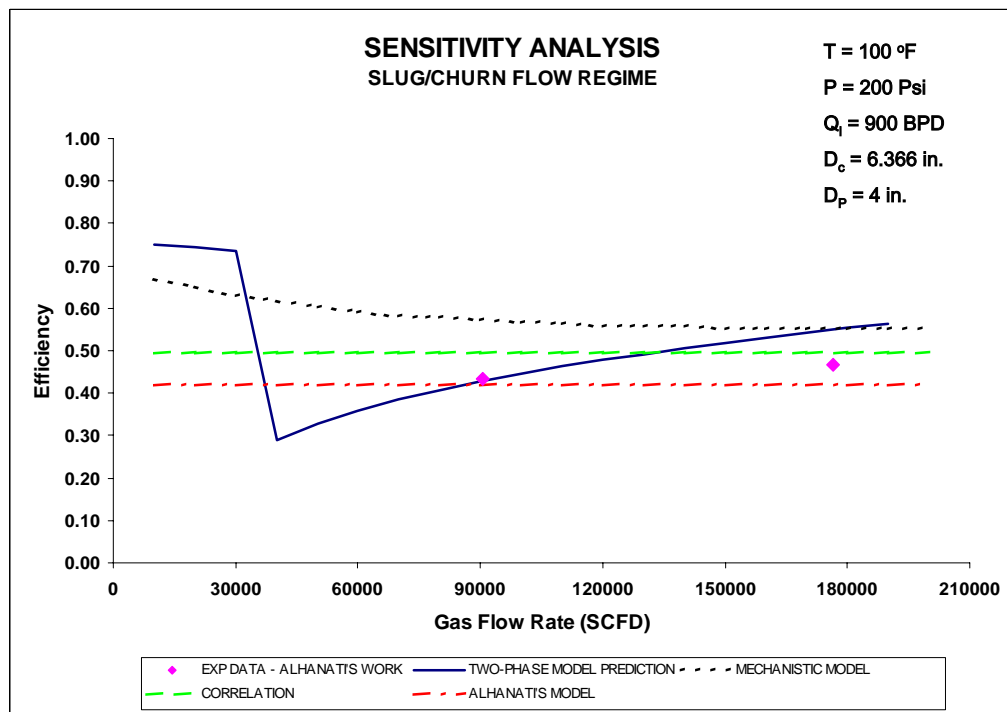


Figure 7.25 – 900 BPD and 200 Psi - Slug/Churn Flow Regime.

Unlike the conditions observed under bubble flow regime, pressure seems to have a significant effect on the separation process.

Comparisons between Figs. 7.22 and 7.24 demonstrate that under similar conditions of gas and liquid flow rates, characteristics of the bottomhole and flow pattern regime, the increment of pressure from 100 psi to 200 psi decreases the separation process. This behavior agrees with the results observed by Alhanati in his experiments. Similar results were obtained from comparisons between Figs. 7.23 and 7.25.

Additional results obtained for different ranges of pressure and liquid flow rates are illustrated in Figs. 7.26 - 7.28.

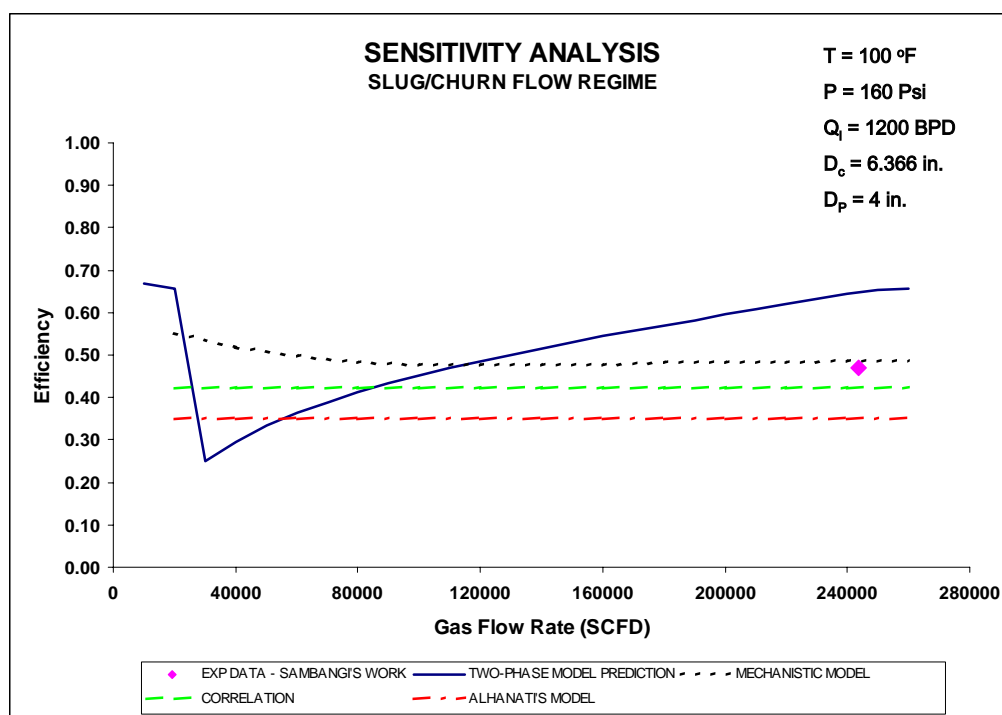


Figure 7.26 – 1200 BPD and 160 Psi - Slug/Churn Flow Regime.

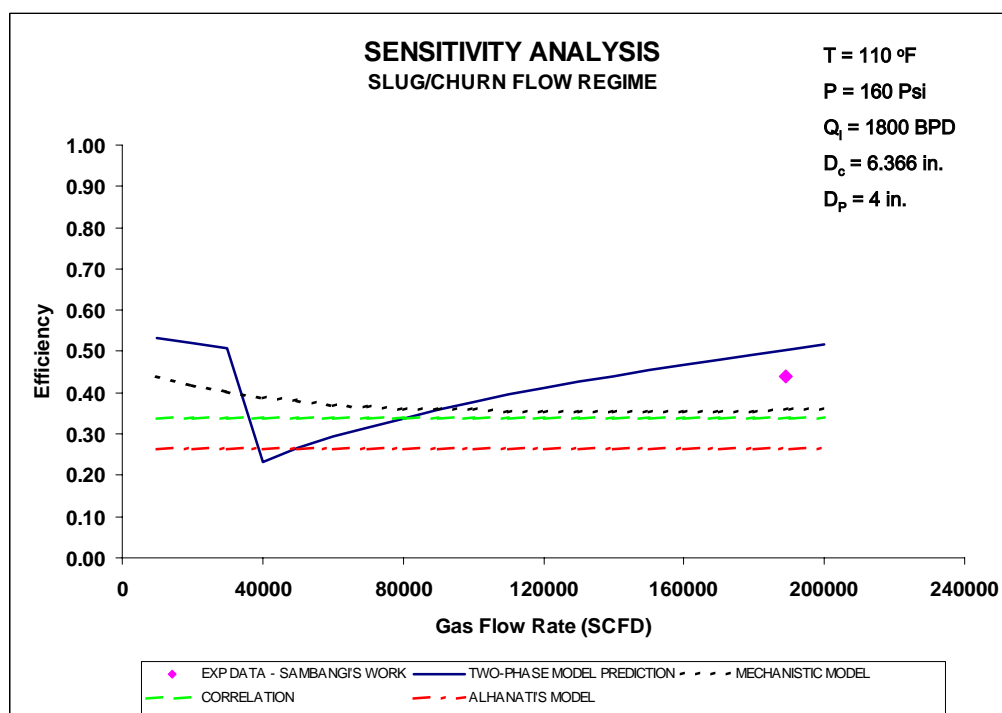


Figure 7.27 – 1800 BPD and 160 Psi - Slug/Churn Flow Regime.

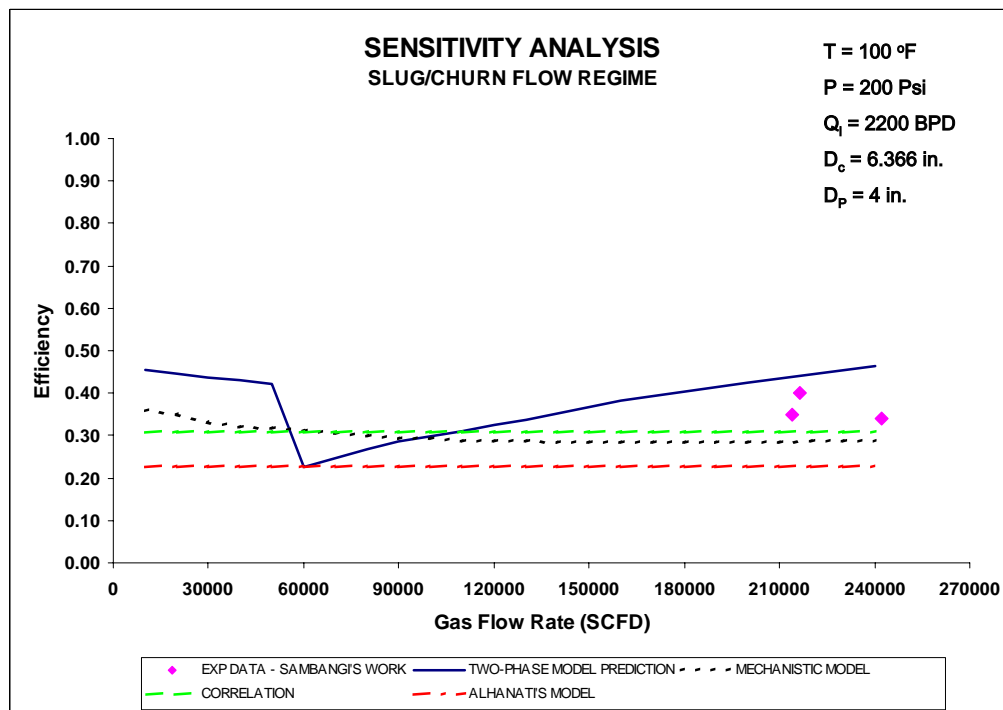


Figure 7.28 – 2200 BPD and 200 Psi - Slug/Churn Flow Regime.

2. Gas Liquid Ratio Effect

The analysis presented in this section has been separated according to the flow pattern regime. Synthetic data will be used to show the effect of the gas-liquid ratio on the separation process.

Assuming a casing and pump diameter of 6.4 in. and 4 in., respectively, 150 psi, 75° F, pump intake of 3 in., and air and water as experimental fluids, several values of GLR are considered to promote both bubble and slug/churn flow regimes.

Under the operational condition previously selected, the bubble flow regime could be obtained at very low values of GLR. Therefore, three constant values of GLR of 5, 15 and 20 SCF/B are assumed in this analysis. A graph of GLR as a function of the liquid flow rate is shown in Fig. 7.29.

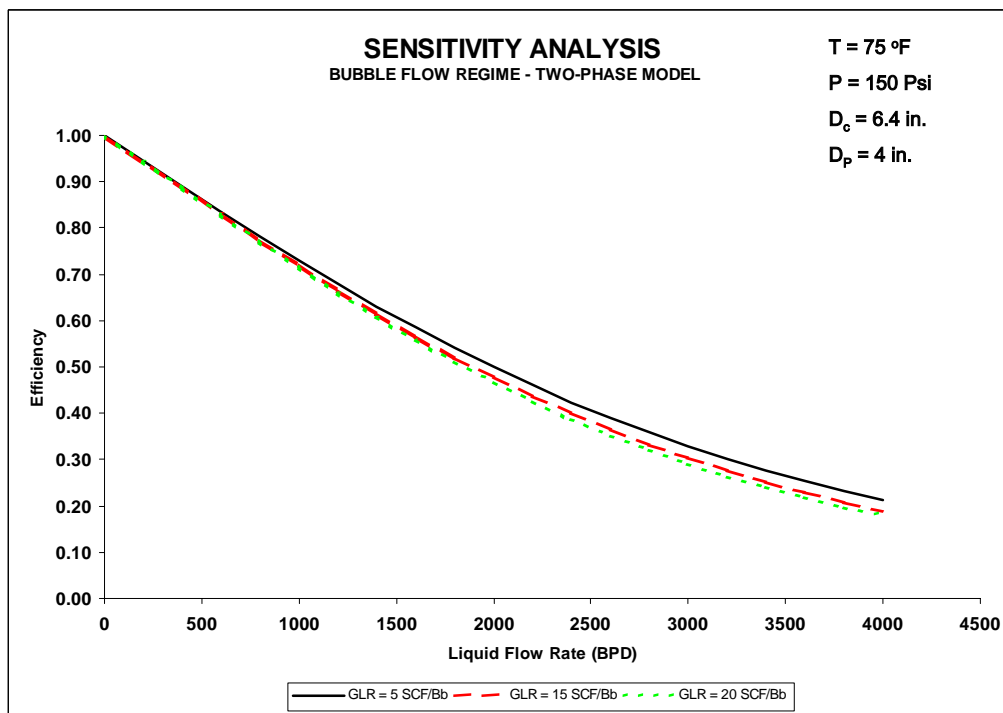


Figure 7.29 – GLR Effect - Bubble Flow Regime.

According to the results observed in Fig. 7.29, the increment of GLR would reduce the separation efficiency.

For higher GLR, a change of flow regime could be promoted. Assuming three GLR values of 30, 60 and 90 SCF/B, the natural separation efficiency is predicted by using the two-phase model. Results are demonstrated in Fig. 7.30. The predicted efficiency for the model has been plotted as a function of the liquid flow rate. Changes of slope observed in low liquid flow rates are caused by variations of the flow pattern, from the bubble to the slug/churn flow regime. According to results observed in Fig. 7.30, the efficiency increases with the increment of GLR. This behavior is completely different to that observed under a bubble flow regime where the higher GLR would decrease the separation efficiency. See Fig. 7.29.

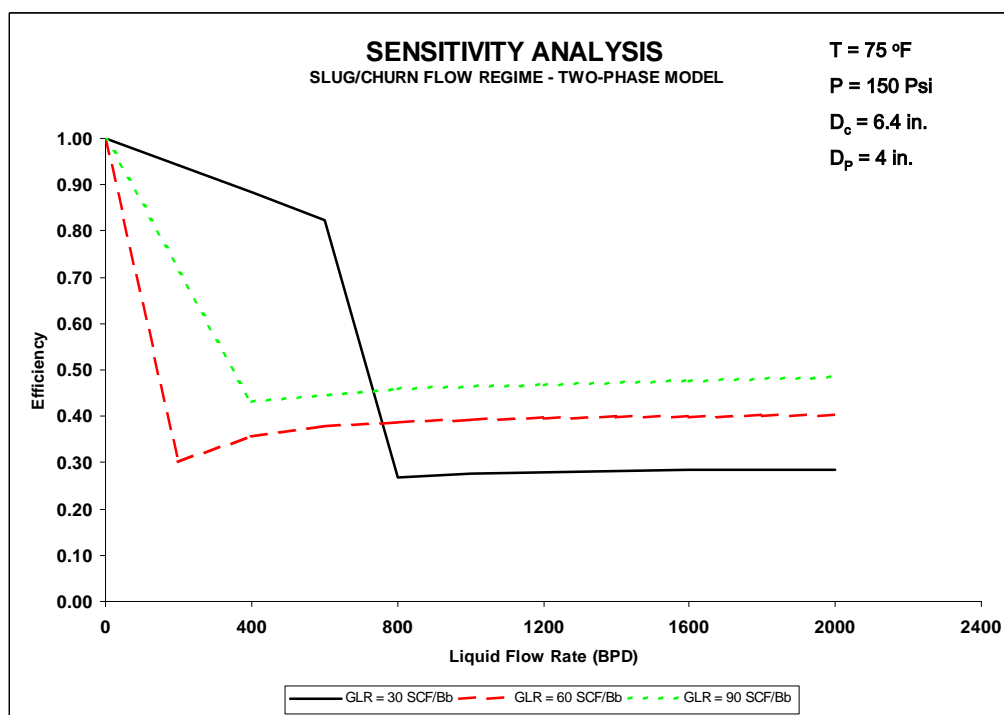


Figure 7.30 – GLR Effect - Slug/Churn Flow Regime.

One possible explanation for the conditions observed in Fig. 7.30 would be that the existence of more gas in the annulus, which would promote the formation of larger gas bubbles, which are much more difficult to drag inside the pump, thus increasing the separation process. However, the increment of the efficiency does not necessarily mean less gas entering the pump.

3. Casing Size Effect

Considering the same synthetic data, the two-phase model is used to predict natural separation efficiency and analyze the effect of the casing size. Under bubble flow conditions, the larger the casing size, the greater the separation process. Those results can be observed in Fig. 7.31.

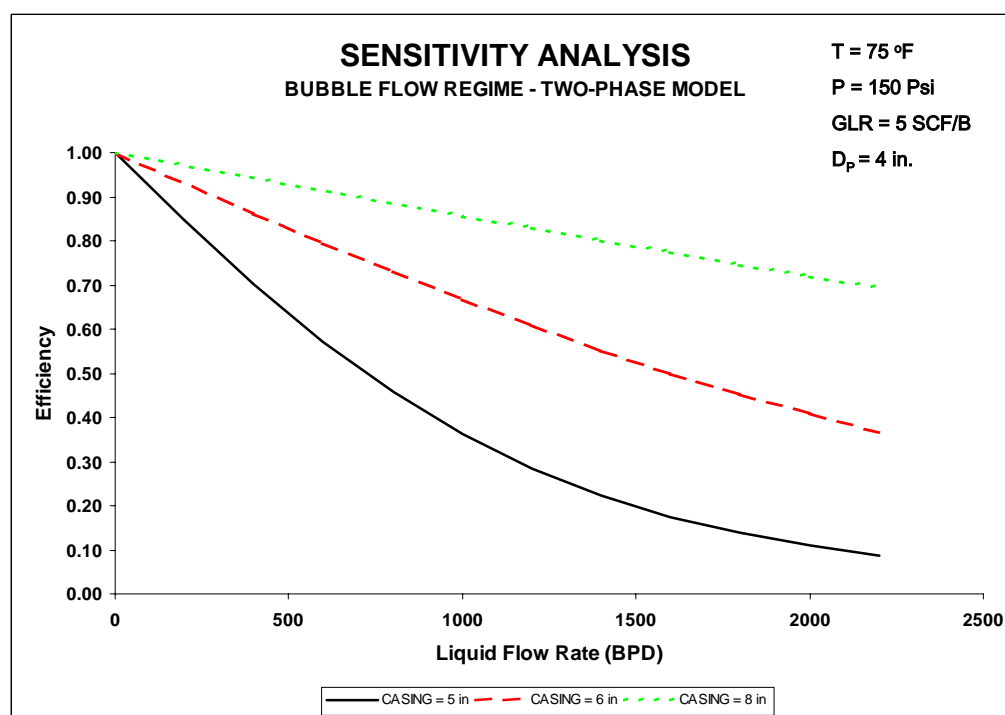


Figure 7.31 – Casing Size Effect - Bubble Flow Regime.

However, under the slug/churn flow regime, results appear completely different to those observed in Fig. 7.31.

The predicted results of natural separation, using the two-phase model, do not appear to be affected by changes in the casing size. Those results can be observed in Fig. 7.32. The same case was analyzed for a higher GLR value of 60 SCF/B, obtaining similar behavior. See Fig. 7.33 for more information.

Results regarding the casing size's effect on predicting natural separation efficiency under slug/churn flow regime, using the two-phase model proposed in this work, cannot be fully demonstrated. Consequently, these results must be analyzed carefully with experimental data in future research.

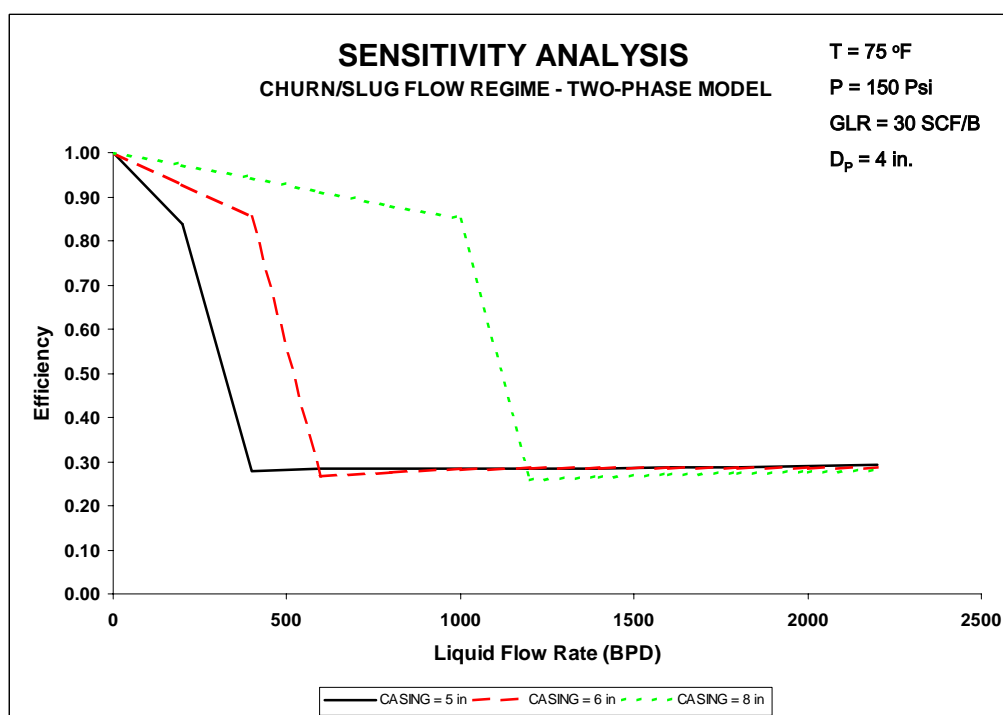


Figure 7.32 – Casing Size Effect. 30 SCF/B - Slug/Churn Flow Regime.

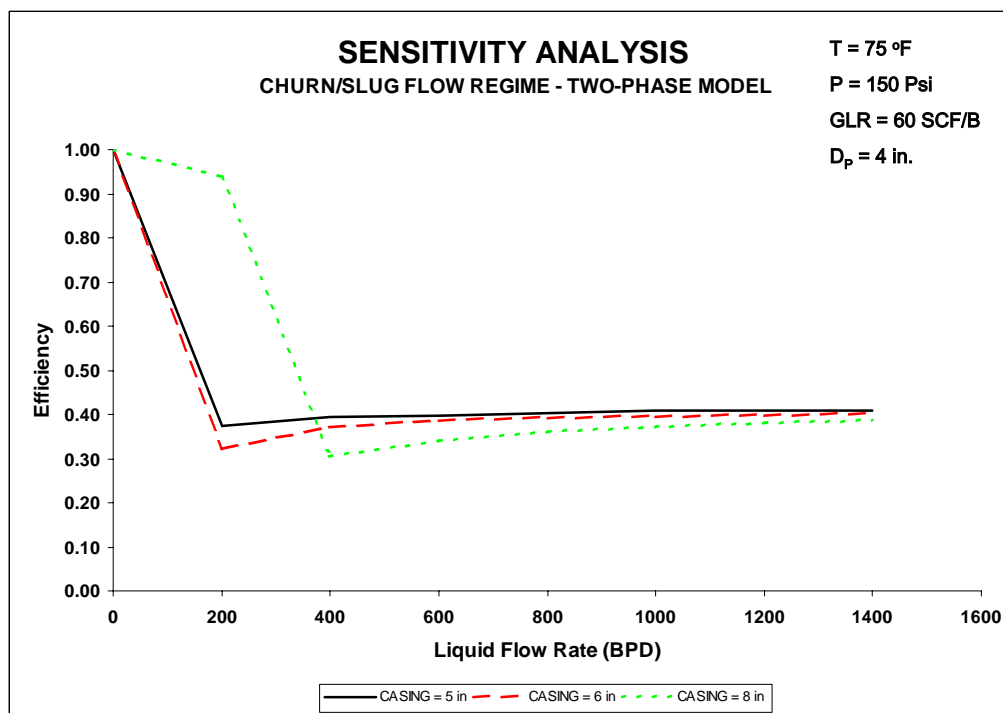


Figure 7.33 – Casing Size Effect. 60 SCF/B - Slug/Churn Flow Regime.

4. Viscosity Effect

Although no experimental data is available to analyze and verify this effect, two viscosity values have been considered and simulated by the two-phase model.

Each set of viscosity values has been separately evaluated for both the bubble and slug/churn flow regimes. Results regarding predicted natural separation values are also presented on graphs, as a function of the liquid flow rates.

Under bubble flow conditions, Fig. 7.34 illustrates that the efficiency would decrease with an increment of the viscosity from 1.1 cps to 50 cps.

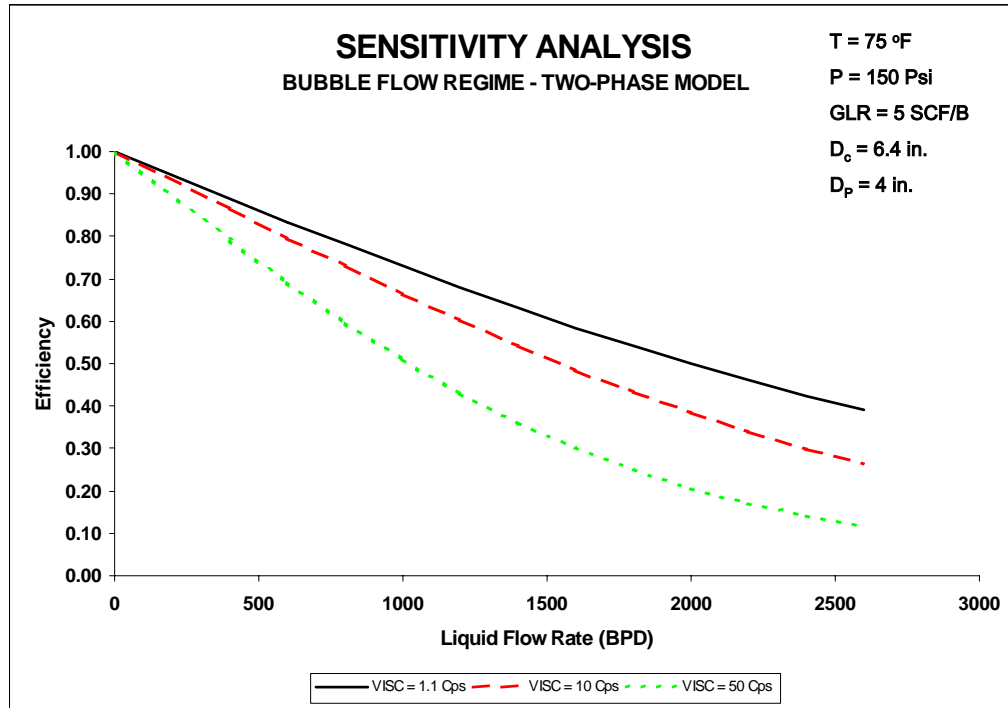


Figure 7.34 – Viscosity Effect - Bubble Flow Regime.

Similar behavior is observed under slug/churn flow conditions. However, according to results obtained from the simulation, the viscosity effect appears larger under this flow regime than under the bubble flow regime. See Fig. 7.35 for details. However, the model needs to be validated using new experimental data, therefore, new research in this area is strongly recommended.

5. Predictions

Finally, the accuracy of the two-phase model proposed here for the prediction of natural separation efficiency is tested against available experimental data, obtained from the work of Alhanati, Sambangi and Serrano. Note that although Sambangi's data was not considered in the development of the correlation for predicting the bubble drag radius under a slug/churn flow regime, his experimental results were used in the two-phase

model to estimate the efficiency and compare it with his data. Results obtained from the predicted and measured efficiency are illustrated in Fig. 7.36.

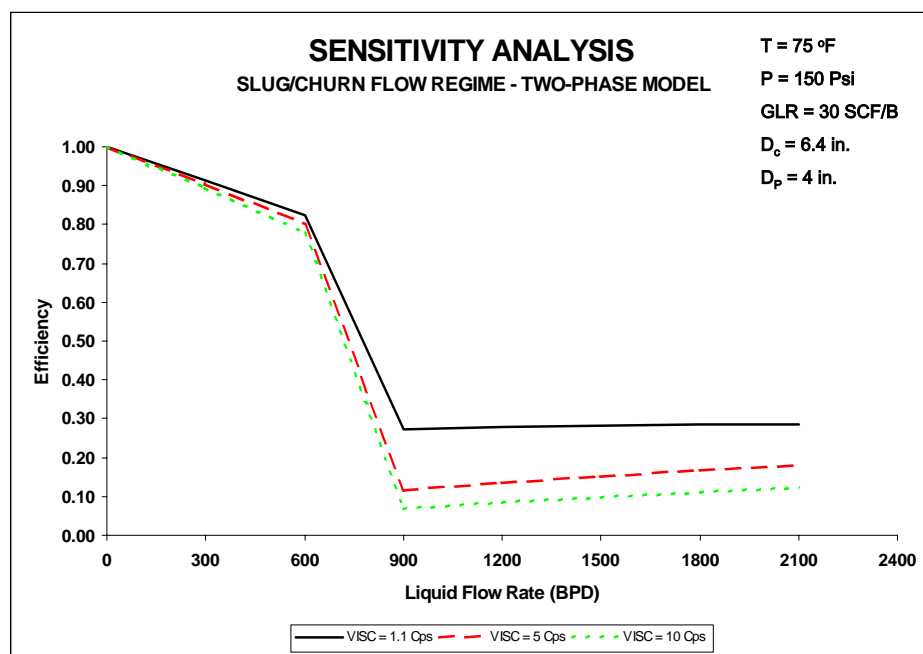


Figure 7.35 – Viscosity Effect - Slug/Churn Flow Regime.

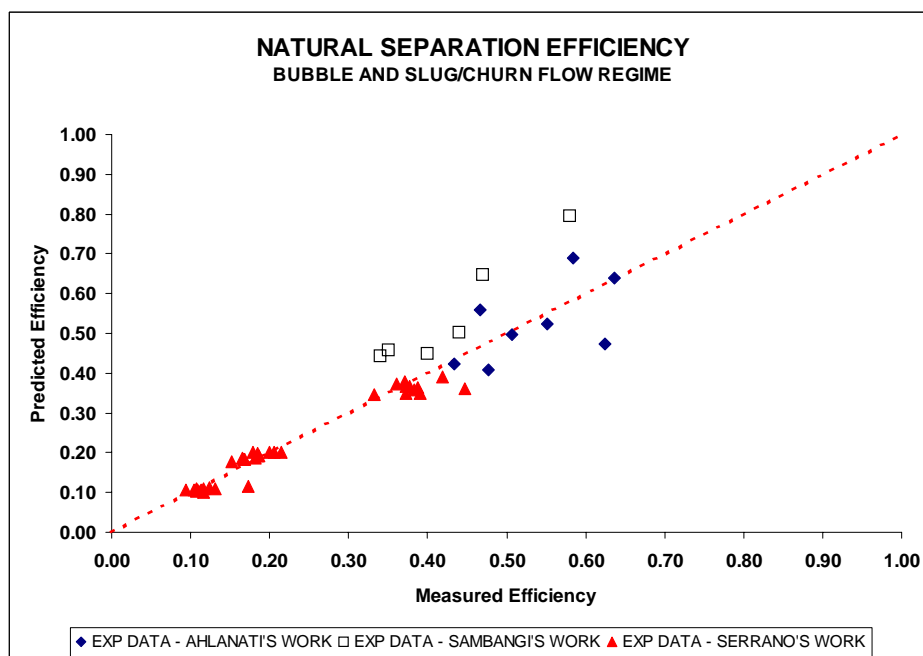


Figure 7.36 – Predicted vs. Measured Efficiency - Two-Phase Model.

According to Fig. 7.36, the predicted efficiency for the two-phase flow model confirms a good agreement with the experimental data, specifically under bubble flow conditions. However, certain disagreements between the experimental data and predicted values of natural separation are observed under slug/churn flow regime conditions. The average error of the two-phase model, considering both flow regimes, is approximately 10%.

6. Applicability of the Model

To date, the two-phase model has satisfactorily predicted the annulus' efficiency, according to results previously demonstrated. It has also been observed that flow pattern regimes considerably affect predictions. Additionally, it has been discussed in this work that the effect of important variables such as GLR, pressure, liquid and gas flow rates, pressures, characteristics of the bottomhole and viscosity, among others, have in the prediction of natural separation efficiency.

Based on all these results and the experimental data gathered, the following procedure and subsequent analysis will demonstrate the impact and applicability that the results of the two-phase model have in the design and performance of any artificial lift system. Under no-slip conditions, the gas void fraction in the annulus, λ_g^i , can be estimated from Eq. 7.9 as:

$$\lambda_g^i = \frac{q_g^i}{q_g^i + q_l^i},$$

where q_g^i and q_l^i represent the gas and liquid flow rate coming from the annulus, respectively. In addition, for no-slip conditions, the gas void fraction that enters the pump, λ_g^p , can be estimated as:

$$\lambda_g^p = \frac{q_g^p}{q_g^p + q_l^i}, \quad (7.13)$$

where q_g^p represent the gas flow rate entering the pump. Additionally, natural separation efficiency E is given by:

$$E = 1 - \frac{q_g^p}{q_l^i}. \quad (7.14)$$

The combination of Eqs. 7.9, 7.13 and 7.14 would define one additional relationship, which can be used to quantify how much gas enters the pump. This equation is given by:

$$\lambda_g^p = \frac{1}{1 + \frac{(1 - \lambda_g^i)}{\lambda_g^i (1 - E)}}. \quad (7.15)$$

Assuming several constant no-slip gas void fraction values of 0.20, 0.30, 0.40, 0.50, 0.60 and 0.70, the two-phase model can be used to predict the annulus efficiency, as shown in Fig. 7.37. The predicted efficiency by the model is plotted on a graph as a function of the liquid flow rate.

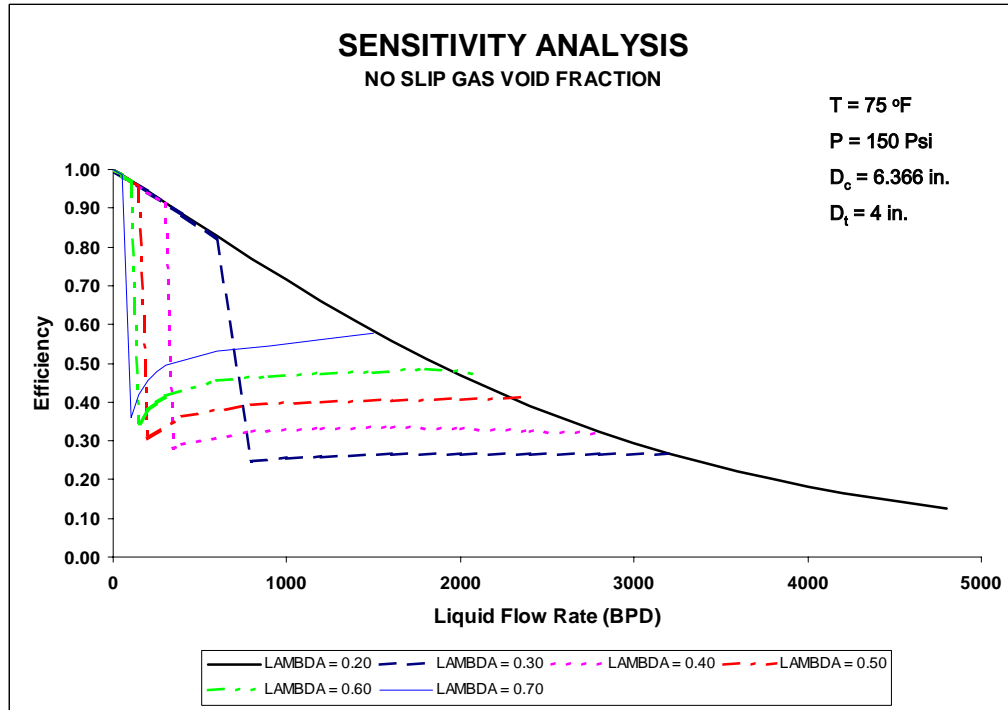


Figure 7.37 – No-slip Gas Void Fraction Effect - Two-Phase Flow Model.

According to Fig. 7.37, for a certain value of the no-slip gas void fraction coming from the annulus and liquid flow rate, the natural separation efficiency E can be predicted.

As a result, those predicted values could also be used to predict λ_g^p , given by Eq. 7.15. If this procedure is followed for all the values of the liquid flow rates, assuming a constant value of λ_g^i , one graph, as shown in Fig. 7.38, can be obtained.

Results obtained by either Eq. 7.15 or Fig. 7.38 can be used to design any artificial lift system, under gassy environment conditions.

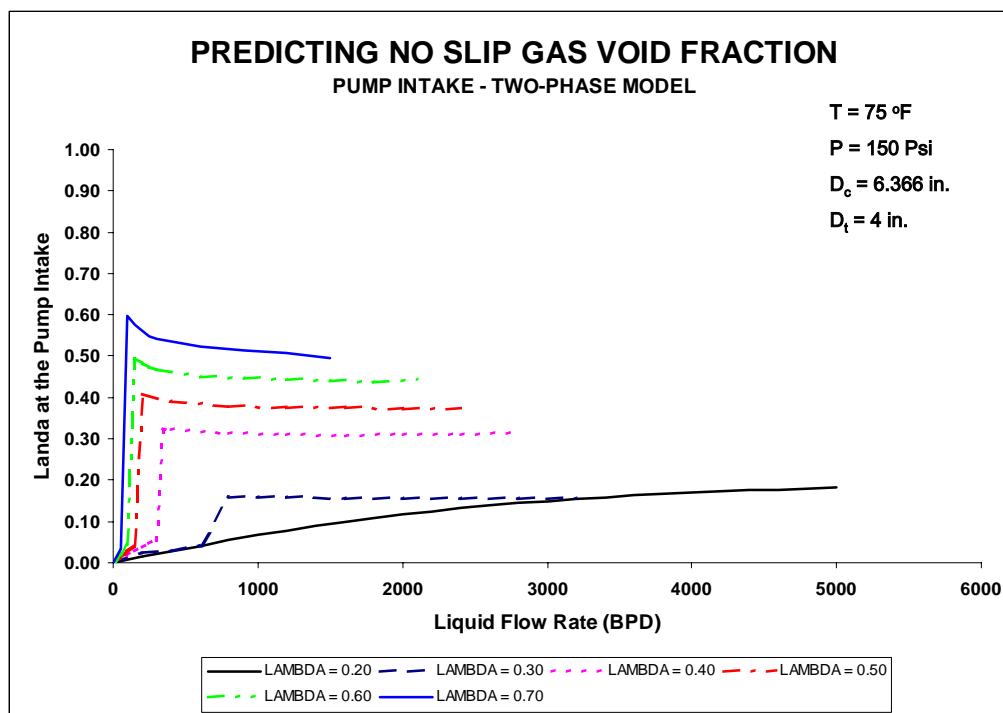


Figure 7.38 – No-slip Gas Void Fraction at the Pump Intake.

CHAPTER VIII

CONCLUSIONS AND RECOMMENDATIONS

Conclusions

1. The slip velocity in the radial direction and the flow pattern regimes have a strong effect on the prediction of natural separation efficiency.
2. Under a slug/churn flow regime, the increment of pressure decreases the separation efficiency. On the other hand, the efficiency decreases with decreasing gas-liquid ratio.
3. Predictions obtained from the two-phase flow model show that under conditions of slug/churn flow the separation efficiency is not affected by changes in the casing size. In addition, a sensibility analysis on viscosity showed that the efficiency would decrease with the increase of liquid viscosity.

Recommendations

1. Gather more experimental data for low gas and liquid flow rates as well as for different liquid viscosities. New data will allow improvement of the correlations for interface characteristic length prediction.
2. Apply the methodology used for the two-phase flow model to the following conditions: 1) Considering the pump intake below the perforations; 2) The

presence of a static separator; 3) Changes of geometry around the pump intake; 4)

Assuming different degree of eccentricity of the pump in the annulus; 5)

Assuming different angles of inclination of the pump.

3. Assume the existence of rotational flow for the gas stream function.
4. Modify the boundary condition at wall for the gas phase. In the proposed approach, the radial gas velocity at walls is set to zero. Instead of this boundary condition, the actual gas radial velocity can be obtained from the radial slip equation applied at the wall.

NOMENCLATURE

a	=	Acceleration
a_i	=	Interfacial area concentration
A	=	Cross sectional area
A_d	=	Projected area of a typical bubble/particle
B_d	=	Volume of a typical bubble/particle
C	=	Constant
C_d	=	Drag coefficient
d_{crit}	=	Critical diameter of gas bubbles to avoid agglomeration
d_{max}	=	Maximum stable diameter of the dispersed phase
D_c	=	Inside casing diameter
D_d^α	=	Diffusivity of phases or drift coefficient based on gas void fraction
D_{ep}	=	Equi-periphery diameter
D_h	=	Hydraulic diameter
D_p	=	Outside pump diameter
D_t	=	Outside tubing diameter
e	=	Degree of eccentricity
E	=	Natural separation efficiency
$E^{Alhanati}$	=	Natural separation efficiency by Alhanati's model

$E^{Serrano}$	=	Natural separation efficiency by Serrano's model
E_v	=	Volumetric efficiency
f	=	Fanning friction factor
$^{\circ}F$	=	Degree Fahrenheit
F_b	=	Buoyancy force
F_{ca}	=	Friction geometric parameter for a concentric annulus
F_d	=	Drag force
F_{ca}	=	Friction geometric parameter for an eccentric annulus
F_g	=	Gravity force
F_p	=	Force due to drop pressure, friction geometric parameter
g	=	Acceleration due to gravity
h_p	=	Port high
k	=	Annulus pipe diameter ratio, k parameter
ℓ_i	=	Interface characteristic length
m	=	Mass
M	=	Dimensionless parameter
\vec{M}_k	=	Interfacial drag force
n	=	Effect due to presence of others bubbles (flow regime)
N	=	Particle density number
N_{EO}	=	Eotvos Number
N_{we}	=	Weber Group

P	=	Pressure
$\langle P_{Inlet} \rangle$	=	Average pressure
q_g^i	=	Total gas flow rate coming from the annulus
q_g^v	=	Gas flow rate vented
q_g^p	=	Gas flow rate goes inside the pump
q_l^i	=	Total liquid flow rate coming from the annulus
q_l^p	=	Liquid flow rate goes inside the pump
R	=	Radius of a particle
Re	=	Reynolds number
r	=	Radius
r_c	=	Inside casing radius
r_d	=	Average drag radius of a typical bubble/particle
r_p	=	Outside pump radius
r_s	=	Separation circle
r_{sm}	=	Sauter mean radius
S_d	=	Surface area
V_g	=	Actual gas velocity
V_{dj}	=	Drift velocity
V_{km}	=	Diffusion velocity
V_l	=	Actual liquid velocity
V_M	=	Mixture velocity

V_p	=	Total volumetric capacity of the pump
V_s	=	Slip velocity
V_{sg}	=	Superficial gas velocity
V_{sg}^p	=	Superficial gas velocity goes into the pump
V_{sgz}^i	=	Superficial gas velocity in the vertical direction
$\langle V_{sgz}^i \rangle$	=	Average superficial gas velocity in the vertical direction
V_{sl}	=	Superficial liquid velocity
V_{slz}^i	=	Superficial liquid velocity in the vertical direction
$\langle V_{slz}^i \rangle$	=	Average superficial liquid velocity in the vertical direction
V_{vi}	=	Viscosity Group
V_{Tb}	=	Taylor bubble rise velocity
V_∞	=	Terminal velocity of the gas bubbles
v_t	=	Turbulent diffusivity

Greek Letters

Ω	=	Vorticity
φ	=	Stream function, function
β	=	Geometric angle, dimensionless factor
ϕ	=	Function
η	=	Ordinate in complex plane
μ	=	Viscosity

∇	=	“Nabla” operator
α	=	Void fraction
$\langle \alpha \rangle$	=	Average Void fraction
ρ	=	Density
σ	=	Surface tension
τ	=	Stress tensor
ε	=	Error tolerances, energy dissipation per unit mass

Subscripts

a	=	Annulus
c	=	Continuous phase
d	=	Dispersed phase
g	=	Gas
i	=	Inner, label of grid in x direction
j	=	Label of grid in y direction
k	=	Phase
l	=	Liquid
m	=	Mixture
o	=	Outer
p	=	Pump, port
r	=	Radial
v	=	Vented
z	=	Axial

Superscripts

i = Inlet

p = Pump

Abbreviations

BPD = Standard barrels per day

Bbl = Barrels

CFD = Computational fluid dynamics

ESP = Electrical submersible pump

GLR = Gas-liquid ratio

I.D. = Inside diameter

LHS = Left hand side

O.D. = Outside diameter

RHS = Right hand side

SCFD = Standard cubic feet per day

TUALP = Tulsa University Artificial Lift Projects

REFERENCES

1. Alhanati, F .J. S.: “Bottomhole Gas Separation Efficiency in Electrical Submersible Pump Installation”, Dissertation. The University of Tulsa, 1993.
2. Bird, R., Stewart, W. E., and Lightfoot, E. N.: Transport Phenomena, John & Sons, 1960.
3. Brodkey, R. S.: “The Phenomena of Fluid Motions”, Addison-Wesley Press (1967).
4. Barnea, D., Shoham, O. and Taitel, Y.: “Flow Pattern Transition for Vertical Downward Two Phase Flow”, Chem. Eng. Sci., 37, No. 5, pp. 741-744 (1981).
5. Barnea, D., Shoham, O., Taitel, Y. and Duckler, A. E.: “Gas Liquid Flow in Inclined Tubes: Flow Pattern Transition for Upward Flow”, Chem. Eng. Sci., 40, pp. 131-136 (1985).
6. Barnea, D., “A Unified Model for Predicting Flow-Pattern Transition for the whole Range of Pipe Inclinations”, Intl. J. Multiphase Flow (1987) 13,1.
7. Calderbank, P. H.: “Physical Rate Processes in Industrial Fermentation”. Part I: The Interfacial Area in Gas-Liquid Contacting with Mechanical Agitation. Trans. Instn. Chem. Engrs, Vol. 36, 1958.
8. Cambell, J. H. and Brimhall, R. M.: “An Engineering Approach to Gas Anchor Design”, SPE 18826, Presented at the SPE Production Operations Symposium held in Oklahoma City, Oklahoma, March 13-14, 1989, pp.71-80.

9. Caetano, E. F., Shoham, O. and Brill, J. P.: "Upward Vertical Two-Phase Flow Through an Annulus-Part I: Single-Phase Friction Factor, Taylor Bubble Rise Velocity, and Flow Pattern Prediction", *Journal of Energy Resources Technology*, Vol. 114. (March 1992).
10. Datta, R. L., Napier, D. H. and Newitt, D.M.: *Trans. Inst. Chem. Engrs. (London)*, 28, 14 (1950).
11. Drew, D. A. and Lahey, R. T. Jr.: "Application of General Constitutive Principles to the Derivation of Multidimensional Two-Phase Flow Equations", *Int. J. Multiphase Flow*, Vol. 5, pp. 243-264, 1979.
12. Gunn, R., and Kinzer, G. D., *J. Meteorol.*, 6, 243 (1949).
13. Gun, D. J., and Darling, C. W. W., 1963, "Fluid Flow and Energy Losses in Non-Circular Conduits", *Transactions of the Institution of Chemical Engineers*, Vol. 41, pp. 163-173.
14. Ghauri, W. K.: "Production Technology Experience in a Large Carbonate Water-Flood, Denver Unit, Wasson San Andres Field, West Texas", paper SPE 8406 presented at the 1979 SPE Annual Technical Conference and Exhibition, Las Vegas, NV, Sep. 23-26.
15. Gomez, L. E.: "Dispersed Two-Phase Swirling Flow Characterization For Predicting Gas Carry-Under In Gas-Liquid Cylindrical Cyclone Compact Separators", Ph.D. Dissertation, The University of Tulsa, Tulsa 2001.
16. Hu, Shengen, and Kintner, R. C., *A.I.Ch.E. Journal*, 1, 42 (1955).
17. Hinze, J. O.: "Fundamentals of the Hydrodynamic Mechanism of Splitting in Dispersion Processes". *AIChE Journal*, Vol. 1, No. 3, pp. 289-295, 1955.

18. Harmathy, T. Z., Velocity of Large Drops and Bubbles in Media of Infinite or Restricted Extent, AIChE, 6, 281(1960).
19. Hasan, A. R. and Kabir, C. S.: "Predicting Multiphase Flow Behavior in a Deviated Well", SPE Prod. Eng. 3, pp. 472-482. (1988).
20. Hasan, A. R. and Kabir, C. S.: "Two-Phase Flow in Vertical and Inclined Annuli", Int. J. Multiphase Flow Vol 18, No. 2, pp. 279-293. (1992).
21. Harun, A. F., Prado, M. G., Serrano, J. C. and Doty, D. R.: "A Simple Model to Predict Natural Gas Separation Efficiency in Pumped Wells", paper SPE 63045 presented at the 2000 SPE Annual Technical Conference and Exhibition held in Dallas, Texas, 1-4 October 2000.
22. Ihme, F., Schmidt-Traud, H., Brauer, H., 1972, Chemie-Ingd Tech., Vol. 44, No. 5 pg. 306.
23. Ishii, M.: "Thermo Fluid Dynamic Theory of Two Phase Flow", Eyrolles, Paris, 1975.
24. Ishii, M. and Zuber, N.: "Drag Coefficient and Relative Velocity in Bubbly, Droplet or Particulate Fluids", AIChE Journal (September 1979) 25, No. 5, 843-855.
25. Johnson, A. I., and Braida, L., Can. J. Chem. Eng., 35, 165 (1957).
26. Klee, A. J., and Treybal, R. E., A.I.Ch.E. Journal, 2, 444 (1956).
27. Lea, J. F. and Bearden, J. L.: "Effect of Gaseous Fluids on Submersible Pump Performance", paper SPE 9218 presented at the 1980 SPE Annual Technical Conference and Exhibition, Dallas, TX, Sep. 21-24.

28. Lackner, G.: "The Effect of Viscosity on Downhole Gas Separation in a Rotary Gas Separator", Dissertation. The University of Tulsa, 1997.
29. Liu, B.: "Modeling Downhole Natural Separation Using Bubble Tracking Method", Dissertation. The University of Tulsa, 2001.
30. Nicklin, D. J., Wilkes, M. A. and Davidson, J. F.: "Two-Phase Flow in Vertical Tubes", Transactions of the Institution of Chemical Engineers (February 1962) 40, 61-68.
31. Migagi, O., Phil. Mag. 1925 50 112.
32. Mei, R., Klausner, J. F. and Lawrence, C. J.,: "A Note on the History Force on a Spherical Bubble at Finite Reynolds Number", Phys. Fluids, Vol. 6, No. 1, January 1994, pg. 418-420.
33. McCoy, J. N., Podio, A. L. Woods, M. D. and Nygaard, H. S.: "Field and Laboratory Testing of a Decentralized Continuous-Flow Gas Anchor", Presented at the 46th Annual Technical Meeting of the Petroleum Society of CIM, May 14-17, 1995.
34. Marquez, R. and Prado, M: "Consolidation of the experimental data for natural separation efficiency". Technical Report. The University of Tulsa, Tulsa, Ok. (2001).
35. Marquez, R. and Prado, M: "Classification of the experimental natural separation data according to flow pattern regime". Technical Report. The University of Tulsa, Tulsa, Ok. (2002).
36. Marquez, R., Barrios, L., Beltur, R. and Prado, M: "TUALP fluid properties standards". Technical Report. The University of Tulsa, Tulsa, Ok. (2002).

37. Marquez, R. and Prado, M: "A comparative analysis of previous simplified models for natural separation efficiency". Technical Report. The University of Tulsa, Tulsa, Ok. (2002).
38. Marquez, R. A. and Prado, M. G., "A new correlation for predicting natural separation efficiency". Southwestern Petroleum Short Course. April 16-17, 2003. Lubbock Memorial Civic Center, Lubbock, Texas.
39. Marquez, R. A. and Prado, M. G., "A new robust model for natural separation efficiency", SPE Production and Operation Symposium held in Oklahoma City, Ok. 23-25 March 2003.
40. Rosenberg, B., The David W. Taylor Model Basin Report 727, (1950).
41. Robles, J.: "Characterization of Static Downhole Gas Separator", Dissertation. The University of Texas at Austin, 1996.
42. Schiller, L. and Naumann (1933), VDI Zeits., 77, pg. 318.
43. Sadatomi, M., Sato, Y., and Saruwatari, S., 1982, "Two-Phase Flow in Vertical Noncircular Channels", International of Journal of Multiphase Flow, Vol. 8, pp. 641-655.
44. Sambangi, S. R.: "Gas Separation Efficiency in Electrical Submersible Pump Installation with Rotary Gas Separator", Dissertation. The University of Tulsa, 1994.
45. Serrano, J. C.: "Natural Separation Efficiency in Electric Submersible Pump Systems", Dissertation. The University of Tulsa, 1999.

46. Taitel, Y., Barnea, D. and Dukler, A. E., Modeling Flow Pattern Transitions for Steady Upward Gas-Liquid Flow in Vertical Tubes. *AIChE Journal*, 26 No. 3, pp. 345-354 (1980).
47. Wallis, G. B.: "One-dimensional Two-Phase Flow", McGraw-Hill, New York, NY, 1969.
48. Wallis, G. B.: "The Terminal Speed of Single Drops or Bubbles in an Infinite Medium", *International Journal of Multiphase Flow* (1974) 1, 491-511.
49. Zuber, N.: "On the Dispersed Two-Phase Flow in the Laminar Flow Regime", *Chem. Eng. Sci.*, 19, 897 (1964).

APPENDIX A

Bubbles Terminal Rise Velocity

According to Harmathy (1960) under turbulent flow conditions, the drag coefficient is strongly affected by the dispersed particle shape.

Generally, the drag coefficient, C_d , is defined as:

$$C_d = -\frac{F_d}{\frac{1}{2} \rho_c V_\infty^2 A_d}, \quad (\text{A.1})$$

where F_d , ρ_c and V_∞ represent the drag force, the density of the continuous phase and the terminal velocity of the dispersed phase, respectively.

The area of a particle projected onto a horizontal plane is A_d . The equivalent radius, r_d , is defined as the radius of a spherical particle with the same volume as the distorted particle, as shown in Fig. A.1.

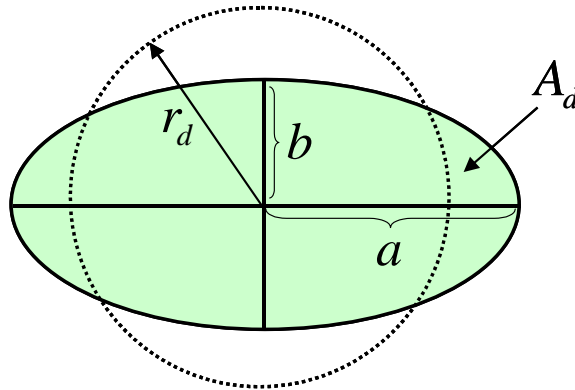


Figure A.1 - Distorted bubble Shape.

The equivalent radius of the particle r_d can be used to define a new drag coefficient, called C_d^* , given by:

$$C_d^* = -\frac{F_d}{\frac{1}{2} \rho_l V_\infty^2 \pi r_d^2}. \quad (\text{A.2})$$

The shape factor, β , is defined as:

$$\beta^2 = \frac{A_d}{\pi r_d^2}. \quad (\text{A.3})$$

The combination of Eqs. A.1 - A.3 yields the following relationship between the two drag coefficients:

$$C_d^* = \beta^2 C_d. \quad (\text{A.4})$$

Now consider a single gas bubble flowing vertically inside an infinite liquid medium, as shown in Fig. A.2.

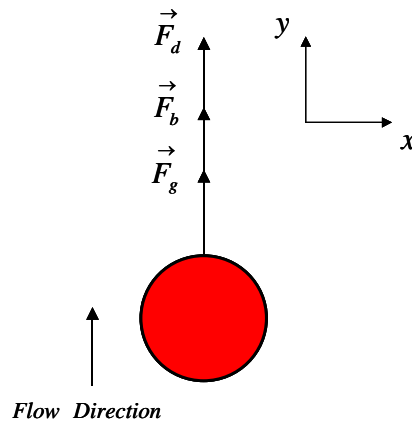


Figure A.2 - Force Balance Analysis - Single Bubble/Particle.

According to Fig. A.2, there are three forces acting on a gas bubble in the vertical direction. These forces are a drag force, \vec{F}_d , which occurs in the direction of the slip due

to pressure and shear forces on the surface of the bubble; a fluid force called the buoyancy force, \vec{F}_b ; and a force due to gravity called the gravity force, \vec{F}_g .

Under steady state conditions, a force balance in the vertical direction results in the following set of equations:

$$\vec{F}_d + \vec{F}_g + \vec{F}_b = 0, \quad (\text{A.5})$$

$$F_d = -\frac{1}{2} \rho_l V_\infty^2 A_d C_{d\infty}^*, \quad (\text{A.6})$$

$$F_g = -B_d \rho_g |g|, \quad (\text{A.7})$$

$$F_b = B_d \rho_l |g|, \quad (\text{A.8})$$

where B_d represents the bubble volume and is defined as:

$$B_b = \frac{4}{3} \pi r_d^3. \quad (\text{A.9})$$

Therefore, the combination of Eqs. A.5 - A.9 yields an expression for the terminal velocity of a particle in an infinite medium, V_∞ . This equation is given by:

$$V_\infty = \sqrt{\frac{8}{3} \frac{1}{C_\infty^*}} \sqrt{\frac{r_d (\rho_l - \rho_g) |g|}{\rho_l}}. \quad (\text{A.10})$$

Using the shape factor given by Eq. A.4, Eq. A.10 can also be rewritten as:

$$V_\infty = \frac{1}{\beta} \sqrt{\frac{8}{3} \frac{1}{C_\infty^*}} \sqrt{\frac{r_d (\rho_l - \rho_g) |g|}{\rho_l}}. \quad (\text{A.11})$$

For spherical particles, the shape factor is equal to one, and therefore, the terminal velocity of a spherical gas bubble in an infinite medium $V_{s\infty}$ can be given, from Eq. A.11, by the following equation:

$$V_{s\infty} = \sqrt{\frac{8}{3 C_{s\infty}}} \sqrt{\frac{r_d (\rho_l - \rho_g) |g|}{\rho_l}}. \quad (\text{A.12})$$

Since under turbulent flow conditions, the drag coefficient depends only on the particle shapes, a relationship between the terminal velocity of the distorted particle and the terminal velocity of a spherical particle can be obtained using Eqs. A.10 and A.12 as:

$$\frac{V_{\infty}}{V_{s\infty}} = \sqrt{\frac{C_{s\infty}}{C_{\infty}^*}} = \phi(\text{shape}). \quad (\text{A.13})$$

Hinze (1955) proved that the shape of the a fluid particle depends only on a dimensionless group, called the Eotvos number N_{Eo} , and which is given by:

$$N_{Eo} = \frac{4 r_d^2 (\rho_l - \rho_g) |g|}{\sigma}. \quad (\text{A.14})$$

Also, Harmathy studied the relationship of the $C_{s\infty} / C_{\infty}^*$ ratio with the Eotvos number based on available experimental data of Gunn and Kinzer (1949), Datta et al. (1950), Rosenber (1950), Hu and Kintner (1955), Klee and Treybal (1956), and Johnson and Braida (1957). This relationship is shown in Fig. A.3.

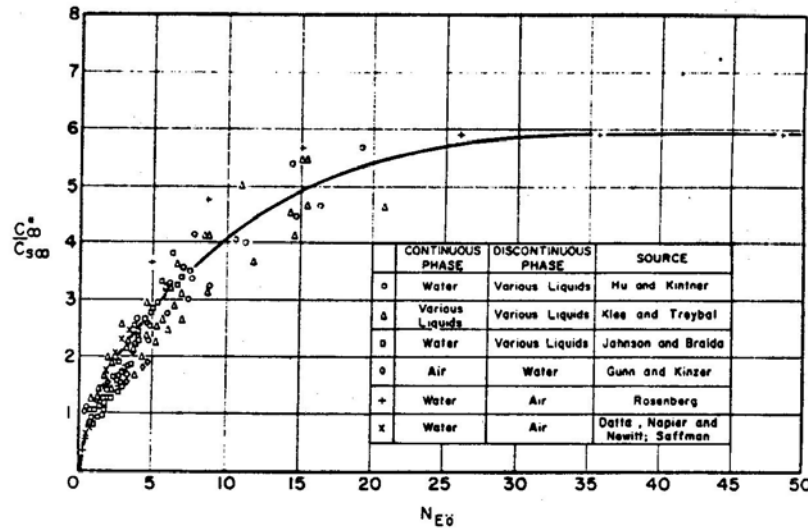


Figure A.3 - Variation of the Drag Coefficient with the Eotvos Number.

For the condition, $N_{Eo} < 13$, which roughly corresponds to the region of moderately distorted ellipsoidal shapes, the best approximation for the drag coefficient ratio is given by:

$$\frac{C_{\infty}^*}{C_{s\infty}} = 1.29 N_{Eo}^{1/2}. \quad (\text{A.15})$$

Combining Eqs. A.14 and A.15, the drag coefficient ratio would finally be given by:

$$\frac{C_{\infty}^*}{C_{s\infty}} = 2.58 \sqrt{\frac{r_d^2 (\rho_l - \rho_g) |g|}{\sigma}}. \quad (\text{A.16})$$

Assuming an infinite medium where $C_{s\infty} = 0.44$, the combination of Eqs. A.10 and A.16 yield the following equation for the terminal velocity of particles in an infinite medium, independent of shape and which was proposed by Harmathy, as:

$$V_{\infty} = 1.53 \left[\frac{\sigma (\rho_l - \rho_g) |g|}{\rho_l^2} \right]^{1/4}. \quad (\text{A.17})$$

APPENDIX B

Kinematics Constitutive Equation

According to Ishii (1975), the diffusion velocity for any phase k , V_{km} , i.e. the velocity with respect to the mixture mass center, is defined as:

$$V_{km} = V_k - V_M, \quad (\text{B.1})$$

where the mixture velocity, V_M , is given by:

$$V_M = \frac{\alpha_g \rho_g V_g + (1 - \alpha_g) \rho_l V_l}{\rho_m}, \quad (\text{B.2})$$

and where α_g and ρ_m represent the gas void fraction and the mixture density, respectively. The mixture density is given by the following equation:

$$\rho_m = \alpha_g \rho_g + (1 - \alpha_g) \rho_l. \quad (\text{B.3})$$

If both gas and liquid phases are considered, Eq. B.1 can be written separately for each phase as:

$$V_{gm} = V_g - V_M, \quad (\text{B.4})$$

$$V_{lm} = V_l - V_M. \quad (\text{B.5})$$

Substituting Eq. B.2 into Eqs. B.4 and B.5, the following set of equations can be obtained:

$$V_{gm} = V_g - \frac{\alpha_g \rho_g V_g + (1 - \alpha_l) \rho_l V_l}{\rho_m}, \quad (\text{B.6})$$

$$V_{lm} = V_l - \frac{\alpha_g \rho_g V_g + (1 - \alpha_l) \rho_l V_l}{\rho_m}. \quad (\text{B.7})$$

Rearranging the system given by Eqs. B.6 and B.7, the following set is obtained:

$$\rho_m V_{gm} = \rho_m V_g - (\alpha_g \rho_g V_g + (1 - \alpha_l) \rho_l V_l), \quad (\text{B.8})$$

$$\rho_m V_{lm} = \rho_m V_l - (\alpha_g \rho_g V_g + (1 - \alpha_l) \rho_l V_l). \quad (\text{B.9})$$

Substituting Eq. B.3 into the right hand side of the system given by Eqs. B.8 and B.9, and simplifying, the following new set can be written as:

$$\rho_m V_{gm} = (1 - \alpha_l) \rho_l (V_g - V_l), \quad (\text{B.10})$$

$$\rho_m V_{lm} = -\alpha_g \rho_g (V_g - V_l). \quad (\text{B.11})$$

The slip velocity definition is given by:

$$V_s = V_g - V_l. \quad (\text{B.12})$$

Substituting Eq. B.12 into Eqs. B.10 and B.11 the last equations can also be expressed as:

$$\rho_m V_{gm} = (1 - \alpha_l) \rho_l V_s, \quad (\text{B.13})$$

$$\rho_m V_{lm} = -\alpha_g \rho_g V_s. \quad (\text{B.14})$$

Eliminating ρ_m and V_s from Eqs. B.13 and B.14, the following kinematics constitutive equation results:

$$\alpha_g \rho_g V_{gm} + (1 - \alpha_g) \rho_l V_{lm} = 0. \quad (\text{B.15})$$

Generally, Eq. B.15 is written as:

$$V_{gm} = -\frac{(1 - \alpha_g) \rho_l}{\alpha_g \rho_g} V_{lm} = -\frac{(1 - \alpha_g) \rho_l}{\rho_m} V_s = \frac{\rho_l}{\rho_m} V_{gj} = -\frac{(1 - \alpha_g) \rho_l}{\alpha_g \rho_m} V_{lj}. \quad (\text{B.16})$$

APPENDIX C

Slip Velocity Analysis

The analysis of the slip velocity is based on Ishii and Zuber's work, proposed in 1979, for Cartesian coordinates. Using the same methodology, but in cylindrical coordinates, mass and momentum balance equations can be used to obtain a useful relationship for slip velocity in both the radial and vertical direction.

Basic Equations

The following assumptions are adopted:

1. Steady state
2. Negligible surface tension effects
3. No mass transfer between phases
4. Constant fluid properties
5. Axis-symmetric flow
6. Infinite medium (viscous and friction effects are negligible)
7. The gas phase ($k = g$) is dispersed in a continuous liquid phase ($k = l$)

Therefore, the mass and momentum balance equations for any phase k in cylindrical coordinates are given by:

Mass Balance Equation:

$$\frac{1}{r} \frac{\partial}{\partial r} (\alpha_k \rho_k r V_{kr}) + \frac{\partial}{\partial z} (\alpha_k \rho_k V_{kz}) = 0, \quad (\text{C.1})$$

Momentum Balance Equation in the Radial Direction:

$$\alpha_k \rho_k \left(V_{kr} \frac{\partial V_{kr}}{\partial r} + V_{kz} \frac{\partial V_{kr}}{\partial z} \right) + \alpha_k \frac{\partial P}{\partial r} - \alpha_k \rho_k g_r + \delta_k M_{kr} = 0, \quad (\text{C.2})$$

Momentum Balance Equation in the Vertical Direction:

$$\alpha_k \rho_k \left(V_{kr} \frac{\partial V_{kz}}{\partial r} + V_{kz} \frac{\partial V_{kz}}{\partial z} \right) + \alpha_k \frac{\partial P}{\partial z} - \alpha_k \rho_k g_z + \delta_k M_{kz} = 0, \quad (\text{C.3})$$

where V_{kr} and V_{kz} represent the velocity of a phase k in the radial and vertical direction, respectively. P , M_k and ρ_k are pressure, interfacial momentum transfer term and density, respectively, and g_r and g_z represent the gravitational acceleration terms in the radial and vertical direction, respectively. The phase volumetric fraction is α_k . δ_k is a variable introduced to account for the interface momentum jump condition and is 1 for the gas phase and -1 for the liquid phase.

Slip Velocity in the Vertical Direction

Neglecting the convective terms in the vertical direction, the momentum balance equation, given by Eq. C.3, reduces to a gravity dominated one-dimensional flow. For the gas and liquid phases, the momentum equations can be written as:

$$0 = \alpha_g \frac{dP}{dz} - \alpha_g \rho_g g_z + M_{gz}, \quad (\text{C.4})$$

$$0 = \alpha_l \frac{dP}{dz} - \alpha_l \rho_l g_z - M_{gz}. \quad (\text{C.5})$$

Adding both momentum balance equations, Eqs. C.4 and C.5, the following equation for the pressure gradient can be obtained as:

$$\frac{dP}{dz} = (\alpha_g \rho_g + \alpha_l \rho_l) g_z. \quad (C.6)$$

According to the coordinate system assumed in this work, the gravitational acceleration term in the vertical direction is given by:

$$g_z = -|g|. \quad (C.7)$$

Substituting Eq. C.7 into the Eq. C.6, the pressure gradient in the vertical direction is defined as:

$$\frac{dP}{dz} = -(\alpha_g \rho_g + \alpha_l \rho_l) |g|. \quad (C.8)$$

Defining the mixture density ρ_m as:

$$\rho_m = \alpha_g \rho_g + \alpha_l \rho_l, \quad (C.9)$$

the pressure gradient, given by Eq. C.8, can be rewritten as:

$$\frac{dP}{dz} = -\rho_m |g|. \quad (C.10)$$

From Eqs. C.4 and C.7, the interfacial drag force term for the gas phase M_{gz} is given by:

$$M_{gz} = -\alpha_g \frac{dP}{dz} - \alpha_g \rho_g |g|. \quad (C.11)$$

Substituting Eq. C.10 into Eq. C.11, the interfacial drag force for the gas phase M_{gz} can be defined as:

$$M_{gz} = \alpha_g (1 - \alpha_g) (\rho_l - \rho_g) |g|. \quad (C.12)$$

By neglecting the lift force due to rotations of particles and the diffusion force due to the concentration gradient, the combined interfacial drag forces M_d acting on the dispersed phase may be modeled by a simple form proposed by Zuber (1964) as:

$$\vec{M}_d = -\frac{\alpha_d \vec{F}_d}{B_d}, \quad (C.13)$$

where B_d represents the volume of a typical particle and the subscript d the dispersed phase, which is given, in this case, by the gas phase. The axial drag force between the phases, F_d , for a single bubble can be determined from the following equation:

$$F_d = -\frac{1}{2} C_d \rho_c V_{sz} |\vec{V}_s| A_d, \quad (C.14)$$

where A_d represents the projected area of a typical particle, V_{sz} is the slip velocity in the vertical direction, and the subscript c is the continuous phase, which is given by the liquid phase. $|\vec{V}_s|$, representing the resultant slip velocity. Substituting Eq. C.14 into C.13, the interfacial drag force for the gas phase M_g is defined as:

$$M_{gz} = \frac{\alpha_g \left(\frac{1}{2} C_d \rho_l V_{sz} |\vec{V}_s| A_d \right)}{B_d}. \quad (C.15)$$

Assuming spherical bubbles, the area and volume of spheres, A_d and B_d respectively, are given by:

$$A_d = \pi r_d^2, \quad (C.16)$$

$$B_d = \frac{4}{3} \pi r_d^3. \quad (\text{C.17})$$

The combination of Eqs. C.15 - C.17 defines M_{gz} as:

$$M_{gz} = \frac{3 \alpha_g C_d \rho_l V_{sz} |\vec{V}_s|}{8 r_d}. \quad (\text{C.18})$$

Finally, the combination of Eqs. C.12 and C.18 allows the definition of one equation for the slip velocity in the vertical direction. That equation is given by:

$$V_{sz} |\vec{V}_s| = \frac{8 r_d (1 - \alpha_g) (\rho_l - \rho_g) |g|}{3 C_d \rho_l}. \quad (\text{C.19})$$

For the case of pure vertical flow, $|\vec{V}_s|$ can be considered equal to V_{sz} . On the other hand and according to Ishii and Zuber (1979), for a system with a single particle in an infinite medium, V_{sz} can be considered equal to the terminal velocity of a bubble/particle, $V_{\infty z}$. As a consequence, Eq. C.19 is given as:

$$V_{\infty z}^2 = \frac{8 r_d (1 - \alpha_g) (\rho_l - \rho_g) |g|}{3 C_d \rho_l}. \quad (\text{C.20})$$

The drag coefficient for a single bubble/particle, $C_{d\infty}$, is given by:

$$C_{d\infty} = \frac{C_d}{(1 - \alpha_g)}. \quad (\text{C.21})$$

Therefore, Eq. C.20 can be, finally, given by:

$$V_{\infty z}^2 = \frac{8 r_d (\rho_l - \rho_g) |g|}{3 C_{d\infty} \rho_l}. \quad (\text{C.22})$$

According to Harmathy (1960), the drag coefficient under a slug/churn flow regime, $C_{d\infty}$, can be expressed as:

$$C_{d\infty} = \frac{4}{3} r_d \sqrt{\frac{(\rho_l - \rho_g) |g|}{\sigma}}. \quad (\text{C.23})$$

Therefore, the combination of Eqs. C.22 and C.23 defines the following equation for $V_{\infty z}$ by:

$$V_{\infty z} = \sqrt{2} \left[\frac{\sigma (\rho_l - \rho_g) |g|}{\rho_l^2} \right]^{1/4}. \quad (\text{C.24})$$

Ishii (1979) proposed Eq. C.24 for estimating the terminal velocity of gas bubbles in an infinite medium.

Slip Velocity Analysis in the Radial Direction

Neglecting the convective terms in the vertical direction, the momentum balance equation, given by Eq. C.2, reduces to a system dominated basically by the acceleration terms, pressure gradient and interfacial forces. For the gas and liquid phases, the momentum equations can be written as:

$$\alpha_g \rho_g V_{gr} \frac{\partial V_{gr}}{\partial r} = -\alpha_g \frac{\partial P}{\partial r} - M_{gr}, \quad (\text{C.25})$$

$$\alpha_l \rho_l V_{lr} \frac{\partial V_{lr}}{\partial r} = -\alpha_l \frac{\partial P}{\partial r} + M_{gr}. \quad (\text{C.26})$$

Adding Eqs. C.25 and C.26, the following equation for the pressure gradient is obtained.

$$\alpha_g \rho_g V_{gr} \frac{dV_{gr}}{dr} + \alpha_l \rho_l V_{lr} \frac{dV_{lr}}{dr} = -\frac{dP}{dr}. \quad (\text{C.27})$$

Assuming that $\rho_l \gg \rho_g$, the pressure gradient dP/dr may be defined as:

$$\alpha_l \rho_l V_{lr} \frac{dV_{lr}}{dr} = -\frac{dP}{dr}. \quad (\text{C.28})$$

Eq. C.28 shows that the pressure gradient in the radial direction depends on how fast the liquid phase is moving in that direction. Combining Eqs. C.25 and C.28 and assuming $\rho_l \gg \rho_g$, the following equation for the interfacial drag force for the gas phase M_g is defined as:

$$M_{gr} = \alpha_g (1 - \alpha_g) \rho_l V_{lr} \frac{dV_{lr}}{dr}. \quad (\text{C.29})$$

On the other hand, the model proposed by Zuber (1964) can also be used to obtain an equation for the interfacial drag force for the gas phase M_{gr} in the radial direction. According to Zuber, the combined interfacial drag forces M_d is given by:

$$\vec{M}_d = -\frac{\alpha_d \vec{F}_d}{B_d}, \quad (\text{C.30})$$

where F_d can be determined from the following equation:

$$F_d = -\frac{1}{2} C_d \rho_l V_{sr} |\vec{V}_s| A_d, \quad (\text{C.31})$$

and where A_d and B_d are obtained from Eqs. C.16 and C.17, respectively. V_{sr} is the slip velocity in the radial direction. Therefore, the combination of Eqs. C.16, C.17, C.30 and C.31 allow defining the following relationship for estimating the interfacial drag force for the gas phase M_{gr} in the radial direction:

$$M_{gr} = \frac{3}{8} \frac{\alpha_g C_d \rho_l V_{sr} |\vec{V}_s|}{r_d}. \quad (C.32)$$

The combination of Eqs. C.29 and C.32 permits defining the following equation for the slip velocity in the radial direction V_{sr} as:

$$V_{sr} |\vec{V}_s| = \frac{8}{3} \frac{r_d (1 - \alpha_g)}{C_d} \left(V_{lr} \frac{dV_{lr}}{dr} \right). \quad (C.33)$$

Assuming the flow is only in the radial direction, $|\vec{V}_s|$ can be considered equal to V_{sr} . On the other hand and according to Ishii and Zuber (1979), for a system with a single particle in an infinite medium, V_{sr} in an infinite medium can be considered equal to the terminal velocity of a bubble/particle $V_{\infty r}$. As a result, Eq. C.33 is given by:

$$V_{\infty r}^2 = \frac{8}{3} \frac{r_d (1 - \alpha_g)}{C_d} \left(V_{lr} \frac{dV_{lr}}{dr} \right). \quad (C.34)$$

Considering the drag coefficient for a single bubble/particle, given by Eq. C.21, Eq. C.34 can finally be given by:

$$V_{\infty r}^2 = \frac{8}{3} \frac{r_d}{C_{d\infty}} \left(V_{lr} \frac{dV_{lr}}{dr} \right). \quad (C.35)$$

Auxiliary Slip Closure Relationship

Prado (1995) proposed a general slip velocity equation, valid for either spherical or nonspherical particles and in any direction. This equation is defined as:

$$V_s = -8 \frac{r_d}{r_{sm}} \frac{\alpha_g (1 - \alpha_g) (\rho_l - \rho_g)}{a_i C_{d\infty} \rho_l \rho_m |\vec{V}_s|} \nabla P - \frac{D}{\alpha_g (1 - \alpha_g)} \nabla \alpha_g, \quad (C.36)$$

where r_d and r_{sm} represent the drag radius and the Sauter mean radius, respectively. For the case of spherical particles, both radii are considered equal to the particle radius. D represents the drift coefficient. Very few studies have been conducted on this coefficient. However, some authors adopt the drift coefficient D equal to the turbulent diffusivity v_t . Shoukri et al. (1984) proposed the following correlation to estimate v_t .

$$v_t = 0.068 V_M D_h, \quad (C.37)$$

where V_M and D_h represent the mixture velocity and the hydraulic diameter.

Eq. C.36 also shows an important property given by the interfacial area concentration. For dispersed bubble flow, the interfacial area concentration a_i is given by:

$$a_i = 3 \frac{\alpha_g}{r_d}. \quad (C.38)$$

For dispersed droplet flow, the interfacial area concentration a_i is given by:

$$a_i = 3 \frac{(1 - \alpha_g)}{r_d}. \quad (C.39)$$

In this work it is assumed that the interfacial area concentration, a_i , can be expressed as:

$$a_i = 3 \frac{\alpha_g (1 - \alpha_g)}{r_d}. \quad (C.40)$$

APPENDIX D

Drag Coefficient Models

There is an extensive amount of drag coefficient correlations available in the literature. Five important correlations, developed by Sciller Naumann (1933), Harmathy (1960), Ihme et al. (1972), Ishii and Zuber (1979), and Mei et al. (1994), have been summarized in this Appendix. Stoke flow condition is also included for completeness.

Sciller Naumann (1933)

Valid for undistorted particle regime.

$$C_{d\infty} = \frac{24}{\text{Re}_\infty} \left[1 + 0.15 \text{Re}_\infty^{0.687} \right]. \quad (\text{D.1})$$

Harmathy (1960)

It should be corrected by viscosity effect and is valid for distorted particle regime.

$$C_{d\infty} = \frac{4}{3} r_d \sqrt{\frac{(\rho_l - \rho_g) |g|}{\sigma}}, \quad (\text{D.2})$$

where r_d and σ represent the drag radius and the surface tension, respectively. Gas and liquid densities are given by ρ_g and ρ_l , respectively. g represents the gravitational acceleration terms in the vertical direction.

Ihme et al. (1972)

$$C_{d\infty} = \frac{24}{\text{Re}_\infty} + 5.48 \text{Re}_\infty^{-0.573} + 0.36. \quad (\text{D.3})$$

Ishii and Zuber (1979)

$$C_{d\infty} = \frac{24}{\text{Re}_\infty} \left[1 + 0.1 \text{Re}_\infty^{0.75} \right]. \quad (\text{D.4})$$

Mei et al. (1994)

$$C_{d\infty} = \frac{16}{\text{Re}_\infty} \left\{ 1 + \left[\frac{8}{\text{Re}_\infty} + \frac{1}{2} (1 + 3.315 \text{Re}_\infty^{-0.5}) \right]^{-1} \right\}. \quad (\text{D.5})$$

Stoke's Flow

$$C_{d\infty} = \frac{24}{\text{Re}_\infty}. \quad (\text{D.6})$$

The particle Reynolds number, Re_∞ , which is based on the slip velocity on the particle interface V_s and the continuous-phase molecular viscosity, is defined as:

$$\text{Re}_\infty = \frac{2 r_d |\vec{V}_s| \rho_c}{\mu_c}, \quad (\text{D.7})$$

where ρ_c and μ_c represent the density and viscosity, respectively, for the continuous phase. According to Drew and Lahey (1979), it is not clear whether such models are valid for multidimensional application due to differences between results obtained from the models and available experimental data. Therefore and due to those uncertainties regarding the extension of these relations to local multidimensional two-phase flow situations, a careful selection of the appropriate correlation for $C_{d\infty}$ must be considered.

Fig. D.1 shows the results obtained by using some correlations for drag coefficients, given by Eqs. D.1 and D.3 - D.6, as a function of Reynolds number Re_{∞} .

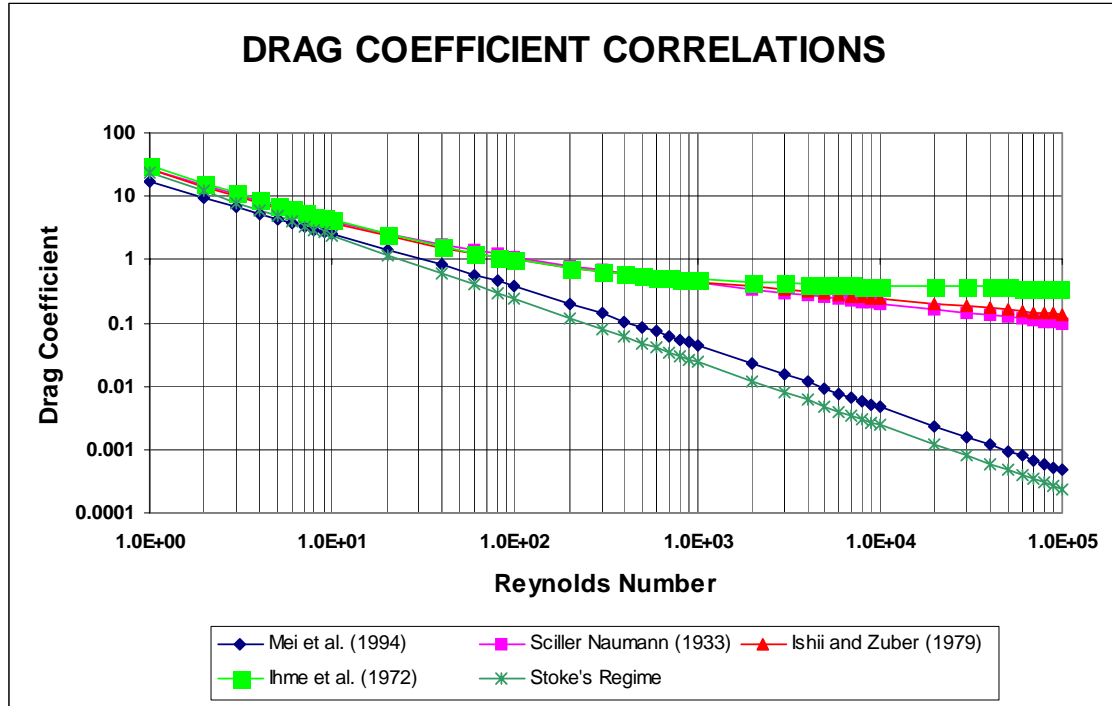


Figure D.1 – Drag Coefficient Correlations.

According to Fig. D.1, all correlations perform very well for low to moderate Reynolds numbers ($Re < 100$). However, for large Reynolds numbers ($Re > 100$), the correlations show large differences. The Ihme et al. (1972) correlation, for example, shows that for Re bigger than 10000, the correlation tends to predict a constant drag coefficient equal to 0.44, approximately. Based on this result, Ihme's correlation was selected for estimating drag coefficient in this work.

APPENDIX E

Two-Phase Flow Model Discretization Scheme

Numerical Grid

The governing equations given by gas and liquid stream functions, pressure and gas void fraction fields will be discretized inside the flow domain, as shown in Fig. E.1.

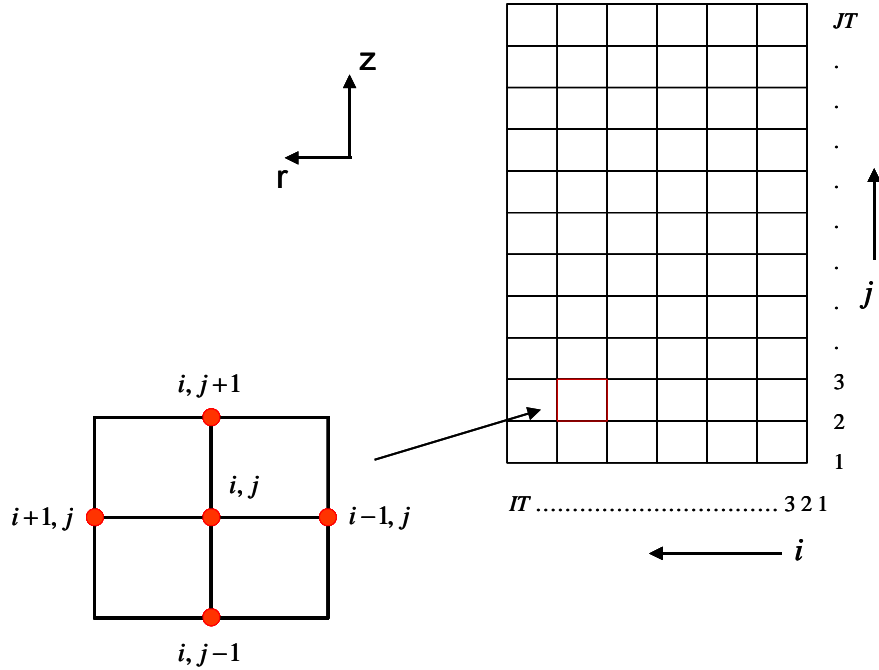


Figure E.1 – Grid of the Annulus Domain.

The primary grid consists of IT and JT points, in the r and z direction, respectively. Also, the primary grid corresponds to the points where the governing equations for φ_g , φ_l , P and α_g are defined, as shown in Fig. E.2.

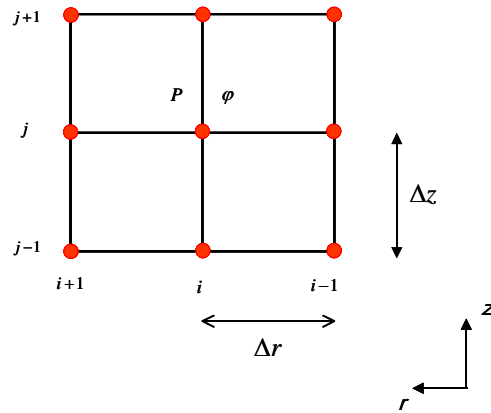


Figure E.2 – Primary Grid.

Fig. E.2 also shows Δr and Δz , which represent the distance between two adjacent nodes in the radial and vertical direction, respectively.

On the other hand, a secondary grid will be used to locate the liquid velocity and the pressure gradient fields in the radial and vertical direction, as shown in Fig. E.3.

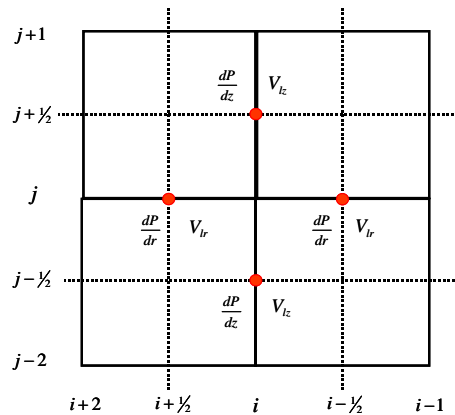


Figure E.3 – Secondary Grid.

Fig. E.4 shows the pump intake, which is located between points $(1, JB)$ and $(1, JA)$. In this figure, r_c and r_p are given by the casing and pump radius, respectively. For any primary node inside the flow domain, the radial distance from the coordinate system shown in Fig. E.4 will be defined as r_i . It is assumed then that: $r_c \geq r_i \geq r_p$.

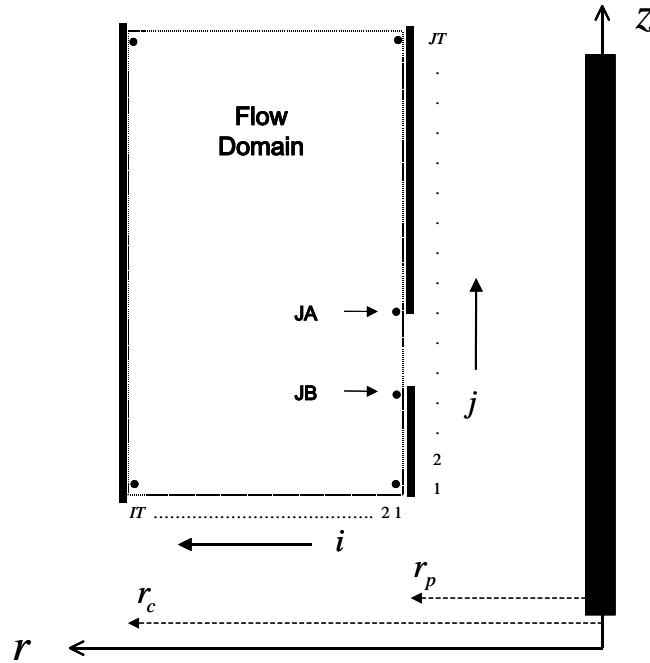


Figure E.4 – Flow domain.

Discretization of Equations - Cylindrical Coordinates System

Gas and Liquid Stream Function

The governing equations for the gas and liquid stream function are given, respectively, by:

$$-\frac{1}{r^2 \alpha_g} \frac{\partial \varphi_g}{\partial r} - \frac{1}{r \alpha_g^2} \left(\frac{\partial \alpha_g}{\partial r} \frac{\partial \varphi_g}{\partial r} + \frac{\partial \alpha_g}{\partial z} \frac{\partial \varphi_g}{\partial z} \right) + \frac{1}{r \alpha_g} \left(\frac{\partial^2 \varphi_g}{\partial r^2} + \frac{\partial^2 \varphi_g}{\partial z^2} \right) = 0, \quad (\text{E.1})$$

$$-\frac{1}{r^2 (1-\alpha_g)} \frac{\partial \varphi_l}{\partial r} + \frac{1}{r (1-\alpha_g)^2} \left(\frac{\partial \alpha_g}{\partial r} \frac{\partial \varphi_l}{\partial r} + \frac{\partial \alpha_g}{\partial z} \frac{\partial \varphi_l}{\partial z} \right) + \frac{1}{r (1-\alpha_g)} \left(\frac{\partial^2 \varphi_l}{\partial r^2} + \frac{\partial^2 \varphi_l}{\partial z^2} \right) = 0. \quad (\text{E.2})$$

Eqs. E.1 and E.2 will be discretized inside the flow domain, according to the index of nodes and the primary grid shown in Figs. E.1 and E.2, respectively.

Core Region:

The numerical solution considers a central difference approximation, using five points into core region. Therefore, the stream functions are given by:

Gas-Phase:

$$\begin{aligned} \frac{\varphi_{g_{i+1,j}} - 2\varphi_{g_{i,j}} + \varphi_{g_{i-1,j}}}{(\Delta r)^2} + \frac{\varphi_{g_{i,j+1}} - 2\varphi_{g_{i,j}} + \varphi_{g_{i,j-1}}}{(\Delta z)^2} = \frac{1}{r_i} \left(\frac{\hat{\varphi}_{g_{i+1,j}} - \hat{\varphi}_{g_{i-1,j}}}{2(\Delta r)} \right) \\ + \frac{1}{\hat{\alpha}_{g_{i,j}}} \left[\left(\frac{\hat{\alpha}_{g_{i+1,j}} - \hat{\alpha}_{g_{i-1,j}}}{2(\Delta r)} \right) \left(\frac{\hat{\varphi}_{g_{i+1,j}} - \hat{\varphi}_{g_{i-1,j}}}{2(\Delta r)} \right) + \left(\frac{\hat{\alpha}_{g_{i,j+1}} - \hat{\alpha}_{g_{i,j-1}}}{2(\Delta z)} \right) \left(\frac{\hat{\varphi}_{g_{i,j+1}} - \hat{\varphi}_{g_{i,j-1}}}{2(\Delta z)} \right) \right] \end{aligned} \quad (E.3)$$

Liquid-Phase:

$$\begin{aligned} \frac{\varphi_{l_{i+1,j}} - 2\varphi_{l_{i,j}} + \varphi_{l_{i-1,j}}}{(\Delta r)^2} + \frac{\varphi_{l_{i,j+1}} - 2\varphi_{l_{i,j}} + \varphi_{l_{i,j-1}}}{(\Delta z)^2} = \frac{1}{r_i} \left(\frac{\hat{\varphi}_{l_{i+1,j}} - \hat{\varphi}_{l_{i-1,j}}}{2(\Delta r)} \right) \\ - \frac{1}{(1 - \hat{\alpha}_{g_{i,j}})} \left[\left(\frac{\hat{\alpha}_{g_{i+1,j}} - \hat{\alpha}_{g_{i-1,j}}}{2(\Delta r)} \right) \left(\frac{\hat{\varphi}_{l_{i+1,j}} - \hat{\varphi}_{l_{i-1,j}}}{2(\Delta r)} \right) + \left(\frac{\hat{\alpha}_{g_{i,j+1}} - \hat{\alpha}_{g_{i,j-1}}}{2(\Delta z)} \right) \left(\frac{\hat{\varphi}_{l_{i,j+1}} - \hat{\varphi}_{l_{i,j-1}}}{2(\Delta z)} \right) \right] \end{aligned} \quad (E.4)$$

Valid for $i = 2, \dots, IT - 1$; $j = 2, \dots, JT - 1$.

Boundary Conditions:

a. Annulus Inlet Boundary

Based on the stream function definitions, the gas and liquid stream function in this boundary are given by the following finite difference approximation:

$$\varphi_{g_{i,j}} - \varphi_{g_{i-1,j}} = -\frac{(\Delta r)(r_i - (\Delta r/2))}{\pi(r_c^2 - r_p^2)} q_g^i, \quad (E.5)$$

$$\varphi_{l_{i,j}} - \varphi_{l_{i-1,j}} = -\frac{(\Delta r)(r_i - (\Delta r/2))}{\pi(r_c^2 - r_p^2)} q_l^i. \quad (E.6)$$

Eqs. E.5 and E.6 are valid for: $i = 2, \dots, IT - 1; j = 1$. There is a special point at $i = IT; j = 1$, where the values of φ for the gas and liquid phases are given, respectively, by:

$$\varphi_{g_{i=IT, j=1}} = -\frac{q_g^i}{2\pi}, \quad (\text{E.7})$$

$$\varphi_{l_{i=IT, j=1}} = -\frac{q_l^i}{2\pi}. \quad (\text{E.8})$$

At the point, $i = 1; j = 1$, the values of φ for the gas and liquid phases are assumed equal to zero.

b. Casing and Upper/Lower Pump Wall Boundaries

It is assumed that the gas and liquid velocities in the radial direction are equal to zero, i.e. the wall is considered as impermeable. Therefore, the stream functions for the gas and liquid phases in this region are given, respectively, by:

$$\varphi_{g_{i,j}} - \varphi_{g_{i,j-1}} = 0, \quad (\text{E.9})$$

$$\varphi_{l_{i,j}} - \varphi_{l_{i,j-1}} = 0. \quad (\text{E.10})$$

Eqs. E.9 and E.10 are valid for $i = IT; j = 2, \dots, JT - 1$, $i = 1; j = 2, \dots, JB$ and $i = 1; j = JA + 1, \dots, JT$, respectively. There is a special point at $i = 1; j = JA$ where the gas and liquid stream function must be defined as:

$$\varphi_{g_{i=1, j=JA}} = \hat{\varphi}_{g_{i=1, j=JT}}, \quad (\text{E.11})$$

$$\varphi_{l_{i=1, j=JA}} = PC \hat{\varphi}_{l_{i=IT, j=1}}, \quad (\text{E.12})$$

and where PC represents the percentage of the total liquid flow rate going into the pump.

c. Annulus Outlet Boundary

Gas-Phase:

In this boundary, fully developed flow is assumed. Therefore, the gas stream function is given by:

$$\varphi_{g_{i,j}} - \varphi_{g_{i,j-1}} = 0, \quad (\text{E.13})$$

valid for node $i = IT ; j = JT$. At the points $i = 2, \dots, IT - 1 ; j = JT$, the gas stream function values are obtained at two adjacent primary grid points by:

$$\varphi_{g_{i,j}} - \varphi_{g_{i-1,j}} = -\frac{(\Delta r)(r_i - (\Delta r / 2))}{4} (\hat{V}_{gz_{i,j}} + \hat{V}_{gz_{i-1,j}}) (\hat{\alpha}_{g_{i,j}} + \hat{\alpha}_{g_{i-1,j}}). \quad (\text{E.14})$$

Liquid-Phase:

At this boundary, fully developed flow is assumed. Therefore, the liquid stream function is given by:

$$\varphi_{l_{i,j}} - \varphi_{l_{i,j-1}} = 0, \quad (\text{E.15})$$

valid for the points $i = 1, \dots, IT ; j = JT$.

d. Pump Intake

The gas and liquid stream function are assumed evenly increased. Therefore, the following set of equations will define the stream function fields in this boundary:

$$\varphi_{g_{i,j}} - \left(1 - \frac{(j - JB)}{(JA - JB)}\right) \varphi_{g_{i,JB}} - \frac{(j - JB)}{(JA - JB)} \varphi_{g_{i,JA}} = 0, \quad (\text{E.16})$$

$$\varphi_{l,i,j} - \left(1 - \frac{(j-JB)}{(JA-JB)}\right) \varphi_{l,i,JB} - \frac{(j-JB)}{(JA-JB)} \varphi_{l,i,JA} = 0, \quad (E.17)$$

valid for $i=1; j=JB+1, \dots, JA-1$.

Pressure field

The governing equation for pressure is given by the following set of equations:

$$\begin{aligned} \frac{\partial^2 P^*}{\partial r^2} + \frac{\partial^2 P^*}{\partial z^2} = & -\frac{\rho_g}{r} \left[-\frac{1}{r} \left(\frac{\partial \hat{\varphi}_g}{\partial z} \frac{\partial \hat{V}_{gr}}{\partial r} - \frac{\partial \hat{\varphi}_g}{\partial r} \frac{\partial \hat{V}_{gr}}{\partial z} \right) + \frac{\partial^2 \hat{\varphi}_g}{\partial r \partial z} \left(\frac{\partial \hat{V}_{gr}}{\partial r} - \frac{\partial \hat{V}_{gz}}{\partial z} \right) + \frac{\partial \hat{\varphi}_g}{\partial z} \left(\frac{\partial^2 \hat{V}_{gr}}{\partial r^2} + \frac{\partial^2 \hat{V}_{gz}}{\partial r \partial z} \right) - \left(\frac{\partial^2 \hat{\varphi}_g}{\partial r^2} \frac{\partial \hat{V}_{gr}}{\partial z} - \frac{\partial^2 \hat{\varphi}_g}{\partial z^2} \frac{\partial \hat{V}_{gz}}{\partial r} \right) - \frac{\partial \hat{\varphi}_g}{\partial r} \left(\frac{\partial^2 \hat{V}_{gr}}{\partial r \partial z} + \frac{\partial^2 \hat{V}_{gz}}{\partial z^2} \right) \right] \\ & -\frac{\rho_l}{r} \left[-\frac{1}{r} \left(\frac{\partial \hat{\varphi}_l}{\partial z} \frac{\partial \hat{V}_{lr}}{\partial r} - \frac{\partial \hat{\varphi}_l}{\partial r} \frac{\partial \hat{V}_{lr}}{\partial z} \right) + \frac{\partial^2 \hat{\varphi}_l}{\partial r \partial z} \left(\frac{\partial \hat{V}_{lr}}{\partial r} - \frac{\partial \hat{V}_{lz}}{\partial z} \right) + \frac{\partial \hat{\varphi}_l}{\partial z} \left(\frac{\partial^2 \hat{V}_{lr}}{\partial r^2} + \frac{\partial^2 \hat{V}_{lz}}{\partial r \partial z} \right) - \left(\frac{\partial^2 \hat{\varphi}_l}{\partial r^2} \frac{\partial \hat{V}_{lr}}{\partial z} - \frac{\partial^2 \hat{\varphi}_l}{\partial z^2} \frac{\partial \hat{V}_{lz}}{\partial r} \right) - \frac{\partial \hat{\varphi}_l}{\partial r} \left(\frac{\partial^2 \hat{V}_{lr}}{\partial r \partial z} + \frac{\partial^2 \hat{V}_{lz}}{\partial z^2} \right) \right] \end{aligned} \quad (E.18)$$

$$\frac{\partial P^*}{\partial r} = -\frac{\rho_g}{r} \left(\frac{\partial \hat{\varphi}_g}{\partial z} \frac{\partial \hat{V}_{gr}}{\partial r} - \frac{\partial \hat{\varphi}_g}{\partial r} \frac{\partial \hat{V}_{gr}}{\partial z} \right) - \frac{\rho_l}{r} \left(\frac{\partial \hat{\varphi}_l}{\partial z} \frac{\partial \hat{V}_{lr}}{\partial r} - \frac{\partial \hat{\varphi}_l}{\partial r} \frac{\partial \hat{V}_{lr}}{\partial z} \right), \quad (E.19)$$

$$\frac{\partial P^*}{\partial z} = -\frac{\rho_g}{r} \left(\frac{\partial \hat{\varphi}_g}{\partial z} \frac{\partial \hat{V}_{gz}}{\partial r} - \frac{\partial \hat{\varphi}_g}{\partial r} \frac{\partial \hat{V}_{gz}}{\partial z} \right) - \frac{\rho_l}{r} \left(\frac{\partial \hat{\varphi}_l}{\partial z} \frac{\partial \hat{V}_{lz}}{\partial r} - \frac{\partial \hat{\varphi}_l}{\partial r} \frac{\partial \hat{V}_{lz}}{\partial z} \right). \quad (E.20)$$

The discretization of Eqs. E.18 - E.20 is shown in next sections, as follows:

Core Region:

From Eq. E.18, the left hand side is discretized inside the flow domain, using five points, by:

$$LHS = \frac{P_{i+1,j}^* - 2P_{i,j}^* + P_{i-1,j}^*}{(\Delta r)^2} + \frac{P_{i,j+1}^* - 2P_{i,j}^* + P_{i,j-1}^*}{(\Delta z)^2}, \quad (E.21)$$

On the other hand, the derivatives of the right hand side of Eq. E.18 are given by:

$$\left. \frac{\partial \hat{\varphi}_g}{\partial z} \right|_{i,j} = \frac{\hat{\varphi}_{g_{i,j+1}} - \hat{\varphi}_{g_{i,j-1}}}{2 (\Delta z)}, \quad (\text{E.22})$$

$$\left. \frac{\partial \hat{\varphi}_l}{\partial z} \right|_{i,j} = \frac{\hat{\varphi}_{l_{i,j+1}} - \hat{\varphi}_{l_{i,j-1}}}{2 (\Delta z)}, \quad (\text{E.23})$$

$$\left. \frac{\partial \hat{V}_{gr}}{\partial r} \right|_{i,j} = \frac{\hat{V}_{gr_{i,j}} - \hat{V}_{gr_{i-1,j}}}{2 (\Delta r)}, \quad (\text{E.24})$$

$$\left. \frac{\partial \hat{V}_{lr}}{\partial r} \right|_{i,j} = \frac{\hat{V}_{lr_{i,j}} - \hat{V}_{lr_{i-1,j}}}{2 (\Delta r)}, \quad (\text{E.25})$$

$$\left. \frac{\partial \hat{\varphi}_g}{\partial r} \right|_{i,j} = \frac{\hat{\varphi}_{g_{i+1,j}} - \hat{\varphi}_{g_{i-1,j}}}{2 (\Delta r)}, \quad (\text{E.26})$$

$$\left. \frac{\partial \hat{\varphi}_l}{\partial r} \right|_{i,j} = \frac{\hat{\varphi}_{l_{i+1,j}} - \hat{\varphi}_{l_{i-1,j}}}{2 (\Delta r)}, \quad (\text{E.27})$$

$$\left. \frac{\partial \hat{V}_{gr}}{\partial z} \right|_{i,j} = \frac{\hat{V}_{gr_{i,j+1}} - \hat{V}_{gr_{i,j-1}}}{2 (\Delta z)}, \quad (\text{E.28})$$

$$\left. \frac{\partial \hat{V}_{lr}}{\partial z} \right|_{i,j} = \frac{\hat{V}_{lr_{i,j+1}} - \hat{V}_{lr_{i,j-1}}}{2 (\Delta z)}, \quad (\text{E.29})$$

$$\left. \frac{\partial^2 \hat{\varphi}_g}{\partial r \partial z} \right|_{i,j} = \frac{\hat{\varphi}_{g_{i+1,j+1}} - \hat{\varphi}_{g_{i-1,j+1}} - \hat{\varphi}_{g_{i+1,j-1}} + \hat{\varphi}_{g_{i-1,j-1}}}{4 (\Delta r) (\Delta z)}, \quad (\text{E.30})$$

$$\left. \frac{\partial^2 \hat{\varphi}_l}{\partial r \partial z} \right|_{i,j} = \frac{\hat{\varphi}_{l_{i+1,j+1}} - \hat{\varphi}_{l_{i-1,j+1}} - \hat{\varphi}_{l_{i+1,j-1}} + \hat{\varphi}_{l_{i-1,j-1}}}{4 (\Delta r) (\Delta z)}, \quad (\text{E.31})$$

$$\left. \frac{\partial \hat{V}_{gr}}{\partial r} \right|_{i,j} = \frac{\hat{V}_{gr_{i+1,j}} - \hat{V}_{gr_{i-1,j}}}{2 (\Delta r)}, \quad (\text{E.32})$$

$$\left. \frac{\partial \hat{V}_{lr}}{\partial r} \right|_{i,j} = \frac{\hat{V}_{lr_{i+1,j}} - \hat{V}_{lr_{i-1,j}}}{2 (\Delta r)}, \quad (\text{E.33})$$

$$\left. \frac{\partial \hat{V}_{gz}}{\partial z} \right|_{i,j} = \frac{\hat{V}_{gz_{i,j+1}} - \hat{V}_{gz_{i,j-1}}}{2 (\Delta z)}, \quad (\text{E.34})$$

$$\left. \frac{\partial \hat{V}_{lz}}{\partial z} \right|_{i,j} = \frac{\hat{V}_{lz_{i,j+1}} - \hat{V}_{lz_{i,j-1}}}{2 (\Delta z)}, \quad (\text{E.35})$$

$$\left. \frac{\partial \hat{\varphi}_g}{\partial z} \right|_{i,j} = \frac{\hat{\varphi}_{g_{i,j+1}} - \hat{\varphi}_{g_{i,j-1}}}{2 (\Delta z)}, \quad (\text{E.36})$$

$$\left. \frac{\partial \hat{\varphi}_l}{\partial z} \right|_{i,j} = \frac{\hat{\varphi}_{l_{i,j+1}} - \hat{\varphi}_{l_{i,j-1}}}{2 (\Delta z)}, \quad (\text{E.37})$$

$$\left. \frac{\partial^2 \hat{V}_{gr}}{\partial r^2} \right|_{i,j} = \frac{\hat{V}_{gr_{i+1,j}} - 2 \hat{V}_{gr_{i,j}} + \hat{V}_{gr_{i-1,j}}}{(\Delta r)^2}, \quad (\text{E.38})$$

$$\left. \frac{\partial^2 \hat{V}_{lr}}{\partial r^2} \right|_{i,j} = \frac{\hat{V}_{lr_{i+1,j}} - 2 \hat{V}_{lr_{i,j}} + \hat{V}_{lr_{i-1,j}}}{(\Delta r)^2}, \quad (\text{E.39})$$

$$\left. \frac{\partial^2 \hat{V}_{gz}}{\partial r \partial z} \right|_{i,j} = \frac{\hat{V}_{gz_{i+1,j+1}} - \hat{V}_{gz_{i+1,j-1}} - \hat{V}_{gz_{i-1,j+1}} + \hat{V}_{gz_{i-1,j-1}}}{4 (\Delta r) (\Delta z)}, \quad (\text{E.40})$$

$$\left. \frac{\partial^2 \hat{V}_{lz}}{\partial r \partial z} \right|_{i,j} = \frac{\hat{V}_{lz_{i+1,j+1}} - \hat{V}_{lz_{i+1,j-1}} - \hat{V}_{lz_{i-1,j+1}} + \hat{V}_{lz_{i-1,j-1}}}{4 (\Delta r) (\Delta z)}, \quad (\text{E.41})$$

$$\left. \frac{\partial^2 \hat{\varphi}_g}{\partial r^2} \right|_{i,j} = \frac{\hat{\varphi}_{g_{i+1,j}} - 2\hat{\varphi}_{g_{i,j}} + \hat{\varphi}_{g_{i-1,j}}}{(\Delta r)^2}, \quad (\text{E.42})$$

$$\left. \frac{\partial^2 \hat{\varphi}_l}{\partial r^2} \right|_{i,j} = \frac{\hat{\varphi}_{l_{i+1,j}} - 2\hat{\varphi}_{l_{i,j}} + \hat{\varphi}_{l_{i-1,j}}}{(\Delta r)^2}, \quad (\text{E.43})$$

$$\left. \frac{\partial \hat{V}_{gr}}{\partial z} \right|_{i,j} = \frac{\hat{V}_{g\eta_{i,j+1}} - \hat{V}_{g\eta_{i,j-1}}}{2(\Delta z)}, \quad (\text{E.44})$$

$$\left. \frac{\partial \hat{V}_{lr}}{\partial z} \right|_{i,j} = \frac{\hat{V}_{lr_{i,j+1}} - \hat{V}_{lr_{i,j-1}}}{2(\Delta z)}, \quad (\text{E.45})$$

$$\left. \frac{\partial^2 \hat{\varphi}_g}{\partial z^2} \right|_{i,j} = \frac{\hat{\varphi}_{g_{i,j+1}} - 2\hat{\varphi}_{g_{i,j}} + \hat{\varphi}_{g_{i,j-1}}}{(\Delta z)^2}, \quad (\text{E.46})$$

$$\left. \frac{\partial^2 \hat{\varphi}_l}{\partial z^2} \right|_{i,j} = \frac{\hat{\varphi}_{l_{i,j+1}} - 2\hat{\varphi}_{l_{i,j}} + \hat{\varphi}_{l_{i,j-1}}}{(\Delta z)^2}, \quad (\text{E.47})$$

$$\left. \frac{\partial \hat{V}_{gz}}{\partial r} \right|_{i,j} = \frac{\hat{V}_{gz_{i+1,j}} - \hat{V}_{gz_{i-1,j}}}{2(\Delta r)}, \quad (\text{E.48})$$

$$\left. \frac{\partial \hat{V}_{lz}}{\partial r} \right|_{i,j} = \frac{\hat{V}_{lz_{i+1,j}} - \hat{V}_{lz_{i-1,j}}}{2(\Delta r)}, \quad (\text{E.49})$$

$$\left. \frac{\partial \hat{\varphi}_g}{\partial r} \right|_{i,j} = \frac{\hat{\varphi}_{g_{i+1,j}} - \hat{\varphi}_{g_{i-1,j}}}{2(\Delta r)}, \quad (\text{E.50})$$

$$\left. \frac{\partial \hat{\varphi}_l}{\partial r} \right|_{i,j} = \frac{\hat{\varphi}_{l_{i+1,j}} - \hat{\varphi}_{l_{i-1,j}}}{2(\Delta r)}, \quad (\text{E.51})$$

$$\left. \frac{\partial^2 \hat{V}_{gr}}{\partial r \partial z} \right|_{i,j} = \frac{\hat{V}_{gr_{i+1,j+1}} - \hat{V}_{gr_{i+1,j-1}} - \hat{V}_{gr_{i-1,j+1}} + \hat{V}_{gr_{i-1,j-1}}}{4 (\Delta r) (\Delta z)}, \quad (\text{E.52})$$

$$\left. \frac{\partial^2 \hat{V}_{lr}}{\partial r \partial z} \right|_{i,j} = \frac{\hat{V}_{lr_{i+1,j+1}} - \hat{V}_{lr_{i+1,j-1}} - \hat{V}_{lr_{i-1,j+1}} + \hat{V}_{lr_{i-1,j-1}}}{4 (\Delta r) (\Delta z)}, \quad (\text{E.53})$$

$$\left. \frac{\partial^2 \hat{V}_{gz}}{\partial z^2} \right|_{i,j} = \frac{\hat{V}_{gz_{i,j+1}} - 2 \hat{V}_{gz_{i,j}} + \hat{V}_{gz_{i,j-1}}}{(\Delta z)^2}, \quad (\text{E.54})$$

$$\left. \frac{\partial^2 \hat{V}_{lz}}{\partial z^2} \right|_{i,j} = \frac{\hat{V}_{lz_{i,j+1}} - 2 \hat{V}_{lz_{i,j}} + \hat{V}_{lz_{i,j-1}}}{(\Delta z)^2}, \quad (\text{E.55})$$

Eqs. E.22 - E.55 are valid only for $i = 2, \dots, IT - 1$; $j = 2, \dots, JT - 1$.

Boundary Conditions:

a-. Annulus Inlet Boundary

A constant pressure is assumed along the inlet boundary, i.e.

$$P_{i,j}^* = P_{Inlet}, \quad (\text{E.56})$$

valid for $i = 1, \dots, IT$; $j = 1$.

b-. Casing Wall Boundary

The pressure gradient is determined from the r -momentum balance equation.

From Eq. E.19, the discretization is given by:

$$\left. \frac{\partial P^*}{\partial r} \right|_{i,j} = \frac{P_{i,j}^* - P_{i-1,j}^*}{(\Delta r)}, \quad (\text{E.57})$$

$$\left. \frac{\partial \hat{\varphi}_g}{\partial z} \right|_{i,j} = \frac{\hat{\varphi}_{g_{i,j+1}} - \hat{\varphi}_{g_{i,j-1}} - \hat{\varphi}_{g_{i-1,j-1}} + \hat{\varphi}_{g_{i-1,j+1}}}{4 (\Delta z)}, \quad (\text{E.58})$$

$$\left. \frac{\partial \hat{\varphi}_l}{\partial z} \right|_{i,j} = \frac{\hat{\varphi}_{l_{i,j+1}} - \hat{\varphi}_{l_{i,j-1}} - \hat{\varphi}_{l_{i-1,j-1}} + \hat{\varphi}_{l_{i-1,j+1}}}{4 (\Delta z)}, \quad (\text{E.59})$$

$$\left. \frac{\partial \hat{V}_{gr}}{\partial r} \right|_{i,j} = \frac{\hat{V}_{gr_{i,j}} - \hat{V}_{gr_{i-1,j}}}{(\Delta r)}, \quad (\text{E.60})$$

$$\left. \frac{\partial \hat{V}_{lr}}{\partial r} \right|_{i,j} = \frac{\hat{V}_{lr_{i,j}} - \hat{V}_{lr_{i-1,j}}}{(\Delta r)}, \quad (\text{E.61})$$

$$\left. \frac{\partial \hat{\varphi}_g}{\partial r} \right|_{i,j} = \frac{\hat{\varphi}_{g_{i,j}} - \hat{\varphi}_{g_{i-1,j}}}{(\Delta r)}, \quad (\text{E.62})$$

$$\left. \frac{\partial \hat{\varphi}_l}{\partial r} \right|_{i,j} = \frac{\hat{\varphi}_{l_{i,j}} - \hat{\varphi}_{l_{i-1,j}}}{(\Delta r)}, \quad (\text{E.63})$$

$$\left. \frac{\partial \hat{V}_{gr}}{\partial z} \right|_{i,j} = \frac{\hat{V}_{gr_{i,j+1}} - \hat{V}_{gr_{i,j-1}} - \hat{V}_{gr_{i-1,j-1}} + \hat{V}_{gr_{i-1,j+1}}}{4 (\Delta z)}, \quad (\text{E.64})$$

$$\left. \frac{\partial \hat{V}_{lr}}{\partial z} \right|_{i,j} = \frac{\hat{V}_{lr_{i,j+1}} - \hat{V}_{lr_{i,j-1}} - \hat{V}_{lr_{i-1,j-1}} + \hat{V}_{lr_{i-1,j+1}}}{4 (\Delta z)}. \quad (\text{E.65})$$

Eqs. E.57 - E.65 are valid for $i = IT$; $j = 2, \dots, JT - 1$.

c-. Upper/Lower Pump Wall and Pump Intake Boundaries

Similar to the casing wall boundary, the pressure gradient can be estimated from the r -momentum balance equation. The discretization of Eq. E.19 is given by:

$$\left. \frac{\partial P^*}{\partial r} \right|_{i,j} = \frac{P_{i+1,j}^* - P_{i,j}^*}{(\Delta r)}, \quad (\text{E.66})$$

$$\left. \frac{\partial \hat{\varphi}_g}{\partial z} \right|_{i,j} = \frac{\hat{\varphi}_{g_{i,j+1}} - \hat{\varphi}_{g_{i,j-1}} - \hat{\varphi}_{g_{i+1,j-1}} + \hat{\varphi}_{g_{i+1,j+1}}}{4 (\Delta z)}, \quad (\text{E.67})$$

$$\left. \frac{\partial \hat{\varphi}_l}{\partial z} \right|_{i,j} = \frac{\hat{\varphi}_{l_{i,j+1}} - \hat{\varphi}_{l_{i,j-1}} - \hat{\varphi}_{l_{i+1,j-1}} + \hat{\varphi}_{l_{i+1,j+1}}}{4 (\Delta z)}, \quad (\text{E.68})$$

$$\left. \frac{\partial \hat{V}_{gr}}{\partial r} \right|_{i,j} = \frac{\hat{V}_{gr_{i+1,j}} - \hat{V}_{gr_{i,j}}}{(\Delta r)}, \quad (\text{E.69})$$

$$\left. \frac{\partial \hat{V}_{lr}}{\partial r} \right|_{i,j} = \frac{\hat{V}_{lr_{i+1,j}} - \hat{V}_{lr_{i,j}}}{(\Delta r)}, \quad (\text{E.70})$$

$$\left. \frac{\partial \hat{\varphi}_g}{\partial r} \right|_{i,j} = \frac{\hat{\varphi}_{g_{i+1,j}} - \hat{\varphi}_{g_{i,j}}}{(\Delta r)}, \quad (\text{E.71})$$

$$\left. \frac{\partial \hat{\varphi}_l}{\partial r} \right|_{i,j} = \frac{\hat{\varphi}_{l_{i+1,j}} - \hat{\varphi}_{l_{i,j}}}{(\Delta r)}, \quad (\text{E.72})$$

$$\left. \frac{\partial \hat{V}_{gr}}{\partial z} \right|_{i,j} = \frac{\hat{V}_{gr_{i,j+1}} - \hat{V}_{gr_{i,j-1}} - \hat{V}_{gr_{i+1,j-1}} + \hat{V}_{gr_{i+1,j+1}}}{4 (\Delta z)}, \quad (\text{E.73})$$

$$\left. \frac{\partial \hat{V}_{lr}}{\partial z} \right|_{i,j} = \frac{\hat{V}_{lr_{i,j+1}} - \hat{V}_{lr_{i,j-1}} - \hat{V}_{lr_{i+1,j-1}} + \hat{V}_{lr_{i+1,j+1}}}{4 (\Delta z)}. \quad (\text{E.74})$$

Equations E.66 - E.74 are valid for $i = 1$ and $j = 2, \dots, JB$; $j = JA, \dots, JT$.

d-. Annulus Outlet Boundary

In this boundary, the pressure gradient is determined by the z -momentum balance equation. The discretization of Eq. E.20 is given by:

$$\left. \frac{\partial P^*}{\partial z} \right|_{i,j-1/2} = \frac{P_{i,j}^* - P_{i,j-1}^*}{(\Delta z)}, \quad (\text{E.75})$$

$$\left. \frac{\partial \hat{\varphi}_g}{\partial z} \right|_{i,j-1/2} = \frac{\hat{\varphi}_{g_{i,j}} - \hat{\varphi}_{g_{i,j-1}}}{(\Delta z)}, \quad (\text{E.76})$$

$$\left. \frac{\partial \hat{\varphi}_l}{\partial z} \right|_{i,j-1/2} = \frac{\hat{\varphi}_{l_{i,j}} - \hat{\varphi}_{l_{i,j-1}}}{(\Delta z)}, \quad (\text{E.77})$$

$$\left. \frac{\partial \hat{V}_{gz}}{\partial z} \right|_{i,j-1/2} = \frac{\hat{V}_{gz_{i,j}} - \hat{V}_{gz_{i,j-1}}}{(\Delta z)}, \quad (\text{E.78})$$

$$\left. \frac{\partial \hat{V}_{lz}}{\partial z} \right|_{i,j-1/2} = \frac{\hat{V}_{lz_{i,j}} - \hat{V}_{lz_{i,j-1}}}{(\Delta z)}. \quad (\text{E.79})$$

The derivatives of each one variable in the r -direction will depend on the position of each node in this boundary.

Point $i = IT$; $j = JT$,

$$\left. \frac{\partial \hat{\varphi}_g}{\partial r} \right|_{i,j-1/2} = \frac{3(\hat{\varphi}_{g_{i,j}} + \hat{\varphi}_{g_{i,j-1}}) - 4(\hat{\varphi}_{g_{i-1,j}} + \hat{\varphi}_{g_{i-1,j-1}}) + (\hat{\varphi}_{g_{i-2,j}} + \hat{\varphi}_{g_{i-2,j-1}})}{4(\Delta r)}, \quad (\text{E.80})$$

$$\left. \frac{\partial \hat{\varphi}_l}{\partial r} \right|_{i,j-1/2} = \frac{3(\hat{\varphi}_{l_{i,j}} + \hat{\varphi}_{l_{i,j-1}}) - 4(\hat{\varphi}_{l_{i-1,j}} + \hat{\varphi}_{l_{i-1,j-1}}) + (\hat{\varphi}_{l_{i-2,j}} + \hat{\varphi}_{l_{i-2,j-1}})}{4(\Delta r)}, \quad (\text{E.81})$$

$$\left. \frac{\partial \hat{V}_{gz}}{\partial r} \right|_{i,j-1/2} = \frac{3(\hat{V}_{gz_{i,j}} + \hat{V}_{gz_{i,j-1}}) - 4(\hat{V}_{gz_{i-1,j}} + \hat{V}_{gz_{i-1,j-1}}) + (\hat{V}_{gz_{i-2,j}} + \hat{V}_{gz_{i-2,j-1}})}{4(\Delta r)}, \quad (\text{E.82})$$

$$\left. \frac{\partial \hat{V}_{lz}}{\partial r} \right|_{i,j-1/2} = \frac{3(\hat{V}_{lz_{i,j}} + \hat{V}_{lz_{i,j-1}}) - 4(\hat{V}_{lz_{i-1,j}} + \hat{V}_{lz_{i-1,j-1}}) + (\hat{V}_{lz_{i-2,j}} + \hat{V}_{lz_{i-2,j-1}})}{4(\Delta r)}, \quad (\text{E.83})$$

Point $i = 1; j = JT$,

$$\left. \frac{\partial \hat{\varphi}_g}{\partial r} \right|_{i,j-1/2} = \frac{-3(\hat{\varphi}_{g_{i,j}} + \hat{\varphi}_{g_{i,j-1}}) + 4(\hat{\varphi}_{g_{i+1,j}} + \hat{\varphi}_{g_{i+1,j-1}}) - (\hat{\varphi}_{g_{i+2,j}} + \hat{\varphi}_{g_{i+2,j-1}})}{4(\Delta r)}, \quad (\text{E.84})$$

$$\left. \frac{\partial \hat{\varphi}_l}{\partial r} \right|_{i,j-1/2} = \frac{-3(\hat{\varphi}_{l_{i,j}} + \hat{\varphi}_{l_{i,j-1}}) + 4(\hat{\varphi}_{l_{i+1,j}} + \hat{\varphi}_{l_{i+1,j-1}}) - (\hat{\varphi}_{l_{i+2,j}} + \hat{\varphi}_{l_{i+2,j-1}})}{4(\Delta r)}, \quad (\text{E.85})$$

$$\left. \frac{\partial \hat{V}_{gz}}{\partial r} \right|_{i,j-1/2} = \frac{-3(\hat{V}_{gz_{i,j}} + \hat{V}_{gz_{i,j-1}}) + 4(\hat{V}_{gz_{i+1,j}} + \hat{V}_{gz_{i+1,j-1}}) - (\hat{V}_{gz_{i+2,j}} + \hat{V}_{gz_{i+2,j-1}})}{4(\Delta r)}, \quad (\text{E.86})$$

$$\left. \frac{\partial \hat{V}_{lz}}{\partial r} \right|_{i,j-1/2} = \frac{-3(\hat{V}_{lz_{i,j}} + \hat{V}_{lz_{i,j-1}}) + 4(\hat{V}_{lz_{i+1,j}} + \hat{V}_{lz_{i+1,j-1}}) - (\hat{V}_{lz_{i+2,j}} + \hat{V}_{lz_{i+2,j-1}})}{4(\Delta r)}, \quad (\text{E.87})$$

Points $i = 2, \dots, IT - 1; j = JT$,

$$\left. \frac{\partial \hat{\varphi}_g}{\partial r} \right|_{i,j-1/2} = \frac{\hat{\varphi}_{g_{i+1,j}} - \hat{\varphi}_{g_{i-1,j}} - \hat{\varphi}_{g_{i-1,j-1}} + \hat{\varphi}_{g_{i+1,j-1}}}{4(\Delta r)}, \quad (\text{E.88})$$

$$\left. \frac{\partial \hat{\varphi}_l}{\partial r} \right|_{i,j-1/2} = \frac{\hat{\varphi}_{l_{i+1,j}} - \hat{\varphi}_{l_{i-1,j}} - \hat{\varphi}_{l_{i-1,j-1}} + \hat{\varphi}_{l_{i+1,j-1}}}{4(\Delta r)}, \quad (\text{E.89})$$

$$\left. \frac{\partial \hat{V}_{gz}}{\partial r} \right|_{i,j-1/2} = \frac{\hat{V}_{gz_{i+1,j}} - \hat{V}_{gz_{i-1,j}} - \hat{V}_{gz_{i-1,j-1}} + \hat{V}_{gz_{i+1,j-1}}}{4(\Delta r)}, \quad (\text{E.90})$$

$$\left. \frac{\partial \hat{V}_{lz}}{\partial r} \right|_{i,j-1/2} = \frac{\hat{V}_{lz_{i+1,j}} - \hat{V}_{lz_{i-1,j}} - \hat{V}_{lz_{i-1,j-1}} + \hat{V}_{lz_{i+1,j-1}}}{4(\Delta r)}, \quad (\text{E.91})$$

Gas Void Fraction Field

The governing equation for the gas void fraction is obtained from the mass balance equation for the gas phase.

Assuming steady state conditions, this equation for α_g is given by:

$$\beta \alpha_g + \frac{\partial}{\partial r}(\alpha_g \hat{V}_{gr}) + \frac{\partial}{\partial z}(\alpha_g \hat{V}_{gz}) = \beta \hat{\alpha}_g - \frac{1}{r}(\hat{\alpha}_g \hat{V}_{gr}), \quad (\text{E.92})$$

where β is a relaxation factor. The discretization of Eq. E.92 inside the flow domain depends on the gas velocity direction in the radial and vertical direction and will be defined according to the following methodology.

Core Region:

$$\text{if } \hat{V}_{gr,j} \geq 0 \text{ then } \left. \frac{\partial(\alpha_g \hat{V}_{gr})}{\partial r} \right|_{i,j} = \frac{\alpha_{g,i,j} \hat{V}_{gr,i,j} - \alpha_{g,i-1,j} \hat{V}_{gr,i-1,j}}{(\Delta r)}, \quad (\text{E.93})$$

$$\text{if } \hat{V}_{gr,j} < 0 \text{ then } \left. \frac{\partial(\alpha_g \hat{V}_{gr})}{\partial r} \right|_{i,j} = \frac{\alpha_{g,i+1,j} \hat{V}_{gr,i+1,j} - \alpha_{g,i,j} \hat{V}_{gr,i,j}}{(\Delta r)}, \quad (\text{E.94})$$

$$\text{if } \hat{V}_{gz,j} \geq 0 \text{ then } \left. \frac{\partial(\alpha_g \hat{V}_{gz})}{\partial z} \right|_{i,j} = \frac{\alpha_{g,i,j} \hat{V}_{gz,i,j} - \alpha_{g,i,j-1} \hat{V}_{gz,i,j-1}}{(\Delta z)}, \quad (\text{E.95})$$

$$\text{if } \hat{V}_{gz,j} < 0 \text{ then } \left. \frac{\partial(\alpha_g \hat{V}_{gz})}{\partial z} \right|_{i,j} = \frac{\alpha_{g,i,j+1} \hat{V}_{gz,i,j+1} - \alpha_{g,i,j} \hat{V}_{gz,i,j}}{(\Delta z)}, \quad (\text{E.96})$$

valid for $i = 2, \dots, IT - 1$; $j = 2, \dots, JT - 1$.

Boundary Conditions:

a. Annulus Inlet Boundary

The gas void fraction in the inlet is considered constant along to this boundary and given by:

$$\alpha_g = \alpha_{g \text{ Inlet}}, \quad (\text{E.97})$$

where $\alpha_{g \text{ Inlet}}$ represents a boundary condition constant and known in the annulus inlet.

b. Casing Wall Boundary

The derivatives are conditioned as follows:

$$\left. \frac{\partial(\alpha_g \hat{V}_{gr})}{\partial r} \right|_{i,j} = \frac{\alpha_{g_{i,j}} \hat{V}_{gr_{i,j}} - \alpha_{g_{i-1,j}} \hat{V}_{gr_{i-1,j}}}{(\Delta r)}, \quad (\text{E.98})$$

$$\text{if } \hat{V}_{gz_{i,j}} \geq 0 \text{ then } \left. \frac{\partial(\alpha_g \hat{V}_{gz})}{\partial z} \right|_{i,j} = \frac{\alpha_{g_{i,j}} \hat{V}_{gz_{i,j}} - \alpha_{g_{i,j-1}} \hat{V}_{gz_{i,j-1}}}{(\Delta z)}, \quad (\text{E.99})$$

$$\text{if } \hat{V}_{gz_{i,j}} < 0 \text{ then } \left. \frac{\partial(\alpha_g \hat{V}_{gz})}{\partial z} \right|_{i,j} = \frac{\alpha_{g_{i,j+1}} \hat{V}_{gz_{i,j+1}} - \alpha_{g_{i,j}} \hat{V}_{gz_{i,j}}}{(\Delta z)}, \quad (\text{E.100})$$

valid for $i = IT ; j = 2, \dots, JT - 1$.

c. Upper/Lower Pump Wall and Pump Intake Boundaries

In this boundary, the derivatives are conditioned as follow:

$$\left. \frac{\partial(\alpha_g \hat{V}_{gr})}{\partial r} \right|_{i,j} = \frac{\alpha_{g_{i+1,j}} \hat{V}_{gr_{i+1,j}} - \alpha_{g_{i,j}} \hat{V}_{gr_{i,j}}}{(\Delta r)}, \quad (\text{E.101})$$

$$\text{if } \hat{V}_{gz_{i,j}} \geq 0 \text{ then } \left. \frac{\partial(\alpha_g \hat{V}_{gz})}{\partial z} \right|_{i,j} = \frac{\alpha_{g_{i,j}} \hat{V}_{gz_{i,j}} - \alpha_{g_{i,j-1}} \hat{V}_{gz_{i,j-1}}}{(\Delta z)}, \quad (\text{E.102})$$

$$\text{if } \hat{V}_{gz_{i,j}} < 0 \text{ then } \left. \frac{\partial(\alpha_g \hat{V}_{gz})}{\partial z} \right|_{i,j} = \frac{\alpha_{g_{i,j+1}} \hat{V}_{gz_{i,j+1}} - \alpha_{g_{i,j}} \hat{V}_{gz_{i,j}}}{(\Delta z)}, \quad (\text{E.103})$$

valid for $i = 1 ; j = 2, \dots, JT - 1$.

d. Annulus Outlet Boundary

Fully developed flow is considered in this boundary. Therefore, the following condition results valid:

$$\alpha_{g_{i,j}} - \alpha_{g_{i,j-1}} = 0, \quad (\text{E.104})$$

valid for $i = 1, \dots, IT ; j = JT$.

Additional Equations

Liquid Velocity Field Solution

The liquid velocity field can be obtained by using the liquid stream function values, previously calculated at the primary grid.

Core Region:

Using a central finite difference approximation, the liquid velocity fields in the r and z -direction are given, respectively, by:

$$\hat{V}_{lr} \Big|_{i,j} = \frac{1}{r_i (1 - \hat{\alpha}_{g_{i,j}})} \frac{\hat{\varphi}_{g_{i,j+1}} - \hat{\varphi}_{g_{i,j-1}}}{2 (\Delta z)}, \quad (\text{E.105})$$

$$\hat{V}_{lz} \Big|_{i,j} = -\frac{1}{r_i (1 - \hat{\alpha}_{g_{i,j}})} \frac{\hat{\varphi}_{l_{i+1,j}} - \hat{\varphi}_{l_{i-1,j}}}{2 (\Delta r)}, \quad (\text{E.106})$$

valid for $i = 2, \dots, IT - 1$; $j = 2, \dots, JT - 1$.

Boundary Conditions:

a-. Annulus Inlet Boundary

In the radial direction, no r -component is assumed. Therefore, the following condition results valid:

$$\hat{V}_{lr} \Big|_{i,j} = 0, \quad (\text{E.107})$$

valid for $i = 1, \dots, IT$; $j = 1$. In the vertical direction, the liquid velocity is given by:

$$\hat{V}_{lz} \Big|_{i,j} = -\frac{1}{r_i (1 - \hat{\alpha}_{g_{i,j}})} \frac{\hat{\varphi}_{l_{i+1,j}} - \hat{\varphi}_{l_{i-1,j}}}{2 (\Delta r)}, \quad (\text{E.108})$$

valid for $i = 2, \dots, IT - 1; j = 1$.

b-. Casing Wall Boundary

In this boundary, no r -component is assumed. Therefore, the liquid velocity is given, similar to Eq. E.107, by:

$$\hat{V}_{lr} \Big|_{i,j} = 0,$$

valid for $i = IT; j = 1, \dots, JT$. In the vertical direction, the liquid velocity is located on a secondary grid. Therefore, the velocity is evaluated at the middle point between two primary nodes, by:

$$\hat{V}_{lz} \Big|_{i,j} = - \left[\frac{2}{(r_i - (\Delta r / 2)) (1 - ((\hat{\alpha}_{g_{i,j}} + \hat{\alpha}_{g_{i-1,j}}) / 2))} \frac{(\hat{\phi}_{l_{i,j}} - \hat{\phi}_{l_{i-1,j}})}{(\Delta r)} + \hat{V}_{lz_{i-1,j}} \right], \quad (\text{E.109})$$

valid for $i = IT; j = 2, \dots, JT$.

c-. Upper/Lower Pump Wall Boundary

Similar to the casing wall section, the liquid velocity is given by:

$$\hat{V}_{lr} \Big|_{i,j} = 0,$$

valid for the points $i = 1; j = 2, \dots, JB - 1$ and $i = 1; j = JA + 1, \dots, JT$.

$$\hat{V}_{lz} \Big|_{i,j} = - \left[\frac{2}{(r_i + (\Delta r / 2)) (1 - ((\hat{\alpha}_{g_{i,j}} + \hat{\alpha}_{g_{i+1,j}}) / 2))} \frac{(\hat{\phi}_{l_{i+1,j}} - \hat{\phi}_{l_{i,j}})}{(\Delta r)} + \hat{V}_{lz_{i+1,j}} \right], \quad (\text{E.110})$$

valid for $i = 1; j = 2, \dots, JB - 1$ and $i = 1; j = JA + 1, \dots, JT$.

d-. Pump Intake Boundary

The liquid velocity in the radial and vertical direction is given, respectively, by:

$$\hat{V}_{lr} \Big|_{i,j} = \frac{1}{r_i (1 - \hat{\alpha}_{g_{i,j}})} \frac{\hat{\varphi}_{g_{i,j+1}} - \hat{\varphi}_{g_{i,j-1}}}{2 (\Delta z)}, \quad (\text{E.111})$$

$$\hat{V}_{lz} \Big|_{i,j} = - \left[\frac{2}{(r_i + (\Delta r / 2)) (1 - ((\hat{\alpha}_{g_{i,j}} + \hat{\alpha}_{g_{i+1,j}}) / 2))} \frac{(\hat{\varphi}_{l_{i+1,j}} - \hat{\varphi}_{l_{i,j}})}{(\Delta r)} + \hat{V}_{lz_{i+1,j}} \right], \quad (\text{E.112})$$

valid for $i = 1; j = JB, \dots, JA$.

e-. Annulus Outlet Boundary

The liquid velocity in the radial direction is given by:

$$\hat{V}_{lr} \Big|_{i,j} = \left[\frac{2}{r_i (1 - ((\hat{\alpha}_{g_{i,j}} + \hat{\alpha}_{g_{i,j-1}}) / 2))} \frac{(\hat{\varphi}_{l_{i,j}} - \hat{\varphi}_{l_{i,j-1}})}{(\Delta z)} - \hat{V}_{lr_{i,j-1}} \right], \quad (\text{E.113})$$

valid for $i = 2, \dots, IT - 1; j = JT$. In the vertical direction, the liquid velocity is given by:

$$V_{lz} \Big|_{i,j} = \frac{1}{r_i (1 - \alpha_{g_{i,j}})} \frac{\varphi_{l_{i+1,j}} - \varphi_{l_{i-1,j}}}{2 (\Delta r)}, \quad (\text{E.114})$$

valid for $i = 2, \dots, IP - 1; j = JT$.

Pressure Gradient Field Solution

Core Region:

Using a central finite difference approximation, the derivative of total pressure can be estimated as:

$$\frac{\partial P^*}{\partial r} \Big|_{i,j} = \frac{P_{i+1,j}^* - P_{i-1,j}^*}{2 (\Delta r)}, \quad (\text{E.115})$$

$$\left. \frac{\partial P^*}{\partial z} \right|_{i,j} = \frac{P_{i,j+1}^* - P_{i,j-1}^*}{2(\Delta z)}, \quad (\text{E.116})$$

valid for $i = 2, \dots, IT - 1; j = 2, \dots, JT - 1$

Boundary Conditions:

a-. Annulus Inlet Boundary

In the radial direction, the following equation for the pressure gradient is given by:

$$\left. \frac{\partial P^*}{\partial r} \right|_{i,j} = \frac{P_{i+1,j}^* - P_{i-1,j}^*}{2(\Delta r)}, \quad (\text{E.117})$$

valid for $i = 2, \dots, IT - 1; j = 1$. In the vertical direction, the average definition allows the estimation of the pressure gradient at each node of the annulus inlet boundary, by:

$$\left. \frac{\partial P^*}{\partial z} \right|_{i,j} = \frac{2}{(\Delta z)} (P_{i,j+1}^* - P_{i,j}^*) - \left. \frac{\partial P^*}{\partial z} \right|_{i,j+1}, \quad (\text{E.118})$$

valid for $i = 1, \dots, IT; j = 1$.

b-. Casing Wall Boundary

In this boundary, the pressure gradient is governed by the following equations:

$$\left. \frac{\partial P^*}{\partial r} \right|_{i,j} = \frac{2}{(\Delta r)} (P_{i,j}^* - P_{i-1,j}^*) - \left. \frac{\partial P^*}{\partial r} \right|_{i-1,j}, \quad (\text{E.119})$$

valid for $i = IT; j = 1, \dots, JT$.

$$\left. \frac{\partial P^*}{\partial z} \right|_{i,j} = \frac{P_{i,j+1}^* - P_{i,j-1}^*}{2(\Delta z)}, \quad (\text{E.120})$$

valid for $i = IT; j = 2, \dots, JT - 1$.

c-. Upper/Lower Pump Wall and Pump Intake Boundaries

The pressure gradient in the radial and vertical direction is given, respectively, by:

$$\left. \frac{\partial P^*}{\partial r} \right|_{i,j} = \frac{2}{(\Delta r)} (P_{i+1,j}^* - P_{i,j}^*) - \left. \frac{\partial P^*}{\partial r} \right|_{i+1,j}, \quad (\text{E.121})$$

valid for $i = 1; j = 1, \dots, JT$.

$$\left. \frac{\partial P^*}{\partial z} \right|_{i,j} = \frac{P_{i,j+1}^* - P_{i,j-1}^*}{2(\Delta z)}, \quad (\text{E.122})$$

valid for $i = 1; j = 2, \dots, JT - 1$.

d-. Annulus Outlet Boundary

In the annulus outlet boundary, the pressure gradient in the radial and vertical direction is given, respectively, by:

$$\left. \frac{\partial P^*}{\partial r} \right|_{i,j} = \frac{P_{i+1,j}^* - P_{i-1,j}^*}{2(\Delta r)}, \quad (\text{E.123})$$

valid for $i = 2, \dots, IT - 1; j = JT$.

$$\left. \frac{\partial P^*}{\partial z} \right|_{i,j} = \frac{2}{(\Delta z)} (P_{i,j}^* - P_{i,j-1}^*) - \left. \frac{\partial P^*}{\partial z} \right|_{i,j-1}, \quad (\text{E.124})$$

valid for $i = 1, \dots, IT; j = JT$.

Gas Velocity Field Solution

The gas velocity field is estimated at each primary node, inside the flow domain, and according to the methodology proposed at Chapter VI. Equations for V_{gr} and V_{gz} are given, respectively, by:

$$V_{gr}|_{i,j} = -8 \frac{\hat{\alpha}_{g_{i,j}} (1 - \hat{\alpha}_{g_{i,j}}) (\rho_l - \rho_g)}{\hat{a}_{i,j} \hat{C}_{d\phi_{i,j}} \rho_l \hat{\rho}_{m_{i,j}} |\hat{V}_s|_{i,j}} \frac{\partial \hat{P}^*}{\partial r} \bigg|_{i,j} + \hat{V}_{lr} \bigg|_{i,j}, \quad (\text{E.125})$$

$$V_{gz}|_{i,j} = -8 \frac{\hat{\alpha}_{g_{i,j}} (1 - \hat{\alpha}_{g_{i,j}}) (\rho_l - \rho_g)}{\hat{a}_{i,j} \hat{C}_{d\phi_{i,j}} \rho_l \hat{\rho}_{m_{i,j}} |\hat{V}_s|_{i,j}} \left(\frac{\partial \hat{P}^*}{\partial z} \bigg|_{i,j} - ((1 - \hat{\alpha}_{g_{i,j}}) \rho_l + \hat{\alpha}_{g_{i,j}} \rho_g) g_z \right) + \hat{V}_{lz} \bigg|_{i,j}, \quad (\text{E.126})$$

valid for $i = 1, \dots, IT$; $j = 1, \dots, JT$. $\hat{\alpha}_{g_{i,j}}$ is obtained from the solutions of the system of equations. The liquid velocities and the pressure gradients are obtained from the liquid velocity and pressure gradient fields solutions, explained in previous sections, i.e.

$$\hat{V}_{lr} \bigg|_{i,j} = V_{lr}|_{i,j}, \quad (\text{E.127})$$

$$\hat{V}_{lz} \bigg|_{i,j} = V_{lz}|_{i,j}, \quad (\text{E.128})$$

$$\frac{\partial \hat{P}^*}{\partial r} \bigg|_{i,j} = \frac{\partial P^*}{\partial r} \bigg|_{i,j}, \quad (\text{E.129})$$

$$\frac{\partial \hat{P}^*}{\partial z} \bigg|_{i,j} = \frac{\partial P^*}{\partial z} \bigg|_{i,j}. \quad (\text{E.130})$$

The interfacial area concentration is calculated as:

$$\hat{\alpha}_{i,j} = 3 \frac{\hat{\alpha}_{g_{i,j}} (1 - \hat{\alpha}_{g_{i,j}})}{r_d}. \quad (\text{E.131})$$

The mixture density is given by:

$$\hat{\rho}_{m_{i,j}} = (1 - \hat{\alpha}_{g_{i,j}}) \rho_l + \hat{\alpha}_{g_{i,j}} \rho_g. \quad (\text{E.132})$$

The drag coefficient is estimated by using Ihme's correlation. This correlation is given by:

$$\hat{C}_{d\varphi_{i,j}} = \frac{24}{\hat{R} e_{\varphi_{i,j}}} + 5.48 \hat{R} e_{\varphi_{i,j}}^{-0.573} + 0.36, \quad (\text{E.133})$$

where

$$\hat{R} e_{\varphi_{i,j}} = \frac{2 r_d \rho_{m_{i,j}} \hat{V}_s|_{i,j}}{\mu_l}. \quad (\text{E.134})$$

Since an iterative method is required to estimate the gas velocity field, a convergence criterion is based on the resultant slip velocity, where $\left| V_s|_{i,j} - \hat{V}_s|_{i,j} \right| \leq \varepsilon$. In case

the criterion is not satisfied, $\hat{V}_s|_{i,j}$ will be estimated as:

$$\hat{V}_s|_{i,j} = V_s|_{i,j} = \sqrt{(V_{gr_{i,j}} - \hat{V}_{lr_{i,j}})^2 + (V_{gz_{i,j}} - \hat{V}_{lz_{i,j}})^2}. \quad (\text{E.135})$$

APPENDIX F

Gas Void Fraction in the Inlet Boundary

According to Prado (1995), the slip velocity between phases is given by:

$$V_s = -8 \frac{r_d}{r_{sm}} \frac{\alpha_g (1 - \alpha_g) (\rho_l - \rho_g) \nabla P}{a_i C_{d\infty} \rho_l \rho_m |\vec{V}_s|} - \frac{D_d^\alpha}{\alpha_g (1 - \alpha_g)} \nabla \alpha_g, \quad (\text{F.1})$$

where r_d and r_{sm} represent the drag radius and the Sauter mean radius, respectively. D represents the drift coefficient. a_i is defined as the interfacial area concentration. Gas and liquid densities are given by ρ_g and ρ_l , respectively. ρ_m represents the mixture density. α_g and P are defined as the gas void fraction and pressure, respectively.

Assuming spherical particles, no mass transfer and one-dimensional flow in the vertical direction only, the slip velocity can be expressed, from Eq. F.1, as:

$$V_{sz}^2 = -8 \frac{\alpha_g (1 - \alpha_g) (\rho_l - \rho_g)}{a_i C_{d\infty} \rho_l \rho_m} \frac{\partial P}{\partial z}. \quad (\text{F.2})$$

As shown in Appendix C, the pressure gradient for one-dimensional flow in the vertical direction is given by:

$$\frac{\partial P}{\partial z} = -\rho_m |g|. \quad (\text{F.3})$$

Therefore, the combination of Eqs. F.2 and F.3 permits obtaining the following equation for the slip velocity in the vertical direction:

$$V_{sz}^2 = 8 \frac{\alpha_g (1 - \alpha_g) (\rho_l - \rho_g) |g|}{a_i C_{d\infty} \rho_l}. \quad (\text{F.4})$$

On the other hand, the slip velocity definition is also given by:

$$V_{sz} = \frac{V_{sgz}^i}{\alpha_g} - \frac{V_{slz}^i}{(1 - \alpha_g)}. \quad (\text{F.5})$$

Therefore, the combination of Eqs. F.4 and F.5 allows defining the following relationship:

$$\left[\frac{V_{sgz}^i}{\alpha_g} - \frac{V_{slz}^i}{1 - \alpha_g} \right]^2 = 8 \frac{\alpha_g (1 - \alpha_g) (\rho_l - \rho_g) |g|}{a_i C_{d\infty} \rho_l}. \quad (\text{F.6})$$

Eq. F.6 can be also be rewritten as:

$$\frac{1}{8} a_i C_{d\infty} \rho_l \left[\frac{V_{sgz}^i}{\alpha_g} - \frac{V_{slz}^i}{1 - \alpha_g} \right]^2 - \alpha_g (1 - \alpha_g) (\rho_l - \rho_g) |g| = 0. \quad (\text{F.7})$$

Considering the velocity, density and interfacial area concentration units as in/sec , lbm/ft^3 and $1/in$, respectively, Eq. F.7 is finally given by:

$$\frac{1}{96} a_i C_{d\infty} \rho_l \left[\frac{V_{sgz}^i}{\alpha_g} - \frac{V_{slz}^i}{1 - \alpha_g} \right]^2 - \alpha_g (1 - \alpha_g) (\rho_l - \rho_g) |g| = 0. \quad (\text{F.8})$$

APPENDIX G

Error Calculations

The evaluation of this study was based on statistical parameters given by average percentage error $E1$, absolute average percentage error $E2$ and the standard deviation $E3$ defined by the following equations:

$$E1 = \left(\frac{1}{N} \sum_{i=1}^N e_{ri} \right) 100, \quad (G.1)$$

$$E2 = \left(\frac{1}{N} \sum_{i=1}^N |e_{ri}| \right) 100, \quad (G.2)$$

$$E3 = \sqrt{\left(\frac{1}{N-1} \sum_{i=1}^N \left(e_{ri} - \frac{E1}{100} \right)^2 \right)} 100. \quad (G.3)$$

where N and e_{ri} represent the number of data points and the error of each data point, respectively. The e_{ri} value is estimated by using the following equation:

$$e_{ri} = \frac{E_{cal,i} - E_{meas,i}}{E_{meas,i}}, \quad (G.4)$$

where $E_{meas,i}$ represents the measured natural separation efficiency and $E_{cal,i}$ represents the calculated or predicted natural separation efficiency.